An Investigation of Contoured Wall Injectors for Hypervelocity Mixing Augmentation

Thesis by

Ian A. Waitz

In partial fulfillment of the requirements
for the degree of

Doctor of Philosophy

California Institute of Technology

Pasadena, California

1991

(defended May 17, 1991)

Acknowledgements

Foremost I thank my wife, Lisa, for providing much needed distractions and constant support and understanding. I thank my father, for instilling in me a love of science and nature, and my mother, for teaching me that there is more to life than science and nature.

Most of the real learning at Caltech occurs at the blackboards in the offices. I thank my friends for all of the discussions and help. I also express gratitude to my advisors: Edward Zukoski, for making my life at Caltech very easy, Frank Marble, for being as interested in the work as I was, and Toshi Kubota, for many patient discussions. Also, I greatly appreciate the willingness of the other members of the faculty, without exception, to stop what they were doing and provide advice. Thank you to Dorothy Eckerman and to the staff of the Aero shop.

Funding for this work was provided largely through NASA Grant NAG 1-842. I thank Dennis Bushnell for initiating the effort and providing continued guidance. Conducting research on two coasts would not have been possible without help from many members of the staff at NASA Langley Research Center, particularly members of the Experimental Flow Physics Branch (especially Mike Walsh, Ben Anders and Steve Robinson), the High Reynolds Number Mach 6 Wind-Tunnel technicians, John Ellis and Rick Clark, members of the Computational Methods Branch (especially Mark Carpenter and Ajay Kumar), and members of the Instrument Research Division's Optical Spectroscopy Section (especially Behrooz Shirinzadeh and Jeff Balla). Computing support for these efforts was provided by the following facilities: JPL/Caltech Cray, San Diego Supercomputer Center via a National Science Foundation Grant, NASA Ames NAS Supercomputing Facilities, and the NASA Langley Supercomputing Facilities.

Abstract

A parametric study of a class of contoured wall fuel injectors is presented. The injectors were aimed at enabling shock-enhanced mixing for the supersonic combustion ramjet engines currently envisioned for applications on hypersonic vehicles. Short combustor residence time, a requirement for fuel injection parallel to the freestream, and strong sensitivity of overall vehicle performance to combustion efficiency motivated the investigation. Several salient parametric dependencies were investigated. Injector performance was evaluated in terms of mixing, losses, jet penetration and heating considerations.

A large portion of the research involved a series of tests conducted at the NASA Langley High - Reynolds Number Mach 6 Wind-Tunnel. Helium was used as an injectant gas to simulate hydrogen fuel. The parameters investigated include injector spacing, boundary layer height, and injectant to freestream pressure and velocity ratios. Conclusions concerning injector performance and parameter dependencies are supported by extensive three-dimensional flow field surveys as well as data from a variety of flow visualization techniques including Rayleigh scattering, Schlieren, spark-shadowgraph, and surface oil flow.

As an adjunct to these experiments, a three-dimensional Navier-Stokes solver was used to conduct a parametric study which closely tracked the experimental effort. The results of these investigations strongly complemented the experimental work. Use of the code also allowed research beyond the fairly rigid bounds of the experimental test matrix. These studies included both basic investigations of shock-enhanced mixing on generic injectors, and applied efforts such as combining film-cooling with the contoured wall injectors.

Location of an oblique shock at the base of the injection plane was found to be a loss-effective method for enhancing hypervelocity mixing through baroclinic generation of vorticity and subsequent convection and diffusion. Injector performance was strongly dependent on the displacement effect of the hypersonic boundary layer which acted to modify the effective wall geometry. Strong dependence on injectant to freestream pressure ratio was also displayed. Mixing enhancement related to interaction of the unsteady component of the boundary layer with both steady and unsteady components of the flow field was found to be secondary, as were effects due to variation in mean shear between the injectant and the freestream in the exit plane.

Table of Contents

	page
Acknowledgements	iii
Abstract	iv
List of Figures	x
Nomenclature	xxiii
CHAPTER 1: INTRODUCTION	1
1.1 Motivation	1
1.2 Shock-enhanced mixing	2
1.3 The contoured wall fuel injector	4
1.4 Studies by other authors	5
1.5 Scope of the current investigation	7
1.5.1 Mixing and combustion	8
1.5.2 Experimental scope	9
1.5.3 Scope of the computational effort	11
CHAPTER 2: EXPERIMENTAL METHODS AND APPARATUS	13
2.1 The wind-tunnel and wind-tunnel subsystems	13
2.2 The wind-tunnel model	15
2.3 The data acquisition system	18
2.4 Three-dimensional flow field survey apparatus	19
2.4.1 Gas composition measurements	20

page

2.4.2 Cone static pressure measurements 28

2.4.3 Pitot pressure measurements 30

2.4.4 Total temperature measurements 30

2.5 Reduction of flow field survey data 31

2.6 Presentation of flow field survey data 35

2.7 Flow visualization techniques 36

2.7.1 Schlieren flow visualization 37

2.7.2 Shadowgraph flow visualization 37

2.7.3 Planar Rayleigh scattering 38

2.7.4 Surface oil flow visualization 40

CHAPTER 3: COMPUTATIONAL METHODOLOGY 41

3.1 Description of code 41

3.1.1 Governing equations 42

3.2 Application of the code 45

3.2.1 Grid generation 45

3.2.2 Boundary conditions 47

3.2.3 Turbulence modelling 47

3.2.4 Boundary layer modelling 48

CHAPTER 4: ANALYSIS OF EXPERIMENTAL AND COMPUTATIONAL DATA 50

4.1 Mixedness measure 50

4.2 Helium mass fraction contour lengths 51

page

4.3 Circulation 52

4.4 Decay of maximum helium mass fraction 52

4.5 Jet lift-off height 53

4.6 Entropy 54

CHAPTER 5: THE PARAMETRIC STUDY 57

5.1 Experimental 57

5.2 Computational 60

CHAPTER 6: DISCUSSION OF RESULTS 64

6.1 Baseline geometry and conditions 64

6.1.1 Flow field survey results 65

6.1.2 Data from the numerical simulation 68

6.1.3 Thoughts on sub grid-scale structure 71

6.1.4 Planar Rayleigh scattering data, the time-fluctuating flow field 72

6.1.5 Analysis of injector performance 75

6.2 Boundary layer/injector spacing effects 81

6.2.1 Experimental results 82

6.2.2 Data from numerical simulations 88

6.3 The influence of injectant/freestream pressure ratio 92

6.3.1 Experimental evidence 92

6.3.2 Computational modelling 94

6.4 Injectant/freestream velocity ratio effects 96

page

6.5 The roles of ramp-generated and baroclinically-generated vorticity in injector performance 99

6.6 Additional numerical investigations 103

6.6.1 Angled injection 104

6.6.2 Non-uniform injectant Mach number profile 104

6.6.3 Elevated injection 105

6.6.4 Addition of film-cooling to the injection scheme 105

CHAPTER 7: DESIGN RECOMMENDATIONS AND SUGGESTIONS FOR FURTHER STUDY 107

7.1 Comparison with other studies 107

7.1.1 General mixing performance 107

7.1.2 Other parallel injector configurations 108

7.1.3 Angled transverse wall injection 110

7.2 Recommendations 111

7.3 Unresolved influences and suggestions for further study 114

CHAPTER 8: CONCLUSIONS 116

REFERENCES 122

FIGURES 134

List of Figures

Figure		page
1.	Laser induced fluorescence images after normal shock impingement on a two-dimensional cylinder of helium. (Marble, *et al.* [1990])	135
2.	Schematic of vorticity generation process associated with shock impingement on light circular gas inhomogeneity.	136
3.	Schematic view of oblique shock passage through light gas cylinder imbedded in air.	137
4.	Diagram of contoured wall fuel injector and definition of axes.	138
5.	Photograph of wind-tunnel model with full-scale, narrow spacing, injector array installed.	139
6.	Three-view drawing of model in wind-tunnel.	140
7.	Photograph of model mounted in the NASA Langley High Reynolds Number Mach 6 Wind-Tunnel.	141
8.	Photographs of the wind-tunnel model.	142
9.	Photograph of the boundary layer trip plate.	143
10.	Cross-section view of injector region.	144
11.	Photograph of flow-field survey probes.	145
12.	Schematic of gas composition analyzer.	146
13.	Photograph of gas composition analyzer.	146
14.	Gas composition analyzer sensing device.	147

Figure page

15. a. Cone static pressure probe. 148

b. Pitot pressure probe.

c. Gas composition probe.

d. Total temperature probe.

16. Sample gas composition analyzer calibration data. 149

17. Gas composition analyzer interpolation technique. 150

18. Conical flow coordinate system and variables. 151

19. Experimental sampling grids, (scale 1:1). 152

20. Planar Rayleigh scattering experimental set-up. (Courtesy NASA Langley Research Center) 153

21. Computational grid for wide spacing, $\alpha_e = \alpha_c = 4.76^o$ geometry. 154

22. Computational grid for wide spacing, $\alpha_e = \alpha_c = 4.76^o$ geometry. 155

23. Shock development for two-dimensional smooth grid edge. 156

24. Shock development for two-dimensional rough grid edge. 156

25. Comparison of calculation methods for jet lift-off height. Wide spacing, $\overline{\delta} = 0.20$, $\overline{p} = 1.0$, $\overline{v} = 1.0$, $\alpha_c = \alpha_e = 4.76^o$ (computational). 157

26. Shadowgraph of injector flowfield. Wide spacing, $\overline{\delta} = 0.20$, $\overline{p} = 1.0$, $\overline{v} = 1.33$, $\alpha_c = \alpha_e = 4.76^o$. 158

27. Helium mass fraction. Full-scale model, wide spacing, natural boundary layer, $\overline{\delta} = 0.20$, $\overline{p} = 1.0$, $\overline{v} = 1.0$ (experimental). 159

28. Cone static pressure (psia). Full-scale model, wide spacing, natural boundary layer, $\overline{\delta} = 0.20$, $\overline{p} = 1.0$, $\overline{v} = 1.33$ (experimental). 160

29. Pitot pressure (psia). Full-scale model, wide spacing, natural boundary layer, $\overline{\delta} = 0.20$, $\overline{p} = 1.0$, $\overline{v} = 1.33$ (experimental). 161

Figure page

30. Total temperature (^{o}C). Full-scale model, wide spacing, natural boundary layer, $\overline{\delta}$ = 0.20, $\overline{p}$ = 1.0, $\overline{v}$ = 1.33 (experimental). 162

31. Mach number. Full-scale model, wide spacing, natural boundary layer, $\overline{\delta}$ = 0.20, $\overline{p}$ = 1.0, $\overline{v}$ = 1.33 (experimental). 163

32. Static pressure (psia). Full-scale model, wide spacing, natural boundary layer, $\overline{\delta}$ = 0.20, $\overline{p}$ = 1.0, $\overline{v}$ = 1.33 (experimental). 164

33. Static temperature (^{o}C). Full-scale model, wide spacing, natural boundary layer, $\overline{\delta}$ = 0.20, $\overline{p}$ = 1.0, $\overline{v}$ = 1.33 (experimental). 165

34. Density (lbm/in^{3}). Full-scale model, wide spacing, natural boundary layer, $\overline{\delta}$ = 0.20, $\overline{p}$ = 1.0, $\overline{v}$ = 1.0 (experimental). 166

35. Contours of constant helium mass fraction. Wide spacing, $\overline{\delta}$ = 0.20, $\overline{p}$ = 1.0, $\overline{v}$ = 1.0, $\alpha_c = \alpha_e = 4.76^{o}$ (computational). 167

36. Helium mass fraction. Wide spacing, $\overline{\delta}$ = 0.20, $\overline{p}$ = 1.0, $\overline{v}$ = 1.0, $\alpha_c = \alpha_e$ = 4.76^{o} (computational). 168

37. Mach number. Wide spacing, $\overline{\delta}$ = 0.20, $\overline{p}$ = 1.0, $\overline{v}$ = 1.0, $\alpha_c = \alpha_e = 4.76^{o}$ (computational). 169

38. Static pressure (psia). Wide spacing, $\overline{\delta}$ = 0.20, $\overline{p}$ = 1.0, $\overline{v}$ = 1.0, $\alpha_c = \alpha_e$ = 4.76^{o} (computational). 170

39. Static temperature (^{o}C). Wide spacing, $\overline{\delta}$ = 0.20, $\overline{p}$ = 1.0, $\overline{v}$ = 1.0, $\alpha_c = \alpha_e = 4.76^{o}$ (computational). 171

40. Density (lbm/in^{3}). Wide spacing, $\overline{\delta}$ = 0.20, $\overline{p}$ = 1.0, $\overline{v}$ = 1.0, $\alpha_c = \alpha_e$ = 4.76^{o} (computational). 172

41. Pitot pressure (psia). Wide spacing, $\overline{\delta}$ = 0.20, $\overline{p}$ = 1.0, $\overline{v}$ = 1.0, $\alpha_c = \alpha_e$ = 4.76^{o} (computational). 173

Figure		page
42.	Total temperature (^{o}C). Wide spacing, $\bar{\delta}$ = 0.20, $\bar{p}$ = 1.0, $\bar{v}$ = 1.0, $\alpha_c = \alpha_e$ = 4.76^{o} (computational).	174
43.	Vorticity, $\omega_x \left(\frac{h_i}{U_\infty}\right)$. Wide spacing, $\bar{\delta}$ = 0.20, $\bar{p}$ = 1.0, $\bar{v}$ = 1.0, $\alpha_c = \alpha_e$ = 4.76^{o} (computational).	175
44.	Far-field behavior. Wide spacing, $\bar{\delta}$ = 0.20, $\bar{p}$ = 1.0, $\bar{v}$ = 1.0, $\alpha_c = \alpha_e$ = 4.76^{o} (computational).	176
45.	Far-field behavior. Wide spacing, $\bar{\delta}$ = 0.20, $\bar{p}$ = 1.0, $\bar{v}$ = 1.0, $\alpha_c = \alpha_e$ = 4.76^{o} (computational).	177
46.	Particle traces. Wide spacing, $\bar{\delta}$ = 0.20, $\bar{p}$ = 1.0, $\bar{v}$ = 1.0, $\alpha_c = \alpha_e$ = 4.76^{o} (computational).	178
47.	Particle traces. Wide spacing, $\bar{\delta}$ = 0.20, $\bar{p}$ = 1.0, $\bar{v}$ = 1.0, $\alpha_c = \alpha_e$ = 4.76^{o} (computational).	179
48.	Particle traces. Wide spacing, $\bar{\delta}$ = 0.20, $\bar{p}$ = 1.0, $\bar{v}$ = 1.0, $\alpha_c = \alpha_e$ = 4.76^{o} (computational).	180
49.	Comparison of mean survey data with mean of 22 planar Rayleigh images at $\bar{x}$ = 10. Wide spacing, $\bar{\delta}$ = 0.20, $\bar{p}$ = 1.0, $\bar{v}$ = 1.33, $\alpha_c = \alpha_e$ = 4.76^{o} (experimental).	181
50.	Instantaneous planar Rayleigh images at $\bar{x}$ = 10. Wide spacing, $\bar{\delta}$ = 0.20, $\bar{p}$ = 1.0, $\bar{v}$ = 1.33, $\alpha_c = \alpha_e$ = 4.76^{o} (experimental).	182
51.	Mean of 22 planar Rayleigh images at $\bar{x}$ = 10. Wide spacing, $\bar{\delta}$ = 0.20, $\bar{p}$ = 1.0, $\bar{v}$ = 1.33, $\alpha_c = \alpha_e$ = 4.76^{o} (experimental).	183

Figure		page
52.	Standard deviation about the mean for planar Rayleigh images at $\overline{x}$ = 10. Wide spacing, $\overline{\delta}$ = 0.20, $\overline{p}$ = 1.0, $\overline{v}$ = 1.33, $\alpha_c = \alpha_e = 4.76^o$ (experimental).	183
53.	Jet lift-off. Wide spacing, thin boundary layer, $\overline{p}$ = 1.0, $\alpha_c = \alpha_e = 4.76^o$.	184
54.	Entropy measure. Wide spacing, $\overline{\delta}$ = 0.20, $\overline{p}$ = 1.0, $\overline{v}$ = 1.0, $\alpha_c = \alpha_e = 4.76^o$ (computational).	184
55.	Circulation. Wide spacing, $\overline{\delta}$ = 0.20, $\overline{p}$ = 1.0, $\overline{v}$ = 1.0, $\alpha_c = \alpha_e = 4.76^o$ (computational).	185
56.	Decay of maximum helium mass fraction. Wide spacing, thin boundary layer, $\overline{p}$ = 1.0, $\alpha_c = \alpha_e = 4.76^o$ (experimental).	185
57.	Mixedness measure. Wide spacing, $\overline{\delta}$ = 0.20, $\overline{p}$ = 1.0, $\overline{v}$ = 1.0, $\alpha_c = \alpha_e = 4.76^o$ (computational).	186
58.	Length of contours of constant mass fraction. Wide spacing, $\overline{\delta}$ = 0.20, $\overline{p}$ = 1.0, $\overline{v}$ = 1.0, $\alpha_c = \alpha_e = 4.76^o$ (computational).	187
59.	Shadowgraph of 'natural' boundary layer. $R_e = 15x10^6$ /ft.	188
60.	Shadowgraph of tripped boundary layer. $R_e = 15x10^6$ /ft.	188
61.	Shadowgraph of 'natural' boundary layer entering injector ramps. $R_e = 15x10^6$ /ft.	189
62.	Shadowgraph of tripped boundary layer entering injector ramps. $R_e = 15x10^6$ /ft.	189
63.	Helium mass fraction. Full-scale model, wide spacing, $\overline{\delta}$ = 0.35, $\overline{p}$ = 1.0, $\overline{v}$ = 1.33, $\alpha_c = \alpha_e = 4.76^o$ (experimental).	190
64.	Pitot pressure (psia). Full-scale model, wide spacing, $\overline{\delta}$ = 0.35, $\overline{p}$ = 1.0, $\overline{v}$ = 1.33, $\alpha_c = \alpha_e = 4.76^o$ (experimental).	191

Figure page

65. Total temperature (^{o}C). Full-scale model, wide spacing, $\overline{\delta}$ = 0.35, $\overline{p}$ = 1.0, $\overline{v}$ = 1.33, $\alpha_c = \alpha_e$ = 4.76^{o} (experimental). 192

66. Helium mass fraction. Half-scale model, wide spacing, $\overline{\delta}$ = 0.40, $\overline{p}$ = 1.0, $\overline{v}$ = 1.33, $\alpha_c = \alpha_e$ = 4.76^{o} (experimental). 193

67. Pitot pressure (psia). Half-scale model, wide spacing, $\overline{\delta}$ = 0.40, $\overline{p}$ = 1.0, $\overline{v}$ = 1.33, $\alpha_c = \alpha_e$ = 4.76^{o} (experimental). 194

68. Total temperature (^{o}C). Half-scale model, wide spacing, $\overline{\delta}$ = 0.40, $\overline{p}$ = 1.0, $\overline{v}$ = 1.33, $\alpha_c = \alpha_e$ = 4.76^{o} (experimental). 195

69. Helium mass fraction. Half-scale model, wide spacing, $\overline{\delta}$ = 0.70, $\overline{p}$ = 1.0, $\overline{v}$ = 1.33, $\alpha_c = \alpha_e$ = 4.76^{o} (experimental). 196

70. Pitot pressure (psia). Half-scale model, wide spacing, $\overline{\delta}$ = 0.70, $\overline{p}$ = 1.0, $\overline{v}$ = 1.33, $\alpha_c = \alpha_e$ = 4.76^{o} (experimental). 197

71. Total temperature (^{o}C). Half-scale model, wide spacing, $\overline{\delta}$ = 0.70, $\overline{p}$ = 1.0, $\overline{v}$ = 1.33, $\alpha_c = \alpha_e$ = 4.76^{o} (experimental). 198

72. Decay of maximum helium mass fraction for wide spacing geometry with boundary layers of various heights (experimental). 199

73. Mean of 22 planar Rayleigh images at $\overline{x}$ = 10. Wide spacing, $\overline{\delta}$ = 0.35, $\overline{p}$ = 1.0, $\overline{v}$ = 1.33, $\alpha_c = \alpha_e$ = 4.76^{o}. 200

74 Standard deviation about the mean for planar Rayleigh images at $\overline{x}$ = 10. Wide spacing, $\overline{\delta}$ = 0.20, $\overline{p}$ = 1.0, $\overline{v}$ = 1.33, $\alpha_c = \alpha_e$ = 4.76^{o}. 200

75. Instantaneous planar Rayleigh images at $\overline{x}$ = 10. Wide spacing, $\overline{\delta}$ = 0.35, $\overline{p}$ = 1.0, $\overline{v}$ = 1.33, $\alpha_c = \alpha_e$ = 4.76^{o}. 201

76. Surface oil flow photograph. Full-scale model, wide spacing, $\overline{\delta}$ = 0.20, $\overline{p}$ = 1.0, $\alpha_c = \alpha_e$ = 4.76^{o}. 202

Figure page

77. Surface oil flow photograph. Full-scale model, wide spacing, $\bar{\delta} = 0.20$, underexpanded jet, $\alpha_c = \alpha_e = 4.76^o$. 202

78. Surface oil flow photograph. Full-scale model, wide spacing, $\bar{\delta} = 0.20$, underexpanded jet, $\alpha_c = \alpha_e = 4.76^o$. 203

79. Schlieren photograph. Full-scale model, narrow spacing, $\bar{\delta} = 0.20$, $\bar{p} = 1.0$, $\alpha_c = \alpha_e = 4.76^o$. 204

80. Helium mass fraction. Full-scale model, narrow spacing, $\bar{\delta} = 0.20$, $\bar{p} = 1.0$, $\bar{v} = 1.33$, $\alpha_c = \alpha_e = 4.76^o$ (experimental). 205

81. Pitot pressure (psia). Full-scale model, narrow spacing, $\bar{\delta} = 0.20$, $\bar{p} = 1.0$, $\bar{v} = 1.33$, $\alpha_c = \alpha_e = 4.76^o$ (experimental). 206

82. Total temperature (^{o}C). Full-scale model, narrow spacing, $\bar{\delta} = 0.20$, $\bar{p} = 1.0$, $\bar{v} = 1.33$, $\alpha_c = \alpha_e = 4.76^o$ (experimental). 207

83. Helium mass fraction. Half-scale model, narrow spacing, $\bar{\delta} = 0.70$, $\bar{p} = 1.0$, $\bar{v} = 1.33$, $\alpha_c = \alpha_e = 4.76^o$ (experimental). 208

84. Pitot pressure (psia). Half-scale model, narrow spacing, $\bar{\delta} = 0.70$, $\bar{p} = 1.0$, $\bar{v} = 1.33$, $\alpha_c = \alpha_e = 4.76^o$ (experimental). 209

85. Total temperature (^{o}C). Half-scale model, narrow spacing, $\bar{\delta} = 0.70$, $\bar{p} = 1.0$, $\bar{v} = 1.33$, $\alpha_c = \alpha_e = 4.76^o$ (experimental). 210

86. Jet lift-off:boundary layer and injector spacing effects, (experimental). 211

87. Decay of maximum helium mass fraction for narrow spacing geometry with boundary layers of various heights (experimental). 212

88. Decay of maximum helium mass fraction for various spacings and boundary layer thicknesses (experimental). 213

Figure page

89. Contours of constant helium mass fraction, Wide spacing $\overline{\delta} = 0$ (inviscid b.c.), $\overline{p} = 1.0$, $\overline{v} = 1.0$, $\alpha_c = \alpha_e = 4.76^o$ (computational). 214

90. Contours of constant helium mass fraction, Wide spacing $\overline{\delta} = 1.0$, $\overline{p} = 1.0$, $\overline{v} = 1.0$, $\alpha_c = \alpha_e = 4.76^o$ (computational). 215

91. Contours of constant helium mass fraction, Narrow spacing $\overline{\delta} = 0$ (inviscid b.c.), $\overline{p} = 1.0$, $\overline{v} = 1.0$, $\alpha_c = \alpha_e = 4.76^o$ (computational). 216

92. Contours of constant helium mass fraction, Narrow spacing $\overline{\delta} = 0.2$, $\overline{p} = 1.0$, $\overline{v} = 1.0$, $\alpha_c = \alpha_e = 4.76^o$ (computational). 217

93. Contours of constant helium mass fraction, Narrow spacing $\overline{\delta} = 1.0$, $\overline{p} = 1.0$, $\overline{v} = 1.0$, $\alpha_c = \alpha_e = 4.76^o$ (computational). 218

94. Jet lift-off: Boundary layer and injector spacing effects, $\overline{p} = 1.0$, $\overline{v} = 1.0$, $\alpha_c = \alpha_e = 4.76^o$ (computational). 219

    a. finite thickness boundary layers

    b. inviscid boundary conditions

95. Circulation: Boundary layer and injector spacing effects, $\overline{p} = 1.0$, $\overline{v} = 1.0$, $\alpha_c = \alpha_e = 4.76^o$ (computational). 220

    a. finite thickness boundary layers

    b. inviscid boundary conditions

96. Mixedness measure for various spacings and boundary layer thicknesses, $\overline{p} = 1.0$, $\overline{v} = 1.0$, $\alpha_c = \alpha_e = 4.76^o$ (computational). 221

97. Length of contours of constant mass fraction for various spacings and boundary layer thicknesses, $\overline{p} = 1.0$, $\overline{v} = 1.0$, $\alpha_c = \alpha_e = 4.76^o$ (computational). 222

Figure page

98. Entropy measure for wide and narrow spacing, $\overline{\delta} = 0$ (inviscid b.c.), $\overline{p} = 1.0$, $\overline{v} = 1.0$, $\alpha_c = \alpha_e = 4.76^o$ (computational). 223

99. Entropy measure for various spacings and boundary layer thicknesses, $\overline{p} = 1.0$, $\overline{v} = 1.0$, $\alpha_c = \alpha_e = 4.76^o$ (computational). 224

100. Helium mass fraction. Full-scale model, wide spacing, $\overline{\delta} = 0.20$, $\overline{p} = 4.0$, $\overline{v} = 1.27$, $\alpha_c = \alpha_e = 4.76^o$ (experimental). 225

101. Pitot pressure (psia). Full-scale model, wide spacing, $\overline{\delta} = 0.20$, $\overline{p} = 4.0$, $\overline{v} = 1.27$, $\alpha_c = \alpha_e = 4.76^o$ (experimental). 226

102. Total temperature (^{o}C). Full-scale model, wide spacing, $\overline{\delta} = 0.20$, $\overline{p} = 4.0$, $\overline{v} = 1.27$, $\alpha_c = \alpha_e = 4.76^o$ (experimental). 227

103. Helium mass fraction. Half-scale model, wide spacing, $\overline{\delta} = 0.40$, $\overline{p} = 4.0$, $\overline{v} = 1.27$, $\alpha_c = \alpha_e = 4.76^o$ (experimental). 228

104. Pitot pressure (psia). Half-scale model, wide spacing, $\overline{\delta} = 0.40$, $\overline{p} = 4.0$, $\overline{v} = 1.27$, $\alpha_c = \alpha_e = 4.76^o$ (experimental). 229

105. Total temperature (^{o}C). Half-scale model, wide spacing, $\overline{\delta} = 0.40$, $\overline{p} = 4.0$, $\overline{v} = 1.27$, $\alpha_c = \alpha_e = 4.76^o$ (experimental). 230

106. Mean of 22 planar Rayleigh images at $\overline{x} = 10$. Wide spacing, $\overline{\delta} = 0.20$, $\overline{p} = 4.0$, $\overline{v} = 1.28$, $\alpha_c = \alpha_e = 4.76^o$. 231

107. Standard deviation about the mean for planar Rayleigh images at $\overline{x} = 10$. Wide spacing, $\overline{\delta} = 0.20$, $\overline{p} = 4.0$, $\overline{v} = 1.28$, $\alpha_c = \alpha_e = 4.76^o$. 231

108. Instantaneous planar Rayleigh images at $\overline{x} = 10$. Wide spacing, $\overline{\delta} = 0.20$, $\overline{p} = 4.0$, $\overline{v} = 1.28$, $\alpha_c = \alpha_e = 4.76^o$. 232

109. Decay of maximum helium mass fraction: Pressure ratio effects (experimental). 233

Figure page

110. Jet lift-off: Pressure ratio effects (experimental). 233

111. Contours of constant helium mass fraction. Wide spacing $\overline{\delta} = 0.2$, $\overline{p} = 4.0$, $\overline{v} = 1.0$, $\alpha_c = \alpha_e = 4.76^o$ (computational). 234

112. Contours of constant helium mass fraction. Wide spacing $\overline{\delta} = 0.2$, $\overline{p} = 0.4$, $\overline{v} = 1.0$, $\alpha_c = \alpha_e = 4.76^o$ (computational). 235

113. Jet lift-off: Pressure ratio effects (computational). 236

114. Mixedness measure for high and low injectant to freestream pressure ratios. Wide spacing, $\overline{\delta} = 0.2$, $\overline{v} = 1.0$, $\alpha_c = \alpha_e = 4.76^o$ (computational). 237

115. Length of contours of constant mass fraction for high and low injectant to freestream pressure ratios. Wide spacing, $\overline{\delta} = 0.2$, $\overline{v} = 1.0$, $\alpha_c = \alpha_e = 4.76^o$ (computational). 238

116. Entropy measure variations with pressure ratio. Wide spacing, $\overline{\delta} = 0.2$, $\overline{v} = 1.0$, $\alpha_c = \alpha_e = 4.76^o$ (computational). 239

117. Helium mass fraction. Full-scale model, wide spacing, $\overline{\delta} = 0.20$, $\overline{p} = 1.0$, $\overline{v} = 1.12$, $\alpha_c = \alpha_e = 4.76^o$ (experimental). 240

118. Pitot pressure (psia). Full-scale model, wide spacing, $\overline{\delta} = 0.20$, $\overline{p} = 1.0$, $\overline{v} = 1.12$, $\alpha_c = \alpha_e = 4.76^o$ (experimental). 241

119. Total temperature (^{o}C). Full-scale model, wide spacing, $\overline{\delta} = 0.20$, $\overline{p} = 1.0$, $\overline{v} = 1.12$, $\alpha_c = \alpha_e = 4.76^o$ (experimental). 242

120. Far field data. Half-scale model, wide spacing, $\overline{\delta} = 0.40$, $\overline{p} = 1.0$, $\overline{v} = 1.14$, $\alpha_c = \alpha_e = 4.76^o$ (experimental). 243

121. Decay of maximum helium mass fraction: Velocity ratio effects (experimental). 244

Figure page

122. Mean of 22 planar Rayleigh images at $\overline{x} = 10$. Wide spacing, $\overline{\delta} = 0.20$, $\overline{p} = 1.0$, $\overline{v} = 1.12$, $\alpha_c = \alpha_e = 4.76^o$. 245

123. Standard deviation about the mean for planar Rayleigh images at $\overline{x} = 10$. Wide spacing, $\overline{\delta} = 0.20$, $\overline{p} = 1.0$, $\overline{v} = 1.12$, $\alpha_c = \alpha_e = 4.76^o$. 245

124. Instantaneous planar Rayleigh images at $\overline{x} = 10$. Wide spacing, $\overline{\delta} = 0.20$, $\overline{p} = 1.0$, $\overline{v} = 1.12$, $\alpha_c = \alpha_e = 4.76^o$. 246

125. The all-shock geometry. 247

126. The no-shock geometry. 248

127. Contours of constant helium mass fraction. Wide spacing $\overline{\delta} = 0$ (inviscid b.c.), $\overline{p} = 1.0$, $\overline{v} = 1.0$, $\alpha_c = 9.46^o$, $\alpha_e = 0^o$ (computational). 249

128. Contours of constant helium mass fraction. Wide spacing $\overline{\delta} = 0.2$, $\overline{p} = 1.0$, $\overline{v} = 1.0$, $\alpha_c = 9.46^o$, $\alpha_e = 0^o$ (computational). 250

129. Contours of constant helium mass fraction. Wide spacing $\overline{\delta} = 1.0$, $\overline{p} = 1.0$, $\overline{v} = 1.0$, $\alpha_c = 9.46^o$, $\alpha_e = 0^o$ (computational). 251

130. Contours of constant helium mass fraction. Wide spacing $\overline{\delta} = 0$ (inviscid b.c.), $\overline{p} = 1.0$, $\overline{v} = 1.0$, all-shock geometry, $\alpha_e = 4.76^o$ (computational). 252

131. Contours of constant helium mass fraction. Wide spacing $\overline{\delta} = 0.2$, $\overline{p} = 1.0$, $\overline{v} = 1.0$, all-shock geometry, $\alpha_e = 4.76^o$ (computational). 253

132. Contours of constant helium mass fraction. Wide spacing $\overline{\delta} = 1.0$, $\overline{p} = 1.0$, $\overline{v} = 1.0$, all-shock geometry, $\alpha_e = 4.76^o$ (computational). 254

133. Static pressure (psia). Wide spacing, $\overline{\delta} = 0$ (inviscid b.c.), $\overline{p} = 1.0$, $\overline{v} = 1.0$, all-shock geometry, $\alpha_e = 4.76^o$ (computational). 255

134. Vorticity, $\omega_x \left[\frac{h_i}{U_\infty}\right]$. Wide spacing, $\overline{\delta} = 0$ (inviscid b.c.), $\overline{p} = 1.0$, $\overline{v} = 1.0$, all-shock geometry, $\alpha_e = 4.76^o$ (computational). 256

Figure page

135. Static pressure (psia). Wide spacing, $\overline{\delta} = 0$ (inviscid b.c.), $\overline{p} = 1.0$, $\overline{v} = 1.0, \alpha_e = 9.46^o$, $\alpha_e = 0^o$ (computational). 257

136. Vorticity, $\omega_x \left(\frac{h_i}{U_\infty} \right)$. Wide spacing, $\overline{\delta} = 0$ (inviscid b.c.), $\overline{p} = 1.0$, $\overline{v} = 1.0, \alpha_e = 9.46^o$, $\alpha_e = 0^o$ (computational). 258

137. Effects of boundary layer thickness on jet lift-off for the no-shock model. Wide spacing, $\overline{p} = 1.0$, $\overline{v} = 1.0, \alpha_e = 9.46^o$, $\alpha_e = 0^o$ (computational). 259

138. Effects of boundary layer thickness on jet lift-off for the all-shock model. Wide spacing, $\overline{p} = 1.0$, $\overline{v} = 1.0$, all-shock geometry, $\alpha_e = 4.76^o$ (computational). 259

139. Effects of boundary layer thickness on circulation for the no-shock model. Wide spacing, $\overline{p} = 1.0$, $\overline{v} = 1.0, \alpha_e = 9.46^o$, $\alpha_e = 0^o$ (computational). 260

140. Effects of boundary layer thickness on circulation for the all-shock model. Wide spacing, $\overline{p} = 1.0$, $\overline{v} = 1.0$, all-shock geometry, $\alpha_e = 4.76^o$ (computational). 260

141. Mixedness measure for various boundary layer thicknesses for all-shock and no-shock models, $\overline{p} = 1.0$, $\overline{v} = 1.0$ (computational). 261

142. Length of contours of constant mass fraction for various boundary layer thicknesses for all-shock and no-shock models, $\overline{p} = 1.0$, $\overline{v} = 1.0$ (computational). 262

143. Entropy measure. Wide spacing, $\overline{\delta} = 0$ (inviscid b.c.), $\overline{p} = 1.0$, $\overline{v} = 1.0, \alpha_e = 9.46^o$, $\alpha_e = 0^o$ (computational). 263

144. Entropy measure. Wide spacing, $\overline{\delta} = 0$ (inviscid b.c.), $\overline{p} = 1.0$, $\overline{v} = 1.0$, all-shock geometry, $\alpha_e = 4.76^o$ (computational). 263

Figure page

145. Contours of constant helium mass fraction. Wide spacing $\overline{\delta}$ = 0.2, $\overline{p}$ = 1.0, $\overline{v}$ = 1.0, $\alpha_c = \alpha_e = 4.76^o$, angled injection $\alpha_i = 7.5^o$ (computational). 264

146. Effects of injectant flow angle on jet lift-off. Wide spacing $\overline{\delta}$ = 0.2, $\overline{p}$ = 1.0, $\overline{v}$ = 1.0, $\alpha_c = \alpha_e = 4.76^o$ (computational). 265

147. Contours of constant helium mass fraction. Wide spacing $\overline{\delta}$ = 0.2, $\overline{p}$ = 1.0, $\overline{v}$ = 1.0, $\alpha_c = \alpha_e = 4.76^o$, non-uniform injectant Mach number profile: ramped from 1.9 to 1.5 (computational). 266

148. Contours of constant helium mass fraction. Wide spacing $\overline{\delta}$ = 0.2, $\overline{p}$ = 1.0, $\overline{v}$ = 1.0, $\alpha_c = \alpha_e = 4.76^o$, injection elevated above surface (computational). 267

149. Addition of film-cooling to the injection scheme, $\alpha_c = \alpha_e = 4.76^o$. 268

150. Contours of constant helium mass fraction. Wide spacing $\overline{\delta}$ = 0.2, $\overline{p}$ = 1.0, $\overline{v}$ = 1.0, $\alpha_c = \alpha_e = 4.76^o$, film-cooling model (computational). 269

151. Decay of maximum helium concentration for experimental data. 270

152. The all expansion geometry, $\alpha_c = 0^o$, $\alpha_e = 9.46^o$ 271

153. Contours of constant helium mass fraction. Wide spacing, $\overline{\delta}$ = 0.2, $\overline{p}$ = 1.0, $\overline{v}$ = 1.0, $\alpha_c = 0^o$, $\alpha_e = 9.46^o$ (computational). 272

154. Mixedness measure. Wide spacing, $\overline{\delta}$ = 0.2, $\overline{p}$ = 1.0, $\overline{v}$ = 1.0, $\alpha_c = 0^o$, $\alpha_e = 9.46^o$ (computational). 273

155. Entropy measure. Wide spacing, $\overline{\delta}$ = 0.2, $\overline{p}$ = 1.0, $\overline{v}$ = 1.0, $\alpha_c = 0^o$, $\alpha_e = 9.46^o$ (computational). 274

156. Combination of angled transverse injection and shock-enhancement. 275

Nomenclature

A	area
$\bar{A}$	injectant to freestream area ratio
a	speed of sound
$\mathbf{b}_i$	body force vector of i^{th} species
c	mass fraction
c_i	mass fraction of i^{th} species
c_{He}	helium mass fraction
C_p	specific heat at constant pressure
C_{p_i}	constant pressure specific heat of i^{th} species
d	characteristic dimension
D	binary diffusion coefficient
Da	Damköhler number
D_{ij}	binary diffusion coefficient of i^{th} and j^{th} species
D_{T_i}	thermal diffusion coefficient of i^{th} species
E	hot wire anemometer output
$\mathcal{E}$	total (internal and kinetic) energy
h_i	height of injection plane
h_i	enthalpy of i^{th} species
h^R_i	base enthalpy of i^{th} species
k	thermal conductivity
Kn	Knudsen number, ℓ/d

ℓ	mean free path
L_α	length of contour of constant mass fraction $c_{He} = \alpha$
$\dot{m}$	mass flow
$\dot{m}_{He}$	helium mass flow
$\overline{\dot{m}}$	injectant to freestream mass flux ratio
$\overline{\dot{m}}_{st}$	stoichiometric injectant to freestream mass flux ratio
M	Mach number
M_c	convective Mach number
M_∞	freestream Mach number
$\mathcal{m}_i$	molecular weight of i^{th} species
$\overline{\mathcal{m}}$	injectant to freestream molecular weight ratio
n_i	number of moles of i^{th} species
N_S	number of chemical species
p	static pressure
p_c	static pressure on surface of cone
p_t	pitot pressure
p_0	stagnation pressure
p_∞	freestream static pressure
$\overline{p}$	injectant to freestream static pressure ratio
q_x	heat flux in the x-direction
q_y	heat flux in the y-direction
q_z	heat flux in the z-direction
r	radial coordinate (conical flow)
R	mixture gas constant
Re	Reynolds number
R_i	gas constant of i^{th} species

R_u	Universal gas constant
s	entropy
t	time
T	temperature
T_0	stagnation temperature
T^R	reference temperature = 298 K
$\overline{T}$	injectant to freestream static temperature ratio
u	velocity vector in physical domain
u	x-component of the velocity
u_r	radial velocity component (conical flow)
u_θ	azimuthal velocity component (conical flow)
$\tilde{\mathbf{u}}_i$	diffusion velocity of i^{th} species
$\tilde{u}_i$	x-component of diffusion velocity of i^{th} species
U	velocity
v	y-component of the velocity
$\overline{v}$	injectant to freestream velocity ratio
$\tilde{v}_i$	y-component of diffusion velocity of i^{th} species
V_i	volume of i^{th} species
w	z-component of the velocity
w_i	width of injection plane
$\tilde{w}_i$	z-component of diffusion velocity of i^{th} species
x	streamwise, axial coordinate
$\overline{x}$	non-dimensional distance downstream of injection plane, x/h_i
X_i	mole fraction of i^{th} species
y	cross-stream coordinate
$\overline{y}$	non-dimensional cross-flow coordinate, y/h_i

z	vertical coordinate
$\overline{z}$	non-dimensional vertical coordinate, z/h_j
$\overline{z}_j$	jet lift-off height
α_c	geometric compression angle of upper ramp surface
α_e	geometric expansion angle of upper ramp surface
α_i	angle of injectant vector with respect to freestream vector
β	shock angle
γ	ratio of specific heats for gas mixture
γ_i	ratio of specific heats for i^{th} species
Γ	circulation
δ	boundary layer height
δ^*	boundary layer displacement thickness
$\overline{\delta}$	non-dimensional boundary layer height, δ/h_j
Δs	change in entropy
θ	azimuthal coordinate (conical flow)
θ_c	cone half-angle
λ	second viscosity coefficient,
	wavelength of light
μ	dynamic viscosity
ξ	average depth of penetration of molecule due to diffusion
ρ	density
$\overline{\rho}$	injectant to freestream density ratio
σ_x	normal stress in the x-direction
σ_y	normal stress in the y-direction
σ_z	normal stress in the z-direction
τ_{xy}	shear stress in the xy plane

τ_{xz}	shear stress in the xz plane
τ_{yz}	shear stress in the yz plane
ϕ	equivalence ratio
$\underset{\sim}{\omega}$	vorticity vector
$\dot{\omega}_i$	production rate of i^{th} species

CHAPTER 1

INTRODUCTION

The goal of this study was to implement shock-enhancement of hypervelocity mixing in a realistic supersonic combustion ramjet fuel injection scheme. Direct evaluations are presented of injector performance in response to parametric variations of fuel injector geometry and both freestream and external flow field characteristics. Performance is analyzed in terms of mixing, losses, jet penetration and heating considerations.

1.1 Motivation

The primary motivation for the study of hypervelocity mixing is the current effort under way to develop a single-stage-to-orbit hypersonic vehicle. Through much of its flight envelope, the aircraft will be propelled by supersonic combustion ramjet (scramjet) engines relying on hydrogen-air combustion. The requirement for supersonic combustion is dictated by freestream conditions associated with hypersonic (M = 8 to M = 25) cruise. If the flow were to be decelerated to subsonic speeds, the associated static temperature rise would prevent recombination reactions necessary to provide full energy release from the hydrogen-air reaction. Additionally, undesirable total pressure losses would be associated with such a deceleration. Thus, typical design requirements point to combustor flow Mach numbers between 4 and 8. The high flow speeds (typically 6000 to 15000 ft/s) and fixed combustor lengths (< 10 feet) lead to residence times within the combustor on the order of 1 ms. This requires that the mixing-rate

dominated combustion process proceed very rapidly. Kumar, Bushnell, and Hussaini [1989] outlined several difficulties associated with enhancing this process. Primary among these is the requirement that a major component of the injectant flow vector be directed parallel to the freestream to derive as much thrust from the momentum of the fuel as possible and alleviate losses. The problem is compounded by the inherently poor shear-induced mixing characteristic of high Mach number shear layers. Driving these issues is the fact that a hypersonic aircraft must be designed around its propulsion system. All aspects of the vehicle configuration and performance are closely tied to the efficacy of the hypersonic combustion process. While this study focused on enhancing this process for scramjet combustors, broader issues were addressed that are applicable to high-speed mixing processes in general.

1.2 Shock-enhanced mixing

Implementation of shock-enhanced mixing in a realistic fuel injector geometry was preceded by extensive efforts carried out at the California Institute of Technology to study the two-dimensional, time-dependent interaction between a weak shock and an initially circular region filled with helium imbedded in air. This work was first presented by Haas and Sturtevant [1987], who sought to explore it as a technique to generate turbulence and intensify mixing in a flow field with sharp density inhomogeneities. They noted that " ... interaction of shock waves with fluid non-uniformities modifies the geometry and amplitude of the wave fronts by reflection, refraction, diffraction and scattering, and modifies the morphology of the inhomogeneities by fluid deformation, vorticity and entropy production, and transport." In light of vorticity generation, these phenomena will be generalized as shock-generated vorticity. The predominant mechanism for generation of vorticity in this case is baroclinic torque. Consideration of the baroclinic torque source term in the vorticity equation,

$$\rho \frac{D}{Dt}\left(\frac{\underset{\sim}{\omega}}{\rho}\right) = \frac{1}{\rho^2}\nabla\rho \times \nabla p \ ,$$

reveals that vorticity is produced when a pressure gradient is imposed upon a density gradient in a manner such that the gradients are non-parallel. A graphic demonstration of the utility of such a mechanism in rapidly producing mixing is displayed in Figure 1. The figure contains a series of images from a shock tube study where a cylinder of helium was impinged upon by a Mach 1.093 shock moving from left to right. The study was conducted at the California Institute of Technology by J. Jacobs (Marble *et al.* [1990]). The helium was seeded with byacetyl which fluoresced in response to a planar laser sheet. A schematic of the vorticity generation process is shown in Figure 2. As the shock passes over the density gradient existing between the helium and the air, vorticity is deposited at the location of this gradient. The $(1/\rho)$ factor in the source term leads to preferential deposition of vorticity on the light gas side of the density gradient. The vorticity modifies the geometry of the density interface through strong convective forces. As the interface is deformed, further local generation/annihilation of vorticity occurs via baroclinic torque. The vorticity field generates rapid large-scale convective mixing and eventually coalesces into a counter-rotating vortex pair. The sense of the pair is such that it migrates in the direction of shock motion. It should be noted that other mechanisms for vorticity generation in such a flow (*e.g.*, curvature of the shock as it passes through the light gas) play a minor role in relation to generation by means of baroclinic torque. Subsequent studies (Yang [1991]) have elucidated the effects of shock strength and the scale and nature of the density gradient on the development of the flowfield. Yang also presented studies of multiple density inhomogeneities of various geometries and orientations.

Marble, Hendricks, and Zukoski [1987] suggested that the above phenomena be used as a means for improving scramjet combustor performance. Marble *et al.* [1990] have shown that the time-scale on which the mixing occurs is short enough to be of interest in scramjet applications. The direct application of such a vorticity generation mechanism in a three-dimensional flow-field is displayed heuristically in Figure 3. Passage of a column of light gas through the pressure

gradient associated with a weak oblique shock is a three-dimensional, steady analogy to the two-dimensional unsteady case discussed above. As the column passes through the shock, longitudinal vorticity is deposited where the shock intersects the density gradient existing between the column of light gas and the heavier external flow. The vorticity will act to modify the surface of jet. Large-scale stirring of the flow will result directly in increased molecular-scale mixing as the interfacial area between the two gases is increased. The validity of the analogy between the two-dimensional unsteady problem and the three-dimensional steady case is limited for realistic injection schemes (see Section 6.5). The analogy associated with the simplified system of Figure 3 was demonstrated by Marble, Hendricks and Zukoski [1987] and described in more detail by Hendricks and Marble [1990]. Yang [1991] has investigated two-dimensional, rectangular density inhomogeneities, and boundary conditions which extend the analogy further toward geometries of interest in the current study.

1.3 The contoured wall fuel injector

The success of the two-dimensional shock-induced mixing program and demonstration of the three-dimensional analogy encouraged the exploration of a low drag injection system in which the basic concept of shock-generated streamwise vorticity could be incorporated into an injector for a scramjet combustor. A geometry was conceived in April of 1987 and presented by Marble *et al.* [1990]. A diagram of the injection geometry is shown in Figure 4. This basic geometrical form and variations of it are the focus of the current study. The geometry allows formation of strong pressure gradients in proximity to fuel/air density gradients. Further, the fuel is injected parallel to the intended thrust vector, providing full utilization of the momentum of the injectant.

The injector consists of alternate compression ramps and expansion troughs. The end of each ramp houses a nozzle discharging the injectant. In the plane of injection, the flow in each trough is turned back to the freestream direction, forming a weak oblique shock. The action of the shock

is two-fold. First, the pressure gradient associated with the shock impinges upon the density gradients existing between the light injectant and the air, generating strong streamwise vorticity through baroclinic torque. Second, based on the two-dimensional analogy, it was hypothesized that the vorticity would form into a counter-rotating vortex pair of a sense that would cause migration of the fuel away from the wall. Thus, it was hoped that the shock would act to enhance both mixing and jet penetration.

Detailed on the diagrams of Figure 4 are definitions of axes and geometrical parameters. The barred quantities ($\bar{x}$, $\bar{y}$, and $\bar{z}$), denote distances normalized by the height of the injection plane (h_j). All of the injectors studied had 2x1 rectangular injection planes ($h_j = 2w_j$). The geometries were characterized by the expansion and compression angles of the ramps (α_e and α_c respectively), and the spacing between the injectors.

1.4 Studies by other authors

The above geometry is of interest because it provides a direct mechanism for enhancement of mixing by baroclinically generating vorticity. Several other scientific efforts have been directed towards the study of injection schemes to enhance hypervelocity mixing. A brief review will show the variety of work contained in the literature. A discussion of the results of the current study in light of some of these investigations is presented in Section 7.1.

A large body of work exists concerning sonic normal wall injection into both subsonic and supersonic flows. One technique of interest for scramjet applications is that of streamwise, staged normal injection studied by Clement and Rodriguez [1989]. The area of succeeding orifices was increased exponentially with distance downstream, to increase mixing, penetration, and reduce the strong shock typical of normal injection. King, Thomas and Schetz [1989] combined tangential slot injection with normal injection in an attempt to provide strong mixing

augmentation. Mixing rates for this configuration were significantly higher than for tangential injection alone. In scramjet applications it is necessary to extract as much thrust from the system as possible. As a result, typical configurations direct the injectant vector nearly parallel to the intended thrust vector. Thus, the momentum of the fuel itself adds to the thrust obtained from combustion. The requirement for utilizing the momentum of the fuel has led investigators (Mays, Thomas and Schetz [1989]) to study low-angled transverse fuel injection. A technique similar to normal injection was applied but the jets were directed downstream to within 15 to 30 degrees of the freestream flow vector. While far-field decay rates for these configurations approached those of normal injection, initial mixing was not as effective. Notably, they reported the penetration of the angled jets to be comparable to normal jets.

Several researchers (Drummond *et al.* [1989], Hartfield, Hollo and McDaniels [1990], Riggins and McClinton [1990], and Riggins *et al.* [1990]) have studied a parallel injector geometry similar to those presented in this study. Triangular injectors were mounted on a flat wall. The scheme is equivalent to the injectors of Figure 4 with $\alpha_c = 10^o$ and $\alpha_e = 0^o$. While exhibiting many flow characteristics similar to the injectors of this study, they provided no means for strong baroclinic generation of vorticity. An interesting augmentation applied to these injectors was that of sweeping the side walls of the ramp. While enhancing vorticity production, this was found to generate additional total pressure losses within the flow field. The tests performed with these ramps were conducted at freestream Mach numbers ranging from 2.0 to 3.0. The studies have included both computational and experimental investigations directed at both mixing and hydrogen/air combustion. Work was also conducted to combine the parallel wall injectors with normal injection at the base of the injection plane (Northam, Greenberg and Byington [1989]). The difficulty in obtaining detailed, accurate measurements in high-speed flow fields as well as the lack of a meaningful standardized basis for comparison between the various configurations makes direct interpretation of much of this work impossible.

To date, the most comprehensive effort to correlate the results from the wide variety of supersonic injection schemes was presented by Thomas, Schetz and Billig [1989]. The configurations included in the study were free jets, transverse jets, wall slot jets, and hybrid jets. The authors stressed the difficulty in such a broad correlation due to a sparse and inaccurate database. The configurations were plotted in terms of maximum injectant concentration versus distance from the injection plane. Typically, maximum concentration decayed as $(x/d)^{-0.8}$, but scatter about this factor was strong. It was shown that the mixing rate decreased by a factor of two when the cross-stream spacing of some of the injector configurations fell below a critical value.

Additional work has been conducted in areas applicable to scramjets. This work includes preconditioning, or turbulizing the jet (Schadow, *et al.* [1987]) and studies of non-circular jet dynamics (Gutmark, *et al.* [1989]). In both instances mixing was enhanced. Key issues of unsteady boundary layer effects (Ballal and Chen [1988]), and passage of mixing interfaces through strong pressure gradients (Drummond, Carpenter and Mukunda [1989], Kumar, Bushnell, and Hussaini [1989], and Wilder and Hindersinn [1953]), have also received attention.

1.5 Scope of the current investigation

The goal of the study was to demonstrate the application of shock-induced mixing in a realistic injector geometry. Further, it was desired to understand the influences of geometry, injectant conditions and free-stream conditions on injector performance. It was hoped also that these investigations would lend insight into fundamental phenomena associated with hypervelocity mixing, and produce guidelines for a second generation injection scheme with enhanced performance. Helium was used as an injectant to simulate hydrogen fuel. The effort involved extensive experimental wind-tunnel testing as well as a significant computational effort which

both complemented and extended the experimental investigations. Performance was analyzed in terms of mixing, losses, jet penetration and heating considerations, with mixing performance presented in most detail.

The limited scope of the study as a whole is addressed directly below. Discussions of the extent of the experimental and computational investigations follow in Sections 1.5.2 and 1.5.3, respectively.

1.5.1 Mixing and combustion

Combustion requires mixing on a molecular scale. Limits of spatial and temporal resolution precluded direct measurement of molecular-scale mixing in these studies. Herein referrals to mixing performance relate solely to spatial scales which were discernable within the experimental and computational resolution, unless stated otherwise. Mixing on a molecular scale will be inferred from these results. Increase in large-scale stirring of the flow field is related to an increase in molecular-scale mixing via an increase in interfacial surface area and narrowing of gradient dimensions between the two gases. These processes act to facilitate diffusion. Lack of temporal resolution required that phenomena associated with the time-fluctuating component of the flow field be realized largely as they were manifested in the time-mean flow field. While this allowed for estimation of the scale and importance of these effects, it did not provide sufficient information for detailed analyses.

The scope of the study was further limited in that helium was used to simulate the hydrogen fuel. Yeung [1991] has modelled hydrogen-air reactions (pre-mixed) for conditions corresponding to a variety of flight Mach numbers. For flight at Mach 15 with Mach 5 combustor flow, combustor inlet static conditions of T = 1630^{o} C, and p = 15 psia, and mean flow speeds of 13000 ft/s may be typical. Yeung has calculated that the time required for initiation of a hydrogen-air reaction in

such a system is on the order of 25 μs. While strongly dependent on the pressure, the result allows estimation of the extent to which scramjet combustion is controlled by mixing. The pertinent non-dimensional number is the Damköhler number, Da, defined as the ratio of the flow passage time, to the reaction time. Systems where Da >> 1 are described as mixing-controlled. For the above conditions, and a geometry with a characteristic length scale of 1 inch, fluid travel of four characteristic lengths is required for Da > 1. So combustion in typical scramjet applications will not be mixing-controlled in the classic sense. It will however, be mixing-rate dominated. Thus, investigation of hypervelocity mixing augmentation is germane to combustion enhancement. In general, treatment of the reacting system must include finite-rate chemistry. It is unclear what effects the heat release associated with the reaction will have in damping/amplifying both large-scale and fine-scale mixing. In Yeung's simulation, a combustor end temperature of T = 3100^{o} C was projected, so significant heat release is expected. Any dependence of the fluid dynamics on chemical forcing will not be represented in these mixing studies.

1.5.2 Experimental scope

Wind-tunnel experiments were conducted on fuel injector arrays. Injection of Mach 1.7 helium into a Mach 6 airstream was used to model hydrogen injection into a typical scramjet combustor flowfield. Of primary interest in these tests was the definition of salient flow field features, particularly those relating to shock-enhancement of the mixing process.

Several important parameters for scramjet applications were addressed including injectant to freestream pressure and velocity ratios, injector geometry and boundary layer effects. Concerning the boundary layer, two areas were investigated. The first of these was the influence of the displacement effect of the boundary layer and its role in changing mixing performance through changing the effective injector geometry. This effect was addressed in detail. The

second, the strength of the coupling between the unsteady boundary layer structure and the temporal component of the mixing region was addressed largely as it was manifested in the time mean, and thus received a less satisfactory treatment. The effect of the injectant/freestream pressure ratio, $\overline{p}$, was investigated primarily in an effort to determine the most efficient means of mixing a given injectant mass flux; delivery via small high pressure jets or larger low momentum jets. Further studies were directed at variations in injectant to freestream velocity ratio ($\overline{v}$). This effort was undertaken to understand the importance of shear-induced mixing, with particular interest directed towards cases where the nominal velocity ratio approached 1.0. This case is critical because in the absence of strong shear instabilities, mixing will be primarily dependent upon the various mixing augmentation techniques applied to the flow field. Tests were not conducted to investigate convective Mach number effects. The mixing was not strongly compressible since convective Mach numbers did not exceed 0.4.

Further interest existed in the influences of geometrical variations of the injector arrays. The experimental study of these was limited by the cost of constructing additional injector array modules for the wind-tunnel model. The only geometric parameter studied experimentally was injector spacing. Equal compression and expansion angles of $\alpha_c = 4.76^o$ and $\alpha_e = 4.76^o$ were used on all of the wind-tunnel models. The widely-spaced geometry, with spacing between the ramps approximately equal to three injector widths, is shown in the diagram in Figure 4. A photograph of the narrow spacing (with trough width equal to ramp width) appears in Figure 5.

Additional experimental effort was directed towards understanding the importance of various unsteady flow field phenomena. Due to mean flow speeds of 3000ft/s and interest in molecular-scale mixing, this area was a considerable challenge. A joint effort was undertaken with personnel of the Optical Spectroscopy Section of NASA Langley Research Center's Instrument Research Division to use time-resolved, planar Rayleigh scattering to investigate these

phenomena. These measurements were of strictly limited applicability in terms of quantitative analysis. They did provide an insight into the significance of unsteady phenomena in this flow field which was vital in correctly interpreting the time-mean data.

While a fully-populated, parametric test matrix might be desired to elucidate coupling between the various parameters, financial and time constraints dictated a sparser, more directed approach to the experimental study. A crude assumption of parameter independence was applied to changes in velocity and pressure ratios, in the interests of limiting the scale of the tests. Thus, one condition was fixed as the baseline configuration against which variations of a single parameter were compared. The one area where independence was not assumed, was in the changes in boundary layer scale and injector geometry. Here both spacing and boundary layer height were changed simultaneously as the effects were strongly interdependent.

1.5.3 Scope of the computational effort

Due to the generally intractable nature of making measurements in a high-speed binary mixing field, as well as significant equipment and facility costs, a strong computational effort was undertaken to model the flow field. While limited in scope to a laminar mixing model, the study did allow qualitative analysis of the global aspects of injector performance. Detailed quantitative analyses were also performed and used as a basis for comparison between computations. The numerical results provided knowledge of flow variables at every point in the computational domain, and allowed study of derived quantities such as vorticity. They were also used to go beyond the fairly rigid bounds of the experimental test matrix, allowing investigation of a variety of geometrical variations.

A large portion of the effort involved a series of parametric tests which closely followed the experimental test matrix. These included investigations of pressure ratio, boundary layer

displacement, and injector spacing effects. Not included in the computational study were velocity ratio effects, as the laminar mixing model could not accurately model turbulent shear phenomena. Further studies involved changing the degree of compression and expansion of the injector surfaces. Work is also presented on non-uniform injectant profiles, angled injectant velocity vectors, raised injection, and addition of film-cooling to the injection scheme. These fairly applied efforts were conducted with an interest in pointing the direction towards a second generation geometry with enhanced performance. Also presented are studies of generic injector schemes aimed at elucidating the importance of shock-generated vorticity in relation to other vorticity generation mechanisms.

CHAPTER 2

EXPERIMENTAL METHODS AND APPARATUS

The data presented are the result of a series of tests conducted in the NASA Langley High Reynolds Number Mach 6 Wind-Tunnel. The facility is currently under the direction of the Experimental Flow Physics Branch of the Fluid Mechanics Division. Following is a discussion of the apparatus and methods used these experiments.

2.1 The wind-tunnel and wind-tunnel subsystems

The High Reynolds Number Mach 6 Wind-Tunnel is an open-loop blowdown type facility, with a 42 in. long, 12 in. diameter circular test section. Air flow was established by means of a pressure difference across the test section. The model was inserted into the flow following tunnel start and was removed prior to shutdown by means of a pneumatic jack. A more detailed presentation of the operation and capabilities of the wind-tunnel may be found in the paper by Jones and Feller [1970]. Optical access was provided through 42 in. long by 6 in. wide windows on the top and both sides of the test section. Unless otherwise noted, operating conditions for these tests were p_0 = 1000 psia and T_0 = 246^o C with fluctuations of ±10 psia and ±5^o C respectively. These conditions were chosen so that the constituents of the air would remain in the gaseous phase after expansion to M = 6. (Some condensation did occur. See section 2.7.3.) The static properties associated with these conditions were p_∞ = 0.63 psia and T_∞ = -210^o C, with a

freestream Reynolds number of 15 x 10^6/foot. Run durations of greater than one hour allowed sufficient time for detailed three-dimensional flow field surveys.

The tunnel was equipped with a three-axis traverse. Axial (x-axis) travel allowed measurement from the leading edge of the model to 13 inches downstream of the plane of injection. The error of the absolute location of the traverse along this axis, was less than ± 0.10 inches. Full vertical travel (z-axis) was allowed from the upper wall of the test section to the surface of the model. The span of the traverse in the crossflow direction (y-axis), was approximately 3 inches. Absolute positioning error in the y and z axes was less than ±0.02 inches. However, inaccuracies due to the model injection mechanism caused an error associated with the relative position of the model. Thus the accuracy of the positioning of the traverse relative to the location of the model was x ± 0.10 in., y ± 0.02 in., and z ± 0.05 in.

A helium supply system was designed and constructed by NASA personnel for these studies. The system was capable of delivering mass flows up to 30 lb./min. Pressure was regulated with remote solenoid valves in a feedback loop using commercially available controllers. For most of the test conditions the total pressure of the helium remained constant to within ±0.02 psia (less than ±0.6% variation from the operating point). However, at lower mass flows (half-scale, wide spacing model with $\overline{p}$ = 1.0 only), the fluctuations were more pronounced with variations as large as ±0.25 psia or ±7% of the desired level. This was due to the fact that the mass flow associated with this condition was at the bottom of the operating range for the large valves in the delivery system. The helium supply system also provided the ability to control the temperature of the injectant. A portion of the helium was diverted through a liquid nitrogen cooled heat exchanger. The percentage of total mass flow that passed through this bath was controlled remotely using a feedback loop, allowing maintenance of a desired injectant temperature. Only two cases were run in support of these experiments. The majority of the tests were conducted using ambient

temperature helium, with all of the mass bypassing the liquid nitrogen bath. Additional tests were completed with the helium as cold as possible, diverting all flow through the heat exchanger. For the tests with ambient helium, the total temperature realized in the model injectors was between 30^{o} C and 50^{o} C depending on the heating of the gas as it passed through the different injector configurations. The fluctuations associated with these temperatures were less than $\pm 4^{o}$ C. Cooling the helium allowed total temperatures between -50^{o} C and -30^{o} C with similar fluctuations.

2.2 The wind-tunnel model

A versatile platform was designed for the study of contoured wall fuel injectors. An array of injectors was built into a flat plate to simulate one interior wall of a scramjet combustor. A three-view drawing of the model is shown in Figure 6. The model was 42 inches long, with a 7.625 in. wide upper surface, and weighed approximately 400 pounds. The model was constructed of 17-4 PH, heat-treated stainless steel by Tri-Models Inc. of Torrance, California. This material was chosen for its exceptional strength (170 ksi yield stress) and machinability. Figure 7 contains a photograph of the model mounted in the wind-tunnel. The model was designed to meet the NASA mandate for this tunnel of not failing under 90 psi differential pressure loading on all surfaces exposed to the flow. Important dimensions on the model were held to within ±0.001 in. with all injector and upper surface walls flat and parallel to within ±0.001 in. with a 32μin./in. rms surface finish. The model, shown in Figure 8, was in the form of a 'T', with a flat plate mounted on a center strut. The upper surface of the plate was used to model the internal wall of a combustor. The center strut was sized to place the upper surface of the model 0.5 in. above the tunnel centerline. Side plates were attached to contain the pressure rise associated with the leading edge of the model. If not contained, this disturbance would have reflected from the wall of the circular test section and eventually impinged upon the upper surface of the model. Fairing blocks on the base of the model were designed to match the circular test section.

A modular design was chosen to allow testing of a variety of injector configurations. For the injectors tested, the flat plate extended 15 in. (full-scale injectors) or 18 in. (half-scale injectors) upstream of the start of the injector ramps. The flat plate downstream of the injection plane extended 21 inches. A boundary layer trip plate (Figure 9) was located one inch from the leading edge of the model . The plate contained a row of 41, 0.020 in. diameter holes spaced 0.167 in. apart through which air was injected to vary the nature and scale of the boundary layer. While the plate was designed to be interchangeable, only one plate was used for these studies. The air supply for these holes as shown in the cross-section of Figure 10, was via a passageway in the center strut.

The center section of the model was termed the nozzle block. The block was hollowed on the inside to form an injectant plenum chamber that was 6 in. wide, 6 in. long and 1 in. high. The helium was delivered through two 0.5 in. diameter supply tubes which attached at the base of the model. It then flowed through a 0.375 in. by 2.0 in. rectangular duct which passed through the center strut. This rectangular duct was surrounded by an air cavity which acted as a thermal buffer to limit the influence of variations in the temperature of the model on the temperature of the helium. Exiting this duct, the helium entered the front portion of the plenum chamber. The plenum chamber was divided by a choke plate. This plate contained 0.0625 in. diameter chamfered holes and was designed to both spread the flow and give a total pressure drop. The pressure drop was desirable as sub-atmospheric total pressures were required by the injectors. The holes were sized to provide a total pressure drop of 1/10, based on quasi one-dimensional, isentropic flow analysis. In practice, a total pressure drop of approximately 1/9 was realized. Three inches downstream of the choke plate, the array of two-dimensional injector nozzles was formed. The flow in the plenum chamber transitioned to the two-dimensional nozzles by way of smooth, 2:1 elliptical contractions. The model was designed to accept a variety of internal nozzle

geometries, by changing the blocks which formed the bottom walls of each nozzle. For all of the tests presented the nozzles were designed to provide M = 1.7 exit flow, based on quasi, one-dimensional, isentropic analysis neglecting internal boundary layer and heat transfer effects. A lower Mach number would have been desirable to meet some of the parameter requirements (particularly $\bar{v} = 1.0$), but the increased sensitivity to geometry would have decreased confidence in performance to design specifications. A two-dimensional Euler study of the nozzle geometry was conducted to evaluate exit flow conditions. For the M = 1.7 design, exit Mach numbers decreased monotonically from M = 1.72 at the bottom of the exit plane to M = 1.65 at the top. Further, the velocity vector was aligned with the horizontal to within $+2^{o}$. Two scales of injectors were designed, termed 'full' and 'half'. The full-scale nozzles were 1.0 in. high (h_j), and 0.5 in. wide (w_j), with 0.063 in. thick side walls, and a 0.033 in. thick top wall in the exit plane. The half-scale nozzles had $h_j = 0.5$ in., $w_j = 0.25$ in. and 0.033 in. wall thicknesses on the top and sides. Wide and narrow array spacings were built in each scale. The wide spacing models were designed with trough widths of $3.125w_j$ ($\Delta\bar{y} = 2.25$, jet centerline to jet centerline). The narrow spacing was $1.0w_j$ ($\Delta\bar{y} = 1.125$, jet centerline to jet centerline). In each model one of the lower nozzle contours was instrumented with two static pressure ports and a total pressure tube. The total pressure tube was constructed of 0.030 in. diameter stainless steel tubing. It rose from the bottom wall of the nozzle and turned in the flow direction in the form of an 'L' so that it was located in the center of the subsonic portion of the nozzle. A chromel-alumel thermocouple was installed in the helium plenum chamber and was used to record injectant total temperature. The expansion surface between the injector ramps was instrumented with static pressure arrays numbering between 5 and 18 ports each depending on the scale and spacing of the injector array.

Downstream of the injection plane was a flat, 21 in. long, plate which was instrumented from below with 44 chromel-alumel thermocouples and 24 static pressure ports (0.020 diameter). Due

to the difficulty in accurately determining heat transfer, the thermocouples, while included in the model, were not used in the tests.

The wind-tunnel model was aligned in the tunnel to $+0.02^{o}$ roll, -0.01^{o} pitch and less than 0.05^{o} yaw. Surface oil flow and static pressure measurements were used to determine the extent to which global pressure gradients existed on the surface of the model. Flow on the front of the model was parallel with the tunnel centerline. The expansion associated with the injector arrays allowed some migration of flow to the upper surface of the model. However, this flow was redirected within 8 inches of the injection plane and surface streamlines downstream of this point were parallel to the centerline. These results do not preclude the existence of strong pressure gradients away from the wall. The limited cross-stream span of the traverse did not allow for investigation with the survey apparatus. However, planar Rayleigh scattering showed that the center injector flow field was shielded by the outer injectors in the array. In general the simulation of an infinite array of injectors was adequate for the level of this study.

2.3 The data acquisition system

The investigation required the design and development of an automated, personal computer-based, data acquisition system. The core of the system was a Metrabyte DAS-20, 16-channel, 12 bit, analog to digital converter. Addition of five 16-channel multiplexers allowed monitoring of 91 channels with a maximum single channel sample rate of 100,000 Hz. While formally maintaining 12 bit accuracy, temperature variations in the control room ($\pm 8^{o}$ C at times), substantially degraded the accuracy of the system producing zero and span shifts. The error introduced was a function of the amplifier gain used in measuring each channel and will be included in the error bounds quoted for the various instrumentation discussed in Sections 2.4.1-2.4.4. For some measurements, external amplifiers were employed to increase accuracy.

The data acquisition algorithm shown below was the basis for all of the flow field surveys conducted.

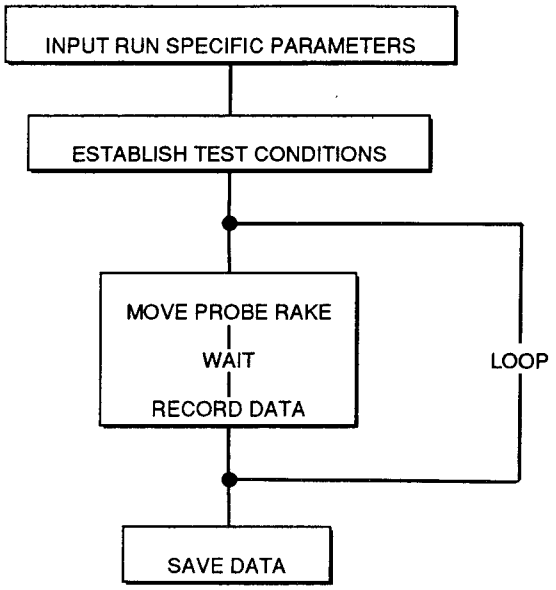

At each point in the flow field the data were recorded in a specific order related to the time response of the individual measurements. In general, tunnel and helium plenum chamber parameters such as $p_{0\text{-air}}$, $T_{0\text{-air}}$, and $p_{0\text{-he}}$, $T_{0\text{-he}}$, were taken first in the measurement loop as they did not vary strongly during the run. These measurements were followed by data from the probe rake in an order commensurate with individual probe time response. The time response of these measurements will be discussed in Sections 2.4.1-2.4.4. Surveying was completed at a rate of 2.5 seconds per point.

2.4 Three-dimensional flow field survey apparatus

Four rake-mounted probes were used to investigate the flow field: a pitot pressure probe, a cone static pressure probe, a total temperature probe, and a gas sampling probe. Each of these probes will be discussed in detail in Sections 2.4.1 - 2.4.4. Given the measurements from these four probes, Mach number, density, and static pressures and temperatures were determined.

This procedure is discussed in Section 2.5. A photograph of the four probes mounted in the rake is shown in Figure 11. The spacing between the total temperature, pitot pressure, and sampling probes was 0.125 in., centerline to centerline. The centerline of the cone static probe was set 0.25 in. away to eliminate undesirable interference from the other probes. Accurate spacing of the probes was critical to allow reduction of the data as discussed in Section 2.5. The relative spacing between the probes was accurate to within ± 0.005 in. The probes were aligned with the freestream to within $\pm 2^{o}$ yaw and pitch.

2.4.1 Gas composition measurements

The studies required development of a gas analyzer for determining the concentration of helium at a given point in the flow field. The design and application of this device are discussed below. Design requirements included operation in a wide range of flow conditions. The endpoints of the operating envelope were Mach 6 air with p_0 = 1000 psia, $T_0 = 246^{o}$ C, and Mach 1.7 helium with p_0 = 3.4 psia, $T_0 = -50^{o}$ C. Due to the difficulty in designing a probe with frequency response that would allow time-resolved measurements (order 10KHz), a time-mean device was developed. It was important however, that the analyzer provide measurements rapidly to allow detailed three-dimensional surveying of the flow field. For the run times possible in the High Reynolds Number Mach 6 facility, this required response on the order of one second per measurement. Further, a composition probe with less than ±2% mole fraction accuracy over the entire operating envelope would provide confidence in analyzing the flow field. In addition to these requirements, the device had to be robust, easy to use, and allow calibration in a reasonable time period.

Several devices to determine composition of a binary mixture are described in the literature. Many are based on the response of a hot-wire anemometer probe, including those of Adler [1972], Brown and Rebollo [1972], Jones and Wilson [1977], Mcquaid and Wright [1973], Ng,

Kwok and Ninneman [1989], Simpson and Wyatt [1973], and Way and Libby [1970]. The analyzer developed for this study was most closely based on that described by Adler though considerable additional development was necessary to allow suitable performance in the difficult conditions of this study.

In general, the heat loss from a cylinder in a binary mixture is a function of velocity, pressure, temperature and composition,

$$E = fnc\ (\ U,\ p,T,\ c)\ .$$

Here E is the output voltage of a constant temperature, hot-wire anemometer. Thus the response is represented by one relation in five variables. In a general binary flow field, E, U, p and T must be fully specified to allow determination of gas composition, c. With the exception of the work of Ng, Kwok, and Ninneman [1989], previous studies have focused on less general applications. Often constant total pressure and constant total temperature were assumed. In this case, only hot-wire output, velocity and composition are unspecified. A sample is withdrawn from the flow into a tube using a vacuum pump, and allowed to pass over a hot-wire probe. Downstream of the probe is a contraction. The vacuum pump is used to maintain choked flow through this orifice. Thus with the other variables fixed, velocity across the wire is constant, and gas composition can be obtained from a simple calibration of the anemometer output. This technique was applied by Adler [1972]. A similar technique has been described by Brown and Rebollo [1972], however instead of locating the analyzer outside of the flow field, the sensing elements were located in the tip of the probe itself. This configuration provides more rapid time response, but is difficult to apply in hot environments both because of probe survivability and poor hot-wire sensitivity. The sensitivity of a constant temperature hot-wire anemometer system is proportional to the difference in temperature which is maintained between the wire and the free-stream. This difference is usually expressed in terms of an overheat ratio, the ratio of

sensor operating resistance to ambient resistance. An overheat ratio of greater than 1.5 is desirable in terms of sensitivity and signal to noise ratio. Use of a Brown and Rebollo configuration in these tests, where total temperatures ranged to 250^{o} C, would require the wire temperature to exceed the operating range of standard hot-wire materials.

Mcquaid and Wright [1973], and Simpson and Wyatt [1973] recognized the importance of employing quartz-coated hot-wires (hot-film probes) rather that the more standard platinum-plated tungsten wires. Simpson and Wyatt noted that for helium-air flows over platinum or tungsten hot-wire sensors, sensor calibration was subject to drift because of changes in the thermal accommodation coefficient. This coefficient may change in response to the adsorption of various trace gases by the sensor surface. The relatively good thermal accommodation coefficient that exists between a helium-air mixture and a quartz coating allows for relatively weak influence of thermal slip effects on hot-film sensors. However, use of probes with quartz coatings compounds the difficulties of measuring in a hot flow since hot-film sensors have a lower peak operating temperature than hot-wires. Thus sensitivity is diminished.

The devices that have been described were applied in less general flow fields than the one of interest in this study, where total temperature and total pressure variations must be accounted for as well. The Ng, Kwok, and Ninneman [1989] probe was applied in a general supersonic flow. Temperature and pressure variations were accounted for, but the range of temperatures was benign. In fact, they found that the total temperature effects could be ignored without significant degradation of accuracy. Their probe was of a design similar to the Brown and Rebollo [1972] probe. The sensing elements were contained in the tip of a sampling probe. Pressure was sensed through the sampling tip. Temperature was determined separately with an additional probe that was traversed through the flow field. This required that the discrete probes be very accurately aligned so that the measurements were obtained at the same physical point in the

domain. Further, heat transfer effects on the inside of the sampling probe were accepted as errors. As well, a complex three-dimensional calibration (p,T, and c) of the hot-film output was required prior to use.

The design employed in the current study borrowed many points from the probes previously described. Notably, a suggestion first presented by Adler was implemented. That being to thermally condition the gas. A sample was withdrawn from the wind-tunnel, forced to a constant temperature using a heat exchanger and then passed over a hot-film probe which was located upstream of a sonic orifice. The sonic orifice fixed the velocity over the probe for given p, T, and c. At the location of the hot-film, the pressure was measured. With temperature and velocity fixed, composition was determined from a tractable, two-dimensional calibration inversion based on pressure and hot-film voltage. A schematic and photograph of the gas analyzer are shown in Figures 12 and 13. A dimensioned drawing of the device is presented in Figure 14. The gas was temperature-fixed by attaching a cooling coil to the upstream side of the analyzer and locating the entire device within an ice-water bath. While removing an additional variable and simplifying calibration, cooling of the gas also acted to increase sensitivity, effectively raising the overheat ratio. For these tests the hot-film was operated at an overheat ratio of 1.8. Four feet each, of 0.1 in. internal diameter stainless steel tubing and 0.375 in. internal diameter teflon tubing were required between the sampling tip and the cooling apparatus to allow delivery of the gas sample.

The analyzer required many design refinements to improve accuracy and time response. Many parameters affected the proper operation, accuracy, and time response of the device including: cooling coil length, cooling coil internal diameter, hot-film probe overheat ratio, sampling tip diameter, sampling and delivery tube length, internal diameter of sampling and delivery tubes, vacuum source, sonic orifice diameter, internal diameter of sensing device, and accuracy of pressure transducers. The trade-offs associated with changes in these parameters are too

numerous to list and considerable development and trial and error was required to arrive at a configuration which achieved design objectives. Of critical importance to the accuracy of the analyzer was accurate recording of pressures within the probe. For various flow conditions pressures within the probe varied from 20 psia to 0.05 psia. The task was made more difficult because the hot-film output was more sensitive at lower pressures so accuracy of the pressure measurement had to be maintained even at the lowest pressures. A 50 psid barocel head with a 3-range, auto-ranging signal conditioner was used.

After arriving at a configuration, several steps were taken to assure proper performance of the analyzer. Thermal conditioning was verified by monitoring the gas temperature with a thermocouple mounted in the sensing device. Surveys of the flow field were made. Within the level of accuracy of the thermocouple measurement, the temperature matched that of the ice-water bath. Small temperature variations ($\pm 2^{o}$ C), due to instrument errors and noise, were not correlated with variations in freestream total temperature.

Choking of the sonic orifice was assured by monitoring the pressure ratio across the orifice as the vacuum was throttled. For a given upstream condition, independence of the pressure at the hot-film probe to downstream pressure signaled that sonic flow had been achieved. For all cases this was verified to be within the capabilities of the vacuum pump. A 7.5 horsepower pump was used. During use, the pressure difference across the orifice was monitored to assure choking.

Time response of the probe was determined through a series of tests where a solenoid valve was switched between matched pressure helium and air, and the time for the probe to reach a steady state measurement was recorded. This test was conducted for helium to air and air to helium over a wide range of inlet pressures. In general, the time response associated with switching from helium to air was two thirds that found for going from air to helium. In all cases, steady

state values were attained in less than 1.5 seconds. The time response was also verified by taking three flow field surveys with delay times of 1.0, 1.4, and 1.8 seconds in the sampling loop. Occurrence of other measurements in the sampling loop prior to the composition measurement, resulted in the effective settling time for the composition probe after location of the rake at a specified location, of 0.5 seconds greater than the delay time. While some differences in the data were noticed locally between the 1.0s and 1.4s runs, no differences were noted between the 1.4s and 1.8s runs within the accuracy of the probe response. A 1.4 second delay was chosen for all of the experiments.

Of critical importance to the proper operation of the analyzer was the swallowing of the bow shock which formed ahead of the sampling probe in the supersonic flow. If the shock is not swallowed the pressure gradient existing between the shock and the sampling tip will act to deflect light species around the probe more readily than heavy species. Thus, the sample ingested by the probe will be enriched with heavy gas species. This effect was first documented by Reis and Fenn [1963], and has been studied in more detail by Chang and Fenn [1970] and Campargue [1976] among others. The effect can be strong with nearly complete separation possible in some cases. Indeed, removal of a sample using a properly designed tip has been patented as a gas separation device. The degree of separation was shown by Chang and Fenn to scale when plotted as a function of Kn/M_∞, with no separation effects noted in an argon-helium mixture below $Kn/M_\infty = 8 \times 10^{-4}$. Analysis of pertinent parameters in the current effort showed values of this parameter as large as 1.5×10^{-3} in some flow regimes. Therefore an effort was made to assure shock swallowing by the sampling tip. This was accomplished by careful design of the probe tip, employing a sharp edge and an internal expansion, and careful monitoring of mass flow through the probe. A drawing of the sampling tip is shown in Figure 15c. The tip was constructed from stainless steel, using a specially designed cutting tool. The tip diameter was 0.018 in. with a 10^o internal expansion. As the temperature and pressure of the sample were

known at the hot-film probe location, mass flow through the sonic orifice was calculated assuming isentropic, inviscid, one-dimensional flow. Further, knowledge of the conditions at the two endpoints in the operating range (the exit plane of the nozzles and the freestream), allowed determination of the mass flow associated with just swallowing the shock for a given tip diameter. It was verified that the mass flow through the sonic orifice was greater than that required for swallowing the shock.

As an adjunct to the development of a gas composition analyzer, an automated means of calibrating the device was constructed. The system was capable of providing specified mole fractions of helium in air, at various pressures. Mixture control was automated, pressure control was manual. The basis for the calibration system was a Linde model FM4586 two-channel, mass flow-controlled, gas blending system which was operated remotely using a personal computer. The two controllers provided specified mass flows to within ± 1 % of full scale (1.75 scf/min.) within 30 seconds. The two controllers were calibrated by Linde personnel for operation in helium and air respectively. The mixing system was supplied with helium and air from standard 220 scf gas cylinders. Downstream of the gas blender were a bleed valve to allow constant back pressure on the controllers, and a Matheson Model 3494 absolute pressure regulator.

The process of calibrating the gas analyzer consisted of manually setting the pressure regulator and then remotely setting mixture mole fractions (X_{he} = 0.00, 0.10, 0.20, 0.30, 0.40, 0.50, 0.60, 0.70, 0.80, 0.90, 0.95, 1.00) for input to the sampling tip. Forty-five seconds were allowed between each calibration point to allow the gas blender to reach steady state. After recording hot-film anemometer voltage and pressure, diagnostic measurements (gas temperature and downstream pressure) were recorded to assure proper performance. After completing this for each composition setting, the pressure regulator was reset and the process was repeated. Approximately twelve to fifteen pressure settings were used producing about 150 points in the

calibration space. As the mole fraction was varied, pressure changed considerably due to differing flow losses and regulator response. Thus, what resulted from the calibration was a matrix of points defining probe response that were scattered about the calibration space.

An example plot from a calibration is shown in Figure 16. The general response of the analyzer is displayed. Hot-film output (E), increased with increasing pressure and helium mole fraction. Further, at high pressure, output was a strong function of composition and a weak function of pressure. At low pressure, output was a strong function of pressure and a weak function of gas composition. It was the latter characteristic that required very accurate recording of pressure in the low pressure regimes.

Composition was determined from the calibration space by means of a bilinear interpolation. During practice, a sample of unknown composition was withdrawn from the wind-tunnel. The hot-film voltage ($E_{meas.}$) and pressure ($p_{meas.}$) within the analyzer were recorded. Each of these measurements was based on the mean of 400 points taken at a sampling rate of 3000 Hz. A constant pressure line (at $p = p_{meas.}$) was then fit through the calibration space as shown in Figure 17. The hot-film output associated with each point along this line was interpolated in a linear manner from the calibration data. The recorded voltage from the probe was then compared with the voltages along this line. Composition was determined from a linear interpolation between the compositions associated with the voltages on this line. Two strong sources of error are associated with this data reduction procedure. The first results from the locally planar approximation to the calibration surface. This was minimized by taking many calibration points. The second source of error results from ignoring the uncertainty associated with the data. A two-dimensional polynomial regression analysis would have alleviated this problem. However, efforts to fit piece-wise, polynomial basis functions in E and p to the

calibration space resulted in unacceptable deviations on the edges of the domain (where much of the data existed).

In final form, the gas composition analyzer allowed determination of helium mole fraction to within ±3% over the entire range of flow field conditions. It should be noted that this is an upper bound and performance in general was much better, particularly in the regions of higher pressure (>0.2 psia inside the probe), which made up the majority of the flow field. The probe was calibrated once a day prior to testing. Following testing, response was checked to verify that no strong shifts in calibration had occurred. This was accomplished by re-attaching the probe to the calibration apparatus.

Raw data from one experiment were reduced using calibrations taken over a period of ten days to investigate the long-time stability of probe response. The composition values resulting from the various calibration sets were repeatable to within ±4% helium mole fraction. The variation noted resulted from a drift in calibration of the pressure transducer. The data presented were all reduced using the calibration data taken earlier that day to remove this as a possible source of error.

The accuracy of the readings and the time response obtained from the gas composition analyzer allowed very detailed probing of the flow field. The automated means of calibrating the probe allowed daily calibration. The design of the analyzer also proved to be quite robust. No hot-film probes were lost to other than human error during the full extent of the testing.

2.4.2 Cone static pressure measurements

The static pressure on the surface of a cone, p_C, was used with the other measurements taken from the rake to obtain Mach number, static pressure and temperature, and other basic flow

variables. A drawing of the probe used to obtain this measurement is shown in Figure 15a. The probe tip was coarse machined from stainless steel. The final setting of the 10^{o} half-angle was done using a fine grinding stone. Four 0.020 in. holes were drilled perpendicular to the surface, 90^{o} apart. Approximately 3 feet of 0.07 in. internal diameter stainless steel tubing and 3 feet of 0.375 in. internal diameter teflon tubing ran between the probe and a transducer mounted external to the wind-tunnel traverse enclosure box. The cone static pressures measured ranged from 1.0 psia to 3.0 psia. Time response was verified by conducting a planar survey with three different delays in the data acquisition code loop. The 1.4 second delay chosen for the composition probe satisfied the time response requirements of this probe as well. The strain-gage type pressure transducer (CEC 4-326-0003) had a range of 25 psia with a quoted accuracy of 0.25 % full scale. Periodic checks of transducer response showed that the accuracy was ±0.1 psia. The additional uncertainty resulted from the effect of control room temperature variations on the analog to digital data acquisition circuitry. These effects were minimized by using an external amplifier to boost the 0-5mV signal rather than the amplifiers on the data acquisition board. (The performance of these amplifiers was strongly dependent on ambient temperature.) The measurements presented were each the result of an average of 200 points sampled at the rate of 3000 Hz.

Initial measurements made using the cone static probe were higher in magnitude than expected. Schlieren photographs of the flow about the probe revealed that the boundary layer on the surface of the cone was separating due to pressure disturbances associated with the shock from the rake propagating upstream. This problem was alleviated by extending the probes further (0.75 in.) from the rake.

2.4.3 Pitot Pressure Measurements

In a supersonic flow, the pitot pressure, p_t, is a measure of the total pressure downstream of the bow shock generated by a stagnation probe. A drawing of the pitot pressure probe is shown in Figure 15b. The probe used had a 0.030 in. diameter sensing orifice, and was connected to a pressure transducer in the same manner as the cone static probe. A 0-100 psia strain gage pressure transducer (Dynisco APT310B-1C) was used to measure the pressures which ranged from 2 psia to 40 psia. Again, an external amplifier was used to minimize uncertainty. Periodic checks of transducer response showed that error was less that ± 0.5 psia. The measurements presented were means resulting from 200 individual measurements taken with a sampling rate of 3000 Hz. An analysis of time response was conducted in conjunction with the analysis of that for the composition and cone static pressure measurements. The sampling loop delay chosen for these probes was sufficient for this measurement as well.

2.4.4 Total temperature measurements

A thermocouple-based probe was used to measure total temperature (T_0). An effort was made to develop a coiled cold-wire probe (Weinstein [1973]) to minimize end conduction errors by increasing the length to diameter ratio of the sensing element. Poor survivability required use of a more robust, thermocouple-based sensor. A drawing of the probe is shown in Figure 15d. The sensing element was a chromel-alumel thermocouple junction. Conduction errors were minimized by using fine (0.003 in. diameter) wire and a large (0.02 in. diameter) bead. The thermocouple was enclosed in a 0.070 in. internal diameter radiation shield. Two 0.030 in. diameter holes were located in the radiation shield downstream of the thermocouple. The diameter of the holes and length and internal diameter of the radiation shield were chosen to provide strong convective heat transfer while keeping the thermocouple outside the influence of the thermal boundary layer which developed on the interior walls of the shield. Due to the size of the shield, the capture area of this probe was significantly greater than that of the other probes.

Thus, flow field temperature gradients presented will appear broader than gradients in data from the other probes. The thermocouple voltage was reduced using a cold junction signal on the data acquisition multiplexer board. The low level signal from the thermocouple carried a significant noise component which produced fluctuations of $\pm 3^{o}$ C. Comparisons of the output of the total temperature probe with helium and air plenum chamber total temperatures were used to determine the effective recovery factor for the probe. In all cases, the probe measurement was greater than 98% of the settling chamber temperatures. The total temperature data presented were obtained from 200 points sampled at 3000 Hz. The cold junction measurement was based on 100 points sampled at 3000 Hz.

2.5 Reduction of flow field survey data

The raw flow field survey data (p_c, p_t, T_0, c_{he}) were reduced to obtain fundamental variables (M, ρ, p, T, ...). The reduction procedure relied on several assumptions and approximations which had no uniform validity throughout the flow field. However, the reduction was of interest as it provided some means for verifying the validity of measurements through quantitative comparison with computational results.

The conical coordinate system and pertinent variables are defined in Figure 18. Assuming inviscid flow, the flow about the cone is represented by two, coupled, ordinary differential equations.

$$\frac{d^2u_r}{d\theta^2} + u_r = \frac{a^2[u_r + u_\theta \cot\theta]}{u_\theta^2 - a^2}$$

$$\frac{du_r}{d\theta} = u_\theta \quad ,$$

where

$$a^2 + \frac{\gamma - 1}{2}(u_r^2 + u_\theta^2) = \frac{\gamma + 1}{2}a_*^2 \ , \qquad a_*^2 = \frac{\gamma R T_0}{1 + \frac{\gamma - 1}{2}M_\infty^2}\left[\frac{2}{\gamma + 1} + \frac{\gamma - 1}{\gamma + 1}M_\infty^2\right] ,$$

with boundary conditions

$$u_\theta = 0 \qquad \text{at} \quad \theta = \theta_c$$

$$u_\theta = -w_2, \quad u_r = v \qquad \text{at} \quad \theta = \beta \ .$$

This equation set is only valid for the case were the shock wave remains attached to the cone. (~ $M_\infty > 1.2$ for $\theta_c = 10^o$)

Further, it can be shown that

$$\frac{p_\infty}{p_c} = \left[\left(1 + \frac{\gamma - 1}{2}\frac{u_r^2}{a^2}\right)^{\gamma/\gamma-1}\left(\frac{2\gamma}{\gamma + 1}M_\infty^2 \sin^2\beta - \frac{\gamma - 1}{\gamma + 1}\right)^{1/\gamma-1}\left(\frac{\gamma + 1}{2}M_\infty^2 \sin^2\beta\right)^{-\gamma/\gamma-1}\right]_{\theta = \theta c} .$$

Thus for a given θ_c ,

$$p_\infty = \text{fnc}\,(p_c\,,\, T_0\,,\, \gamma\,,\, R\,,\, M_\infty) \ .$$

The above system of equations was derived assuming calorically perfect gases. However, during solution of the system, C_p was calculated from

$$\frac{C_{pi}}{R_i} = A_i + B_i T + C_i T^2 + D_i T^3 + E_i T^4 \ .$$

The coefficients were obtained from a fit to tabulated data for helium, oxygen and nitrogen. Introduction of C_p dependence on temperature, into equations derived assuming constant specific heats, produced only minor error because of the weak dependence of γ on temperature in the regimes of interest in these experiments. Thus while R was strictly a function of gas composition, γ was a function of T_0 and M_∞, as well as c_{he}.

The relation for p_∞ may then be further simplified:

$$p_\infty = \mathbf{F}(M_\infty , + \text{measured quantities}) \quad .$$

Similarly, the relation for pitot pressure,

$$\frac{p_\infty}{p_t} = \left(\frac{2\gamma}{\gamma+1} M_\infty^2 - \frac{\gamma-1}{\gamma+1} \right)^{1/\gamma-1} \left(\frac{\gamma+1}{2} M_\infty^2 \right)^{-\gamma/\gamma-1} ,$$

may be expressed as

$$p_\infty = \mathbf{G}(M_\infty , + \text{measured quantities}) \quad .$$

Here the pressure dependence associated with a normal shock has been assumed for the pitot probe.

The intersection of **F** and **G** defines the unique values of p_∞ and M_∞ which satisfy the measured quantities.

The procedure to reduce the data was based upon a root-bisection iteration in M_∞ on the difference **F - G**. At each iteration step, the conical flow system was solved. The solution of the conical flow system was accomplished by a nested root-bisection iteration in β for a given M_∞. During each of these iterations, the ordinary differential equations were integrated from the shock to the cone surface using a 4^{th}-order Runge-Kutta scheme. The iteration in β continued until the no through-flow condition was met at $\theta = \theta_c$. The data reduction was completed on a Cray Y-MP at a cost of approximately 5 cpu seconds per point.

The assumption of inviscid flow on the cone produced large errors in the reduced data. Use of a cone static probe generally requires calibration and then adoption of an effective cone angle to account for the boundary layer. The flow conditions associated with the contoured wall injectors made such a procedure intractable as it would have required calibration over a wide range of Mach numbers, pressures and gas compositions. An effective cone half-angle of 11.8^o was chosen. For this angle the reduction resulted in $M_\infty = 6.0$ when the probe was located in the undisturbed freestream. It is clear that the effective cone angle is strongly Reynolds number dependent and it is expected that this choice produced errors in other regions of the flow, particularly the lower Reynolds number helium jet. Further error was introduced by spatial misalignment of the various probes on the rake. The raw measurements did not originate from exactly the same physical location in the flow field. Significant error also resulted when the data was taken from regions of strong flow angularity (as high as 30^o in some areas). The unique solution in p_∞ and M_∞ was also influenced by uncertainties in the raw data which resulted from noise and other sources. The solution was very sensitive to small errors in each of the measured pressures, and less so to errors in the composition and total temperature measurements.

As a result of the errors intrinsic in the reduced data, as well as the expense associated with the data reduction process, the majority of data was not reduced. All conclusions based on the

experimental data were drawn on the basis of the raw data. The reduced data that is presented is shown only to provide a very rough quantitative measure of various fundamental flow variables.

2.6 Presentation of flow field survey data

The time response of the various measurement techniques as well long wind-tunnel run times allowed detailed analysis of the flow field for each of the parameter variations of interest in the study. Each run consisted of measuring a series of two-dimensional planes. The survey was completed over one region of symmetry. The grids used for both the full-scale injectors and the half-scale injectors are shown in Figure 19. The full-scale grid consisted of 140 points within the region of interest, while 110 points were used for the half-scale models. Probe designs allowed measurements within 0.125 in. of the wall. The grids extended upwards to $\overline{z}$ = 2.625. Passing each of the probes through the same physical region of space required extension of the survey beyond the bounds of each of the grids. This is shown in the inset of Figure 19. Further, since it was necessary that the measurements from each of the probes be acquired at the same physical location in space, the spacing of the grid in the crossflow direction ($\overline{y}$) had to be evenly divisible into the spacing between the probes themselves. Data was not taken on-the-fly due to the time response of the various probes. The rake was stopped at each grid point as shown in the algorithm of Section 2.3. For the full-scale models, planes of data were taken at $\overline{x}$ = 0, 1, 4, 8, and 13. Half-scale model surveys were conducted at $\overline{x}$ = 0, 4, 8, 16, and 26.

The raw data is presented as a series of contour plots in $\overline{x}$ for each set of conditions. The data have been mirrored about the symmetry plane. After being mirrored, the data was interpolated onto an even grid for contouring. Choice of a contour grid spacing which was nearly the same as the experimental grid prevented representation of sub grid-scale variations in the final plots. A 20 x 20 grid was chosen for the full-scale model data and 20 x 15 grid for the half-scale data in $\overline{y}$ and $\overline{z}$ respectively. (After mirroring, the experimental grids were 19 x 14 and 19 x 11.) Even with

this precaution, contour gridding of two-dimensional data can often produce anomalous results. An interpolation procedure was chosen in an effort to preserve the original data points in the final representation. The data points were weighted such that the influence of neighboring points declined as distance from the point being estimated increased. The higher the weighting power, the less influence neighboring points have on the estimation and the more accurately the actual points are represented. Some influence of other points is desirable as it acts to smooth the variations associated with uncertainty in the data. A weighting power of 6 was chosen for all of the data so that:

$$Z = \frac{\sum_{i=0}^{n} Z_i/d_i^6}{\sum_{i=0}^{n} 1/d_i^6}$$

where Z was the estimation, Z_i were the neighboring points at distance d_i, and n was total number of points. This method was shown to produce contour plots which accurately represented the original data. On the upper regions of the plots, due to the stretching of the experimental grid, some sub grid-scale variations were introduced. It is important when analyzing the data not to interpret spatial variations which are represented on scales smaller than the original grid upon which the measurements were taken. As well, the contours below $\bar{z} = 0.125$ on the full-scale model and $\bar{z} = 0.25$ on the half-scale models are extrapolations towards the wall and should not be given credence.

2.7 Flow visualization techniques

Schlieren, shadowgraph, surface oil and Rayleigh scattering flow visualization techniques were used to investigate the contoured wall injectors. The various apparatus required for each of

these methods were mutually exclusive. Thus, each of these techniques was not used to study the same sets of conditions and geometries, due to lack of sufficient test time. An effort was made to produce some overlap in the studies using each of the techniques to allow more confidence in direct comparisons between the results of each of the methods. The apparatus and techniques employed are described below.

2.7.1 Schlieren flow visualization

The High Reynolds Number Mach 6 Wind-Tunnel is equipped with a standard Schlieren flow visualization system using 16 inch mirrors, a pulsed light source and a horizontal knife edge. The duration of the pulse was approximately 5 ms. A freestream fluid particle moved approximately 15 feet in this time period, so the images obtained were not temporally resolved. The Schlieren system allowed imaging of a 12 in. x 12 in. longitudinal plane. The entire system was traversed to provide full coverage of the 42 inch long test section. In the Schlieren photographs shown, density gradients in the flow field are represented as gradients of intensity in the images. The measurements were the result of a line-of sight integration across the flow field so strongly two-dimensional phenomena were represented more clearly.

2.7.2 Shadowgraph flow visualization

The apparatus used for application of the shadowgraph technique was similar to the Schlieren system. The knife edge was removed and a 30 ns. pulse duration spark source replaced the 5 ms. source. While still producing an image resulting from integration through the flow field, the images obtained were time-resolved, effectively freezing the motion of the flow. The intensity of the shadowgraph images is proportional to changes in the second derivative of density.

2.7.3 Planar Rayleigh scattering

A collaborative effort was undertaken with personnel from the Optical Spectroscopy Section of NASA Langley Research Center, Instrument Research Division to investigate the application of planar Rayleigh scattering in the High Reynolds Number Mach 6 Wind-Tunnel. All issues associated with the application of this technique as a diagnostic measure were resolved by NASA personnel (particularly Drs. Shirinzadeh, Balla, Hillard, Anders and Exton). Interpretation of the results in terms of fluid dynamics was conducted jointly. The difficult conditions in the wind-tunnel strongly limited the applicability of this tool as a quantitative measure of flow properties. The technique did provide highly temporally-resolved planar images which, in light of comparisons with time-mean flow surveys, allowed insight into the qualitative behavior of the flow field. A review of the test technique and data reduction method is presented below. Particular attention is given to factors which limited the applicability of the tool. A more detailed discussion of these topics is presented by Shirinzadeh, *et al.* [1991b].

Rayleigh scattering refers to the elastic scattering of light from molecules or other small particles, ($d/\lambda << 1$ where d is the diameter of the particle and λ is the wavelength of the incident light). In a mixture of gases, the Rayleigh scattering signal is a function of the mole fraction weighted average of the scattering cross sections of the individual gases. Rayleigh scattering is dependent on total flow density, and in general can not be used to identify species in a binary mixing field. However, for the case where the Rayleigh scattering cross section for one of the species is significantly different from that of the other, the technique can be used to identify species gradients. The utility of the technique for identification of species in a binary mixture is dependent therefore upon weak changes in number density and strong differences in refractive index between the species. While the cross section of helium at these test conditions was a factor of 100 less than that of diatomic nitrogen, changes in number density of a factor of 10 were also present. In portions of the flow field where density gradients were coincident with species

gradients, image intensity did track the mixing interface. In other regions of the flow field more careful interpretation was required.

The light source for the measurements was a 130 mJ/pulse argon-fluoride excimer pulsed laser. Use of broadband ultraviolet light (near 193 nm) greatly increased the scattering cross section. (The cross section is proportional to λ^{-4}.) The pulse duration was 15 ns. A 7 in. wide by 1.5 in. high crossflow plane was imaged onto a CCD array. The laser light sheet was located 0.10 in. above the surface of the model and imaged a depth of approximately 0.04 inches. The effective spatial resolution of the system was about 0.04 in. in the image plane. A schematic of the apparatus is shown in Figure 20. For each test condition, 22 consecutive images were recorded at a sampling rate of 10Hz. In 0.1 seconds a fluid particle traveled nearly 300 feet so the images were considered as random samples in time. The images presented were subject to a series of corrections. The processing, discussed in detail by Shirinzadeh *et al.* [1991b] corrects for shot-to-shot laser intensity variations, and individual response characteristics of the pixels in the CCD array. The data are presented in terms of deduced pressure obtained from pre-run calibrations. A linear approximation was used to scale the images geometrically to simulate a 90^{o} viewing angle. The images have not been corrected for distortion which may have occurred since a medium of non-uniform index of refraction existed between the laser sheet and the collection device. It was estimated that these deformations of the image occurred on a scale smaller than the resolution of the system.

Several factors limited the use of planar Rayleigh scattering as a quantitative tool in this flow field. Primary among these was the inability to distinguish gradients in density from composition changes. This problem was compounded by the strong influence of thermodynamics on the scattering cross-section of the air. The image intensities obtained from the freestream were often an order of magnitude greater than that expected for molecular scattering. This suggests that

molecular clustering (condensation) occurred as the air was expanded to M=6. Shirinzadeh, Hillard and Exton [1991] and Shirinzadeh *et al.* [1991a] have addressed the influence of temperature and pressure on molecular clustering in a similar flow field. In the current effort, initial imaging studies were made at a total pressure of 1000 psia. The scattering cross section of the flow entering the mixing region was locally affected by changes in temperature and pressure as it passed through the ramp region, causing strong variations in index of refraction beyond those associated with changes in number density. The magnitude of these variations was reduced by conducting the planar imaging studies at a tunnel total pressure of 600 psia. For this condition the data qualitatively matched that from the probe surveys. The effect was still noted in the images. The lack of scattering in the boundary layer, for instance, may have been as much a result of thermodynamics (*e.g.*, high temperature led to less condensation) as fluid dynamics (low density).

2.7.4 Surface oil flow visualization

Oil flow was used to visualize streamlines on the surface of the model. Fluorescent dye was mixed with 500 cs oil. The oil was lightly coated on the model and then illuminated with ultraviolet flood lights and recorded on video tape after flow initiation. The location of the oil was a measure of surface shear stress and pressure gradient. Typically, regions of flow separation and recirculation allowed oil to collect, while regions of high momentum were noted by an absence of oil.

CHAPTER 3

COMPUTATIONAL METHODOLOGY

The difficulties associated with the experimental investigation of the contoured wall fuel injectors made application of numerical modelling an attractive complement to the experimental effort. Preliminary modelling using an Euler code (Marble *et al.* [1990], and Hendricks and Marble [1990]) lent insight into general flow phenomena. However, early experimental results showed strong evidence of the important role of the boundary layer in injector performance. This mandated a three-dimensional, viscous simulation. These computations were used to enhance the understanding provided by the experimental data. Investigations beyond the scope of the experimental studies were also conducted.

3.1 Description of the code

The SPARK3D code (Carpenter [1989]) was obtained from NASA Langley Research Center's Computational Methods Branch for the purpose of modelling the complex flow field associated with the contoured wall injectors. The code allows solution of the three-dimensional Navier-Stokes, energy and species continuity equations, for a multiple species system. A chemical source term may also be added to include the effects of finite-rate chemistry. This system is advanced in time using a compact, spatially fourth-order accurate, symmetric, predictor-corrector algorithm until convergence at steady state is obtained. The code has been used by several investigators to predict reacting and non-reacting flow about other scramjet combustor injection schemes (Drummond *et al.* [1989], Eklund, Northam, and Fletcher [1990], Riggins, Drummond,

and Carpenter [1990], Riggins *et al.* [1990], and Riggins and McClinton [1990]). In this study the code was used in a non-reacting mode with M = 1.7 helium injected into a M = 6 airstream to allow direct comparison with the experiments.

3.1.1 Governing equations

The governing equations solved by the SPARK3D code are presented below. For three-dimensional flows, the continuity, momentum, energy and species equations can be expressed in Cartesian coordinates as:

$$\frac{\partial \boldsymbol{U}}{\partial t} + \frac{\partial \boldsymbol{E}}{\partial x} + \frac{\partial \boldsymbol{F}}{\partial y} + \frac{\partial \boldsymbol{G}}{\partial z} = \boldsymbol{H}$$

where,

$$\boldsymbol{U} = \begin{pmatrix} \rho \\ \rho u \\ \rho v \\ \rho w \\ \rho \mathcal{E} \\ \rho c_1 \\ \cdots \\ \rho c_{N_s} \end{pmatrix} \qquad \boldsymbol{H} = \begin{pmatrix} 0 \\ 0 \\ 0 \\ 0 \\ 0 \\ \dot{\omega}_1 \\ \cdots \\ \dot{\omega}_{N_s} \end{pmatrix} \qquad \boldsymbol{E} = \begin{pmatrix} \rho u \\ \rho u^2 - \sigma_x \\ \rho uv - \tau_{xy} \\ \rho uw - \tau_{xz} \\ (\rho \mathcal{E} - \sigma_x)u - \tau_{xy}v - \tau_{xz}w + q_x \\ \rho c_1 (u + \tilde{u}_1) \\ \cdots \\ \rho c_{N_s} (u + \tilde{u}_{N_s}) \end{pmatrix}$$

$$\boldsymbol{F} = \begin{pmatrix} \rho v \\ \rho uv - \tau_{xy} \\ \rho v^2 - \sigma_y \\ \rho vw - \tau_{yz} \\ (\rho \mathcal{E} - \sigma_y)v - \tau_{xy}u - \tau_{yz}w + q_y \\ \rho c_1 (v + \tilde{v}_1) \\ \cdots \\ \rho c_{N_s} (v + \tilde{v}_{N_s}) \end{pmatrix} \qquad \boldsymbol{G} = \begin{pmatrix} \rho w \\ \rho uw - \tau_{xz} \\ \rho vw - \tau_{yz} \\ \rho w^2 - \sigma_z \\ (\rho \mathcal{E} - \sigma_z)w - \tau_{xz}u - \tau_{yz}v + q_z \\ \rho c_1 (w + \tilde{w}_1) \\ \cdots \\ \rho c_{N_s} (w + \tilde{w}_{N_s}) \end{pmatrix}$$

for i = 1, ..., (N_S - 1) where

$$\sigma_x = -p + 2\mu\frac{\partial u}{\partial x} + \lambda\nabla\cdot\mathbf{u} \qquad \sigma_y = -p + 2\mu\frac{\partial v}{\partial y} + \lambda\nabla\cdot\mathbf{u} \qquad \sigma_z = -p + 2\mu\frac{\partial w}{\partial z} + \lambda\nabla\cdot\mathbf{u}$$

$$\tau_{xy} = \mu\left(\frac{\partial u}{\partial y} + \frac{\partial v}{\partial x}\right) \qquad \tau_{yz} = \mu\left(\frac{\partial v}{\partial z} + \frac{\partial w}{\partial y}\right) \qquad \tau_{xz} = \mu\left(\frac{\partial u}{\partial z} + \frac{\partial w}{\partial x}\right)$$

$$q_x = -k\frac{\partial T}{\partial x} + \rho\sum_{i=1}^{N_S} h_i c_i \tilde{u}_i \qquad q_y = -k\frac{\partial T}{\partial y} + \rho\sum_{i=1}^{N_S} h_i c_i \tilde{v}_i \qquad q_z = -k\frac{\partial T}{\partial z} + \rho\sum_{i=1}^{N_S} h_i c_i \tilde{w}_i$$

$$\mathcal{E} = \sum_{i=1}^{N_S} h_i c_i - \frac{p}{\rho} + \frac{u^2 + v^2 + w^2}{2}$$

$$p = \rho R_u T \sum_{i=1}^{N_S} \frac{c_i}{m_i}$$

$$h_i = h^R_i + \int_{T^R}^{T} C_{p_i} dT$$

$$\frac{C_{p_i}}{R_i} = A_i + B_i T + C_i T^2 + D_i T^3 + E_i T^4$$

Only $(N_S - 1)$ species equations were considered in the formulation since the mass fraction of the species which was left out was prescribed by satisfying the constraint equation

$$\sum_{i=1}^{N_S} c_i = 1$$

which was obtained from mass conservation.

Coefficients in the specific heat at constant pressure expression were determined by a curve fit to tabulated data.

The multicomponent diffusion equation for the diffusion velocity of the i^{th} species,

$$\tilde{\mathbf{u}}_i = \tilde{u}_i\mathbf{i} + \tilde{v}_i\mathbf{j} + \tilde{w}_i\mathbf{k}$$

is expressed:

$$\nabla X_i = \sum_{j=1}^{N_S} \left(\frac{X_iX_j}{D_{ij}}\right)(\tilde{\mathbf{u}}_j - \tilde{\mathbf{u}}_i) + \left(\frac{\rho}{p}\right)\sum_{j=1}^{N_S} c_ic_j(\mathbf{b}_i - \mathbf{b}_j) + (c_i - X_i)\left(\frac{\nabla p}{p}\right) + \sum_{j=1}^{N_S} \left(\frac{X_iX_j}{\rho D_{ij}}\right)\left(\frac{D_{Tj}}{c_j} - \frac{D_{Ti}}{c_i}\right)\left(\frac{\nabla T}{T}\right)$$

The body force and temperature terms were assumed negligible. This equation was applied to only (N_S - 1) species. The diffusion velocity for the species that was left out was prescribed by satisfying the constraint equation:

$$\sum_{i=1}^{N_S} c_i\tilde{u}_i = 0$$

This system was advanced in time in a spatially discretized domain. Fourth-order artificial viscosity was applied based on gradients in pressure and temperature to suppress numerical

instabilities. A detailed discussion of the numerical algorithms used in the code was presented by Carpenter [1989].

3.2 Application of the code

Gridding and boundary conditions were adopted to simulate an infinite array of contoured wall fuel injectors. Freestream conditions in the air were chosen to match those of the experimental studies (p_0 = 1000 psia, T_0 = 246^o C, M = 6). Specific issues of grid generation, application of boundary conditions, turbulence modelling, and boundary layer modelling are discussed below. Typical domains consisted of approximately 266,000 grid points. Approximately 4 cpu seconds per time step were required to advance the system on a CRAY Y-MP class supercomputer. Local time-stepping was used to increase the speed of convergence. Convergence was determined by monitoring the maximum of

$$\frac{\rho_t - \rho_{t-\Delta t}}{\rho_t}$$

in the computational domain. In all cases, this was driven below 1%. In addition,

$$\frac{\rho_t - \rho_{t-500\Delta t}}{\rho_t}$$

was monitored to assure steady-state was achieved. Typically, convergence was attained in less than 4 cpu hours.

3.2.1 Grid generation

An example of one of the computational grids is shown in Figures 21 and 22. The entire domain was gridded and then the injector ramp was formed by blanking out a region of the domain. The

blanking was performed within the code by setting the velocity equal to zero at all points within the ramp, and applying appropriate boundary conditions on the walls of the ramp and the injection plane. Development of a grid which allowed adequate refinement of the solution throughout the flow field was difficult because of the rough grid edge required due to fitting the triangular ramp in a rectilinear domain. Refinement of the grid was closely tied to the quality of flow obtained over the rough grid edge. The problem was alleviated by performing a convolution (with a nine grid point kernel) on the temperature and pressure at the boundary prior to applying first-order boundary conditions.

It was difficult to determine the proper form of the shock for such a geometry due to effects of three-dimensional relief and interaction with the boundary layer. Grid performance was verified by studying the rough grid edge in a two-dimensional converging duct where shock angle and strength could be calculated analytically. Performance was compared against a solution obtained for a smooth-walled converging duct. Examples of pressure contours obtained from such a study are shown in Figures 23 and 24. For both the rough and smooth walls the shock angle of 13.5^{o} compares well with the expected angle of 13^{o}. (The difference may be due to the boundary layer which was allowed to grow in the computations.) The pressure rise associated with the rough grid edge was 10% higher than that of the smooth wall. The disturbances generated by the rough wall were confined to a thin numerical boundary layer along the wall. In this sense the solution was globally grid-resolved. It was difficult to determine the extent to which the performance of the grid in two dimensions carried over to the three-dimensional case, but good general agreement was obtained between the experiments and the numerical simulations.

Each of the geometries was gridded by fixing the spacing of points required in x and z to provide a globally grid-resolved solution over the ramp region. Downstream of the injection plane, grid spacing was matched to the ramp region and then increased exponentially with downstream

distance. The algorithm for exponential expansion and compression of the grid was taken from Anderson, Tannehill and Pletcher [1984]. Upstream of the ramp region the grid spacing increased towards the beginning of the domain. In z, exponential grid compression was used as the wall was approached to resolve the boundary layer. Expansion was used above the ramp. The domain in z extended to four injector heights above the wall of the combustor. In y, a smooth exponential variation was employed to cluster the grid points near the wall of the injector ramp. One plane of symmetry was calculated. The computations were conducted on 266,000 grid points (175 in x, 29 in y, and 51 in z).

3.2.2 Boundary conditions

First-order, viscous boundary conditions were applied on the lower wall and sides of the injector ramp (with convolution on the upper ramp wall as described above) for the majority of the computations. For the cases where inviscid conditions were desired, first-order, free-slip conditions were used. Second-order, open boundary treatment was applied on the upper boundary of the domain, and first-order symmetry conditions were applied on the two planes of symmetry. On all boundaries, higher order conditions were tried but rapidly produced numerical instability. One area of particular difficulty in applying boundary conditions was the injection plane, particularly the corner of the injector. In dealing with this problem, it was found that modelling the injector with a finite-width wall was advantageous. The width, equal to the spacing between two grid points corresponded closely with that of the experimental model.

3.2.3 Turbulence modelling

A Baldwin and Lomax [1978], two-layer, algebraic eddy-viscosity turbulence model was included with the code. The ability of this model to accurately represent the complex mixing phenomena associated with the contoured wall fuel injectors was strongly questioned. The application of an inappropriate turbulence model can influence the global solution in a manner which is difficult to

determine. As a result, a decision was made to limit the scope of the computations by removing the turbulence model. Thus, no effort was made to accurately simulate the fine-scale mixing seen in the experiments. The laminar mixing study allowed investigation of only time-mean global phenomena. These phenomena were compared directly with experimental data. Mixing rates were compared only qualitatively with the experiments, though quantitative comparisons were made between individual computations.

3.2.4 Boundary layer modelling

Initial experimental results showed that the size of the wall boundary layer at the beginning of the ramp geometry strongly influenced injector performance. Instead of providing a long initial flat plate region for a sizable boundary layer to develop, a thick boundary layer was modelled at the inlet to the computational domain. Two important classes of mechanisms exist for boundary layer influence. The first of these is the strong displacement effect of a hypersonic boundary layer ($\delta \sim \delta^*$) which acts to modify effective wall geometry. The second class are the phenomena associated with the unsteady nature of a turbulent boundary layer, and the subsequent interaction with the steady and unsteady components of the mixing field. Due to lack of appropriate turbulence modelling, the latter class of effects were not treated. A generic M = 6 turbulent boundary layer velocity profile (Figure 34 of Korkegi [1954]) was fit with a polynomial. The temperature profile was determined directly by assuming constant pressure and an adiabatic wall. The turbulent profile was chosen as it corresponded to the state of the boundary layer studied experimentally. Absence of a turbulence model in the code constrained the dynamics of the layer to be determined by laminar mechanics. There was some fear that the elliptic portion of the boundary layer would give rise to feedback instabilities at the inlet of the computational domain. No such problem was noted. In fact, the small streamwise gradients associated with the fully developed profile worked to alleviate some local instabilities near the floor of the

combustor inlet which were previously a problem. These instabilities were generated by inadequate grid resolution in the initial developing region of the boundary layer.

CHAPTER 4

ANALYSIS OF EXPERIMENTAL AND COMPUTATIONAL DATA

The methods used to analyze injector performance in response to parameter changes are described below. Four general areas of interest were addressed: mixing performance, loss analysis, jet penetration and heat transfer. These were interpreted in terms of scales much greater than those on which molecular mixing was achieved. Further, temporal aspects were addressed for the most part, as they were manifest in the mean. These caveats result from the limited scope of the study as discussed in Section 1.5.

The utility of the computational solutions is evident in the extensive analysis of mixing and flow losses which they allowed. Less satisfactory treatment was possible for the experimental data. As no attempt was made to correctly model turbulent mixing numerically, quantitative comparisons between the computational and experimental data were limited. The methods described in Sections 4.1 - 4.4 are directed towards analysis of mixing performance. Jet penetration and heating considerations are addressed in Section 4.5. A description of the loss analysis performed appears in Section 4.6.

4.1 Mixedness measure

A understanding of the effectiveness of an injection geometry requires detailed knowledge of the level to which the injectant is mixed as a function of distance downstream from the plane of

injection. The numerical data allow determination of the fraction of total helium mass flux which was present in various concentrations at each axial station,

$$\frac{\dot{m}_{He}}{\dot{m}_{He\text{-}total}} \quad \text{vs.} \quad c_{He} \quad \text{vs.} \quad \bar{x} \quad .$$

This measure will be displayed on both surface and contour plots to provide qualitative and quantitative means for comparison. Quantitative comparisons between test cases were made on the bases of the rate of decay of the maximum helium concentration and the percentage of injectant which was mixed to less than $c_{He} = 0.05$. The latter is important as the stoichiometric mass fraction for a hydrogen-air reaction is approximately $c_{H_2} = 0.03$.

4.2 Helium mass fraction contour lengths

The ability of a given injector geometry to generate large-scale convective mixing of the injectant is important as it facilitates molecular-scale mixing via diffusion. Change of interfacial surface area will be displayed by considering the length of contours of constant helium mass fraction as a function of distance downstream of the injection plane,

$$\frac{L_\alpha(\bar{x})}{L_\alpha(\bar{x}=0)} \quad \text{vs.} \quad c_{He} \quad \text{vs.} \quad \bar{x} \quad ,$$

where L_α corresponds to the length of a contour of helium mass fraction $c_{He} = \alpha$. In general, longer more convoluted contours represent stronger convective mixing. Extension and narrowing of species gradients is a necessary precursor to effective diffusive processes. For these injectors, rapid stretching of material line elements would be expected in the near-field due to the strong convection associated with the applied vorticity field. Downstream, diffusion, discretization errors and progression towards steady state damp the growth rates displayed. This measure

was calculated for the numerical data only and is presented on both carpet plots and contour plots. Quantitative comparisons were made based on the change in length of contours of $c_{He} \approx 0.05$.

4.3 Circulation

Generation of large-scale convective mixing is closely tied to formation of vorticity within the mixing region of the flow field. The circulation in each y-z computational plane, Γ, was calculated as a gross measure of the level of vorticity present in the flow field. This provided information concerning the importance of various vorticity sources associated with the contoured wall fuel injectors. This measure can only be interpreted in combination with a thorough understanding of the flow field. Generation of vorticity in regions remote from the injectant does not increase mixing. Rather, such vorticity detracts from injector performance as it requires an expense of energy which does not lead to mixing of the injectant.

4.4 Decay of maximum helium mass fraction

The experimental data allowed a considerably less detailed analysis of mixing performance due to difficulty in acquiring sufficient information about the flow field. One marker for time-mean performance is the decay of the maximum helium mass fraction downstream of the injectors,

$$c_{He\ max} \quad \text{vs.} \quad \bar{x} \ .$$

This measure was tabulated from the composition probe measurements at each surveyed plane for a given test condition and geometry. It represents a bulk measure of the extent to which the injectant has mixed with the freestream. It is often heavily relied upon in grading injector performance due to the relative ease in obtaining the measure. However, the typical injectant mass fraction of interest for a hydrogen/air reaction system is $c_{H2} \approx 0.03$. Thus, relying on

decay of maximum injectant concentration is not entirely satisfactory. The measure is further clouded by the influence of unsteady effects and spatial averaging.

4.5 Jet lift-off height

Strong penetration of the fuel jet into the freestream is desirable for alleviating adverse heating effects at the combustor wall and allowing full use of the oxidizer flow through the combustion chamber. Three measurements may be used to characterize the lift-off of the jet as a function of distance downstream of the injection plane. The maximum and minimum heights above the combustor wall at which helium is present define the upper and lower bounds of the jet. It is the location of the lower boundary of the injectant which is most important for heating considerations. The third measure, the height of the helium mass flux center ($\bar{z}_j$), marks the bulk behavior of the injectant. This measure was obtained from the numerical data by calculating the expected value of the height of the helium mass flux,

$$\bar{z}_{j\,(num.)} = \frac{\sum_{p,q} \dot{m}_{He}(p,q)\,\bar{z}(p,q)}{\sum_{p,q} \dot{m}_{He}(p,q)} \qquad \text{where } \dot{m}_{He}(p,q) = \dot{m}(p,q)c_{He}(p,q)$$

and p = 1... ny, q = 1 ... nz, with ny ≡ number of grid points in y, and nz ≡ number of grid points in z. The uncertainties and costliness associated with reducing the experimental data to obtain density and velocity prevented an identical analysis of the experimental data. Accurate accounting of helium mass fraction was provided experimentally. The expected value of the height of helium mass fraction was calculated to define the bulk behavior of the helium observed experimentally. This measure was calculated as

$$\bar{z}_{j\,(exp.)} = \frac{\sum_{p,q} c_{He}(p,q)A(p,q)\,\bar{z}(p,q)}{\sum_{p,q} c_{He}(p,q)A(p,q)}$$

where A(p,q) is the area associated with grid point (p,q). Due to a general concentric stratification of the helium jet about the mass flux center, this measure mimicked that obtained from the numerical data. This is displayed in Figure 25. The jet lift-off height was calculated by both methods from a computational data set. Based on the close correspondence between the two measures, the experimentally obtained lift-off heights were compared directly with those of the numerical studies. Both were plotted in terms of their variation in $\bar{x}$.

4.6 Entropy

The above measures of injector performance are focused on mixing effectiveness and jet behavior. It is important as well to grade various injectors and test conditions on a loss basis. The losses associated with the injectors can be split into three general categories: losses which are associated with phenomena that enhance mixing, losses associated with phenomena which do not enhance mixing, and losses directly associated with mixing. The losses directly associated with mixing may be measured by the entropy rise due to pure diffusion. A purely diffusive process between two gases gives rise to an entropy increase through a change in the partial pressure of the gases. Considering the simple problem of two different gases in a box separated by a membrane, the entropy rise which results from removing the membrane is

$$\Delta S = R_u\left[n_1 \ln\left(\frac{V_{1\,final}}{V_{1\,initial}}\right) + n_2 \ln\left(\frac{V_{2\,final}}{V_{2\,initial}}\right)\right]$$

where R_u is the universal gas constant , n_i are the number of moles of each gas, and V is the volume. Since this entropy rise results directly from mixing, it is accepted, if not welcomed. As

well, losses which are associated with phenomena that enhance mixing are acceptable if they are efficacious. An example of such losses would be those associated with the generation of baroclinic torque at an injectant/freestream interface. An efficient injection scheme would limit all other losses. However, due to the non-linear, coupled nature of this flow field, such losses are difficult to define. A cursory analysis might lead to the conclusion that the losses associated with the shock generated by the compression of the injector ramp were ineffective as the shock did not propagate into the mixing region. However, the shock did cause a pressure rise which was fundamental in generating a vortical roll-up off of the ramp. These matters will be discussed in greater detail in Section 6.5.

Plots are presented based on the numerical results in which the change in total entropy of the fluid is displayed as a function of position in the computational domain. The entropy of the fluid contained in the volume associated with each cross-flow plane (y-z) was normalized by the mass contained in that plane and plotted as a function of $\bar{x}$. The entropy of the fluid which passed in or out of the open boundary on the top of the domain was corrected for. On the same plots the entropy rise directly associated with diffusive mixing processes is shown. This rise was obtained by considering each computational cell as if it were a box with a membrane as described above. The entropy rise due to mixing the gases to a given concentration if they were initially separate is

$$\Delta S = R_u\left[n_{He} \ln\left(\frac{1}{X_{He}}\right) + n_{air} \ln\left(\frac{1}{X_{air}}\right) \right] ,$$

where X_{He} and X_{air} are the mole fractions of helium and air, and n_{He} and n_{air} are the number of moles of helium and air in the cell. The greater the percentage of total entropy rise that is due to mixing, the more effective the mixing process is on a loss basis.

The local pressure disturbances generated by the rough grid edge on the upper surface of the ramp introduced entropy into the flow field in a manner which did not allow comparison between different geometries and boundary conditions. The problem was present only for cases where a no-slip boundary condition was applied at surfaces in the computational domain. For these cases the entropy rise was plotted downstream of the injection plane only, and was referenced to the entropy present in the fluid after the ramps. This removed effects associated with the rough grid edge. For cases where inviscid boundary conditions were applied, flow along the ramp grid edge was smooth and no additional entropy was added to the system as a result of the rough grid. For these cases direct comparisons were made between various geometries throughout the computational domain.

CHAPTER 5

THE PARAMETRIC STUDY

This chapter is devoted to presenting a tabulation of all of the test cases studied both experimentally and numerically. The motivation for each of the tests as well as the results of the tests will be addressed in Chapter 6.

5.1 Experimental

The conditions for the experimental tests are tabulated below in Table 5.1. All of the tests were conducted with a p_0 = 1000 psia, T_0 = 246 ^oC, M = 6 airstream. At this condition, p = 0.63 psia, T= -210^o C, and R_e = 15 x 10^6 /foot. For each of the tests listed, two-dimensional surveys of the flow field were conducted at several axial stations downstream of the injection plane. All of the experimental models employed even expansion and compression of the ramp surfaces, $\alpha_c = \alpha_e = 4.76^o$.

Table 5.1 Experimental test conditions

Case #	Geometry	Pressure Ratio $\overline{p}$	Velocity Ratio $\overline{v}$	Boundary Layer $\overline{\delta}$
E1	wide spacing, full-scale $\alpha_c = \alpha_e = 4.76^o$	1.0	1.33	0.2
E2	wide spacing, full-scale $\alpha_c = \alpha_e = 4.76^o$	1.0	1.33	0.35
E3	wide spacing, full-scale $\alpha_c = \alpha_e = 4.76^o$	4.0	1.27	0.2

Table 5.1 continued:

Case #	Geometry	Pressure Ratio $\overline{p}$	Velocity Ratio $\overline{v}$	Boundary Layer $\overline{\delta}$
E4	wide spacing, full-scale $\alpha_c = \alpha_e = 4.76^o$	1.0	1.12	0.2
E5	wide spacing, half-scale $\alpha_c = \alpha_e = 4.76^o$	1.0	1.36	0.4
E6	wide spacing, half-scale $\alpha_c = \alpha_e = 4.76^o$	1.0	1.36	0.7
E7	wide spacing, half-scale $\alpha_c = \alpha_e = 4.76^o$	4.0	1.30	0.4
E8	wide spacing, half-scale $\alpha_c = \alpha_e = 4.76^o$	1.0	1.14	0.4
E9	narrow spacing, full-scale $\alpha_c = \alpha_e = 4.76^o$	1.0	1.28	0.2
E10	narrow spacing, full-scale $\alpha_c = \alpha_e = 4.76^o$	1.0	1.28	0.35
E11	narrow spacing, half-scale $\alpha_c = \alpha_e = 4.76^o$	1.0	1.35	0.4
E12	narrow spacing, half-scale $\alpha_c = \alpha_e = 4.76^o$	1.0	1.35	1.0

Case E1 was defined as the baseline condition: wide spacing, matched pressure ratio, ambient temperature helium and thin boundary layer. The ambient helium resulted in $\overline{v}$ = 1.33 for this case. Variations in one parameter were made about the baseline case, in keeping with the rough assumption of parametric independence discussed in Section 1.5.2.

Cold helium was injected for cases E4 and E8. It was hoped that the helium supply system would provide helium at a temperature cold enough to result in a velocity ratio of 1.0. However, heating of the injectant as it passed through the model and injector nozzles raised the minimum attainable velocity ratio to 1.12. The variation in velocity ratio noted in all of the other cases (where no cooling was applied to the helium), resulted from changes in mass flow and plenum

chamber surface area for the different injector arrays and pressure ratios. These factors affected the heat transfer to the injectant.

Two boundary layer conditions were investigated: natural and tripped. For the tripped case, 80 psi total pressure air was injected from the boundary layer trip plate on the front of the model. The two conditions resulted in $\overline{\delta} = 0.2$ and $\overline{\delta} = 0.35$ for the full-scale injectors and $\overline{\delta} = 0.4$ and $\overline{\delta} = 0.7$ for the half-scale injectors. The heights of the boundary layer were obtained by measurements from Schlieren photographs. The effects associated with the boundary layer were investigated on both the wide and narrow spacing geometries as a strong interaction between the boundary layer and nozzle spacing was found.

The effects of variations in velocity ratio and pressure ratio were investigated only on the wide spacing models. Non-dimensionalizing the velocity and pressure by those of the freestream in general bears no relation to jet dynamics. A more appropriate normalization would involve the local conditions at the jet exit. However, all of the configurations tested experimentally and the majority of those tested computationally had matched compression and expansion of the injectant ramp surfaces. Thus, the average local pressure and velocity around the exit of the jet was close to that of the freestream.

A fully populated test matrix where each possible combination of conditions could be tested was not possible. While some effects due to coupling between two or more parameter variations may have been missed, the tests did elucidate the general dependence of injector performance on each of the parameters investigated.

It should be noted, that variations of the above parameters at the injection plane in the mixing field of the current study, produced changes in the characteristics of the jet that were not

independent. Dynamics of the jet changed rapidly as information was transmitted along characteristic lines. In general the response of the injectant was more rapid than that of the surrounding flow as the Mach angles were less acute in the nominally Mach 1.7 helium injectant. Specifically, changes in pressure ratio generated strong changes in velocity ratio, as the jet expanded, accelerating the gas after injection. Changes in pressure ratio also gave rise to changes in density altering the magnitude of the baroclinic torque source term. Similarly, changes in velocity ratio, produced by changes in temperature and hence density, were directly realized as changes in baroclinic torque. Thus, while convenient for performance labelling, parameter variations generally resulted in changes which belied their name. This again was a result of the non-linear, closely-coupled nature of the flow field.

5.2 Computational

The computations were performed in a manner to allow direct comparison with the experimental results where possible. Freestream conditions corresponded to those present in the wind-tunnel during testing: p_0 = 1000 psia, T_0 = 246 ^oC, M = 6. A uniform M = 1.7 helium injectant was used to model the flow from the injectors. The computational investigations are listed in Table 5.2.

Table 5.2 Computational test conditions

Case #	Geometry	Pressure Ratio $\overline{p}$	Velocity Ratio $\overline{v}$	Boundary Layer $\overline{\delta}$
C1	wide spacing, $\alpha_c = \alpha_e = 4.76^o$	1.0	1.0	0.0
C2	wide spacing, $\alpha_c = \alpha_e = 4.76^o$	1.0	1.0	0.2
C3	wide spacing, $\alpha_c = \alpha_e = 4.76^o$	1.0	1.0	1.0
C4	wide spacing, $\alpha_c = \alpha_e = 4.76^o$	0.4	1.0	0.2

Table 5.2 continued:

Case #	Geometry	Pressure Ratio $\bar{p}$	Velocity Ratio $\bar{v}$	Boundary Layer $\bar{\delta}$
C5	wide spacing, $\alpha_c = \alpha_e = 4.76^o$	2.0	1.0	0.2
C6	wide spacing, $\alpha_c = \alpha_e = 4.76^o$	4.0	1.0	0.2
C7	wide spacing, $\alpha_c = \alpha_e = 4.76^o$	1.0	0.8	0.2
C8	wide spacing, $\alpha_c = \alpha_e = 4.76^o$	1.0	1.2	0.2
C9	narrow spacing, $\alpha_c = \alpha_e = 4.76^o$	1.0	1.0	0.0
C10	narrow spacing, $\alpha_c = \alpha_e = 4.76^o$	1.0	1.0	0.2
C11	narrow spacing, $\alpha_c = \alpha_e = 4.76^o$	1.0	1.0	1.0
C12	wide spacing, $\alpha_c = \alpha_e = 4.76^o$, $\alpha_i = 7.5^o$	1.0	1.0	0.2
C13	wide spacing, $\alpha_c = \alpha_e = 4.76^o$, ramped injectant M# profile	1.0	1.0	0.2
C14	wide spacing, $\alpha_c = \alpha_e = 4.76^o$, elevated injectant	1.0	1.0	0.2
C15	wide spacing, $\alpha_c = 0^o$, $\alpha_e = 9.46^o$	1.0	1.0	0.2
C16	wide spacing, $\alpha_c = 0^o$, $\alpha_e = 9.46^o$	0.4	1.0	0.2
C17	wide spacing, $\alpha_c = 0^o$, $\alpha_e = 9.46^o$, $\alpha_i = 7.5^o$	0.4	1.0	0.2
C18	wide spacing, $\alpha_c = 9.46^o$, $\alpha_e = 0^o$	1.0	1.0	0.0
C19	wide spacing, $\alpha_c = 9.46^o$, $\alpha_e = 0^o$	1.0	1.0	0.2
C20	wide spacing, $\alpha_c = 9.46^o$, $\alpha_e = 0^o$	1.0	1.0	1.0
C21	all-shock geometry, $\alpha_e = 4.76^o$	1.0	1.0	0.0

Table 5.2 continued:

Case #	Geometry	Pressure Ratio $\overline{p}$	Velocity Ratio $\overline{v}$	Boundary Layer $\overline{\delta}$
C22	all-shock geometry, $\alpha_e = 4.76^o$	1.0	1.0	0.2
C23	all-shock geometry, $\alpha_e = 4.76^o$	1.0	1.0	1.0
C24	wide spacing, $\alpha_c = \alpha_e = 4.76^o$, film-cooling	1.0	1.0	0.2

The baseline condition (C2) for the computations was the same as that of the experiments with the exception of the velocity ratio. As no attempt was made to accurately numerically model shear-induced mixing, $\overline{v} = 1.0$ was chosen. Tests were conducted at $\overline{v} = 0.8$ and $\overline{v} = 1.2$ (C7 and C8) but the effects of the change in velocity ratio were overwhelmed by the artificial viscosity required to damp numerical instabilities in regions of strong gradients.

Cases C1 through C11 closely tracked the experimental test matrix. The geometry was characterized by matched compression and expansion of the ramp surfaces ($\alpha_c = \alpha_e = 4.76^o$). Runs C1-C3 and C9-C11 were directed towards developing an understanding of the interaction between the spacing and the boundary layer displacement. A useful feature of numerical modelling was that it allowed prescription of boundary conditions not allowable in a real flow. Inviscid boundary conditions were applied to understand the performance of the injectors in the absence of a boundary layer. These cases are denoted by $\overline{\delta} = 0.0$, (C1 and C9). The influence of pressure ratio was addressed in C4-C5. The application of $\overline{p} = 0.4$ was not feasible experimentally as it would have led to unstart of the injectant nozzles.

The remaining studies shown in Table 5.2, (C12-C24), were directed towards geometry and injectant variations which were not investigated experimentally. In the first three of these (cases C12 - C14), angled injection, a non-uniform injectant profile, and elevated injection were applied to the baseline geometry. Variations in ramp geometry were addressed in cases C15 through C20.

Cases C18 through C23 formed an effort the more clearly understand the role of two important vorticity generation mechanisms in enhancing mixing, and the effects of the boundary layer on their effectiveness. The first of the mechanisms is associated with the vortical roll-up generated by the pressure difference on top of and between the injector ramps. This mechanism was studied by considering the case $\alpha_c = 9.46^o$ and $\alpha_e = 0^o$, termed the 'no-shock' geometry, where no strong, shock-generated vorticity was present. The performance of this geometry was compared with a generic injector where the injectant exited into a uniform stream and was impinged upon by a shock. This geometry was termed the 'all-shock' geometry.

The final study tabulated, (C24), was computed as an initial step towards integrating film-cooling with the contoured wall injector scheme.

CHAPTER 6

DISCUSSION OF RESULTS

This chapter is divided into several parts. The first section contains a detailed presentation of the data obtained both experimentally and computationally for the baseline test condition: Wide spacing, $\overline{\delta}$ = 0.20, $\overline{p}$ = 1.0, and $\overline{v}$ = 1.33 (experimental) or $\overline{v}$ = 1.0 (computational). The discussion is intended to provide a complete description of the characteristics of the flow field and injector performance as a starting point against which other configurations and conditions will be compared. These comparisons will be made in Sections 6.2- 6.4 where effects of the boundary layer, injectant/freestream pressure ratio and injectant to freestream velocity ratio will be treated. Following these sections are discussions of the role of shock-induced mixing in injector performance (Section 6.5), and presentation of additional computational investigations which were beyond the bounds of the experimental test matrix (Section 6.6).

6.1 Baseline geometry and conditions

In Sections 6.1.1 and 6.1.2, time-mean experimental and computational results are presented for the baseline configuration. The influence of spatial averaging on the representation of the flow is addressed in Section 6.1.3. Qualitative insight into the importance of the time-fluctuating component of the flow is provided by the planar Rayleigh imaging presented in Section 6.1.4. Analyses of injector performance based on mixing, losses, jet penetration and heating considerations follow in Section 6.1.5.

Consideration of the shadowgraph image in Figure 26 will highlight many of the salient flow field features described in the following sections. Flow in the photograph is left to right. The density variations in the flow were highly three-dimensional. The locations of their signatures in the image correspond to a line-of-sight integration across the injector array. Both the shock generated by the beginning of the injector ramps and that due to turning of the flow in the troughs between the ramps at the exit plane are apparent. The latter of these was responsible for baroclinic vorticity generation through interaction with the density gradients associated with the injectant/air interfaces. The former played a role in vorticity generation as well through providing for high pressure on the upper surface of the ramps while low pressure existed in the troughs. This pressure imbalance generated flow from the upper surface of the ramps into the troughs. Thus the mechanisms for two sources of vorticity are evidenced in the photograph. The sense of the vorticity which results from these two mechanisms is the same and the effects are additive though not in a linear manner. Also apparent in the shadowgraph is the expansion/recompression system at the top of the injection plane. For $\overline{p} = 1.0$, the helium static pressure was matched to the freestream static pressure which was approximately equal to the average pressure around the injector in the injection plane. Due to the pressure gradients generated by the ramp structure, the pressure ratio near the top of the injection plane was less than one while at the bottom it was greater than one. A final point of interest in the shadowgraph image are the boundaries of the injectant which are represented by the two parallel white lines which intersect the right edge of the photograph nearly perpendicularly. Strong separation between the lower boundary of the jet and the wall occurred prior to $\overline{x} = 1.0$.

6.1.1 Flow field survey results

The dynamics of the jet are displayed in more detail in Figure 27. Shown are contours of constant helium mass fraction for various axial stations downstream of the injection plane, ($\overline{x}$ =

0, 1, 4, 8, and 13). The data shown was obtained experimentally from the full-scale model using the composition probe described in Section 2.4.1. The data has been mirrored about the plane of symmetry at $\bar{y} = 0$. The edges of the injectors are at $\bar{y} = \pm 0.25$. The edges of each of the plots correspond to the planes of symmetry between each of the injectors in the array (labeled S_2 in Figure 19). The maximum helium mass fraction is tabulated above each of the plots. It should be stressed that these data are time-mean and the manifestation of the unsteady component of the flow field in these plots has not been addressed. It will be treated in detail in Section 6.1.4. Further, in these plots and others shown, sub grid-scale features should not be interpreted. The experimental sampling grid for the full-scale model has been overlaid on one of the plots of Figure 27.

The strong lift-off of the jet apparent in the shadowgraph is clear in these data as well. Complete separation of the jet from the surface occurred at approximately one injector height downstream of injection. The location of this point is approximate since the contours may not be interpreted below $\bar{z} = 0.125$ as no data was obtained below this point. The formation of a strong counter-rotating vortex pair in the helium jet is evidenced by the form of the helium signatures. Notably, the sense of vorticity is such that it caused the pair to migrate from the wall into the freestream.

Figures 28-30 show the other data obtained from the survey rake. The first of these figures contains the cone static pressure data. The response of this probe to various flow field phenomena is difficult to interpret visually. The plots are shown for the sake of completeness as the data were used further for reduction purposes. Figures 29 and 30 show the pitot pressure and total temperature contours respectively. Several interesting phenomena are evidenced in these plots. The first of these is the three-dimensional nature of the pressure field surrounding the injection plane at $\bar{x} = 0$. High pressure existed above the ramps as a result of compression of the upper ramp surface, and low pressure between, due to expansion in the troughs. This

pressure gradient resulted in vorticity generation apparent as flow rolled-up along the upper edge of the ramp surface. Also notable in both of these plots is the uniformity of the injectant in the exit plane. The injectant appears slightly less uniform in the total temperature plot due to the larger spatial averaging of the total temperature probe. A final point of interest shown in these plots is the nature and importance of the boundary layer. Because of the pressure gradients associated with the expansion and compression of the ramp surfaces, the boundary layer was drawn off of the compression surfaces and into the troughs between the ramps. Due to the strong displacement effect of a hypersonic boundary layer, it acts to effectively modify the wall geometry from the perspective of the flow external to the boundary layer. This can detrimentally affect injector performance by preventing formation of a shock in the exit plane. Considering the pitot pressure contours in the injection plane, the form of the boundary layer was such that it did not inhibit shock formation in the vicinity of the helium/air density gradients for this configuration. Counter to expectations, a tongue of high momentum flow was maintained in the corner of the troughs, with the low momentum boundary layer fluid collecting in the center of the passageway. This allowed shock formation precisely where it was required to produce baroclinic torque: the region of helium/air density gradients. The collection of boundary layer fluid in the center of the channel between the injectors was a result of positive interaction between the geometry and the boundary flow. This positive interaction was not present for all injector spacings and boundary layer thicknesses and will be discussed in detail in Section 6.2.

The iterative procedure discussed in Section 2.5, was used to reduce the raw rake data to base variables such as Mach number, static pressure, static temperature, and density. The results of this reduction procedure are presented in Figures 31-34 for these variables respectively. The errors associated both with the measurements and the data reduction techniques allow little confidence locally in these solutions. There are some areas in particular where flow angularity, misalignment of the probes, and Reynolds number effects have produced clearly erroneous local

behavior. Examples of this are the extremely high Mach number peaks displayed in Figure 31. The data allow only a rough quantitative measure of the derived quantities. A check was made of helium mass flux conservation based on these results to verify performance of the composition probe. The helium mass flux represented in each of the downstream planes was within 20% of that at $\bar{x} = 0$, with no trend displayed in the data. This variation was considered to be within the error band associated with the reduction technique. No other experimental cases were reduced in this manner. Further conclusions in general are based on the raw survey data and numerical simulations.

6.1.2 Data from the numerical simulation

Figure 35 shows data obtained from a numerical simulation of the baseline case. Shown are contours of constant helium mass fraction in various planes downstream of the injector. Note the formation of a counter-rotating vortex pair in the helium. The general form is reminiscent of the two-dimensional, unsteady shock impingement on a circular light gas inhomogeneity shown previously in Figure 1. The level of the analogy between these two systems will be discussed at the end of this section. An additional item of note in Figure 35 is the rapid separation of the helium jet from the wall of the combustor also displayed in the experimental results.

For comparison purposes the numerical data for the baseline case has been plotted in the same form, scale and axial planes as the experimental data plots. These plots are contained in Figures 36-42. The spacing between the injectors for the computational case was slightly different from that of the experimental case and the plots extend to $\bar{y} = \pm 1.0$ rather than $\bar{y} = \pm 1.125$. Again, these bounds represent the planes of symmetry between each of the injectors in the array (labeled S_2 in Figure 19). The edges of the injector ramp still correspond to $\bar{y} = \pm 0.25$. Also, while the computations were carried out in a domain $0 < \bar{z} < 4.0$, they were cropped above $\bar{z} = 2.625$ which was the maximum height measured experimentally. The spatial resolution provided

by the computational grid was considerably better than that of the experiments. The grid has been overlaid on one of the plots of Figure 36.

Helium mass fraction contours are shown in Figure 36. Since no attempt was made to accurately model the turbulent mixing phenomena, the mass fraction levels displayed in the simulation differ greatly from those measured experimentally. However, the qualitative behavior and the location and form of species gradients are accurately reproduced in the computations. Mach number, static pressure, static temperature and density plots are shown in Figures 37-40 respectively for comparison with the reduced experimental data shown in Figures 31-34. The comparison is clouded by the inherent difficulties in reducing the experimentally obtained rake data to base flow variables.

A different approach was taken to allow more accurate comparison between the computations and experiments. The approach involved computing rake data, pitot pressure and total temperature, from the numerical data. Comparisons were then made against the raw experimental data, assuring considerably higher confidence. The pitot pressure and total temperature from the computations are shown in Figures 41 and 42 respectively, and are presented for comparison with the experimental data in Figures 29 and 30. Considering first the pitot pressure, very close quantitative and qualitative agreement is apparent. The region above the helium jet was different in the experimental case because of pressure disturbances from the opening for the probe support strut in the top of the wind tunnel. Also, inability to obtain measurements very close to the wall in the experiments limits comparison below $\bar{z} = 0.125$. The total temperature contours compare only qualitatively. Quantitative comparison was not allowed because the experimental case was conducted with a velocity ratio of 1.33 while that of the computations was 1.0. Thus the total temperature of the injectant for the two cases differed.

It should be noted that the numerical investigations were conducted almost entirely before the experiments. The excellent agreement between the results of the two was not the result of *a posteriori* tuning. In fact, further adjustment, particularly with respect to turbulence modelling, may allow even more confidence in the predictive ability of the simulations.

A utility of the numerical simulation was that it allowed presentation of derived quantities such as vorticity which were difficult to obtain experimentally. Contours of vorticity normalized by the freestream velocity and the height of the injector are shown in Figure 43. The solid lines represent vorticity of a positive sense (counter-clockwise when looking upstream) while that of a negative sense is shown with dashed contours. The complex vorticity field began to coalesce into a simple counter-rotating vortex pair in the last two axial stations shown. Strong vorticity was present in the flow at $\overline{x} = 0$, prior to introduction of the strong baroclinic torque mechanism associated with shock formation in the exit plane. This vorticity resulted from the pressure gradients associated with the ramp geometry and was of the same general sign as that produced by shock impingement on the helium/air density gradients. It is this vorticity and in general the non-uniformity of the flow field about the injection plane, as well as out of plane generation of vorticity which limit the direct analogy between this case and the two-dimensional problem of shock impingement on a light circular gas inhomogeneity. When these factors are removed, the analogy is nearly direct and substantial knowledge may be gained by careful consideration and analysis of the two-dimensional problem. A presentation of such a case as well as a general discussion of the relative importance and effectiveness of the two major vorticity generation mechanisms in the flow field (baroclinic torque, and ramp generation), is given in Section 6.5.

The computational data are shown at axial stations farther downstream of the injection plane in Figures 44 and 45. Development of the two tails of helium below the jet was not seen experimentally.

6.1.3 Thoughts on sub grid-scale structure

The representation of the helium jet in both the experimental and computational contour plots suffers from two strong influences: temporal averaging and spatial averaging. A qualitative judgement of the unsteady effects will be made in Section 6.1.4 where the Rayleigh scattering data is presented. The influence of spatial averaging on the form of the helium signatures can be estimated by considering the dynamics of the jet with respect to diffusion and convection.

Convective mixing is demonstrated by the interaction of particle traces from neighboring points in the flow field. Several examples of such interactions are shown in Figures 46-48. The entrainment of air into the helium jet is displayed in Figure 46 where a fluid particle in the air is swept into the mixing helium jet. The strength of the vortical flow is shown in Figure 47. The particle path shown with the solid line makes three complete orbits about the vortex core by $\overline{x}$ = 30. Notably, the two helium particles, located one just above the other, take considerably different paths through the domain with the lower particle exhibiting an additional orbit. Fluid interfaces are stretched and injectant/freestream gradient dimensions are strongly narrowed. The final interaction is shown in Figure 48. Particles located $\Delta\overline{y}$ = 0.15 apart, one in the helium and one in the air, each take three turns about the vortex core in which time the paths are entwined.

The relation of the strong convection displayed in these figures to the diffusive mixing was estimated by considering the growth of helium/air diffusion gradients in a steady system. The average depth of penetration of a molecule in a species gradient, ξ, may be approximated (Kuo, [1986]) as:

$$\xi = \sqrt{2Dt}$$

The diffusion coefficient for helium and air at -170 ^{o}C and 0.63 psia was estimated using the Chapman-Enskog theory (Cussler, [1984]) to be D = 3.75 x 10^{-3} ft^2/s. At flow speeds of 3000 ft/s, a particle resides between the injection plane and the end of the computational domain for 1 x 10^{-3} seconds. Thus ξ = 0.033 in. or 3.3% of h_j. Based on this, it is apparent that much of the mixing region may be in the form of tightly rolled spiral species gradients which have not yet merged due to diffusion. This signature would be hidden by artificial viscosity and spatial discretization in the computations, and by the spatial averaging of the probes and limited spatial resolution of the sampling grid in the experiments. Determination of the extent to which these layers merge and actually take on the form displayed in the experimental and numerical data was not possible, though the small diffusive length scales suggest that a least part of the flow field contains tightly layered species gradients. The extent to which these fine mixing scales may be dominated by unsteady effects is addressed below in Section 6.1.4.

6.1.4 Planar Rayleigh scattering data, the time-fluctuating flow field

The above results and discussions of injector performance are based entirely on time-mean data. Time-resolved, planar Rayleigh scattering was employed to impart a qualitative knowledge of the level and importance of the time-fluctuating component of the flow field. Before discussing the unsteady component of the flow field, it is necessary to address the limitations of the imaging technique by comparing the results with time-mean rake survey data. Additional information on the limitations of the technique was presented in Section 2.7.3.

Four plots are shown in Figure 49. Figure 49b is an average of 22 time-resolved planar Rayleigh images taken for the baseline case at $\overline{x}$ = 10. Each of the images was scaled and corrected as described in Section 2.7.3. Included in the figure are contour plots of static pressure, static temperature (both obtained from the raw data through the reduction technique described in Section 2.5), and helium mass fraction. Due to limitations associated with condensation the

optical technique was applied at T_0 = 246 ^oC, p_0 = 600 psia resulting in a Reynolds number of 9 x 10^6/ft. While all of the other tests presented were conducted at Re= 15 x 10^6/ft., the data shown in Figure 49 were obtained at Re= 10.5 x 10^6/ft (T_0 = 246 ^oC, P_0 = 700 psia) to allow closer comparison with the Rayleigh data.

The data (in terms of deduced pressure in units of torr) are scaled linearly between zero and the maximum signal level in the image. The small statistical sample and the strong sensitivity of molecular clustering (and hence signal intensity) to run-to-run variations in tunnel conditions, preclude quantitative comparison of the deduced pressure for this case with cases that will be presented in other sections. As the scattering cross-section for helium is much less than that for the air, lower signal levels are expected in regions containing significant concentrations of helium. Lower signal levels are also noted in low pressure or high temperature regions of the air. Some regions of the flow field (*e.g.*, the core of the helium jet and the base of the boundary layer) were below the sensing threshold of the instrumentation. White bands have been added to the gray scale to aid in identification of intensity gradients in the images. The dynamic range and spatial resolution of the Rayleigh measurements did not allow analysis of the fine-scale structure within the jet. The representation of the location of pressure and/or temperature gradients within the flow field is accurate in the Rayleigh image. The representation of the location of gradients in helium mass fraction is accurate only in regions where the species gradients were coincident with pressure and/or temperature gradients. Thus the utility of the method for tracking the mixing interface is strongly limited.

The above must be considered in interpreting the time-resolved data which is presented in Figure 50. Each of these images was the result of a 15ns duration pulse. The frames were taken 0.1 seconds apart. In 0.1s a fluid particle moved approximately 300 ft. so the images are considered random in time. On the sides and top edges of the jet, it is assumed that the image corresponds

to a line of roughly constant helium mass fraction. Below the jet, a similar conclusion is not allowed, as pressure and temperature gradients were not coincident with species gradients as described above. In particular, gas sampling measurements show the stem which appears below the jet did not contain any helium (see Figure 49d). It was merely warmer, lower pressure air entrained in-part from the boundary layer. The relative effects of number density variations and thermodynamics (molecular clustering) in producing these variations can not be separated. The maximum peak-to-peak spatial amplitude of the unsteady oscillations of the intensity gradients about the mean is approximately 0.4 h_j. The phenomena leading to production of this strong time-fluctuating component of the flow are discussed in Section 6.4.

Of interest in estimating the importance of the time-fluctuating flow field in injector performance is not only the level of unsteadiness, but the location as well. The standard deviation of the 22 images about the mean is shown in Figure 52. An enlarged image of the mean is shown above this plot in Figure 51. Notably the unsteadiness was confined largely to the edges of the helium jet. The vortex cores contained very little intensity variation in time. However, the lack of unsteadiness in these regions as well as in the boundary layer is not necessarily the result of absence of unsteadiness in the flow field. The dynamic range of the technique was not sufficient to resolve fluctuations in regions of either low pressure, high temperature, or significant helium concentration. Zero standard deviation in these regions resulted from occurrence of signal levels below the measurement threshold of the apparatus, and interpretation of the standard deviation is limited.

The above point makes difficult an estimation of the extent to which mixing in the fine scales was dominated by unsteady shear effects. Broadwell and Mungal [1990] have suggested that the progression from stirred fluid to mixed fluid in simple two-dimensional and three-dimensional high Reynolds number shear flows is driven by the turbulent cascade process, as the scalar diffusion

time across the Kolmogorov viscous scale is negligible compared to the cascade time. For strongly augmented mixing, this is only true in regions of the jet where shear-induced unsteadiness is significant. It is projected that in the near-field of the injectors, diffusive mixing across the fine, spiraled species gradients generated by the time-mean augmentation processes, contributed significantly to the level of molecular mixing. The scale of the unsteadiness in the Rayleigh images suggests that for $\overline{x} > 10$ turbulent mixing became progressively more important. Certainly, the strong large-scale convection displayed in the particle traces of Figures 46-48 was superposed on the turbulent mixing, and may have enhanced this process as well.

6.1.5 Analysis of injector performance

The techniques described in Section 4 were used to evaluate injector performance on four bases: mixing, losses, jet penetration, and heating. The interpretations are based largely upon the form of the flow field represented in the experiments and computations where phenomena were not sufficiently resolved either temporally or spatially.

The lift-off height of the jet from the surface is compared for the experimental and numerical data in Figure 53. Recall the difference in calculation methods for the two cases as discussed in Section 4.5. The lift-off height is a measure of the bulk behavior of the injectant downstream of the injection plane. The agreement between the experimental data and the simulation is excellent. The dip in the curve is a result of the dynamics of the helium as it was acted upon by the vorticity field. After coalescing into a counter-rotating vortex pair, migration from the wall at a constant slope of $\overline{z}_j/\overline{x} = 0.025$ occurred. By $\overline{x} = 30$, the mass flux center was located at $\overline{z} = 1.3$, with the point of maximum penetration at $\overline{z} = 2.0$. Possibly more important than the bulk behavior of the jet for heating considerations, was the complete lift-off of the jet from the surface. Absence of fuel near the surface of the combustor will alleviate some of the detrimental heating envisioned in scramjet combustor applications. It will be seen that impingement upon the

injectant/air density gradients with the shock that was generated at the base of the jets was the factor which provided complete lift-off. Notably, impingement upon the jets from above, such as from a reflected shock, acts to produce vorticity of an opposite sense. If this vorticity is dominant, a counter-rotating vortex pair will be formed of a sense which will cause an undesirable migration of the jet towards the wall.

The losses incurred by the fluid as a result of interaction with the wall geometry are an important measure of injector performance. Rise in mass-averaged entropy of the fluid through the computational domain is shown in Figure 54. The solid line shows the total rise in entropy, with the change due to mixing represented with a broken line. The predominant rise in entropy occurred prior to injection of helium and was due to the ramp-generated shock system and subsequent non-isentropic flow in the boundary layer as well as errors associated with the rough grid edge on the upper surface of the ramp. The entropy rise between $\overline{x} = -6$ and $\overline{x} = 0$ will be removed from subsequent plots where no-slip boundary conditions were applied as no accurate estimate of the magnitude of the rough grid errors in this region could be made. Notably, the largest portion of entropy rise following injection is directly attributable to mixing. Thus, the mixing provided by the injectors was, in general, loss-effective. Details of the losses associated with both shock-enhancement of the mixing process and the other vorticity mechanisms will be addressed in Section 6.5.

While heating considerations, jet penetration and losses are important in developing overall criteria for injector performance, in general more attention was directed towards evaluating the extent to which mixing occurred in the flow field. Again, limitations in the scope of the experimental and numerical methods prevented analysis at the level required to ascertain molecular-scale mixing, and in general the experimental data allowed less detailed treatment than the numerical data.

An integral measure of vorticity production within the flow is presented in Figure 55 based on the computational data. Two strong vorticity generation mechanisms are displayed in this plot. The growth in circulation which begins at $\bar{x}$ = -6.0 will be loosely termed 'ramp-generated' vorticity and was a result of fluid migration from the high pressure region on the upper surface of the ramp to the low pressure region in the trough between ramps. At $\bar{x}$ = 0, a large increase in circulation occurred. This increase was the result of two factors. The first of these was strong vorticity production from baroclinic torque due to shock impingement on injectant/air density gradients. This mechanism produced vorticity of the same sense as that generated by the ramp. It cannot be assumed, however, that the entire increase in circulation following injection was due to baroclinic vorticity production. A portion of the increase was due to the kinematics associated with the ramp-generated vorticity acting on the lighter injectant gas. The relative importance of these two vorticity mechanisms in terms of circulation increase as well as in terms of injector performance in general (jet penetration, heating, mixing, and losses) is considered in Section 6.5.

The peak injectant mass fraction contours in each measurement plane have been plotted for the baseline case in Figure 56. Also shown on the plot are similar data obtained from the half-scale model with a natural boundary layer. Though non-dimensionally the height of the boundary layer for the two cases was different, this data was added to display the behavior farther downstream of the injection plane. The accuracy of the experimental data for the full-scale model was better than that for the half-scale model due to limits in spatial resolution. An outlying measurement is included on the plot. The point represents the peak mass fraction at $\bar{x}$ = 4 for the half-scale model. The factors that produced this erroneous measurement are not entirely clear, though it was probably due to the inability of the composition probe to respond to injectant pressure fluctuations which were quite strong for the half-scale model at this pressure ratio (see Section 2.1). Analysis of this data did not occur until after completion of the final wind-tunnel test entry so

repetition of the case was not possible. The point will be removed from further comparisons in which this data is involved. The peak helium mass fraction decay profile shows that in a macroscopic, non-concentration specific sense, the greatest amount of mixing occurred between $\overline{x}$ = 5 and $\overline{x}$ = 10, with a maximum decay slope of 12% mass fraction per injector height downstream.

More detailed mixing analyses were conducted for the numerical data. These are presented in Figures 57 and 58. The first plot contains the mixedness measure data. The measure was described in Section 4.1. It provides information concerning the percent of total injectant mass flux which is present in each concentration band as a function of distance downstream of the injection plane. The general characteristics of such a measure are displayed in the figure, and are highlighted by plotting both a contour map and a surface plot. Initially (at $\overline{x}$ = 0), all of the injectant existed in a pure state (c_{He} = 1.0). This is represented by a distribution similar to a delta function. Farther downstream from the injector, more of the injected helium occurred at progressively lower mass fractions. Three aspects of this progression will be used for means of comparison with the data from other numerical cases. The first of these is how rapidly the point was reached where there was no longer any pure helium in the flow field. The second, is the extent to which this process continued to occur. This is characterized by the zero contour in the line plot, and corresponds to the decay of maximum helium mass fraction plotted for the experimental results. Only qualitative comparisons between the experimental and numerical data are allowed due to the limited scope of the computational modelling with respect to mixing. Comparison of this line with the experimental data of Figure 56 shows the nature of the decay for the two cases was similar. However, the laminar mixing model produced mixing at a much slower rate. The third aspect of the mixedness measure data that is important in terms of comparison with other numerical tests is the percent of helium mass flux present at the lower mass fractions where the mixture ratio would promote most active burning in a hydrogen/air

reaction system. The level of mass flux occurring at $c_{he} \leq 0.05$ will be used as a measure of this. This level is indicated by the height of the lower edge of the carpet plot. By $\bar{x} = 30$, approximately 17% of the injected mass flux was below 5% mass fraction for the baseline computational case.

A second detailed measure of mixing is shown in Figure 58. The length of contours of constant mass fraction are shown using a combined contour and surface plot. The measure directly implies molecular-scale mixing through an increase in interfacial surface area between the injectant and the freestream. Two opposing mechanisms act to change the contour length: convective mixing, and diffusion. A pure display of the interaction between these phenomena is not provided by the measure. This is due to the spatial discretization of the flow field which imparts an apparent diffusion when convective scales are less than or equal to the grid spacing. The effect is often apparent as ridges which traverse the surface plot over the full band of mass fractions. Thus, the closely layered species gradients suggested in Section 6.1.3 are not represented. The length of contours corresponding to flame sheet location in a hydrogen/air reaction system ($c_{he} \approx 0.05$) will be the basis of comparisons between numerical test conditions. For the baseline case, these levels rose to two times the initial length within 10 injector heights from the injection plane.

It is important as well to cast jet penetration and mixing performance in light of pertinent fuel/air mass flux ratios for scramjet applications. In terms of combustor sizing, it is interesting to consider the freestream area required relative to the area of the injector exit plane if the fuel were to be homogeneously mixed to a desired mass fraction for a given set of conditions. The equivalence ratio, ϕ, can be expressed as

$$\phi = \frac{\overline{\dot{m}}}{\overline{\dot{m}}_{st}} \quad ,$$

where the subscript 'st' refers to stoichiometric, and the injectant to freestream mass flux ratio, $\overline{\dot{m}}$, is

$$\overline{\dot{m}} = \frac{\rho_i U_i A_i}{\rho_\infty U_\infty A_\infty} = \overline{\rho}\,\overline{v}\,\overline{A} \quad ,$$

or

$$\overline{\dot{m}} = \frac{\overline{p}\,\overline{m}\,\overline{v}\,\overline{A}}{\overline{T}} \quad ,$$

where $\overline{m}$ is the injectant to freestream molecular weight ratio. Then the area ratio required to provide a desired equivalence ratio for a given set of injectant and freestream conditions is

$$\overline{A} = \frac{\phi\,\overline{\dot{m}}_{st}\overline{T}}{\overline{p}\,\overline{m}\,\overline{v}} \quad .$$

An estimation of each of these parameters was made for typical scramjet operating conditions. For $\phi = 1.0$, $\overline{\dot{m}}_{st} = 0.03$, $\overline{m} = 2/29$, $\overline{p} = 1.0$, $\overline{v} = 1.0$, and $\overline{T} = 1/6$, then $\overline{A} = 0.07$. So the injectant must be mixed into an area approximately 15 times the area of the injection plane. If this area is fixed laterally by the planes of symmetry separating each of the jets in the array, then the vertical extent of the area would be approximately $\overline{z} = 4.0$ for the wide spacing configuration. For the freestream velocities of these tests, penetration on that order would be expected by $\overline{x} \approx 60$. For the specific conditions of this study with $\phi = 1.0$, $\overline{\dot{m}}_{st} = 0.03$, $\overline{m} = 4/29$, $\overline{p} = 1.0$, $\overline{v} = 1.33$, and $\overline{T} = 2.5$, the area ratio is much higher with $\overline{A} = 0.41$. The high static temperature ratio is only partially offset by the increased molecular weight of the injectant. Considerably less air would be required to be entrained by the helium jet.

6.2 Boundary layer/ injector spacing effects

Early flow visualization results showed that injector performance was strongly dependent on the scale of the boundary layer entering the ramp region, and that this dependence was influenced to a large extent by the spacing between the injector ramps. It was, in fact, this knowledge which led to a viscous numerical modelling of the flow field, rather than an Euler simulation. Three aspects of the boundary layer affect injector performance (in varying degrees): the displacement effect, the addition of shear to the mixing region, and the unsteady component of the boundary layer. A further classification of these factors will make clear the level at which they were addressed both experimentally and numerically. The action of the boundary layer to displace momentum near the wall affects only time-mean performance to first order and is thus directly evidenced in both the experiments and computations. Imposition of additional steady shear to the mixing region affects both steady and unsteady flow components. The third factor, the time-fluctuating component of the boundary layer, will interact to a large extent with the unsteady component of the mixing interface, though interaction with steady phenomena (*e.g.*, passage through strong pressure gradients) may be evidenced as well. Thus, the latter two aspects of the boundary layer are associated with modifications of non-steady flow phenomena. They were treated largely as these effects were manifested in the time-mean flow field, though some time-resolved, planar imaging data is presented in Section 6.2.1.

The nature and the scale of the boundary layer were determined from consideration of time-resolved shadowgraph images and time-mean flow surveys. No measurements were made to determine the magnitude of the fluctuations within the boundary layer. Shadowgraphs of the developing boundary layer for the natural and tripped conditions are shown in Figures 59 and 60. The term for the former is a misnomer as the presence of the trip plate acted to induce laminar to turbulent transition even for the case of no injected trip air. Transition appeared to occur nearly

at the location of the plate for this case (one inch downstream of the leading edge), whereas flat plate transition for these flow conditions would be expected at between 4 and 8 inches from the leading edge. Tripping the boundary layer with air injection increased both the thickness of the boundary layer and the scale of the structure within it. The photographs shown extend to 10 inches downstream of the leading edge of the model. The state of the boundary layer as it entered the ramp geometry is shown in Figures 61 and 62 for the natural and tripped cases. For the full-scale injectors (shown) the ramps were initiated at 15 inches downstream of the leading edge of the model. At the start of the injector ramps, the two boundary layer conditions provided $\overline{\delta} = 0.2$ and $\overline{\delta} = 0.35$ for the full-scale models, and $\overline{\delta} = 0.4$ and $\overline{\delta} = 0.7$ for the half-scale models.

6.2.1 Experimental results

In Figures 63-65 the rake survey data for the full-scale, wide spacing, injector array are presented for the tripped boundary layer case. Direct comparison of these results with the base line case (Figures 27, 29 and 30 respectively) shows that very little change was imparted to the qualitative nature of the flow field through modification of the boundary layer. The thicker boundary layer is apparent in both the pitot pressure and total temperature profiles. Peak helium mass fractions were slightly lower at all axial stations for the tripped case. The extent to which this trend represents better mixing may not be inferred from this data. The trend may be evidence of the superposition of large-scale unsteadiness on the jet rather than mixing on a molecular scale. These topics will be addressed later in the discussion of the Rayleigh scattering data for this case.

Half-scale model investigations provided additional test points and surveys at larger non-dimensional distances from the injection plane, though with less spatial accuracy. Contours of helium mass fraction, pitot pressure and total temperature are shown for the half-scale, wide

spacing model in Figures 66-68 ($\overline{\delta}$ = 0.4) and Figures 69-71 ($\overline{\delta}$ = 0.7). The experimental sampling grid for the half-scale models differed from that of the full-scale models. The half-scale grid has been overlaid on one of the plots of Figure 66. Sub grid-scale features should not be given credence. Also, the plots can not be interpreted below $\overline{z}$ = 0.25 as no measurements were obtained below this point.

Peak helium mass fractions for the natural boundary layer case were marginally higher than those obtained for the tripped case. A plot of the decay of the maximum helium concentration in $\overline{x}$ for both the full and half-scale models for the two boundary layer conditions is shown in Figure 72. The trend for more rapid decay in the time-mean values with increasing boundary layer height is displayed. This result is closely tied to the interaction of the unsteady structure within the boundary layer with the time-fluctuating component of the mixing field. Determination of the extent to which this represents increased mixing on the molecular scale is aided by consideration of the planar Rayleigh imaging results. The mean intensity and standard deviation about the mean are presented for the wide spacing geometry with $\overline{\delta}$ = 0.35, at $\overline{x}$ = 10 in Figures 73 and 74. Qualitative comparison of the mean image with that for the baseline case (Figure 51) is precluded by the strong sensitivity of the scattering signal to small variations in tunnel conditions. (This was a result of the molecular clustering.) Only a qualitative comparison of the location of gradients of intensity in the image can be made. On this basis, the image is similar to that obtained for the baseline conditions with the exception of the thicker boundary layer which is apparent in Figure 73. Quantitative comparison of the standard deviation against that of the natural boundary layer (Figure 54) is valid within the limits of the experimental error and statistical uncertainty associated with the small sample size (22 images). Higher levels of unsteadiness are shown on the edge of the jet for the tripped case. Similarly, the boundary layer is marked by high levels of unsteadiness. As with the baseline data, absence of zero standard deviation in the base of the boundary layer and the core of the jet is due to occurrence of signal levels below the sensing

threshold of the instrumentation. Study of the temporally-resolved images of which four are shown in Figure 75 provides insight into the source for the increase in unsteadiness. Typically, the jet appears to have been subject to more large-scale, global deformation. This deformation was linked to the long wavelength oscillations present in the boundary layer. Locally, however, the scale and nature of the unsteady field on the boundary of the helium jet was similar to that for the natural boundary layer case seen in the images shown in Figure 51. The implication is that the unsteady structure of the boundary layer did not act strongly to enhance mixing on the molecular scale. The small increase in mixing for the tripped boundary layer, displayed by the peak helium mass fraction decay (Figure 72), probably resulted from greater spatial averaging due to the global motion of the jet.

It should be cautioned that while on a macroscopic scale the effects associated with an interaction of the mixing interface with the unsteady boundary layer flow were small, the near-field mixing that would lead to combustion is also small in terms of the macroscopic flow field scales. Thus, it is possible that the effect is more important in terms of combustion efficiency. Direct combustion experiments would be most effective in elucidating these and other issues.

In general, confidence in the conclusions based on the Rayleigh data is weak. Awareness of the limited applicability of the planar images is necessary so that incorrect conclusions are not drawn. An example of this is the apparent better mixing displayed in the instantaneous images for the natural boundary layer case (Figure 50) compared to that of the tripped case (Figure 75). This conclusion might be drawn based on the higher intensity levels present in the center of the jet region. It is likely, however, that the higher levels were produced by thermodynamic effects. The tripped boundary layer was warmer with presumably less molecular clustering. It was also in closer proximity to the vortex field associated with the jet. Thus, the air entrained into the helium

jet possessed a smaller scattering cross section for the tripped boundary layer case, and mixing can not be inferred.

The displacement effects of the boundary layer were resolved with greater confidence since they involved predominantly the mean flow. In the pitot pressure plot for the $\overline{\delta} = 0.7$ case (Figure 70) note the considerable extent to which the boundary layer filled the channels between the injector ramps at $\overline{x} = 0$. Importantly though, a tongue of high momentum fluid was generated in the corner of the ramps, with the lowest momentum fluid collecting in the center of the troughs. This was counter-intuitive as it would be expected that the corners would contain the lowest momentum fluid. The interaction was positive in that it allowed shock formation in the region adjacent to the injectant/freestream density gradients allowing baroclinic vorticity production. The positive interaction is evidenced in the results from the baseline case (Figure 29) as well. The presence of high momentum in the corners of the ramps is further evidenced by the surface oil flow photographs shown in Figures 76-78. The image of Figure 76 is for a matched pressure case. Figure 77 and the close-up shown in Figure 78 are for underexpanded jets. All of the photographs are for the case of a thin boundary layer ($\overline{\delta} = 0.2$). The edges of the injector ramps are marked with arrows on the edges of the photographs. The deflection of the streamlines on top of the ramp surfaces marks the migration of the boundary layer into the troughs between the ramps. The oil tended to collect in the center of the channels with the high momentum fluid scrubbing the oil from the surface in the corners of the ramps.

A similar positive interaction between the boundary layer and the ramp geometry did not occur for the narrow spacing injector arrays. Direct evidence of this is displayed in a Schlieren photograph of such a geometry with $\overline{\delta} = 0.2$ shown in Figure 79. No strong oblique shock appeared from the compression between the injection planes. This forecasts a decline in baroclinic vorticity production associated with the shock impingement on density gradients. The cause for the

absence of the shock is apparent in the time-mean flow field surveys. This data is shown in Figures 80-82 (full-scale model, $\bar{\delta}$ = 0.2) and Figures 83-85 (half-scale model, $\bar{\delta}$ = 0.7). (The anomalous signatures in the upper portion of the $\bar{x}$ = 4 contour plot of total temperature for the full-scale, $\bar{\delta}$ = 0.2 case, of Figure 82, resulted from a loose wire.) The sampling grids used for the narrow spacing were identical to those used for the full and half-scale, wide spacing geometries which were previously shown overlaid on the plots of Figures 27 and 66, respectively. The helium mass fraction contours (Figures 80 and 83) show weaker vortical development and poorer jet lift-off than realized for the wider spacing. The effects on lift-off due to spacing are shown in Figure 86 for the various boundary layer conditions. The slope of the injectant trajectory for the narrow spacing is one-half that for the wide-spacing. For the narrow spacing $\bar{z}_j$ = 0.8 at $\bar{x}$ = 26, while $\bar{z}_j$ = 1.1 at $\bar{x}$ = 26 for the wide spacing. The pitot pressure survey (Figure 84) shows the extent to which the troughs between the ramps were filled with the low momentum boundary layer fluid. Instead of allowing oblique shock formation, the geometry was effectively modified due to the strong displacement effect of the hypersonic boundary layer. The sharp transition in slope of the wall appeared to the external flow as a gradual curvature, producing a broader pressure gradient which remained unfocused below the level of the helium jets. The close proximity of the jets produced strong interaction between the jets. By $\bar{x}$ = 13 the jets fully merged, forming a thick layer of helium/air mixture along the surface of the wall. Considering the jets as simple counter-rotating vortices, it is clear as well that closer proximity will reduce migration rate away from the wall.

As with the wide spacing, imposition of the tripped boundary layer produced a slight increase in the bulk mixing efficiency as evidence by the decay of maximum helium concentration. This data is plotted in Figure 87. Again the extent to which this trend is representative of molecular-scale mixing is difficult to determine from the tests conducted. However, it is clear that on a macroscopic scale the change was minor.

Based on the weaker lift-off and vortical roll-up of the jet for the narrow spacing, it was expected that a similar result would be evidenced in terms of mixing effectiveness. This was not the case as shown in Figure 88 where the decay of maximum helium mass fraction is plotted for both the narrow and wide spacing for the various boundary layer conditions. The wide spacing cases are represented with solid lines. Broken lines are used for the narrow spacing cases. While initially the levels for the narrow cases were higher than those for the corresponding boundary layer conditions for the wide spacing, the trend was reversed after $\bar{x} = 10$. Thus, globally, the time-mean mixing for the narrow geometry was better in the farfield. Again, a determination of the extent to which this represented a similar trend in molecular-scale mixing was not possible, and no planar imaging was conducted on this geometry due to time restraints. The manifestation of better mixing in the mean for the narrow spacing was probably due to the close interaction of the jets with the boundary layer. This is evident in the $\bar{x} = 8$ contour plot of pitot pressure in Figure 81 where the interaction of the neighboring counter-rotating vortex pairs produced a high pressure center between the jets. While the vorticity field was weaker, the close proximity of the jets to the boundary layer resulted in the boundary layer being effectively interred into the vortex pair. The strong unsteadiness in the core of the jets which would result puts in question the accuracy of the time-mean maximum concentration data in representing the time-resolved flow for the narrow spacing. For the wide spacing case, the bulk of the low momentum boundary layer fluid existed between the helium jets, and the jets rose above the boundary layer before strong interaction occurred. Even though farfield time-mean mixing was marginally better for the narrow geometry, consideration of jet penetration and heat transfer suggests that the wide spacing is more effective in terms of overall injector performance as a result of the stronger and more complete lift-off displayed.

6.2.2 Data from numerical simulations

The numerical simulations were conducted primarily to elucidate the detrimental effects of the boundary layer with respect to the baroclinic generation of vorticity. Simulations were computed for both the wide and narrow spacings at $\overline{\delta}$ = 0, 0.2 and 1.0. Perspective views of the development of the helium mass fraction contours for these cases are shown in Figures 35 and 89-93. Comparing the results for various boundary layer heights for the wide spacing case, (Figures 35, 89, and 90), two aspects of the effects of the boundary layer are evidenced. The first of these is the increase in mean shear at the interface provided by increasing boundary layer scale. This increased the size of the jet cross-sections through a broadening of the species gradient at the jet/freestream interface. The second effect was the progressively slower convective development of the jet with increasing boundary layer scale. Similar effects were noted for the narrow spacing geometry of Figures 91-93. Most notable is the strong vortical development which occurred for the case of inviscid boundary conditions for the narrow spacing (Figure 91). This development was not apparent for the case of the $\overline{\delta}$ = 0.2 boundary layer. This shows the sensitivity of the narrow geometry to even thin boundary layers. The result was due to the preponderance of low momentum fluid in the troughs between the injectors. This did not allow shock formation for impingement upon density gradients in the mixing region. The effect was minimized for the wide spacing because of positive interaction of the boundary layer flow with ramp-generated pressure gradients allowing for high momentum and thus strong shock formation in the corners of the troughs.

While the review of the experimental and numerical results presented above shows the influence of boundary layer/injector spacing interactions on general flow field behavior, more detailed analysis is required to show the subsequent effects on injector performance. Lift-off heights for $\overline{\delta}$ = 1.0 and $\overline{\delta}$ = 0.2 cases for the two ramp spacings are shown in Figure 94a. Consideration of the results for the wide spacing shows that the larger boundary layer acted to delay the dynamic

processes associated with jet deformation, and detrimentally affected lift-off. The final slope of the jet trajectory was the same for the two cases. In general, this trajectory is indicative of the strength of the vortex pair. This result supports the conclusion that in an integrated sense, the vorticity produced in the two conditions was of similar magnitude. The delay would be due to the broader pressure gradient formed in the exit plane for the thicker boundary layer, which then acted over a larger spatial area to produce baroclinic torque. However, as described above, positive interaction for the wide spacing produced a tongue of high momentum fluid in the corner of the ramps which minimized the broadening of the pressure gradient in the air. Further, consideration of the circulation produced (shown in Figure 95a) shows that the level of vorticity produced for the two boundary layer conditions was not of a similar magnitude. Thus, the above conclusion is incomplete. The boundary layer affected both the spatial extent of the pressure gradient and the magnitude of the pressure change, at least in the local vicinity of the helium/air density gradients. The decline of circulation produced for the wide spacing case with $\overline{\delta} = 1.0$ forecasts a decline in mixing performance similar to that noted for the narrow geometry with increasing boundary layer thickness. The above results relate to the baroclinic generation of vorticity. The circulation generated in the ramp region was largely unchanged. However, the action of this vorticity on the injectant was also affected by the boundary layer scale. This as well as the relative effects of increasing boundary layer size on both the ramp generation of vorticity and baroclinic vorticity generation are addressed in Section 6.5.

The bulk trajectory of the helium injectant was fairly insensitive to boundary layer thickness for the narrow spacing (Figure 94a). As in the experimental results the lift-off was much poorer than that obtained for the widely-spaced array. For even the thin boundary layer, little circulation was generated beyond that associated with the roll-up from the ramps as shown in Figure 95a. The predominance of low momentum fluid in the troughs negated shock-enhancement of the mixing process.

The comparisons of jet lift-off and circulation production for the two spacings with application of inviscid boundary conditions are made in Figures 94b and 95b respectively. It is clear that the degradation of performance for the narrow spacing was due largely to the boundary layer and not the narrow spacing in an intrinsic sense. The circulation production for the two cases was comparable. The differences in lift-off were due to interaction between the counter-rotating vortex pairs which were in closer proximity for the narrow spacing.

Further analysis of the mixing performance for the various spacings in response to the different boundary layer thicknesses is provided by the mixedness measure and contour length plots displayed in Figures 96 and 97, respectively. Considering the mixedness measure, three factors were recognized as indicators of effectiveness: the distance required for disappearance of pure helium in the flow field, the rate and extent of the decay of maximum helium concentration, and the percent of total helium mass flux occurring at $c_{He} < 0.05$. On all three bases, and for all boundary layer cases, the performance of the wide spacing was superior to that of the narrow spacing. For both geometries, performance was better for $\overline{\delta} = 0.2$ than for either the thicker boundary layer or the inviscid case. The fact that the inviscid cases performed poorer than the same geometry with a thin boundary layer underscores the importance of the boundary layer in enhancing the shear produced between the injectant and the freestream. The analysis of contour lengths for the various cases also shows better performance for the widely-spaced injector array with contour lengths at $c_{he} = 0.05$ typically at 1.5 to 2.0 times the initial length while similar interface lengths for the narrow spacing occurred at 1.0 to 1.5 times the same initial contour length.

The analysis of injector performance on a loss basis for these test conditions is shown in Figures 98 and 99. The total entropy rise and the portion of the entropy rise due solely to mixing are

shown. The data are plotted in terms of mass-averaged entropy, with the total entropy addition in each computational plane normalized by the total mass in each plane. As approximately twice as much helium was injected per total mass for the narrow spacing, the levels of the entropy rise due solely to mixing (the broken lines) for the narrow cases are not directly comparable to those of the wide spacing. Only the inviscid cases allowed consideration throughout the entire domain (Figures 98a and 98b). The losses generated for the narrow spacing case were 50% higher than those for the wide spacing. This resulted from close interaction between the injectors in the array. The data for all of the boundary layer conditions are shown in Figure 99 for $\bar{x} > 0$. For all the boundary layer conditions, the total entropy rise was slightly lower for the wide spacing compared to the narrow cases. Thus, the wide spacing was more effective on a loss basis. In regards to trends associated with increasing boundary layer scale, those displayed by both array spacings are identical. The losses associated with the inviscid cases were approximately 50% less than those with boundary layers of height $\bar{\delta} = 0.2$. A significant portion of the entropy rise beyond that due to mixing was caused by viscous losses associated with the interaction of the boundary layer with the ramps. Notably the cases where $\bar{\delta} = 1.0$ show approximately 50% less undesirable loss generation than the $\bar{\delta} = 0.2$ cases. This highlights the decreasing influence of the boundary layer as the jets interacted with the lower momentum fluid.

A final consideration with respect to the spacing between the injectors is the freestream area required for the injectant to mix into, to provide a desired equivalence ratio. In the latter part of Section 6.1.5 is was shown that for a representative scramjet operating condition ($\phi = 1.0$, $\overline{\dot{m}}_{st} = 0.03$, $\overline{m} = 2/29$, $\bar{p} = 1.0$, $\bar{v} = 1.0$, and $\bar{T} = 1/6$), an injectant to freestream area ratio of $\bar{A} = 0.07$ would be required for mixing to the stoichiometric hydrogen mass fraction. For the wide spacing, this area would extend to $\bar{z} = 4.0$. Due to the lateral confinement of the jets in the narrow spacing array, similar performance would require extension of the vertical scale of the area to $\bar{z} = 8.0$. Penetration of this order is not expected for the narrow spacing. It should not be concluded

however, that in general the narrow spacing is an ineffective configuration. Certainly, for other conditions which require larger area ratios, (such as that of the current study where $\overline{m}$ = 4/29, $\overline{p}$ = 1.0, $\overline{v}$ = 1.33, and $\overline{T}$ = 2.5 rather than $\overline{T}$ = 1/6, so that $\overline{A}$ = 0.41), the narrow geometry may be more effectual.

6.3 The influence of injectant/freestream pressure ratio

In considering injector performance a determination must be made of the most efficient pressure at which to deliver a given mass flux of injectant into the mixing region. In general the gas may be injected through small, high pressure jets or larger, low momentum jets. In this closely-coupled system, varying pressure ratio greatly affected the dynamics of the flow field. The effects occurred on two scales, that of the jet and that of the shear layer which existed between the injectant and the freestream. Pressure ratios greater than one caused rapid expansion of the helium injectant due to the steep Mach angles in the M = 1.7 jet. These jet dynamics produced secondary effects on the scale of the shear layer (*e.g.*, an increase in velocity ratio as the fluid in an underexpanded jet was accelerated). In general, focus was directed towards pressure ratios greater than or equal to one. Low pressure ratios ($\overline{p}$ < 1.0) were not investigated experimentally due to difficulties with unstart of the M = 1.7 nozzles. The experiments and computations were conducted entirely on the wide spacing injector geometry.

6.3.1 Experimental evidence

Flow field survey data for $\overline{p}$ = 4.0 are presented in Figures 100-105. Helium mass fraction, pitot pressure and total temperature surveys of the full-scale model are shown in Figures 100-102 respectively. These may be compared with the baseline case of $\overline{p}$ = 1.0 shown in Figures 27, 29 and 30. Similarly, the measurements from the half-scale model (Figures 103-105) may be compared with the matched pressure case previously shown in Figures 66-68. For both cases, the peak helium mass fraction values in each plane are listed above the plots. Two strong

differences between the $\bar{p}$ = 4.0 and $\bar{p}$ = 1.0 cases are displayed in the data. The first is the strong expansion undergone by the high pressure jet. This acted to produce higher local pressures in the air between the jets. Second, the vortical development of the high pressure jet was delayed by roughly a factor of two in distance from the injection plane. The unique helium signature at $\bar{x}$ = 0 for the full-scale model (Figure 100) was the result of location of grid points directly behind the wall of the injector (see Figure 19). The $\bar{x}$ = 0 survey was actually conducted 0.04 inches downstream of the injection plane. The strong expansion of the high pressure jet allowed occasional measurement of helium directly behind the injector wall. The serpentine signature probably resulted from slight misalignment of the probe depending on the direction of the probe traverse, with one direction placing the probe just inside the helium/air interface. The variation may also have been due to small variations in injectant pressure which acted to move the interface slightly.

The strong expansion of the jet is similarly displayed in the planar Rayleigh image shown in Figure 106. The mean and standard deviation (Figure 107) of the scattering intensity are shown for $\bar{p}$ = 4.0 at $\bar{x}$ = 10. Again, signal levels in the core of the helium jet were below the sensing threshold of the instrumentation. The spatial scale of the unsteadiness at the jet freestream interface shown in Figure 108 was comparable to that for the matched pressure case. Thus the influence of increased velocity ratio due to expansion of the jet appears minimal.

A comparison of the experimentally obtained maximum helium concentrations for the $\bar{p}$ = 1.0 and $\bar{p}$ = 4.0 cases is shown in Figure 109. As with the development of the jet, bulk mixing was delayed by a factor of two for the high pressure ratio case. The jet lift-off height comparison is made in Figure 110. It must be remembered that this data marks the height of the center of helium mass fraction and is a bulk measure of the jet trajectory. While the high pressure cases appear more attractive, consideration of the helium mass fraction contour plots shows that

considerably more helium was in contact with the wall for a longer distance downstream and that separation between the bottom of the helium jet and the wall was considerably less than that obtained for the matched pressure case. Thus, the adverse heat transfer associated with the high pressure jet would be more severe in a combusting flow field. Further, the slope of the trajectory for the high pressure ratio case decayed in $\bar{x}$ while a constant slope of 0.025 is expected for the matched pressure case after $\bar{x} = 20$.

6.3.2 Computational modelling

A perspective plot of computational helium mass fraction contours for the $\bar{p} = 4.0$ case is shown in Figure 111. The numerical modelling provided the opportunity to consider a low pressure ratio case as well ($\bar{p} = 0.4$). This data is shown in Figure 112. These figures may be compared with the baseline case shown in Figure 35. The higher the momentum of the injectant, the less the vorticity generated by the contoured wall geometry affected the jet. This resulted in poor lift-off of the base of the jet from the surface. This is a direct result of the primary manner by which vorticity was generated in the flow. The vorticity was generated by fluid interaction with fixed wall geometry, and thus, to first order, the energy imparted to the flow to enhance large-scale convective mixing was fixed. Action of this energy upon a lower momentum field was more effective. This behavior would not be expected for normal or angled injection from a wall where a significant portion of the energy available for mixing is derived from the dynamics of the jet itself and its interaction with the freestream. For circular sonic nozzles angled at 15 and 30 degrees to the wall, injecting helium into a Mach 3 airflow, Mays, Thomas and Schetz [1989] showed a significant increase in the rate of mixing with increasing pressure ratio.

The bulk behavior of the injectant trajectories for the three pressure ratio cases is shown in Figure 113. Similar trends are displayed as were shown in the experiments. The far-field rate of penetration of the injectant increased with decreasing pressure ratio. The low pressure jet

responded more readily to the imposed vorticity field. The more rapid separation of the base of the jet from the combustor wall for the low pressure case, would alleviate adverse heating in a combustion setting. Notably, far-field penetration for the high pressure jet was dramatically worse, with a zero slope trajectory after $\overline{x} = 25$.

The mixedness measure data for the high and low pressure ratio cases is shown in Figure 114. The low pressure jet mixed to a greater extent in a more rapid manner. By $\overline{x} = 30$, 45% of the initial helium mass flux introduced into the flow field existed at mass fractions less than $c_{He} = 0.05$ for $\overline{p} = 0.4$. At the same point, only 5% of the initial mass flux was mixed to a similar level for the high pressure case. However, normalizing by the total mass flux for each case (a factor of 10), the physical mass in the system mixed to the same level was the same for the two cases. Therefore, the entrainment of air for the two cases was comparable. Consideration of the length of the $c_{He} = 0.05$ contour level for each of the cases in Figure 110, shows that projected flame sheet length is similar as well. Thus while it would cost more fuel, the end result on a mixing basis for the high pressure case would be comparable to that for the low pressure case. This conclusion is accurate only to the extent to which the spatially-averaged results represent the actual flow. The stronger vortical action evident in the low pressure case would result in the formation of more tightly layered species gradients. These fine scales, while not resolved in the computations would lead to enhanced combustion.

The injectant to freestream area ratio, $\overline{A}$, required for complete mixing of the injectant with the freestream to a desired mixture fraction is inversely proportional to pressure ratio. In the latter part of Section 6.1.5 it was shown that for a representative scramjet operating condition with $\overline{p} = 1.0$, an area ratio of $\overline{A} = 0.07$ was required. For the purposes of comparison, if this area were bounded by the symmetry planes between the injectors in the array, then for the wide spacing case, the area would extend roughly to $\overline{z} = 2.0$, 4.0, and 16.0 for pressure ratios of $\overline{p} = 0.4$, 1.0,

and 4.0 respectively. Because of the shallow far-field trajectory of the high pressure ratio case, it is expected that complete mixing of the fuel would not occur for this case until outside the domain of interest. For conditions other than that presented, the $\overline{p} = 4.0$ case may be more effective.

Consideration of the losses for the high and low pressure ratio cases (Figure 116) shows less entropy rise beyond that directly attributable to mixing for $\overline{p} = 0.4$. The strong expansion of the high pressure jet created non-isentropic compression of the air between the jets beyond that present for the low pressure case.

Based on the above results it was concluded that injectant static pressures at or below the average local static pressure in the freestream around the injection plane would be most conducive to both loss-effective mixing and strong lift-off of the jet in scramjet applications.

6.4 Injectant to freestream velocity ratio effects

Varying the velocity ratio acts to change the magnitude of shear induced between the injectant and the freestream. As these effects were predominantly manifested in the time-fluctuating component of the flow, only experimental results are presented. Changing the velocity ratio in the numerical simulations produced only a slight broadening or narrowing of the species gradients in the mixing region. Interest in the effects of velocity ratio variations was focused on questions of performance when the velocity ratio is nominally equal to one. For this case it is important to augment mixing by some other means. Unfortunately, facility limitations did not allow delivery of helium at low enough temperatures to produce $\overline{v} = 1.0$. A minimum velocity ratio of $\overline{v} = 1.12$ was obtained. The baseline cases were conducted at $\overline{v} \approx 1.3$.

In general it is important to determine the extent to which shear-induced mixing can be relied upon in hypervelocity applications. Research in two-dimensional shear flows has shown a strong

decrease in mixing for high Mach number flows (Birch and Eggers [1972], and Brown and Roshko [1974], among others). The results correlate when viewed in terms of a convective Mach number (Papamoschou and Roshko [1986], and Dimotakis [1989]) :

$$M_{c1} = \frac{U_1 - U_c}{a_1}, \qquad \text{and} \qquad M_{c2} = \frac{U_2 - U_c}{a_2} \quad .$$

The convective Mach number is calculated by assuming approximately equal pressure recovery at the large-scale interstitial stagnation points in the mixing layer. For for $p_1 \cong p_2$:

$$\frac{p_{t1}}{p_1} \cong \frac{p_{t2}}{p_2} \quad ,$$

with U_c determined using

$$\frac{p_{ti}}{p_i} = \left[1 + \frac{\gamma_i - 1}{2} \left(\frac{U_i - U_c}{a_i} \right)^2 \right]^{\frac{\gamma_i}{\gamma_i - 1}} \qquad \text{for i=1,2} \quad .$$

Experimentally, significant decline in the growth rates of two-dimensional shear layers is reported for $M_c > 0.3$. Growth rate decay has also been demonstrated in supersonic co-flowing jets by Schadow, Gutmark and Wilson [1989] for $M_c > 0.3$ with the greatest effects noted for $M_c > 0.6$. The convective Mach numbers for the experiments were never greater than $M_c = 0.4$, based on the exit conditions of the nozzles. Local values due to dynamic behavior of the jet were not estimated. Mixing occurred predominantly without strong compressibility effects.

Included in Figures 117-119 are the flow field survey data for the experimental cases of cooled helium. Far-field data are shown in Figure 120. Note that the total temperature of the helium injectant was approximately -40^{o} C. Comparison of these results with those for the baseline conditions (Figures 27, 29 and 30) shows that very little change resulted in the flow field. Slightly

higher peak helium mass fractions were obtained for the lower velocity ratio case. These are plotted and compared against the baseline case in Figure 121. The extent to which these results portray less molecular-scale mixing was not determined with confidence. Consideration of the Rayleigh scattering results (Figures 122-124) shows no perceptible change in the nature or scale of the unsteadiness in the flow field. Compared to the baseline case (Figure 51), a higher scattering signal was obtained in the center of the jet for the lower velocity ratio. This was probably due to maintenance of more condensate in the air as it interacted with the colder helium injectant.

The decline in performance for the lower velocity ratio case may be related only in part to the weaker shear at the mixing interface. For $\bar{v} = 1.12$, the injectant to freestream static temperature ratio was 1.8. For the baseline conditions $\bar{T} = 2.5$. The lower velocity ratio was associated with an increase in the density of the injectant which reduced the magnitude of the baroclinic torque. Further, the vorticity generated was required to convect a jet of higher momentum flux. The poorer mixing displayed may be due to these factors as well as a decrease in shear-induced mixing.

Certainly, the decrease in bulk mixing efficiency was minor when considered on the scale of the global dynamics within the flow field. It may be concluded then, that for the limited range of velocity ratios tested, the magnitude of the mean shear established between the injectant and the freestream at the exit plane did not strongly influence the performance of the injectors. Mixing in the far-field was dominated by turbulent processes, but these processes were not driven by the average velocity ratio at the plane of injection. It is expected that the instabilities which led to the large time-fluctuating component of the flow were generated in part by localized shear associated with the dynamics of the helium jet and its interaction with the non-uniform external flow. Also, oscillatory shock interaction with a mixing interface has been shown to amplify turbulence

(Kumar, Bushnell, and Hussaini [1989]). The exit plane shock would be expected to display oscillations as a result of propagation through flow regions dominated by the turbulent wall boundary layer. The experimental techniques applied did not allow estimation of the relative importance of the above phenomena in generating the unsteady flow.

6.5 The roles of ramp-generated and baroclinically-generated vorticity in injector performance

Experimental and computational results have shown that two strong vorticity generation mechanisms were largely responsible for the dynamics of the mixing region. The first of these was the vorticity generated by passage of the columns of helium, between the oblique shocks formed as the flow between the ramps was compressed in the exit plane. A direct goal of this study was to enable shock-enhancement of the mixing process by such a means. The similarity of the helium mass fraction contours (*e.g.*, Figure 35) to the shadowgraph images of the two-dimensional unsteady problem of shock impingement on a cylindrical, light gas inhomogeneity (Figure 1) suggests an analogy between the two systems. Such an analogy would be desirable as considerable understanding of the two-dimensional unsteady flow field has been developed. (Yang [1991]) The analogy is limited by the existence in the flow field of other strong vorticity generation mechanisms, most notably that associated with migration of fluid from the high pressure regions above the ramps to the lower pressure regions in the troughs. This was termed ramp-generated vorticity. The analogy is further restricted for real systems because of the importance of out of plane, turbulent processes

The flexibility of the numerical simulations allowed analysis of two generic fuel injection schemes. The goal of the effort was to separate the effects of the two vorticity generation mechanisms so that their performance could be analyzed separately. The first of these injector schemes termed the 'all-shock' geometry is shown in Figure 125. The geometry provides shock-generated

vorticity as the predominant mechanism as uniform flow around the injectant is compressed in the exit plane. This flow field is more closely analogous to the two-dimensional unsteady case than the geometries presented earlier. The second geometry, the 'no-shock' geometry is shown in Figure 126. The flat wall allows for no shock-enhancement of the mixing process. The primary means for vorticity production is associated with the differential compression of the flow as a result of the ramps. The all-shock model with $\alpha_e = 4.76^o$ was designed to produce baroclinic torque of approximately the same magnitude as that generated by the baseline model. Similarly, the no-shock model with $\alpha_c = 9.46^o$ was intended to produce similar roll-up of the flow as the baseline ramp geometry of $\alpha_c = \alpha_e = 4.76^o$. The intention of the work concerning these two geometries was to individually determine performance for each of the vorticity generation mechanisms with respect to heating, jet penetration, mixing and flow losses. Due to the non-linear nature of the flow field, the phenomena associated with each of these mechanisms do no add directly when they are both present, (as is the case for the baseline geometry).

Of particular interest was the performance of the two schemes in response to changes in boundary layer height. Simulations were run for each of the geometries for $\overline{\delta} = 0$, 0.2, and 1.0. Figures 127-132 contain perspective views of helium mass fraction contours for the six cases investigated. The first three detail jet behavior for the no-shock case, with the latter three pertaining to the all-shock geometry. In both geometries, increasing boundary layer scale adversely affected large-scale convection of the jet. One difference between the two geometries in terms of injector performance was the amount of injectant with was left at or near the wall. Clean, rapid lift-off of the jet occurred for the case of baroclinic vorticity generation. This important difference was a result of the location at which vorticity was formed with respect to the location of the helium jet.

This result is more clearly understood by considering in detail the generation of vorticity in each of the geometries. Figure 133 contains static pressure contours for several computational planes for the all-shock geometry. The data shown is for the inviscid boundary condition. It is this condition which is most closely analogous to the two-dimensional unsteady problem. The analogy is still limited though, by out of plane vorticity generation, and localized three-dimensional effects. A detailed comparison of this data with a two-dimensional unsteady system where identical geometry (rectangular) and reflective boundary conditions have been applied has been presented by Yang [1991]. Moving downstream, the intersection of the shock with the density gradient between the injectant and the air is apparent. Streamwise vorticity was deposited along this intersection. The final plane shown displays the pressure signature of the counter-rotating vortex pair which was generated after the vorticity coalesced. The vorticity field for this case is shown in Figure 134. The peak values are listed at the top of each plot. No vorticity was present at $\bar{x} = 0$ as the injectant had not yet intersected the oblique shock. As the injectant passed through the oblique shocks, vorticity was generated by baroclinic torque. Location of the vorticity at the base of the jet resulted in rapid and complete lift-off from the surface.

The pressure field for the no-shock case is shown in Figure 135. The bow shock generated by the compression of the upper ramp surface produced high pressure above the ramp. Migration of the fluid from this high pressure region generated vorticity of the same sense and scale as that produced by the all-shock geometry. The vorticity contours for the no-shock case are shown in Figure 136. The vorticity, located near the upper edges of the ramp, was present in the flow field at $\bar{x} = 0$ as a result of preconditioning of the flow field by the ramp geometry. Action of the vortical forces on the lower momentum injectant increased the peak vorticity values. The vorticity first influenced the upper portion of the jet, with the helium being pulled away from the wall rather than lifted cleanly from it.

The trajectory of the helium for each of the geometries for the various boundary layer conditions is shown in Figures 137 and 138. The trajectory for the no-shock case was fairly insensitive to changes in boundary layer. Increasing boundary layer thickness applied to the all-shock model delayed development of the jet. This was due predominantly to the broadening of the pressure gradient which impinged upon the density gradient. While the bulk trajectories for the two geometries were of comparable magnitude, it is the complete lift-off of the jet from the surface for the case of the all-shock model which makes it more desirable from a heating standpoint. The far-field penetration rates for the two schemes were similar.

The circulation produced in the flow field for the two geometries is plotted in Figures 139 and 140. The strong rise in circulation at $\overline{x} = 0$ for the no-shock geometry is evidence that forces in the ramp-dominated flow field acted strongly to convect the lower momentum injectant. Typically higher circulation was obtained for the case of baroclinic vorticity generation shown in Figure 140. The inviscid case shows no generation of vorticity prior to $\overline{x} = 0$. The sustained circulation in the flow field prior to $\overline{x} = 0$ for the $\overline{\delta} = 1.0$ and $\overline{\delta} = 0.2$ conditions resulted from the component of vorticity in the boundary layer which was directed at 4.76^{o} with respect to the vertical plane in which the circulation was calculated.

A more detailed comparison of the mixing effectiveness for the two geometries is provided through consideration of the mixedness measure and contour length data presented in Figures 141 and 142, respectively. The period of time required for all of the fluid to mix below $c_{He} = 1.0$ was shorter for the all-shock geometry for the various boundary layer heights. Also, the rate at which mixing occurred downstream of this point was greater for the all-shock model. This is evidenced by the more rapid decline of the line depicting maximum helium concentration in the field. Similarly on the basis of the percentage of fluid mixed below $c_{He} = 0.05$, (indicated by the height of the near edge of the carpet plot), the all-shock model performed better. For both

boundary layer cases, the all-shock model provided nearly twice the mass flow of helium mixed to this level. The amount provided for the inviscid cases was the same for the two geometries. For the case of combustion, the higher percent of fluid at the proper mixture ratio for the all-shock geometry, would be partially offset by shorter contour lengths in comparison to the no-shock cases. Contour lengths at the lower mass fractions were typically 25 % shorter for the all-shock cases as shown in Figure 142. However, the additional length at the low mass fractions was due entirely to the fluid that was left near the wall which would be undesirable in terms of heating.

While more effective mixing was obtained for the all-shock case, the cost of the mixing in terms of losses must be determined. Consideration of the entropy measures plotted in Figures 143 and 144 shows that the generation of vorticity via baroclinic torque was more loss effective as well. For the $\overline{\delta} = 0$ cases, the total entropy rise through the computational domain was less severe for the all-shock geometry than the no-shock geometry. Thus, greater mixing was afforded for lower losses. The shock generated by the compression of the ramps was not used in an effective manner to generate vorticity, though it did facilitate formation of ramp-generated vorticity. Similar ramp-generated vorticity could be produced by largely isentropic processes by allowing $\alpha_c = 0^o$ and $\alpha_e = 9.46^o$. Such a geometry would also allow strong generation of baroclinic torque. This geometry is discussed further in Section 7.1.2.

6.6 Additional investigations

Several additional computational investigations were performed. Simulations of angled injection, non-uniform injectant profiles, elevated injection and addition of film-cooling to the baseline injection scheme are presented below. These studies were cursory in nature and were intended to provide only a topical treatment of each of the issues addressed. In all cases, the studies were not substantiated with experimental testing. The code was used in a predictive manner to analyze general flow behavior.

6.6.1 Angled injection

The experimental model and the numerical simulations were all designed to provide helium injection parallel to the freestream velocity vector. A simulation was performed to investigate the effect of adding a small vertical component to the injectant velocity vector, (see inset of Figure 145). The study was conducted with $\alpha_j = 7.5^o$ where $\tan(\alpha_j)$ is the ratio of the z and x components of the injectant velocity vector. A larger injectant angle was not investigated due to the requirement that the injectant vector be closely aligned with the intended thrust vector. In terms of injector performance, the only strong difference between the angled injection case and the baseline case was in terms of jet penetration and heating considerations. Mixing performance and loss generation were nearly identical. Comparison of Figure 145 with Figure 35 shows the degree to which the angled injection was similar to the baseline case. A plot of the lift-off height for the two cases is shown in Figure 146. The angled injection provided stronger initial lift-off of the jet and a greater rate of penetration for $\bar{x} > 20$. For most applications, the additional lift-off would be worth the loss in horizontal momentum (< 1 %).

6.6.2 Non-uniform injectant Mach number profile

A schematic of the non-uniform injectant profile tested is shown in the inset of Figure 147. A linear ramp in Mach number was chosen between M = 1.9 at the wall and M = 1.5 at the top of the injector. The variation is greater than, though in the same general sense as that predicted by a two-dimensional Euler solution for the experimental injectant nozzles (M = 1.72 to 1.65). The distribution results in movement of the mass center farther from the wall, and a greater baroclinic torque source term at the base of the injectant than at the top as a result of the change in density. A perspective view of the helium mass fraction contours for this case is shown in Figure 147. No strong differences are noted upon comparison of this case with the baseline case

(Figure 35). On all bases, injector performance was not affected by the non-uniform injectant profile. This result is positive in terms of allowing greater confidence in comparisons between the experiments (where mild variations in the Mach number profile were noted) and the numerical simulations (where uniform injectant profiles were applied).

6.6.3 Elevated injection

The elevated injection geometry was formed by covering the bottom quarter of the exit plane with a solid wall. The investigation of this configuration was motivated by two factors. The first was the possibility of further alleviation of adverse heat transfer at the base of the jet. Secondly, the configuration is a first-order model for a case of a separated injectant flow field. It was the latter of these two considerations that initially spurred interest in the configuration. Helium mass fraction contours at several computational planes are shown in perspective in Figure 148. This geometry allowed complete separation of the helium from the surface throughout the entire domain with no effect on mixing performance.

6.6.4 Addition of film-cooling to the injection scheme.

Many researchers are currently addressing the difficult problem of material survivability within the scramjet combustor. An important part of this effort are studies directed towards fluid dynamic cooling through application of both film-cooling and transpiration cooling. Detailed study is required to effectively combine these techniques with the contoured wall injectors. The single investigation presented below was intended as an initial step towards such an effort. The intention of film-cooling is that application of a thin film of cold hydrogen can be used as a thermal buffer between the combustor wall and the freestream. Addition of film cooling to the contoured wall injector arrays was accomplished as shown in Figure 149. What is particularly interesting in such a scheme is the ability for fluid dynamic control of shock strength for baroclinic generation of vorticity. This control could be applied by varying the pressure of the film coolant. Helium mass

fraction contours for this geometry are shown in Figure 150. There was strong interaction between the vorticity field and the film coolant. The subsequent deformation of the coolant layer and involvement with the primary jet flow would lead to a significant increase in adverse heating beyond that expected for the cases without film-cooling. No mixing of the coolant flow is desired, while the opposite is true of the primary flow. Recent studies (Byington, Northam, and Capriotti [1990]) have shown that transpiration cooling is for some cases an effective means of alleviating adverse wall heating. This may as well be the case for these geometries. The brief study presented here does not rule out application of film-cooling with the contoured wall injectors. It does however, suggest a search for a more effective method of combining the two.

CHAPTER 7

DESIGN RECOMMENDATIONS AND SUGGESTIONS FOR FURTHER STUDY

7.1 Comparison with other studies

Prior to offering specific design recommendations, it is important to cast the results of this study in light of studies of other injector configurations. The difficulty in such a venture is the sparse nature of the database presently available to provide means for comparison. The comparison is thus necessarily topical and incomplete. Directly below is a comparison of mixing performance against a wide variety of injector geometries. Following that, some general, largely qualitative comparisons are made with specific injection schemes.

7.1.1 General mixing performance

The difficulties in making direct comparisons of mixing performance were addressed in detail in the review by Thomas, Schetz and Billig [1989]. Most notably, comparison is limited by the wide ranging accuracy of the diagnostics applied in various studies. In many of the studies the method of sampling the flow to determine gas composition suffered from the species separation problems discussed in Section 2.4.1. Typically, comparisons are made on the basis of the decay of maximum injectant concentration. It is unclear that this is the correct basis for comparison. The percent of fluid mixed to a given level of interest may not correlate in the near region with the rate of decay of the maximum injectant concentration. Further, it is clear from the current study that

the unsteady component of the flow plays a dominant role in some regions of the mixing field. The ability of the time-mean data to represent the physical phenomena must be questioned. Lack of sufficient spatial resolution further impedes the clarity of such a comparison. It is with these caveats that the results of this study will be judged against those of others in terms of mixing efficiency. Comparisons in terms of jet penetration, heating considerations and general qualitative behavior are made with greater confidence.

Thomas, Schetz and Billig [1989] plotted the decay of maximum injectant concentration versus x/d for the studies they reviewed, where x was the distance downstream and d was a characteristic physical scale of the geometry, typically the diameter of the injection nozzle. The data were plotted on a log-log scale and fit with a power law. The data were categorized as free jets, transverse jets, wall slot jets, and hybrid jets. Due to the variety of experimental conditions, direct comparisons were not warranted. Considered as a whole, the data was grouped around a decay exponent of n = -0.8. The data from the current study are plotted in log-log form in Figure 151. The straight line portion of the data is fit with a power law proportional to $\bar{x}^{-1.34}$ for the matched pressure cases. A power of n = -1.22 was obtained when all of the experimental data were considered. The favorable comparison of these values with the gross correlation presented by Thomas *et al.* should be judged in light of the limitations discussed above, and thus given limited weight.

7.1.2 Other parallel injector configurations

As discussed in Section 1.4 several researchers have studied two injector configurations which were very similar to the contoured wall injectors investigated in this study, though test conditions were different from those of the current study. One geometry was identical to the 'no-shock' model presented in Section 6.5. It is this link with the current study that will provide some basis for comparison. The second was a variant of this geometry where the side walls of the ramps

were swept so that the planform of the ramps narrowed towards the injection plane. The sweep was intended to augment the ramp-generated vorticity. Riggins *et al.* [1990] have shown that the magnitude of circulation was greater for the swept case, but the losses associated with the configuration were higher as well, due to less three-dimensional relief. Northam, Greenberg and Byington [1989] found the combustion performance obtained for the swept-ramp injector nearly equaled that expected for normal wall injection. In general, parallel injection, contoured wall schemes are more attractive than normal injection since they allow full use of the momentum of the fuel.

Differences between the two configurations described above and the baseline configuration of the current study exist in terms of heating and mixing effectiveness. In general, without location of a shock at the base of the injectant, separation between the jet and the wall is delayed due to generation of vorticity high in the flow field with respect to the jet. As shown in Figures 127-129 complete separation of the helium from the surface was never attained for the straight-walled, no-shock model. Drummond *et al.* [1989] showed complete jet lift-off for the swept-ramp geometry at $\overline{x} \approx 7$. For the baseline geometry of this study, separation occurred at $\overline{x} \approx 1$. Comparison of the mixing performance for the no-shock geometry (Figure 141e) with that of the baseline configuration (Figure 57) where shock-enhancement was applied, shows more rapid decay of maximum helium concentration for the latter. Losses generated for the two cases (Figures 143 and 98b) were similar.

There is some confusion in the literature concerning the interaction of the compression shock from the ramps with the injectant, after reflection from the upper wall of the combustor, for the straight-walled or no-shock geometry. Two factors limit the ability of this shock to enhance injector performance. First, the oblique shock angles associated with the high Mach number flows anticipated in scramjet applications will cause the shock to impinge upon the fuel jet far

downstream. Further the sense of the vorticity created from impingement by an oblique shock from above will cause migration of the jet towards the wall. This is undesirable in terms of jet penetration and heating considerations. The results of Section 6.5 show the importance of passing the shock from bottom to top. Such an arrangement provides rapid and complete lift-off and a counter-rotating vortex pair of a sense that causes the jet to penetrate further into the flow field.

Further study is required as the relative performance of the various injection schemes may be different depending on whether they are judged in terms of mixing or combustion efficiency. Riggins and McClinton [1990] compared the no-shock geometry with the swept configuration and a 30^{o} transverse wall jet on the bases of mixing efficiency, thrust and combustion efficiency using numerical simulations. They selected the wall jet as the best non-reacting injection configuration for overall performance, followed by the swept ramps and then the straight-walled injectors. However for the case of hydrogen-air combustion, the straight-walled injector provided higher thrust. The results of the study were not corroborated experimentally, and the predictive capabilities of turbulent combustion models are limited.

7.1.3 Angled transverse wall injection

Considerable effort has been invested in studies of angled transverse injection. These geometries differ fundamentally from the parallel injector configurations both of this study and of 7.1.2. The contoured wall schemes rely primarily on interaction between the fluid and the geometry to enhance mixing. Normal injection and angled injection rely predominantly on dynamics of the injectant/freestream interaction to augment mixing. Thus, typically for such schemes, increased injectant/freestream pressure ratio increases the mixing rate while little change is seen for wall geometries.

The boundary layer may either positively or detrimentally affect the performance of wall geometries. The strong displacement effect of hypersonic boundary layers acts to effectively modify wall geometry. For significant boundary layers (of a scale greater than two times a characteristic height of the injection scheme) the wall mounted schemes may be inadequate. No studies have been conducted concerning performance of transverse injection into a flow field dominated by a wall boundary layer. However, the minimal momentum in a hypersonic boundary layer may act to strongly enhance penetration associated with transverse injection. Thus for cases with large boundary layers, transverse injection may be more effective than the various wall geometries.

Mays, Thomas and Schetz [1989] have presented data on low-angled injection. Helium was injected into a Mach 3 airstream through circular, sonic nozzles angled downstream at 15 and 30 degrees incidence to the wall. They presented maximum concentration data at three stations downstream, x/d = 20, 40, and 90. Also presented was the trajectory of the point of maximum concentration. Since scaling laws for these flow fields have not been determined, direct comparison is the only means by which these configurations may be judged against the current data. Thus identical mass flow rates, freestream conditions, and physical distances are required. Lack of satisfaction of these requirements precludes comparison.

7.2 Recommendations

The following recommendations are made based on both the limited scope of the current tests and the sparse database associated with other investigations.

Location of an oblique shock at the base of the injection plane is a loss-effective method of enhancing hypervelocity mixing through baroclinic generation of vorticity and subsequent

convection and diffusion. Other injector configurations present in the literature do not provide for vorticity generation at the base of the jet. Due to the rapid and complete lift-off of the injectant achieved with such a configuration, it is attractive for reducing adverse wall heating. In the current study, two strong vorticity generation mechanisms were ultimately responsible for mixing of the fluid. The first was a loss-effective shock-generation of vorticity. The second, related to fluid migration due to the alternating compression and expansion of the ramp surfaces was less efficient on a loss basis.

For contoured wall injectors in general, injectant static pressures at or below the local static pressure around the injection plane will provide optimal performance. Also, as wall-mounted augmentation techniques are strongly influenced by boundary layer displacement effects, care must be taken to allow sufficient spacing between the injectors for passage of the low momentum boundary flow. Further, consideration of the combustor area required to completely mix the fuel to a desired equivalence ratio must be made in light of pressure ratio and injector spacing. The representative case presented in the latter part of Section 6.1.5 suggests that lower pressure ratios and wide spacing would be most effective for scramjet applications.

An effort was made to further enhance the performance of the baseline geometry by varying the angles of the injector ramps. A geometry such as that shown in Figure 152, with $\alpha_c = 0$ and $\alpha_e = 9.46$, would allow both ramp-generated vorticity and strong baroclinic generation of vorticity. Excepting the viscous dissipation associated with the boundary layer, the ramp-generated vorticity would be produced by largely isentropic processes as there is no compression of the upper ramp surface. The geometry of Figure 152 was tested numerically. The mass fraction contours for this case are shown in Figure 153. For this case, it was important to lower the injectant pressure so that it was approximately equal to the local air pressure around the injection plane. This was achieved for $\bar{p} = 0.4$. The geometry was compared directly with the baseline

geometry for the case of $\overline{p} = 0.4$ (the low pressure, baseline geometry was discussed in Section 6.3.2). Figure 154 shows the mixedness measure for the $\alpha_c = 0$, $\alpha_e = 9.46$, model. Comparison with the baseline case (Figure 114b) shows no strong difference in mixing between the two geometries. The interest in the geometry modification was not directly to enhance mixing but rather to minimize the flow losses associated with the shock from the compression of the ramp surfaces. The entropy rise associated with the model is shown in Figure 155, and may be compared with the baseline case at $\overline{p} = 0.4$ shown in Figure 116b. No measurable reduction in losses is seen for $\overline{x} > 0$. In the region prior to the injection plane entropy addition should be reduced. However, errors associated with the rough grid edge along the ramp precluded analysis of losses in this region. In terms of the geometries presented in this study this configuration achieved performance equal to or better than the others on all bases. Further enhancement of performance could be provided by addition of angled injection as described in Section 6.6.1.

Other schemes which combine the ideas of this study with those of others may provide additional performance gains. A determination has yet to be made on the trade-off of losses versus mixing for addition of sweep to the parallel injector configurations such as was done in the studies discussed in Section 7.1.2. Certainly application of such a modification to the above geometry is feasible (in fact, Northam [1991] has initiated the study of such a geometry).

One factor detracting from the performance of contoured wall geometries in general is the loss of effectiveness with boundary layers of height greater than the scale of the injectors. For cases where large boundary layers are expected, other means may be necessary to provide desired performance. As suggested in Section 7.1.3, one possibility for good performance in flows dominated by large wall boundary layers is angled transverse injection. A recent suggestion to combine angled transverse injection with shock-enhancement (Anders [1991]) is interesting. The

geometry, sketched in Figure 156, may prove most effective for a variety of flow conditions and warrants further investigation.

Additional enhancements which may be incorporated into any of the above configurations including turbulizing of the injectant, preconditioning the boundary layer with subtle wall geometries, and utilization of the non-circular jet dynamics. Further, Yang [1991] has showed for the unsteady two-dimensional case of shock impingement upon a circular light gas inhomogeneity, that greater mixing can be attained in a given area through non-uniform cross-stream spacing of the jets, capitalizing on the asymmetric interaction between the neighboring vorticity fields. Additional studies by Yang suggest that division of a single injection plane into several discrete ports displaced vertically from each other will enhance performance for the case of shock interaction.

A combination of a variety of injection schemes may be necessary to meet scramjet performance requirements for hypersonic aircraft (see Peschke [1990]). Staged schemes in general are attractive as they provide a means for adding new energy for mixing after strong nearfield mixing has completed. This may be more important for schemes (such as those of the current study) where enhancement is via strong axial vorticity. After the axial vorticity coalesces it can act counter to the mixing by separating the light gas species through centrifugal effects. It is felt, however, that this effect will be minimal since shear-induced mixing will dominate the far-field.

7.3 Unresolved influences and suggestions for further study

The above recommendations are based largely on knowledge derived from time-mean studies performed with spatial resolution much greater than that required to determine molecular-scale mixing. A large portion of the mixing in scramjet applications will occur directly as a result of the time-fluctuating component of the flow field. In many cases unsteady effects (*e.g.*, boundary

layer structure, and mean shear effects at the exit plane) were shown to have little or no effect on the global convective mixing achieved. However, small effects in terms of macroscopic mixing may be more important in a combustion setting. The most effective technique for understanding the importance of these effects is to perform studies of reacting flows. This is also the only method acceptable for modelling the effects of the heat release associated with the combustion process. Numerical simulation techniques have not yet progressed to the stage where they can be used accurately in a predictive manner to study compressible turbulent flows with chemistry.

In general the development of efficient injection schemes suffers from lack of fundamental knowledge regarding three-dimensional, compressible, turbulent shear flows, both reacting and non-reacting. Basic studies must be conducted of hypervelocity co-flowing jets to elucidate parameter dependencies associated with convective Mach number, freestream turbulence, shock interaction, and pressure, density and velocity ratios. Subtle effects, such as the variation in entrainment between the high and low-speed fluid seen in two-dimensional shear layers may be employed to enhance mixing.

CHAPTER 8

CONCLUSIONS

A parametric study of contoured wall fuel injectors has been presented. The injector designs were aimed at enabling shock-enhanced mixing for scramjet combustor applications. Short combustor residence times, a requirement for fuel injection parallel to the freestream, and strong sensitivity of overall vehicle performance to combustion efficiency motivated the investigation. The primary goal of the study was to determine the efficacy of shock-enhancement for hypervelocity mixing augmentation. Injector performance was evaluated in terms of mixing, losses, jet penetration, and heating considerations. The following conclusions are supported by both experimental and computational results.

Two-dimensional studies of shock impingement on light gas inhomogeneities were the genesis for this effort. For these problems, baroclinic vorticity generation leads to strong convective mixing. The study showed that a qualified analogy exists between this flow field and the three-dimensional flow field generated by the contoured wall injectors which were designed to introduce vorticity through baroclinic torque. The analogy was limited by the presence of ramp-generated vorticity in the flow field, interaction with the wall boundary layer and three-dimensional vorticity generation/annihilation.

For the case of equal expansion and compression of the ramp surfaces, the ramp-generated vorticity and the shock-generated vorticity were of the same sign, order and scale. The vorticity

from these two sources coalesced into a counter-rotating vortex pair of a sense which caused the helium jet to migrate away from the surface. A constant jet trajectory slope of 0.025 was found for $\bar{x} > 20$. Further, an increase in interfacial surface area and narrowing of species gradients was afforded by the strong convective forces. This led directly to increased mixing on a molecular-scale through facilitation of diffusive processes. It is felt that the lack of spatial resolution in both the experiments and the computations led to a misrepresentation of the detailed form of the helium jet. Estimation of convective and diffusive phenomena showed that the internal structure of the jet may take the form of tightly wound, spiral species gradients. It is postulated that diffusion across these gradients in the near-field contributed significantly to molecular mixing. Farther downstream, molecular mixing was driven by turbulent processes which were enhanced by the large-scale convection. Temporally-resolved planar Rayleigh imaging was used to provide qualitative insight into the scale and nature of the time-fluctuating flow component. The peak-to-peak spatial amplitude of the unsteady oscillations of image intensity about the mean was as large as four tenths of the injector height at $\bar{x} = 10$.

Experimentally, a maximum time-mean decay rate for peak helium concentration of 12% mass fraction per injector height downstream was obtained. When correlated as a whole, the experimental data displayed a decay of maximum helium concentration proportional to $\bar{x}^{-1.22}$. For the matched pressure cases as a whole, the decay was proportional to $\bar{x}^{-1.34}$. For representative scramjet combustor conditions, it was projected that complete mixing of the hydrogen fuel to less than the stoichiometric mass fraction of $c_{H_2} = 0.03$ would require jet penetration into an area approximately 15 times the area of the injection plane. For the freestream velocities of this study, such behavior would be expected by $\bar{x} \approx 60$. Considerably more rapid mixing of helium to a similar mass fraction was displayed in the current effort due to significantly higher injectant to freestream static temperature ratios than would be expected in

practice. Approximately one-half of the losses generated downstream of the injection plane were directly attributed to mixing.

Major features of the time-mean flow field were accurately reproduced by a three-dimensional Navier-Stokes simulation of the injector array. This allowed use of the code in a predictive manner. Two geometries were developed so that the two dominant axial vorticity mechanisms could be investigated independently. These studies showed that the baroclinic generation of vorticity at the base of the helium jet in the exit plane was the dominant factor in producing strong initial lift-off and complete separation of the jet from the surface. The far-field penetration rate for the two cases was the same, due largely to generation of vortex pairs of comparable magnitude. In a general sense, baroclinic vorticity generation was found to be roughly twice as effective in terms of mixing efficiency as the ramp-generated vorticity.

The effects of several salient parameters on injector performance were presented. First-order effects were noted due to the strong displacement of the hypersonic boundary layer which acted to modify the effective wall geometry. Effects due to the interaction of the unsteady component of the boundary layer with both steady and unsteady components of the mixing field were of second order. A particularly strong interaction was displayed between the boundary layer and the spacing of the injectors in the array. For narrow spacing performance was strongly sensitive to boundary layer displacement effects. Boundary layers of scale $\overline{\delta} = 0.2$ hindered shock formation in the exit plane resulting in poor convective mixing and poor jet lift-off. Zero slope jet trajectories were noted in the far-field. The poor lift-off as well as close proximity of the jets to each other caused the boundary layer to be fully entrained into the helium injectant. This enhanced mixing to the level realized for the wide spacing geometry. However, for some scramjet applications, the higher fuel density per cross-stream distance provided by the narrow

spacing combined with weaker entrainment and poor jet penetration, would not allow complete mixing of the injectant to desired mass fraction levels.

The wide spacing geometry was insensitive to boundary layer displacement effects due to positive interaction provided by the injector ramps. This produced regions of high momentum fluid in the corners of the troughs allowing strong baroclinic vorticity generation. Collection of the boundary layer in the center of the troughs and the strong lift-off afforded by the baroclinic torque isolated the jet from direct interaction with of the boundary layer. It is expected that for boundary layers greater than the vertical scale of the injectors, performance for the wide spacing geometry will be detrimentally affected in a manner similar to the narrow geometry.

Injector performance was strongly affected by injectant to freestream pressure ratio. This resulted from close coupling between jet dynamics and the external flow field. Computations showed that the injectant mass flux mixed to below $c_{He} = 0.05$ remained constant with increasing pressure ratio. Thus, while it would cost more fuel, it would appear that the end result on a mixing basis would be the same for a high pressure jet as a low pressure jet if the two were of the same dimensions. This conclusion was based on consideration of the experimental and computational data on scales which were not sufficiently spatially resolved to realize fine-scale structure in the jet. It was projected that consideration of spatially resolved data would show the low pressure case to be more effective in terms of mixing. For the case where complete mixing of the fuel to a desired mass fraction is required, pressure ratios less than one would be more effective. For conditions representative of scramjet combustor applications, complete mixing of the fuel for the $\overline{p} = 4.0$ case would not be expected within typical domains of interest.

Separation between the lower extent of the jet and the combustor wall, as well as the far-field penetration rate of the injectant, decreased with increasing pressure ratio. The losses generated in the flow field beyond those due to mixing increased with increasing pressure ratio.

Based on the above results, injectant pressures at or below the average local pressure around the injection plane were judged most conducive to clean separation between the injectant and the surface of the wall, strong penetration and efficient mixing. The energy imparted to the flow by the fixed wall geometry to enhance convective mixing was constant to first order. Action of this energy on a lower momentum injectant was more effective.

Reducing the velocity ratio between the injectant and the freestream from $\overline{v} = 1.33$ to $\overline{v} = 1.12$ produced only a weak decline in mixing performance. The extent to which this decline was associated with a decrease in molecular-scale mixing was not determined. In terms of the global mixing phenomena displayed in the flow field, shear-induced mixing associated with non-unity velocity ratios in the exit plane played a minor role (for the limited range of velocity ratios tested). Thus, strong augmentation techniques are required for hypervelocity applications in this parameter range. The turbulent fluctuations, which dominated mixing in the far-field, were produced by local shear associated with the dynamics of the jet/freestream interaction, and possibly unsteady shock interaction with the mixing interface. These phenomena were not driven by the injectant to freestream velocity ratio.

Additional computational simulations showed that elevated injection and the non-uniform injectant profile tested produced no significant changes in injector performance. Addition of a small vertical component to the injectant did provide additional jet penetration.

The results of this study should be used as guidelines for the design of scramjet injector schemes. The study was preliminary. Its scope was limited by the spatial and temporal resolutions of the methods applied. Two directions for further research are required. Basic investigations of simple, three-dimensional co-flowing hypervelocity jet flows, both reacting and non-reacting must be conducted. These should be directed towards providing a fundamental understanding of hypervelocity mixing and combustion processes. The knowledge from these studies may then be used in applied efforts to develop scramjet combustor configurations which perform to the exacting requirements of hypersonic vehicles.

REFERENCES

Adler, D. [1972], "A Hot Wire Technique for Continuous Measurement in Unsteady Concentration Fields of Binary Gaseous Mixtures," Journal of Physics E: Scientific Instruments, v. 5, pp. 163-169.

Adler, D., and Zvirin, Y. [1975], "The Time Response of a Hot Wire Concentration Transducer," Journal of Physics E: Scientific Instruments, v. 8, no. 3, pp. 185-188.

Anders, J. B. [1991], Experimental Flow Physics Branch, Fluid Mechanics Division, NASA Langley Research Center, personal communication, March 1991.

Anderson, D. A., Tannehill, J. C., and Pletcher, R. H. [1984] Computational Fluid Mechanics and Heat Transfer, Hemisphere Publishing Corporation, New York, pp. 247-255.

Baldwin, B. S., and Lomax, H. [1978], "Thin Layer Approximation an Algebraic Model for Separated Turbulent Flows," AIAA 16th Aerospace Sciences Meeting, AIAA Paper 78-0257.

Ballal, D. R., and Chen, T. H. [1988], "Effects of Freestream Turbulence on the Development of a CO_2 Round Jet," AIAA 26th Aerospace Sciences Meeting, AIAA Paper 88-0536.

Batchelor, G. K. [1952], "The Effect of Homogeneous Turbulence on Material Lines and Surfaces," Proc. Roy. Soc. London 213A, pp. 349-366.

Birch, S. F., and Eggers, J. M. [1972], "A Critical Review of the Experimental Data for Developed Free Turbulent Shear Layers," NASA SP-321, Free Turbulent Shear Flows Volume I - Conference Proceedings.

Broadwell, J. E., and Mungal, M. G. [1990], "Large-Scale Structures and Molecular Mixing," invited general lecture presented at the IUTAM Symposium on Fluid Mechanics of Stirring and Mixing, San Diego, California.

Brown, G. L., and Rebollo, M. R. [1972], "A Small, Fast Response Probe to Measure Composition of a Binary Gas Mixture," AIAA Journal, v. 10, no. 5.

Brown, G. L., and Roshko, A. [1974], "On Density Effects and Large Structure in Turbulent Mixing Layers," J. Fluid Mechanics, v. 64, no. 4, pp. 775-816.

Byington, C. S., Northam, G. B., and Capriotti, D. P. [1990], "Transpiration Cooling in the Locality of a Transverse Fuel Jet for Supersonic Combustors," AIAA/SAE/ASME/ASEE 26th Joint Propulsion Conference, AIAA Paper 90-2341.

Campargue, R. [1976], "The Separation Probe," Aerodynamic Separation of Gases and Isotopes, Lecture Series 82, von Karman Institute for Fluid Dynamics.

Carpenter, M. H. [1989], "Three-Dimensional Computations of Cross-Flow Injection and Combustion in a Supersonic Flow," AIAA 20th Fluid Dynamics, Plasma Dynamics and Lasers Conference, AIAA Paper 89-1870.

Chang, J. H., and Fenn, J. B. [1970], "Species Separation by Stagnation of Argon-Helium Mixtures in Supersonic Flow," Proceedings of the Seventh Rarefied Gas Dynamics Symposium, pp. 599-607.

Chassaing, P. [1977], "Heat-Transfer from Cylindrical Anemometer Probes in CO_2-Air Mixtures," The Physics of Fluids, v. 20, no. 8, pp. 1260-1262.

Clement, P., and Rodriguez, C. [1989], "Shock Wave Structure and Penetration Height in Transverse Jets," AIAA Student Journal, Summer 1989, pp. 7-16.

Cussler, E. L. [1984], Diffusion, Mass Transfer in Fluid Systems, Cambridge University Press, New York, pp. 108-111.

Devillers, J.-F., and Diep, G. B. [1973], "Hot-Wire Measurements of Gas Mixture Concentrations in a Supersonic Flow," DISA Information Measurement and Analysis, no. 14.

Dimotakis, P. E. [1989], "Turbulent Free Shear Layer Mixing," AIAA 27th Aerospace Sciences Meeting, AIAA Paper 89-0262.

Drummond, J. P., Carpenter, M. H., and Mukunda, H. S. [1989], "Mixing and Combustion Enhancement in Supersonic Reacting Flows," Proceedings of the Fifth International Symposium on Numerical Methods in Engineering, pp. 175-184.

Drummond, J. P., Carpenter, M. H., Riggins, D. W., and Adams, M. S. [1989], "Mixing Enhancement in a Supersonic Combustor," AIAA/ASME/SAE/ASEE 25th Joint Propulsion Conference, AIAA Paper 89-2794.

Drummond, J. P., and Mukunda, H. S. [1988], "A Numerical Study of Mixing Enhancement in Supersonic Reacting Flows," AIAA Paper 88-3260.

Drummond, J. P., and Weidner, E. H. [1981], "Numerical Study of a Scramjet Engine Flow Field," AIAA 19th Aerospace Sciences Meeting, AIAA Paper 81-0186.

Eklund, D. R., Northam, G. B., and Fletcher, D. G. [1990], "A Validation Study of the SPARK Navier-Stokes Code for Nonreacting Scramjet Combustor Flowfields," AIAA/SAE/ASME/ASEE 26th Joint Propulsion Conference, AIAA Paper 90-2360.

Ferri, A. [1973], "Mixing-Controlled Supersonic Combustion," Annual Reviews of Fluid Mechanics, v. 5, no. 1, pp. 301-338.

Ferri, A., Libby, P. A., and Zakkay, V. [1964], " Theoretical and Experimental Investigation of Supersonic Combustion," Proceedings of the Third Conference of the International Council of the Aeronautical Sciences, AIAA.

Guirguis, R. H. [1988], "Mixing Enhancement in Supersonic Shear Layers: III. Effect of Convective Mach Number," AIAA 26th Aerospace Sciences Meeting, AIAA Paper 88-0701.

Guirguis, R. H., Grinstein, F. F., Young, T. R., Oran, E. S., Kailasanath, K. and Boris, J. P. [1987], "Mixing Enhancement in Supersonic Shear Layers," AIAA 25th Aerospace Sciences Meeting, AIAA Paper 87-0373.

Gutmark, E., Schadow, K. C., Parr, T. P., Parr, D. M., and Wilson, K. J. [1989], "Combustion Enhancement by Axial Vortices," J. Propulsion, v. 5, no. 5, pp. 555-560.

Gutmark, E., Schadow, K. C., and Wilson, K. J. [1989a], "Mixing Enhancement in Coaxial Supersonic Jets," AIAA 27th Fluid Dynamics, Plasma Dynamics and Lasers Conference, AIAA Paper 89-1812.

Gutmark, E., Schadow, K. C., and Wilson, K. J. [1989b], "Noncircular Jet Dynamics in Supersonic Combustion," J. Propulsion, v. 5, no. 5, pp. 529-533.

Haas, F., and Sturtevant, B. [1987], "Interaction of Weak Shock Waves with Cylindrical and Spherical Gas Inhomogeneities," J. Fluid Mechanics, v. 181, pp.41-76.

Hartfield, R. J., Hollo, S. D., and McDaniel, J. C. [1990a], "Planar Measurement of Flowfield Parameters in a Nonreacting Supersonic Combustor Using Laser-Induced Iodine Fluorescence," AIAA 28th Aerospace Sciences Meeting, AIAA Paper 90-0162.

Hartfield, R. J., Jr., Hollo, S. D., and McDaniel, J. C. [1990b], "Experimental Investigation of a Supersonic Swept Ramp Injector Using Laser Induced Iodine Fluorescence," AIAA 21st Fluid Dynamics, Plasma Dynamics and Lasers Conference, AIAA Paper 90-1518.

Hendricks, G. J., and Marble, F. E. [1990], "Shock Enhancement of Supersonic Combustion Processes," Jet Propulsion Center Report, California Institute of Technology, Pasadena, California.

Hersch, M., and Povinelli, L. A. [1970], "Effect of Interacting Vortices on Jet Penetration into a Supersonic Stream," NASA Technical Memorandum, TM X-2134.

Hersch, M., and Povinelli, L. A. [1971], "Injection into a Supersonic Stream from the Windward Side of Sweptback Injectors at Angle of Attack," Journal of Spacecraft and Rockets, v. 8., no. 10, pp. 1101-1103.

Hollo, S. D., and Hartfield, R. J., and McDaniel, J. C. [1990], "Injectant Mole Fraction Measurements of Transverse Injection In Constant Area Supersonic Ducts," AIAA 21st Fluid Dynamics, Plasma Dynamics and Lasers Conference, AIAA Paper 90-1632.

Jones, R. A., and Feller, W. V. [1970], "Preliminary Surveys of the Wall Boundary Layer in a Mach 6 Axisymmetric Tunnel," NASA Technical Note TN D-5620.

Jones, B. G., and Wilson, R. J. [1977], "Gas Concentration Measurements With A Temperature Compensated Aspirating Probe," Proceedings of the Fifth Biennial Symposium on Turbulence, pp. 205-210.

Kay, I. W., Peschke, W. T., and Guile, R. N. [1990], "Hydrocarbon-Fueled Scramjet Combustor Investigation," AIAA/SAE/ASME/ASEE 26th Joint Propulsion Conference, AIAA Paper 90-2337.

King, P. S., Thomas, R. H., and Schetz, J. A [1989], "Combined Tangential-Normal Injection Into a Supersonic Flow," AIAA 27th Aerospace Sciences Meeting, AIAA Paper 89-0622.

Korkegi, R. H. [1954], "Transition Studies and Skin Friction Measurements on an Insulated Flat Plate at a Hypersonic Mach Number," California Institute of Technology Guggenheim Aeronautical Laboratory Hypersonic Wind Tunnel, Memorandum no. 17, Pasadena, California.

Kumar, A., Bushnell D. M., and Hussaini, M. Y. [1989], "Mixing Augmentation Technique for Hypervelocity Scramjets," J. Propulsion, pp. 514-522.

Kuo, K. K. [1986], Principles of Combustion, John Wiley and Sons, New York, pp. 357-359.

Marble, F. E., Hendricks, G. J., and Zukoski, E. E. [1987], "Progress Toward Shock Enhancement of Supersonic Combustion Processes," presented at the United States - France Joint Workshop on Turbulent Reactive Flows, AIAA Paper 87-1880.

Marble, F. E., Zukoski, E. E., Jacobs, J. W., Hendricks, G. J., and Waitz, I. A. [1990], "Shock Enhancement and Control of Hypersonic Mixing and Combustion," AIAA/SAE/ASME/ASEE 26th Joint Propulsion Conference, AIAA Paper 90-1981.

Mays, R. B., Thomas, R. H., and Schetz, J. A. [1989], "Low Angle Injection Into a Supersonic Flow," AIAA/ASME/SAE/ASEE 25th Joint Propulsion Conference, AIAA Paper 89-2461.

McQuaid, J., and Wright, W. [1973], "The Response of a Hot-Wire Anemometer in Flows of Gas Mixtures," Int. J. Heat and Mass Transfer, v. 16, no. 4, pp. 819-828.

Metwally, O., Settles, G., and Horstman, C. [1989], "An Experimental Study of Shock Wave/Vortex Interaction," AIAA 27th Aerospace Sciences Meeting, AIAA Paper 89-0082.

Morgan, R. G., Paull, A., Morris, N., and Stalker, R. J. [1986], "Hydrogen Scramjet with Side Wall Injection," Paper G1212 originally presented at the Second National Space Engineering Symposium.

Muntz, E. P., and Hamel, B. B. [1974], "Rarefaction Phenomena in Gas and Isotope Separations," Proceedings of the 9th Rarefied Gas Dynamics Symposium.

Ng, W. F., Kwok, F. T., and Ninnemann, T. A. [1989], "A Concentration Probe for the Study of Mixing in Supersonic Shear Flows," AIAA/ASME/SAE/ASEE, 25th Joint Propulsion Conference, AIAA Paper 89-2459.

Northam, G. B. [1991], Experimental Methods Branch, Fluid Mechanics Division, NASA Langley Research Center, personal communication, March 1991.

Northam, G. B., Greenberg, I., and Byington, C. S. [1989], "Evaluation of Parallel Injector Configurations for Supersonic Combustion," AIAA/ASME/SAE/ASEE 25th Joint Propulsion Conference, AIAA Paper 89-2525.

Papamoschou, D., and Roshko, A. [1986], "Observations of Supersonic Free Shear Layers," AIAA Paper 86-0162.

Perry, A. [1977], "The Time Response of an Aspirating Probe in Gas Sampling," Journal of Physics E: Scientific Instruments, v. 10, no. 9, pp. 898-902.

Peschke, W. T. [1990], "Supersonic Combustor Testing," Gas Turbine Combustion, von Karman Institute for Fluid Dynamics Lecture Series 1990-02, v. 2.

Povinelli, F. P., and Povinelli, L. A. [1971], "Correlation of Secondary Sonic and Supersonic Gaseous Jet Penetration into Supersonic Crossflows," NASA Technical Note, TN D-6370.

Povinelli, L. A. [1974a], "Aerodynamic Drag and Fuel Spreading Measurements in a Simulated Scramjet Combustion Module," NASA Technical Note, TN D-7674.

Povinelli, L. A. [1974b], "Drag and Distribution Measurements of Single-Element Fuel Injectors for Supersonic Combustors," NASA Technical Memorandum, TM X-3015.

Povinelli, L. A., and Ehlers, R. C. [1972], "Swirling Base Injection for Supersonic Combustion Ramjets," AIAA Journal, v. 10, no. 9, pp. 1243-1244.

Povinelli, L. A., Povinelli, F. P., and Hersch, M. [1969], "Vortex Enhancement of Jet Penetration in Supersonic Flow," AIAA Fluid and Plasma Dynamics Conference, AIAA Paper 69-664.

Presz, W., Jr., Gousy, R., and Morin, B. [1986], "Forced Mixer Lobes in Ejector Designs," AIAA/ASME/SAE/ASEE 22nd Joint Propulsion Conference, AIAA Paper 86-1614.

Reis, V. H., and Fenn, J. B. [1963], "Separation of Gas Mixtures in Supersonic Jets," The Journal of Chemical Physics, v. 39, no. 12.

Riggins, D. W., Drummond, J. P., and Carpenter, M. H. [1990], "Supersonic Combustor Modelling," Gas Turbine Combustion, von Karman Institute for Fluid Dynamics Lecture Series 1990-02, v. 1.

Riggins, D. W., and McClinton, C. R. [1990], "A Computational Investigation of Flow Losses in a Supersonic Combustor," AIAA/SAE/ASME/ASEE 26th Joint Propulsion Conference, AIAA Paper 90-2093.

Riggins, D. W., Mekkes, G. L., McClinton, C. R., and Drummond, J. P. [1990], "A Numerical Study of Mixing Enhancement in a Supersonic Combustor," 28th Aerospace Sciences Meeting, AIAA Paper 90-0203.

Schadow, K. C., Gutmark, E., Parr, T. P., Parr, D. M., and Wilson, K. J. [1987], "Enhancement of Fine-Scale Mixing for Fuel-Rich Plume Combustion," AIAA 25th Aerospace Sciences Meeting, AIAA Paper 87-0376.

Schadow, K. C., Gutmark, E., and Wilson, K. J. [1989], "Passive Mixing Control in Supersonic Coaxial Jets at Different Convective Mach Numbers," AIAA Paper 89-0995.

Shirinzadeh, B., Hillard, M. E. and Exton, R. J. [1991], "Condensation Effects on Rayleigh Scattering Measurements in a Supersonic Wind Tunnel," AIAA Journal, v. 29, no. 2, pp. 242-246.

Shirinzadeh, B., Hillard, M. E., Blair, A. B., and Exton, R. J. [1991a], "Study of Cluster Formation and Its Effects on Rayleigh and Raman Scattering Measurements in a Mach 6 Wind Tunnel," AIAA Paper 91-1496.

Shirinzadeh, B., Waitz, I. A., Balla, J. Hillard, M. E., Anders, J. B., and Exton, R. J. [1991b],"Planar Rayleigh Scattering Results in Helium/Air Mixing Experiments in a Mach 6 Wind Tunnel," submitted to Optics Letters.

Simpson, F. L., and Wyatt, W. G. [1973], "The Behaviour of Hot-Film Anemometers in Gas Mixtures," Journal of Physics E: Scientific Instruments, v. 6, no. 10, pp. 968-1060.

Thomas, R. H., Schetz, J. A., and Billig, F. S. [1990], "Gaseous Injection in High Speed Flow," presented at the Ninth International Symposium on Air Breathing Engines, AIAA Paper 90-17446.

Tillman, T. G., Patrick, W. P., and Paterson, R. W. [1988], "Enhanced Mixing of Supersonic Jets," AIAA/ASME/SAE/ASEE 24th Joint Propulsion Conference, AIAA Paper 88-3002.

Way, J., and Libby, P. A. [1970], "Hot-Wire Probes for Measuring Velocity and Concentration in Helium-Air Mixtures," AIAA Journal, v. 8, no. 5, pp. 976-978.

Weinstein, L. M. [1973], "Hot-Wire Coil Probe for High-Speed Flows," AIAA Journal, v. 11, no. 12, pp. 1772-1773.

Wilder, J. G., and Hindersinn, K. [1953], "Spreading of Supersonic Jets in Supersonic Streams," Aeronautical Engineering Review.

Yang, J. [1991], "An Analytical and Computational Investigation of Shock-Induced Vortical Flows with Applications to Supersonic Combustion," Ph.D. Thesis, California Institute of Technology, Pasadena, California.

Yeung, M. -T. [1991], unpublished data, California Institute of Technology, Pasadena California.

FIGURES

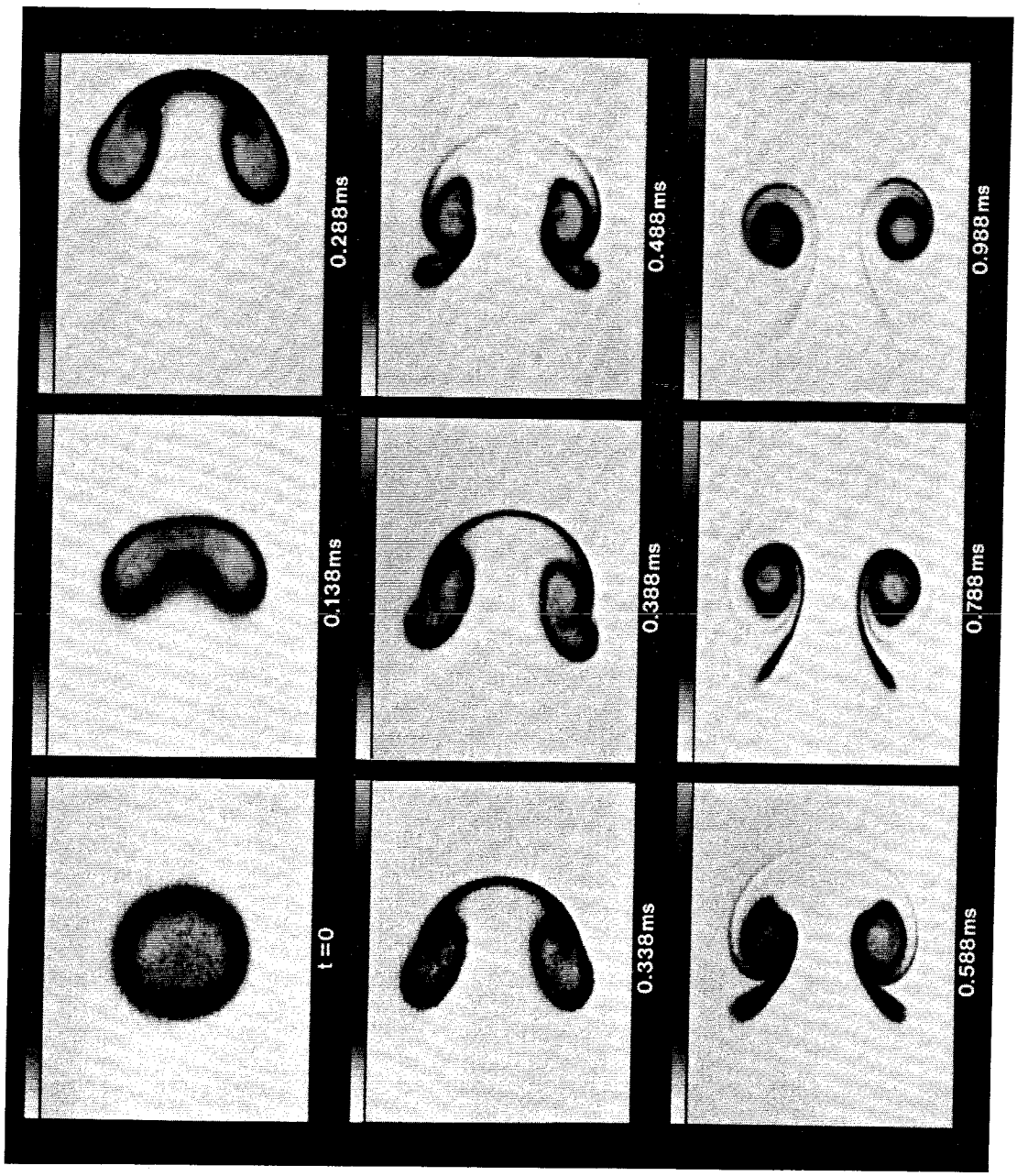

Figure 1. Laser induced fluorescence images after normal shock impingement on a two-dimensional cylinder of helium. (Marble *et al.* [1990])

$$\rho \frac{D}{Dt}\left(\frac{\tilde{\omega}}{\rho}\right) = \frac{1}{\rho^2}\nabla\rho \times \nabla p$$

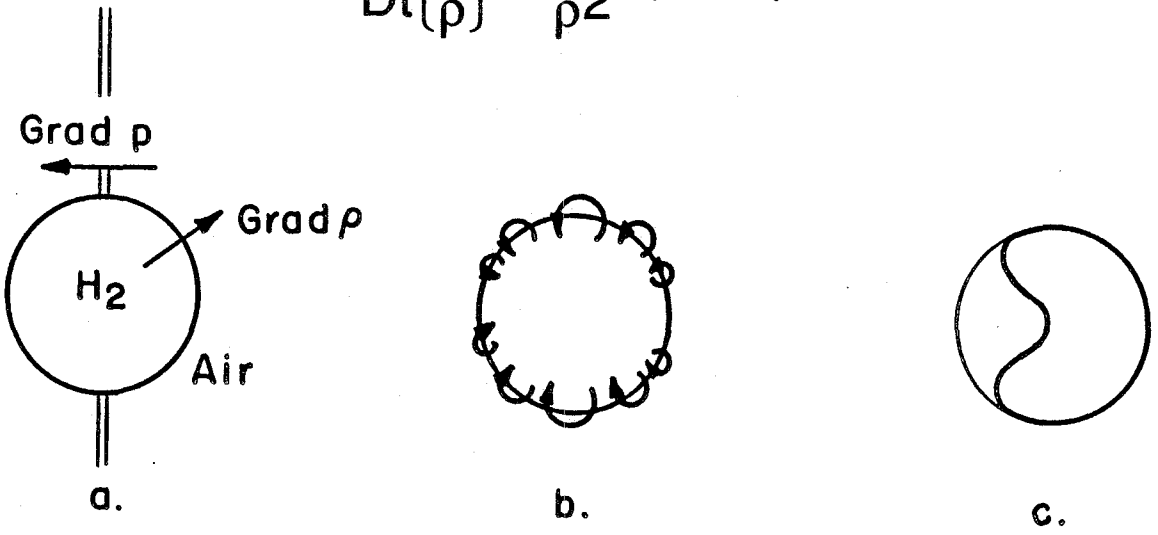

Figure 2. Schematic of vorticity generation process associated with shock impingement on light circular gas inhomogeneity.

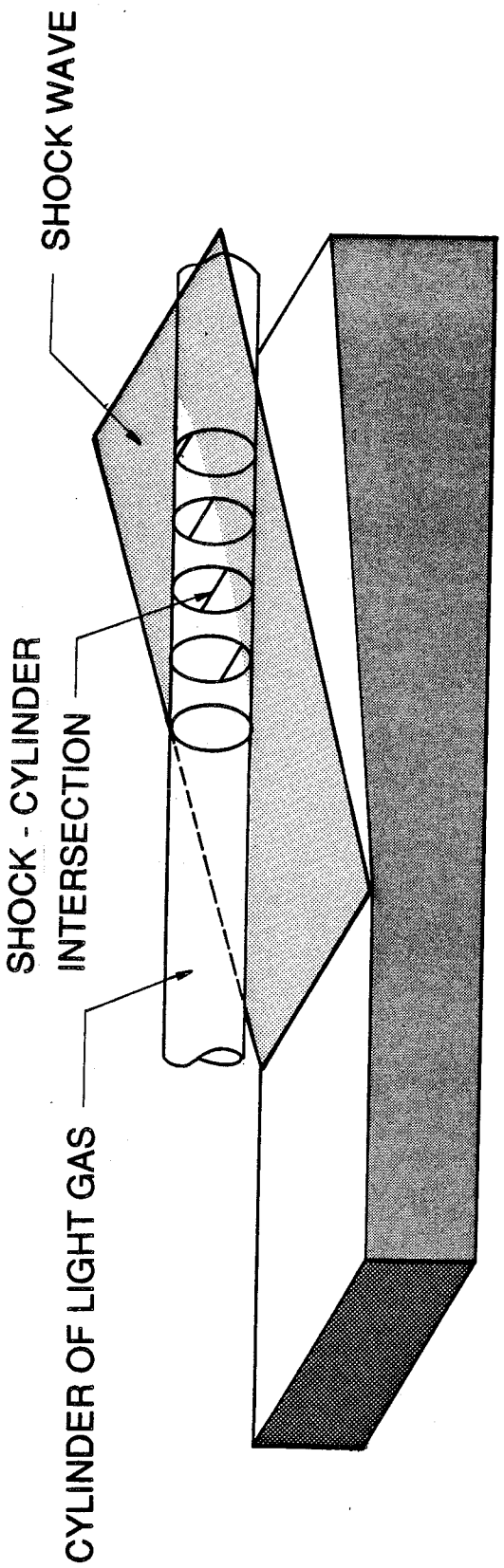

Figure 3. Schematic view of oblique shock passage through light gas cylinder imbedded in air.

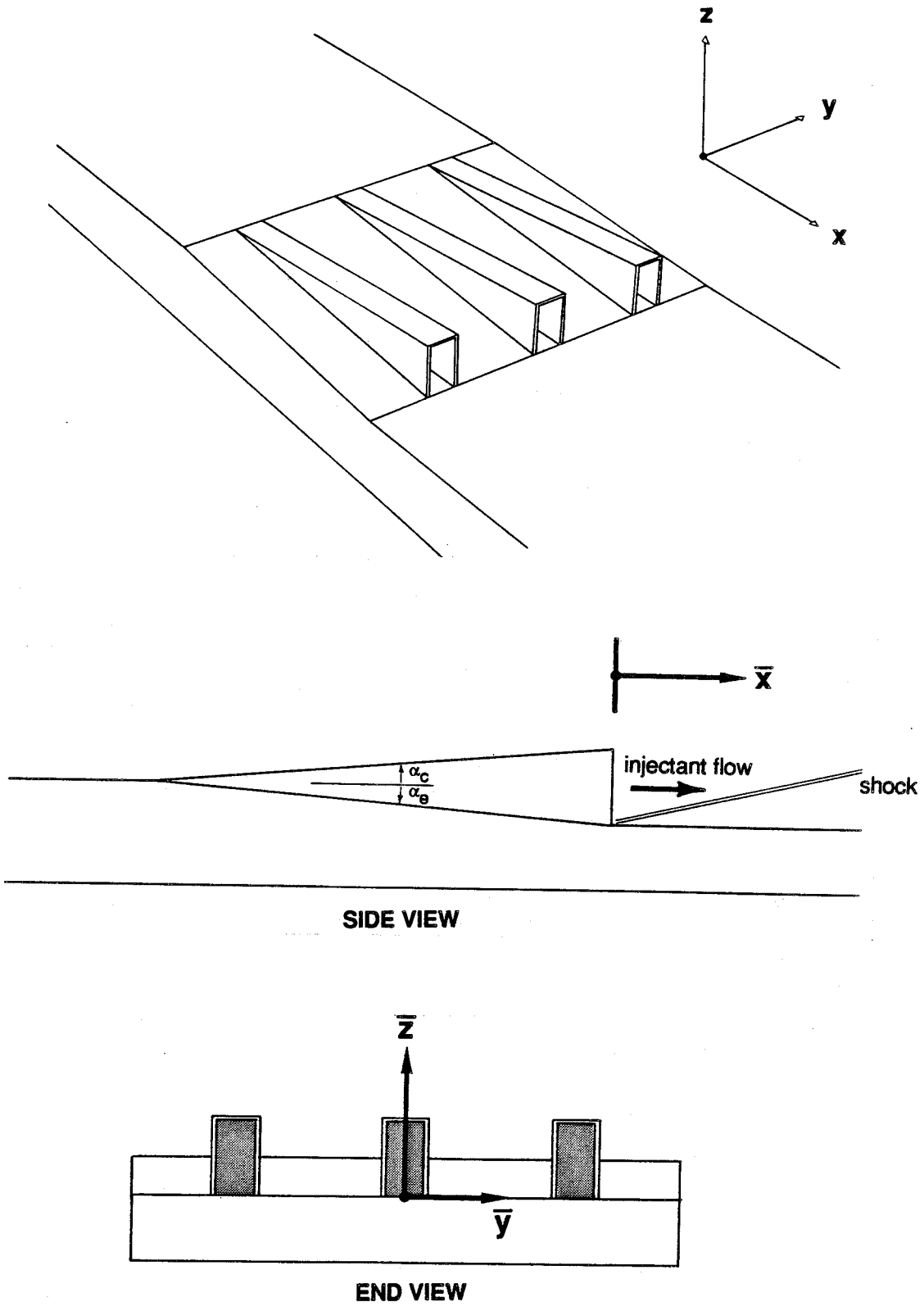

Figure 4. Diagram of contoured wall fuel injectors and definition of axes.

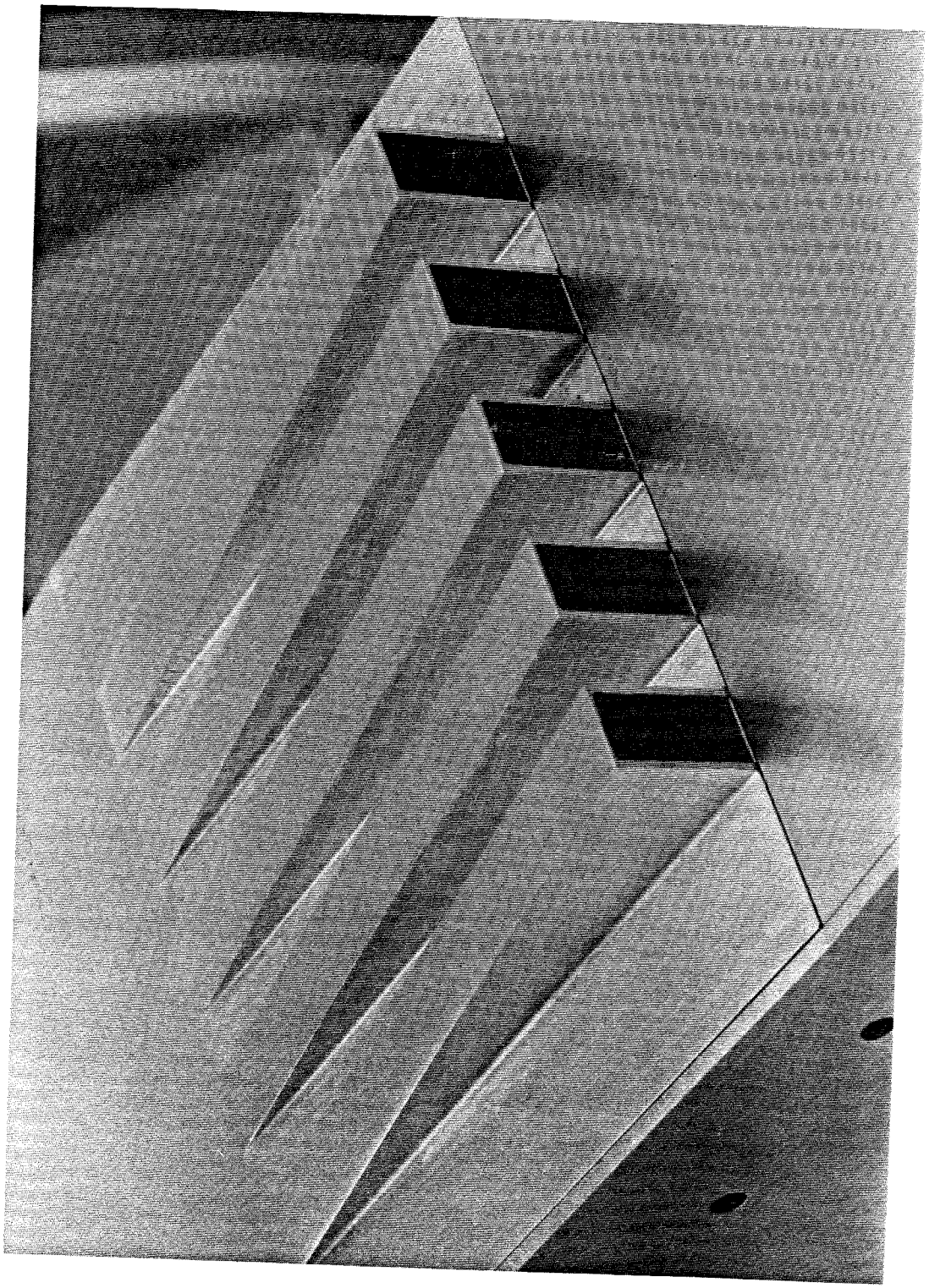

Figure 5. Photograph of wind-tunnel model with full-scale, narrow spacing, injector array installed.

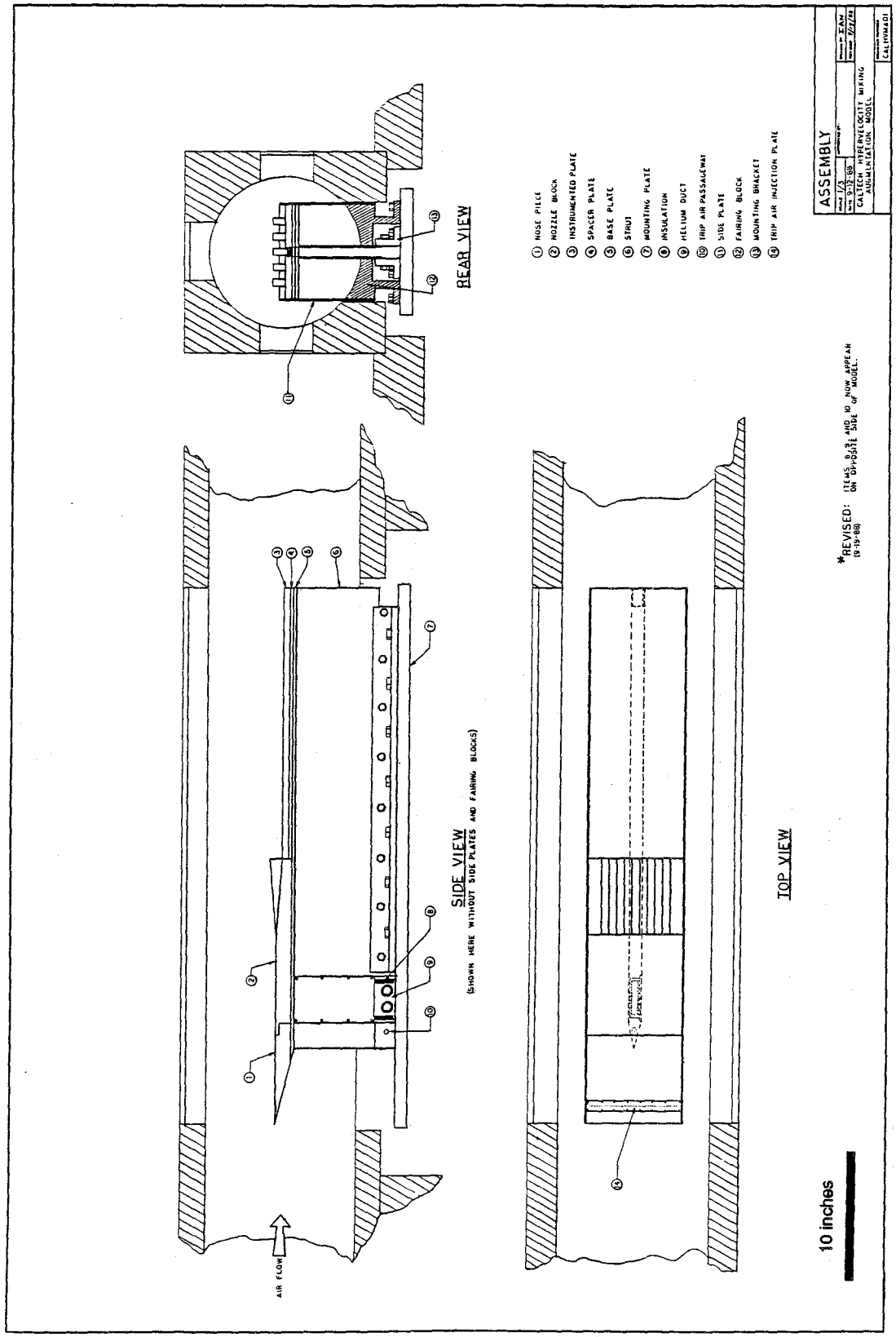

Figure 6. Three-view drawing of model in wind-tunnel.

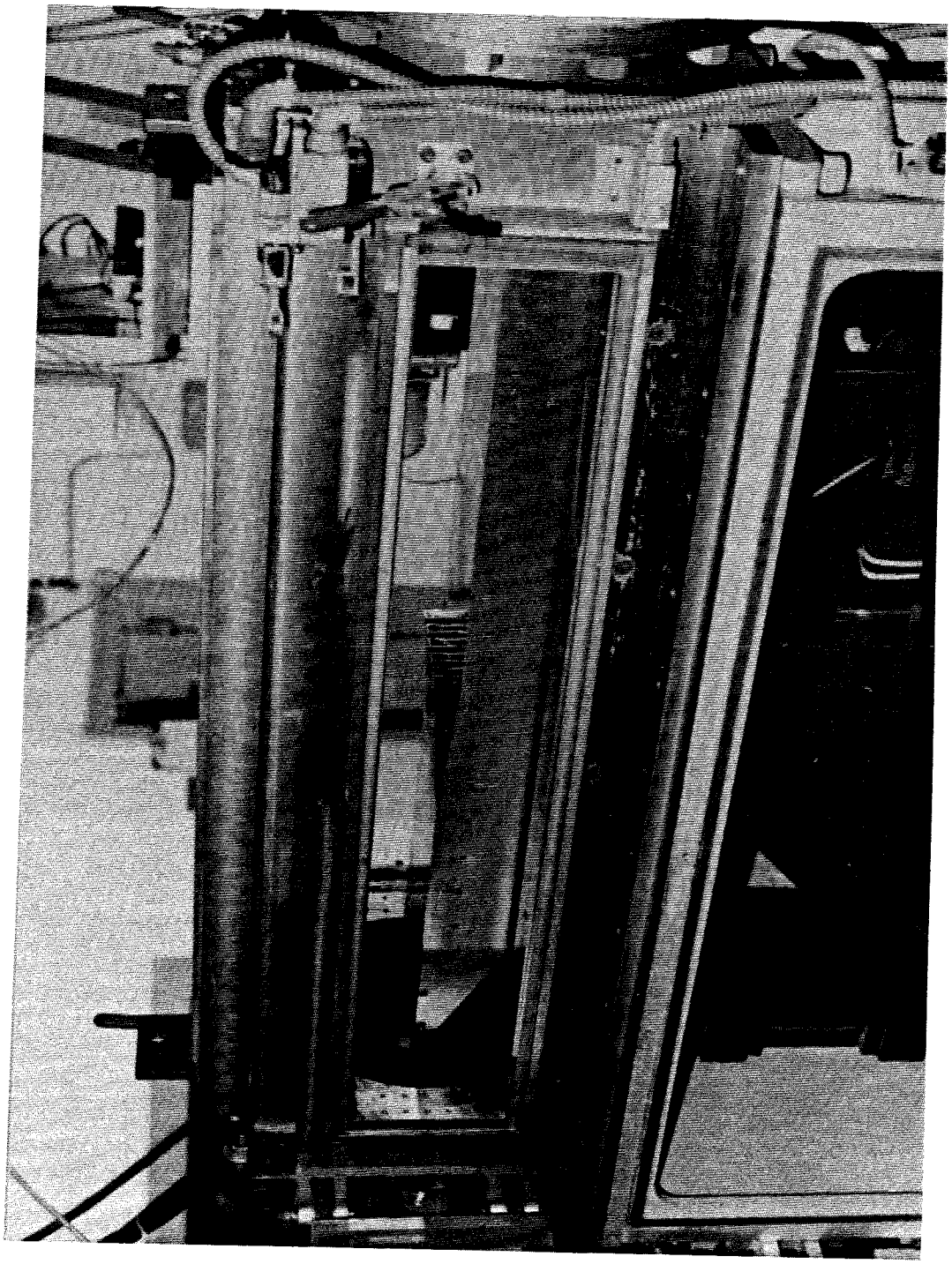

Figure 7. Photograph of model mounted in the NASA Langley High Reynolds Number Mach 6 Wind-Tunnel.

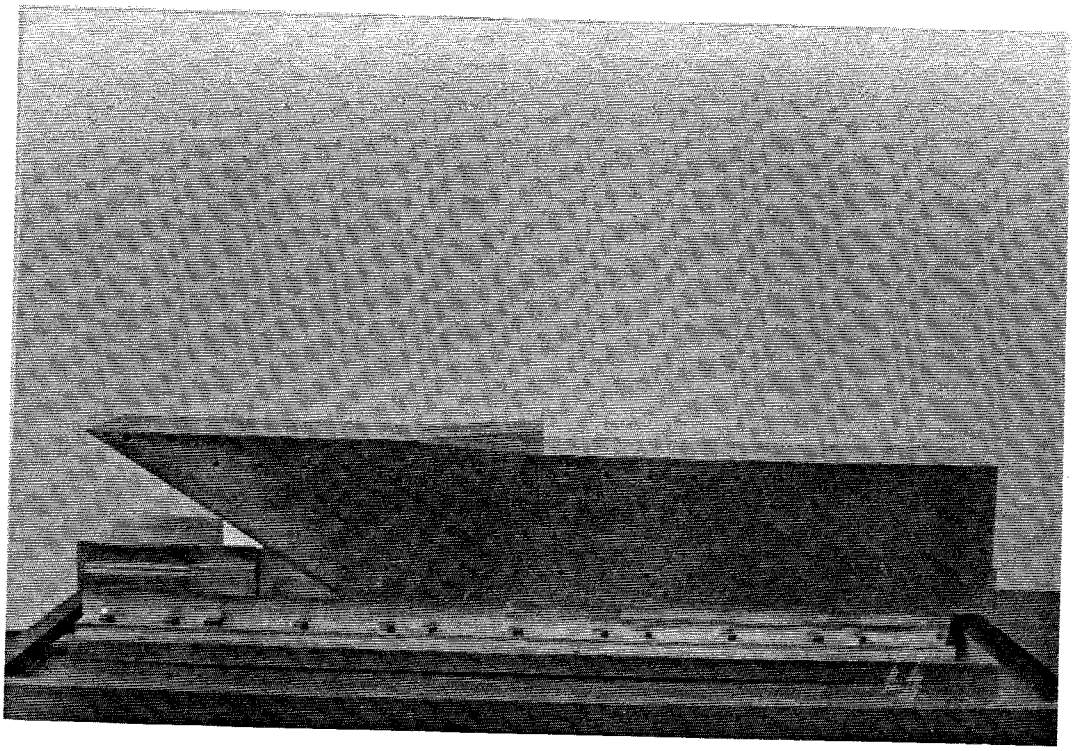

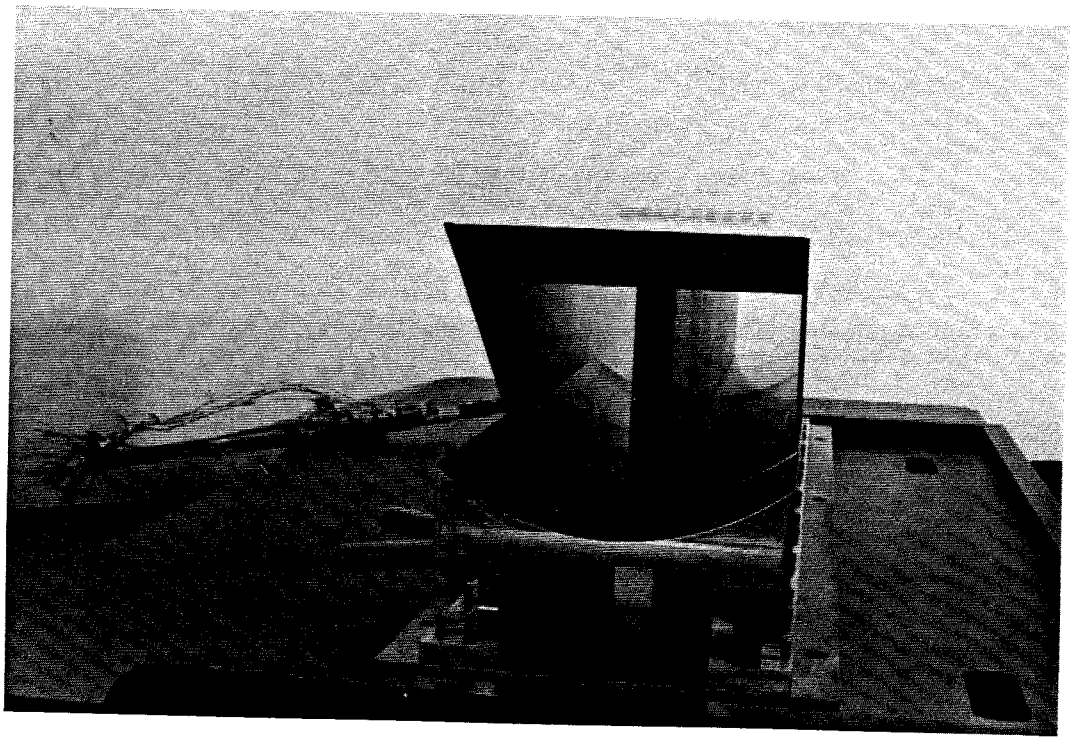

Figure 8. Photographs of the wind-tunnel model.

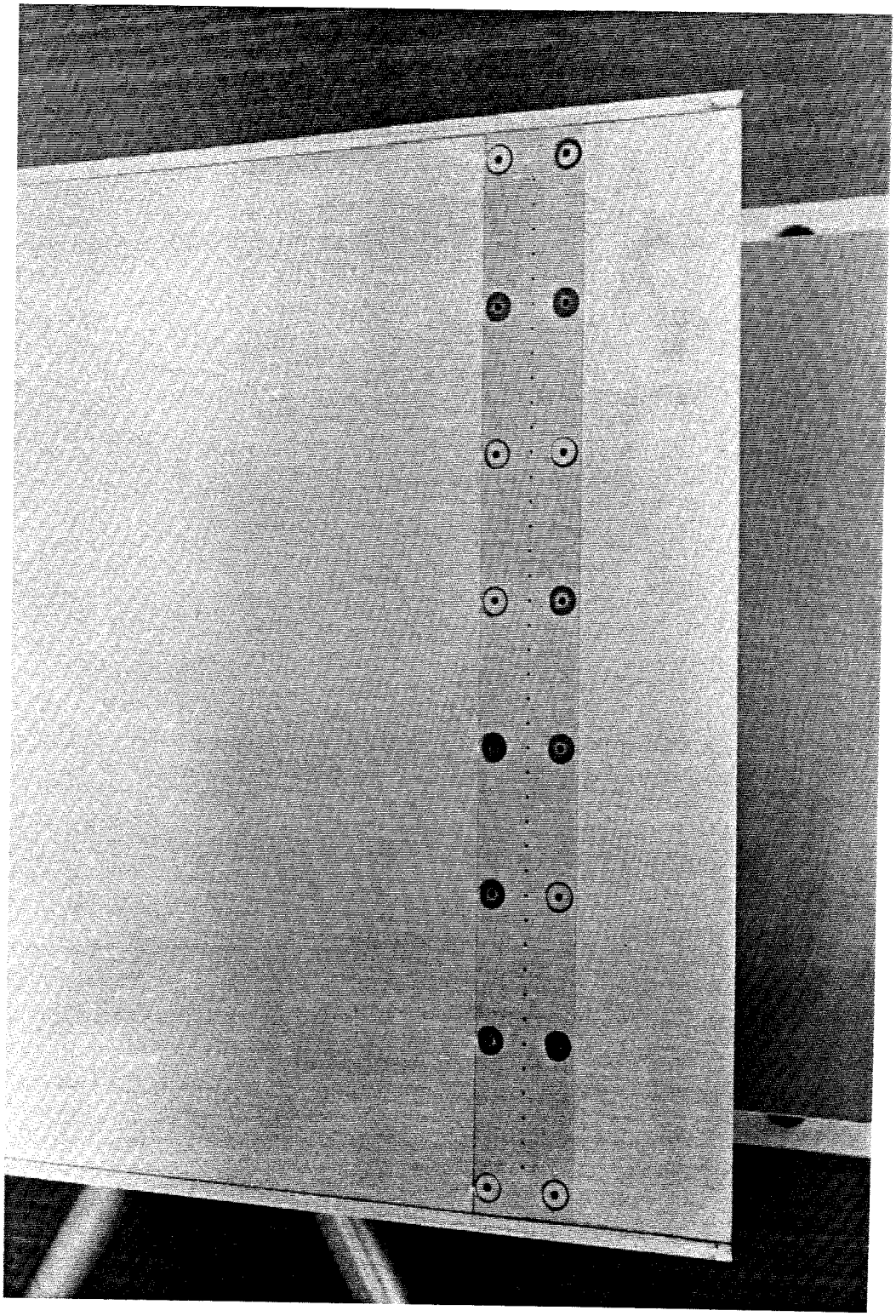

Figure 9. Photograph of the boundary layer trip plate.

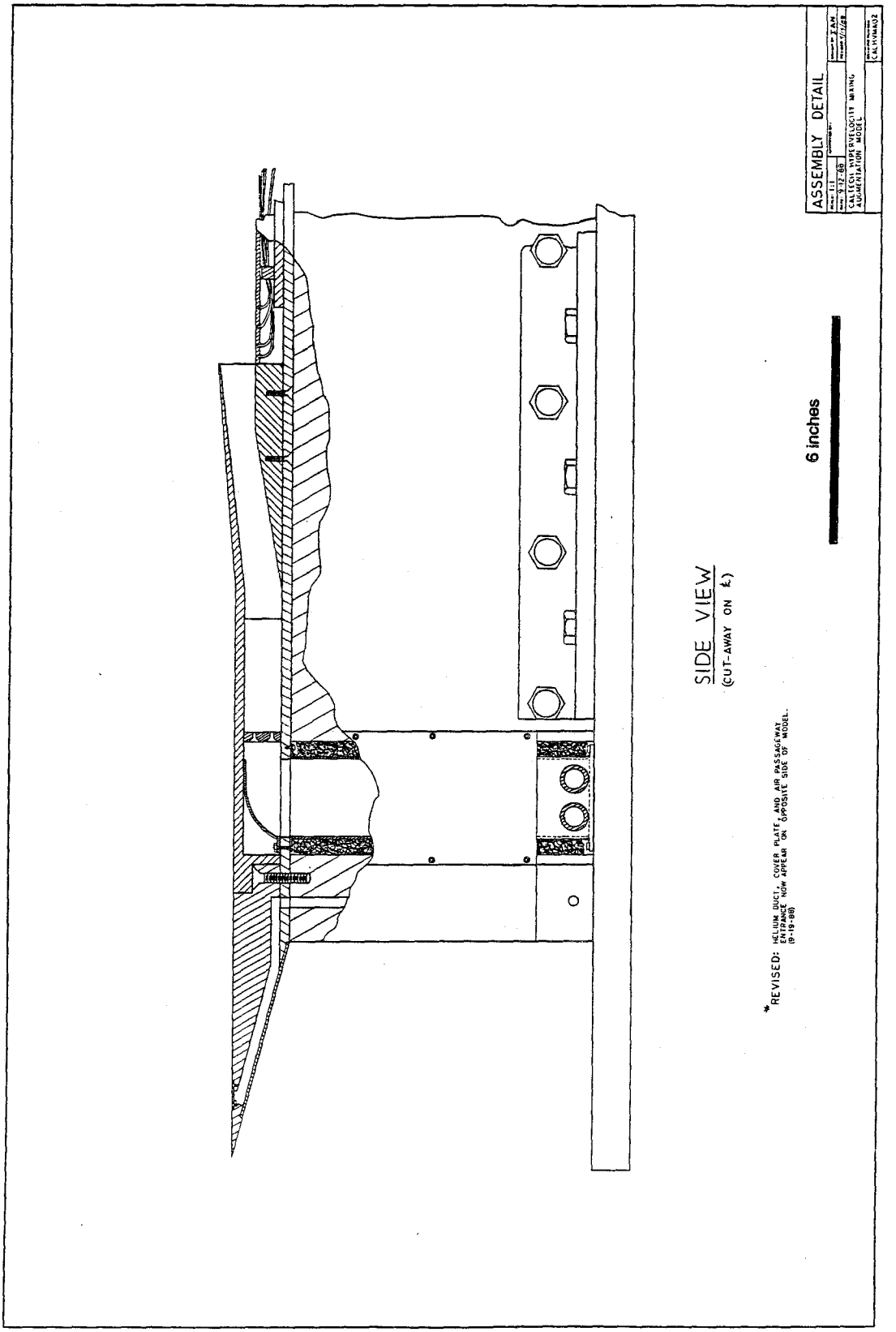

Figure 10. Cross-section view of injector region.

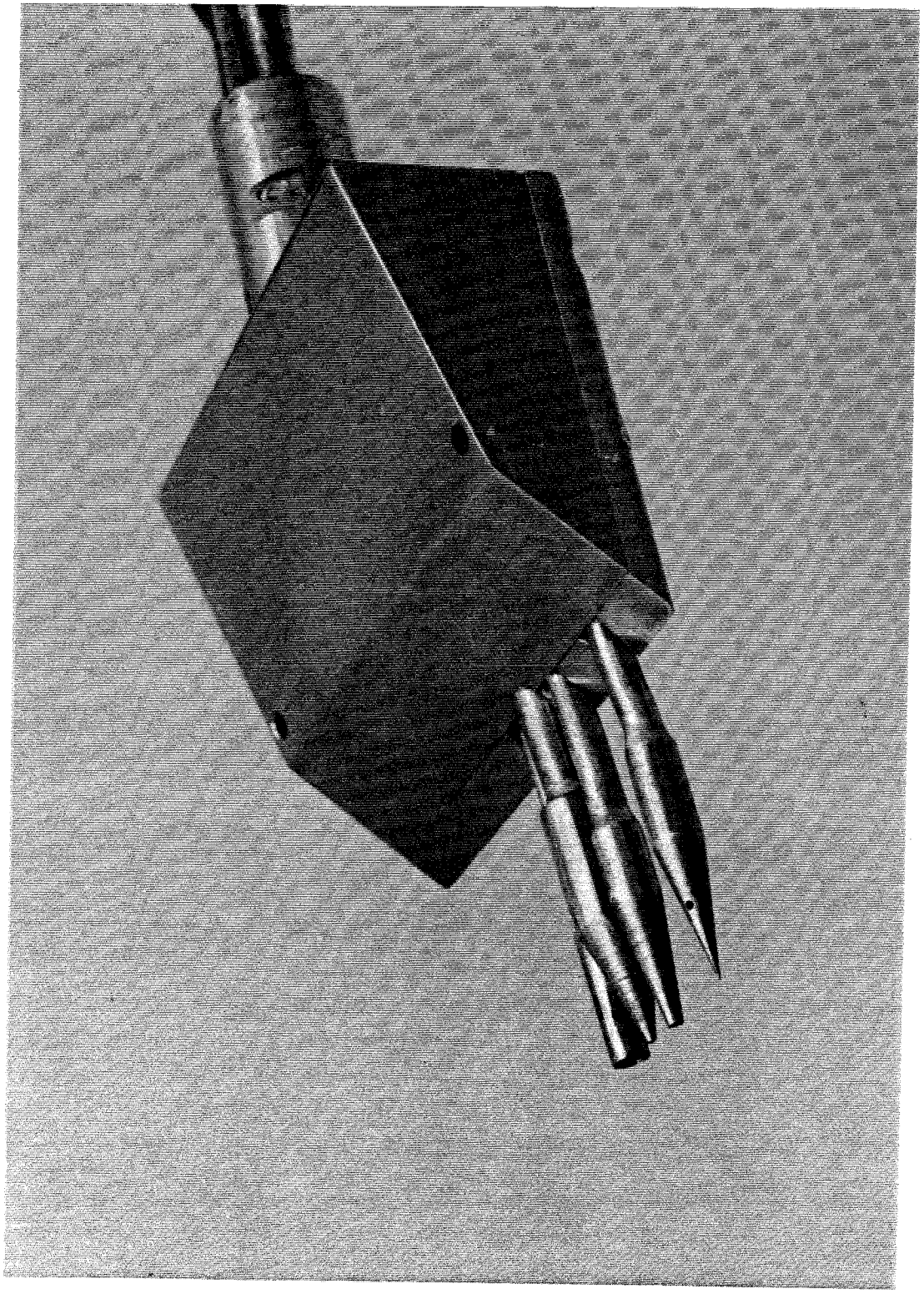

Figure 11. Photograph of flow-field survey probes. (Shown at approximately twice actual size.)

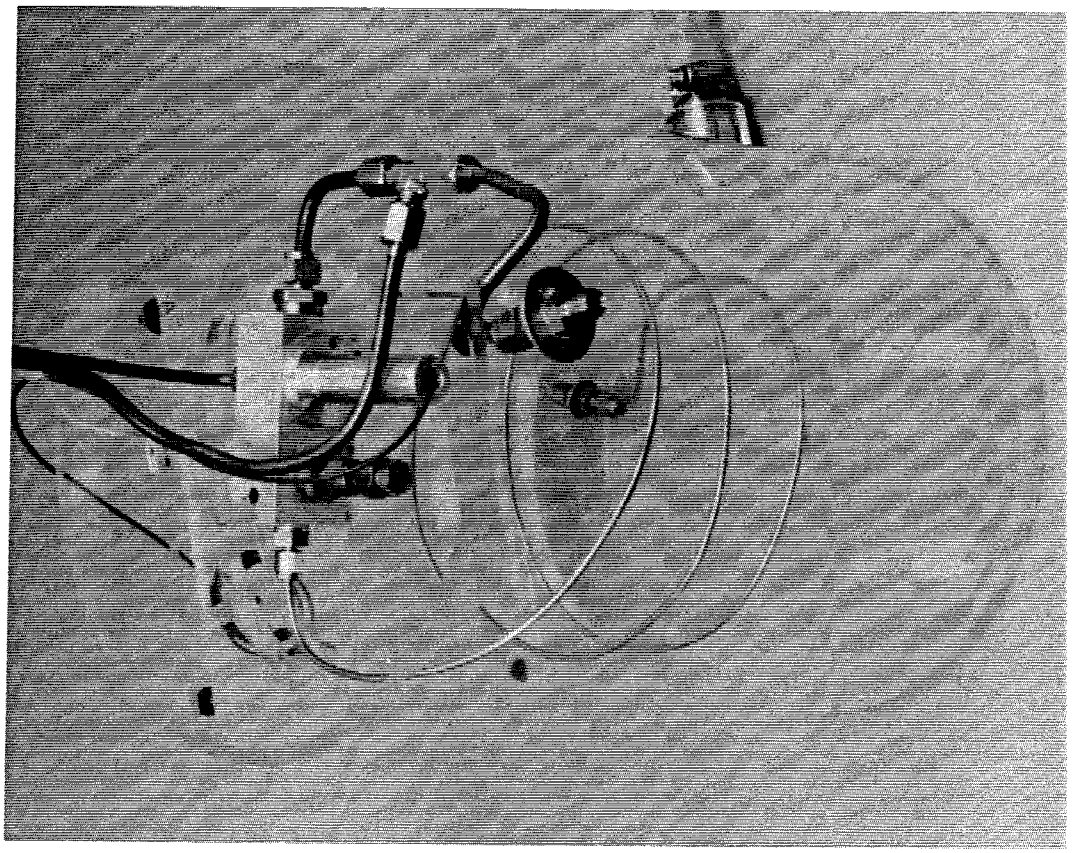

Figure 13. Photograph of gas composition analyzer.

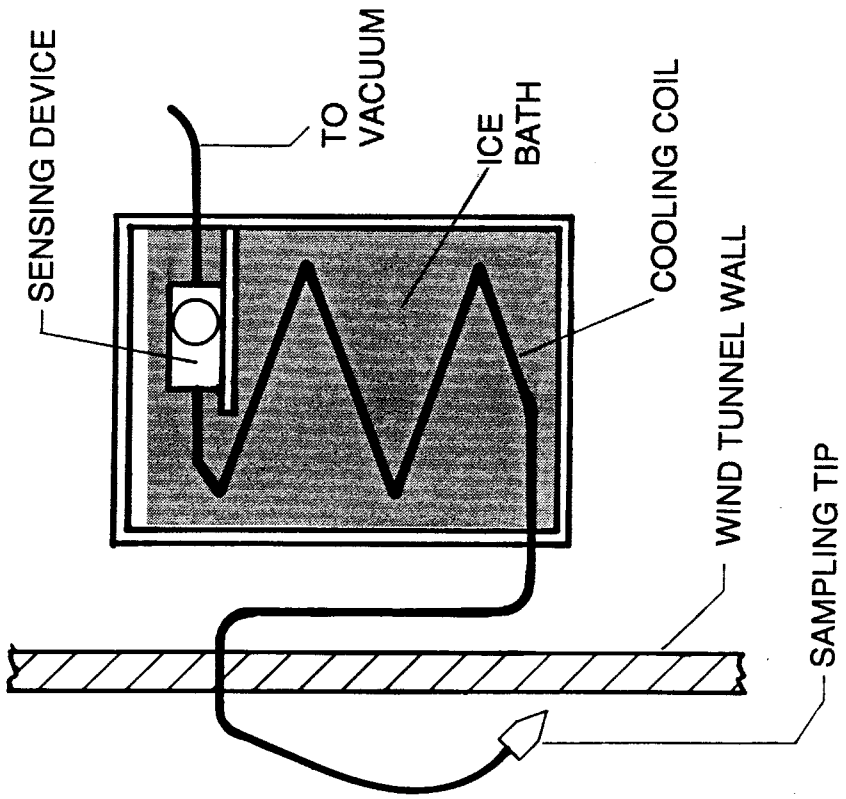

Figure 12. Schematic of gas composition analyzer.

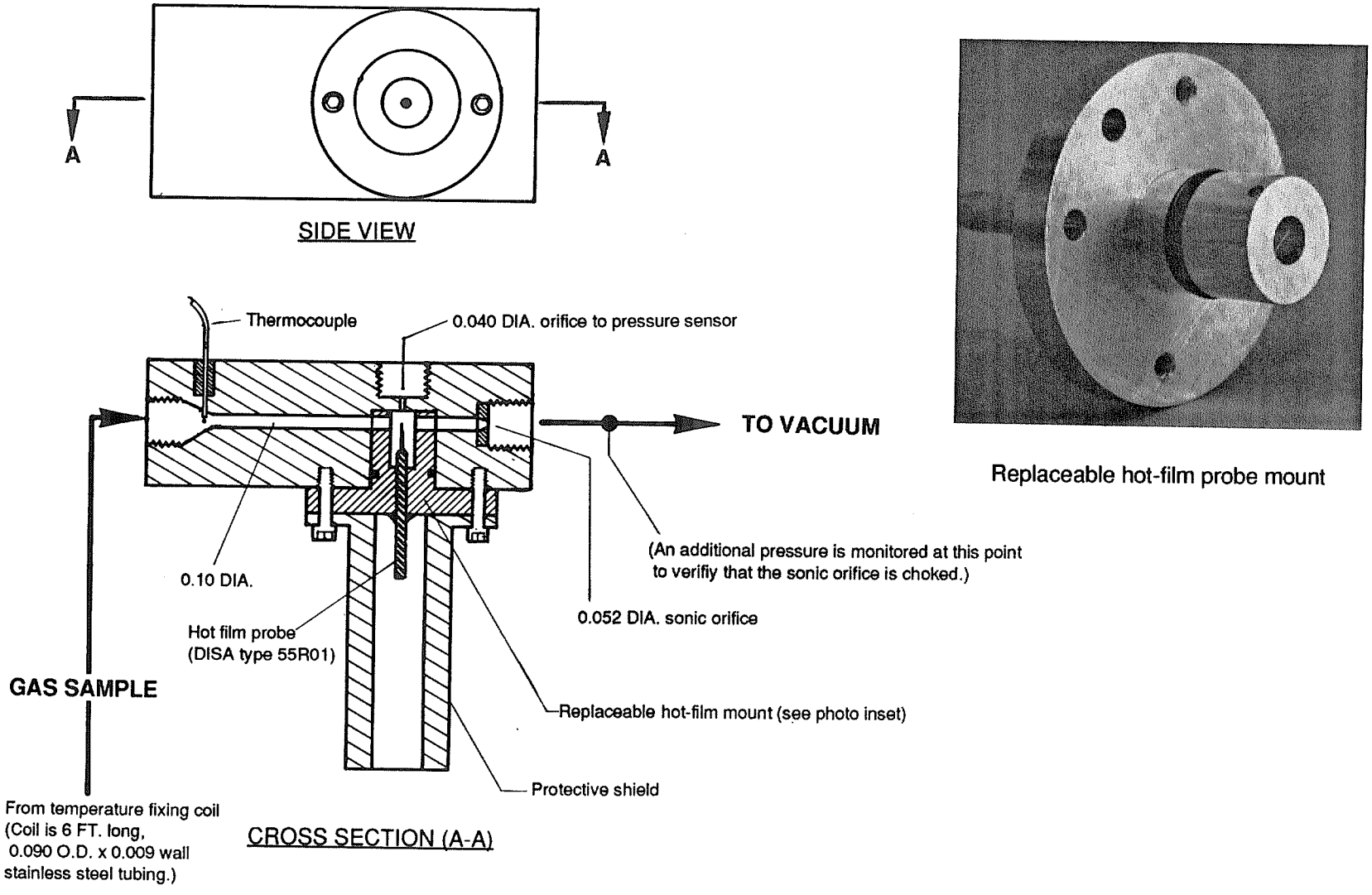

Figure 14. Gas composition analyzer sensing device.

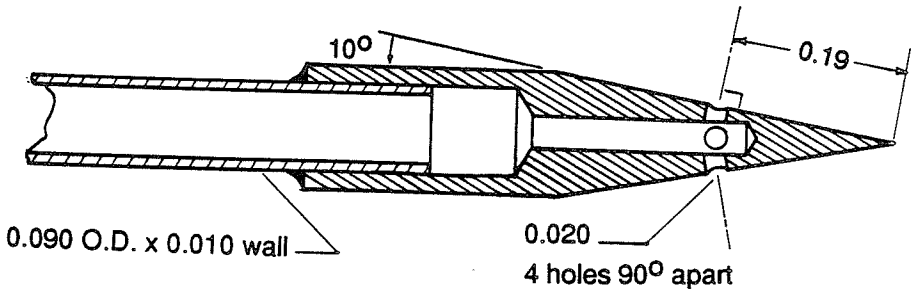

a. Cone static pressure probe.

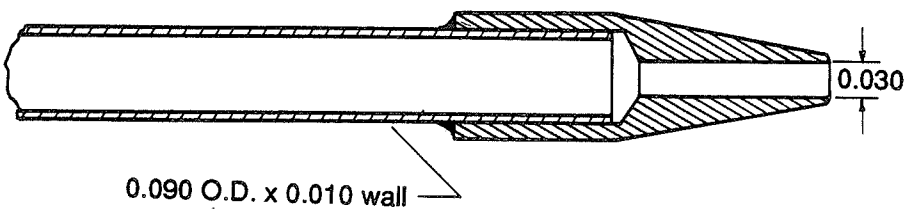

b. Pitot pressure probe.

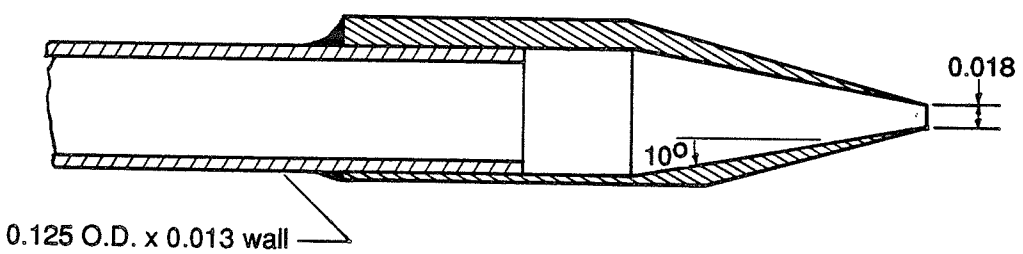

c. Gas composition probe.

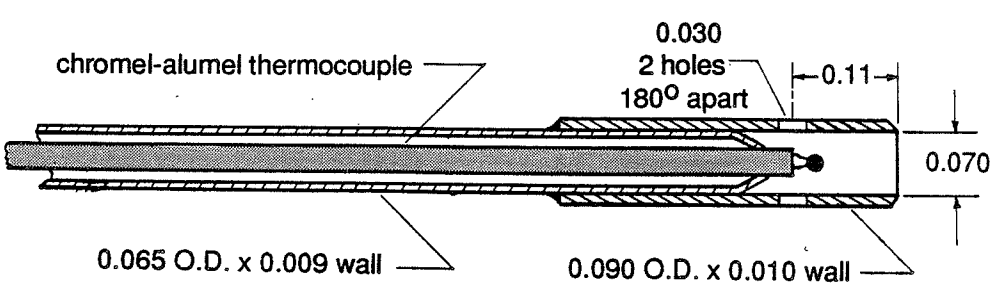

d. Total temperature probe.

Figure 15. Flow field survey probes.

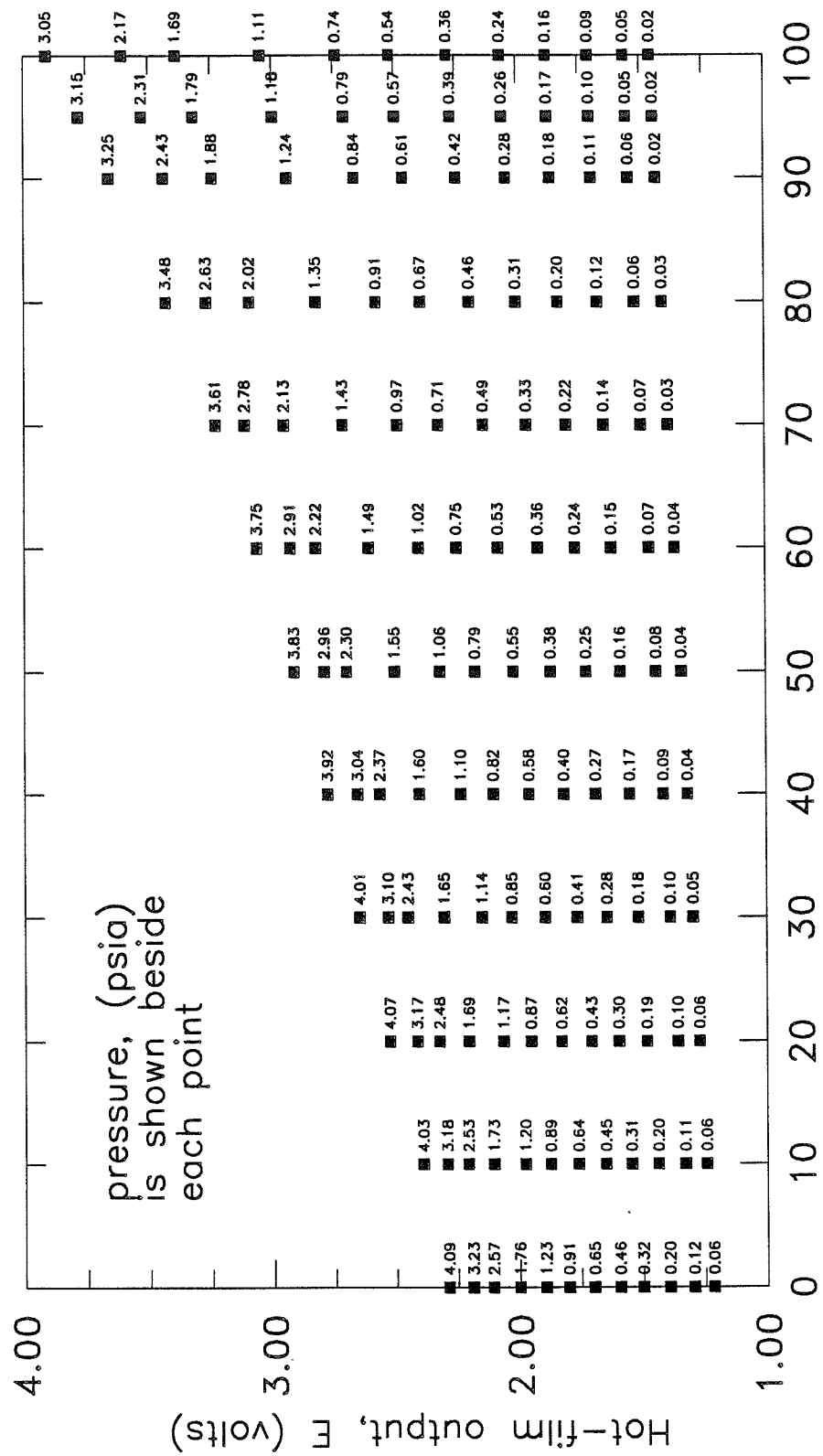

Figure 16. Sample of the calibration data from the gas composition analyzer.

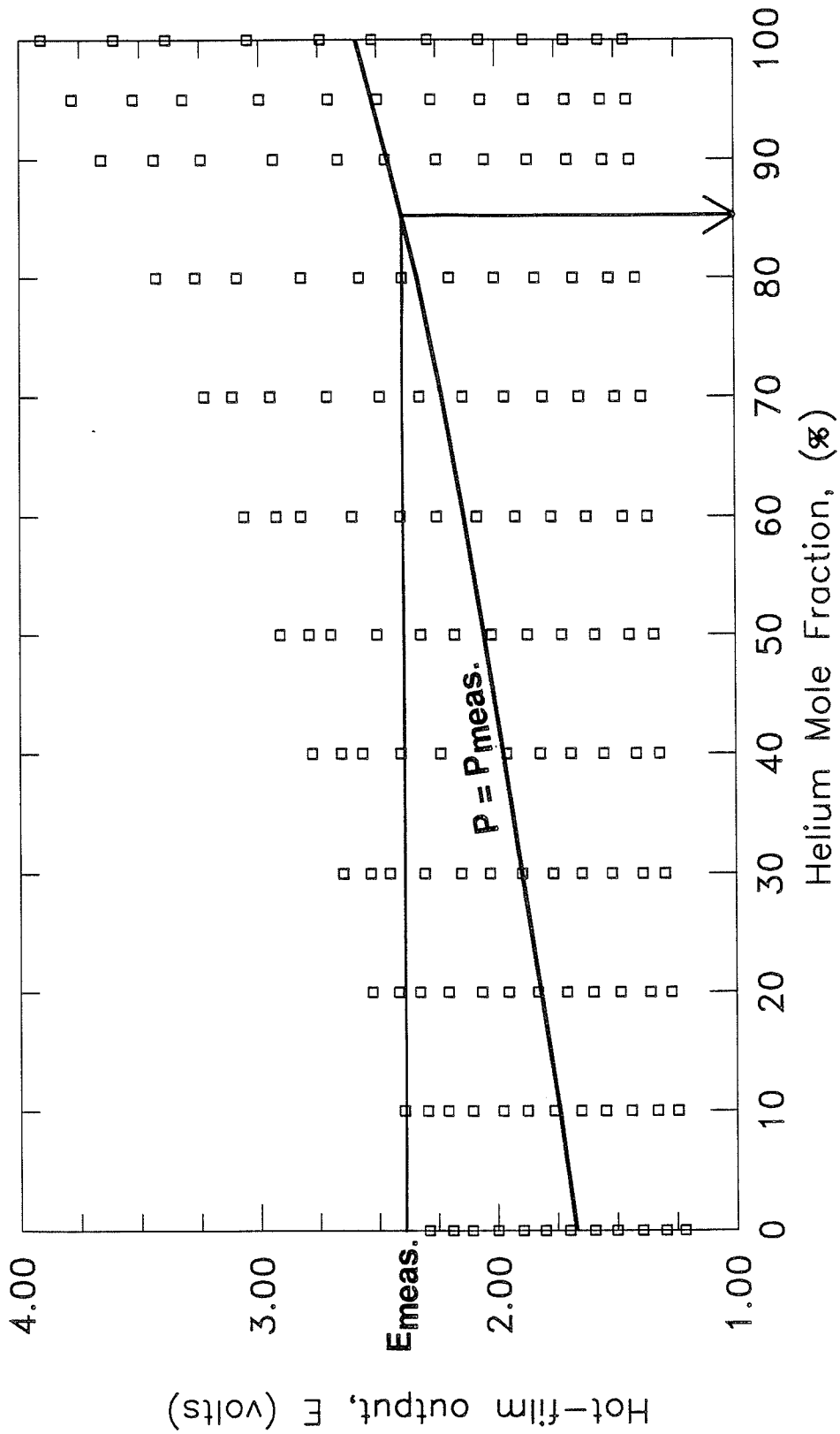

Figure 17. Gas composition analyzer interpolation technique.

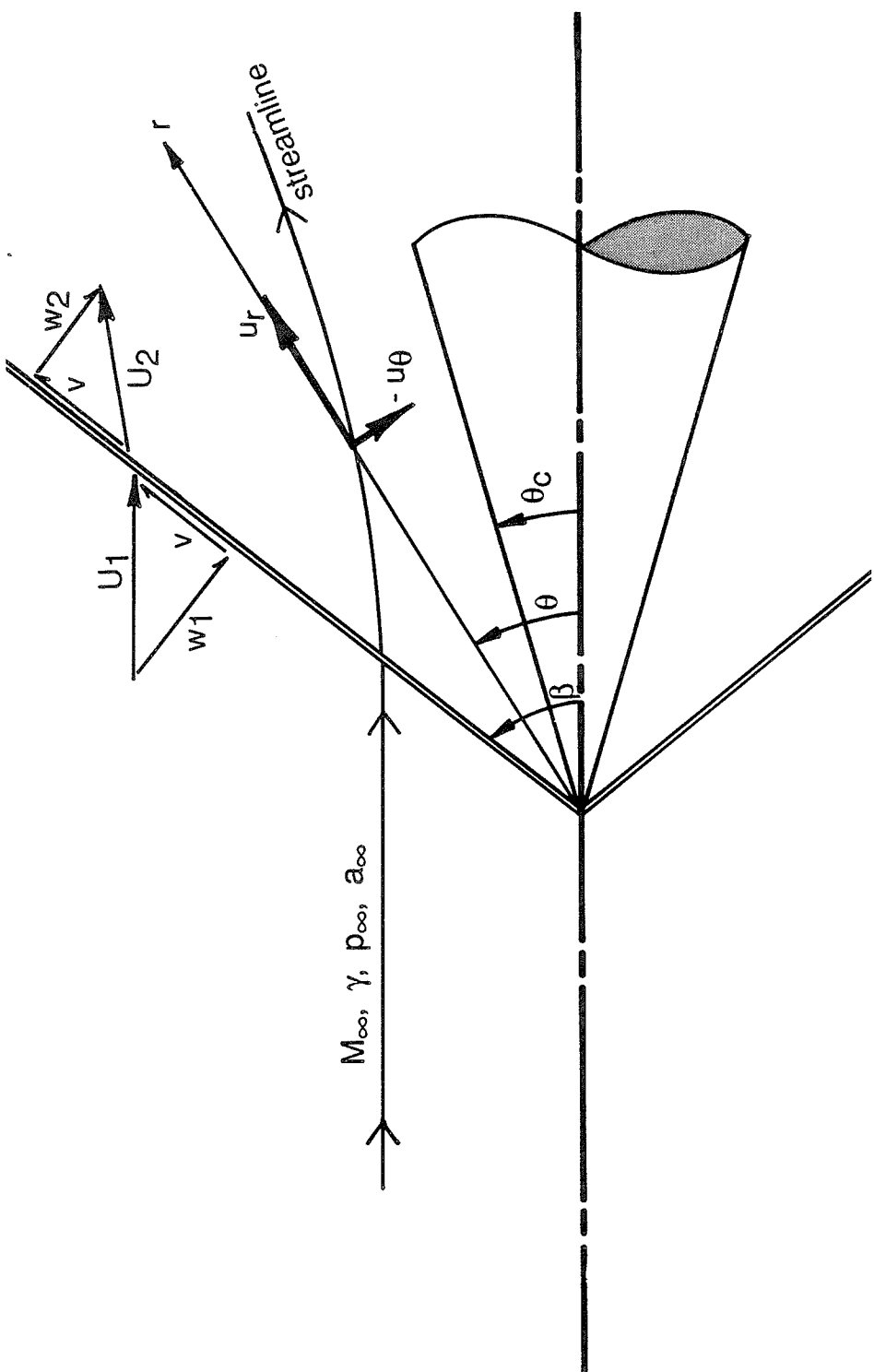

Figure 18. Conical flow coordinate system and variables.

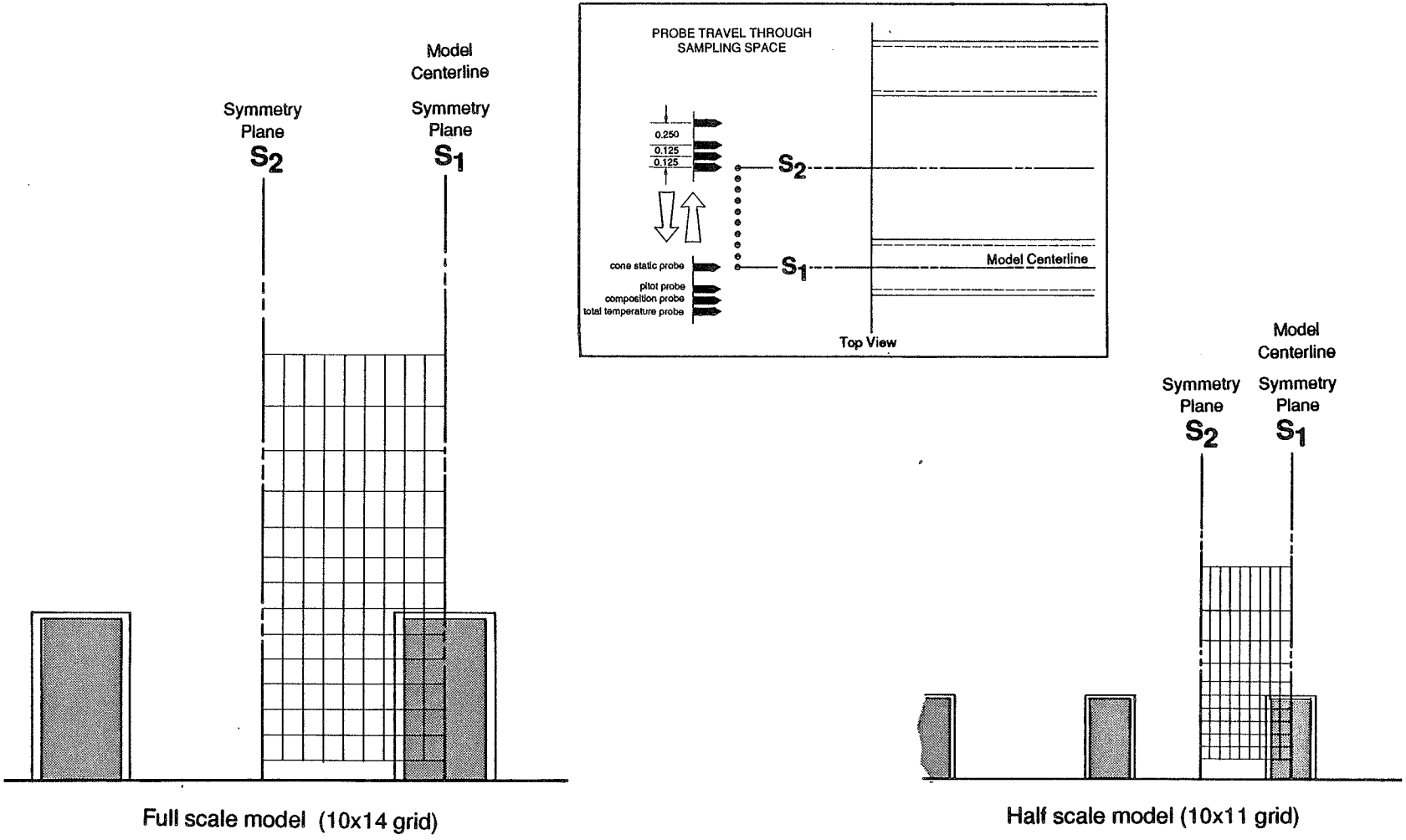

Figure 19. Experimental sampling grids, (scale 1:1).

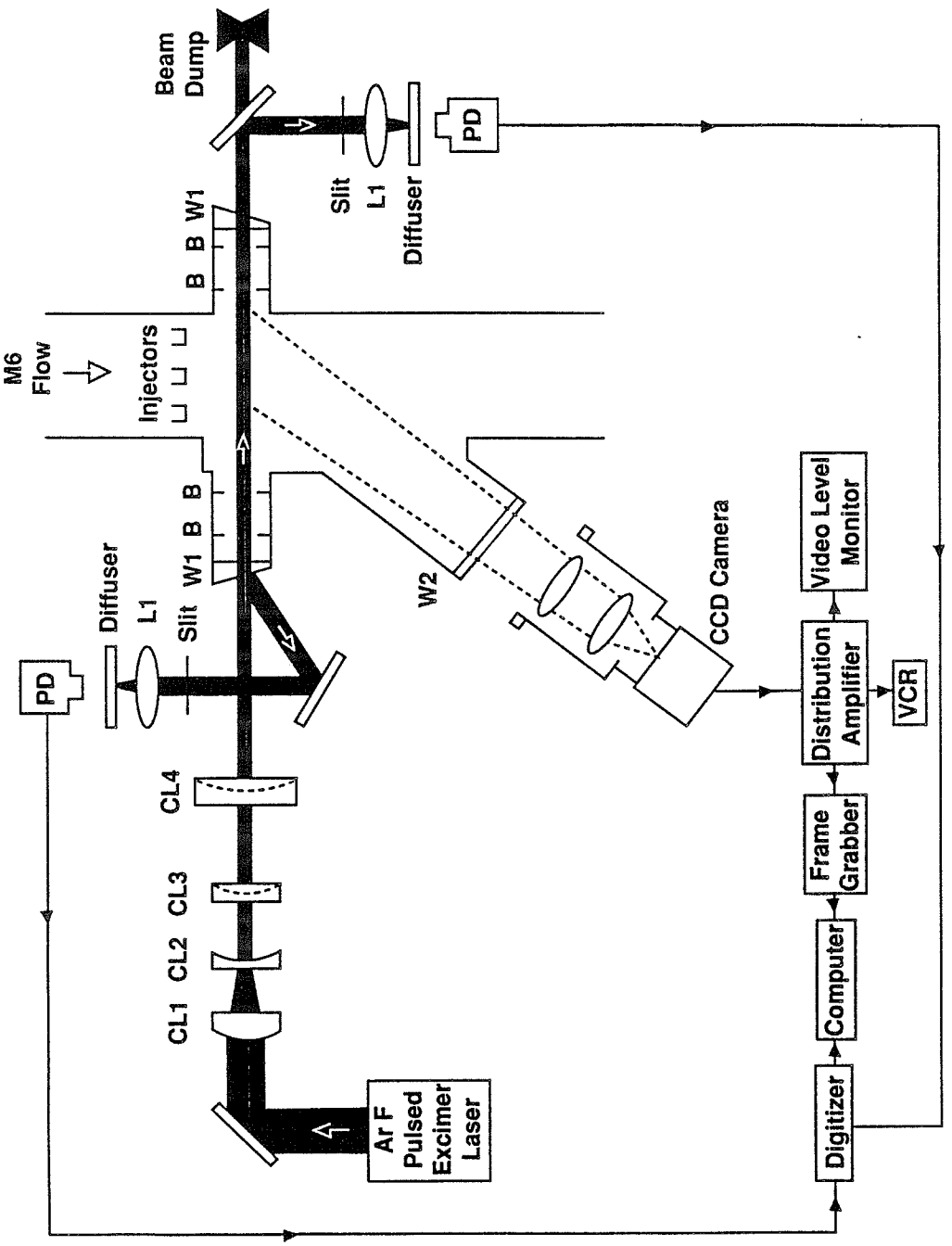

Figure 20. Planar Rayleigh scattering experimental set-up. (Courtesy NASA Langley Research Center)

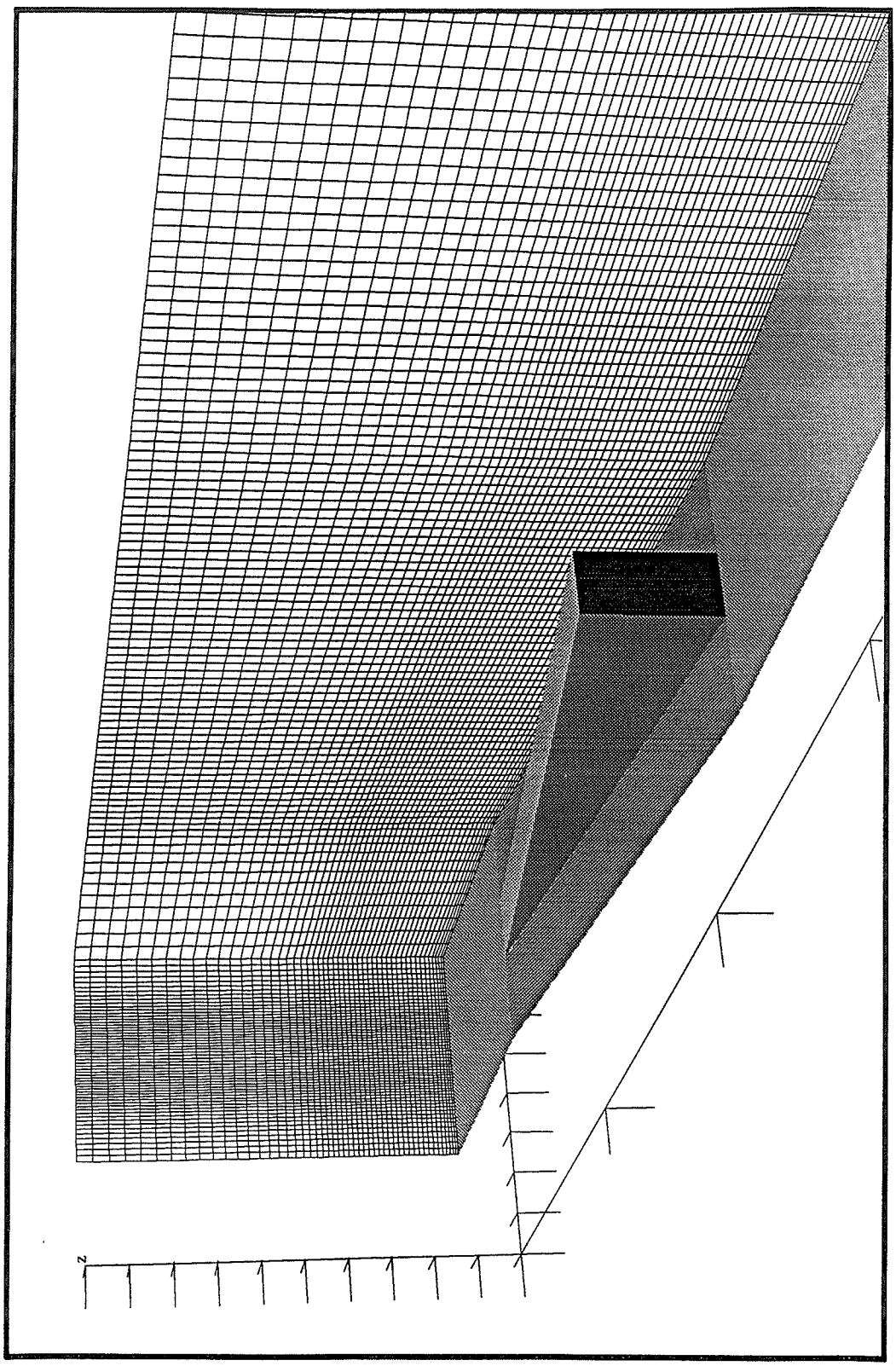

Figure 21. Computational grid for wide spacing, $\alpha_e = \alpha_c = 4.76^o$ geometry

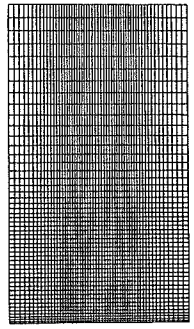

a. Cross-flow plane (doubled over about symmetry plane), $\overline{y}$ = -1 to 1, $\overline{z}$ = 0 to 4

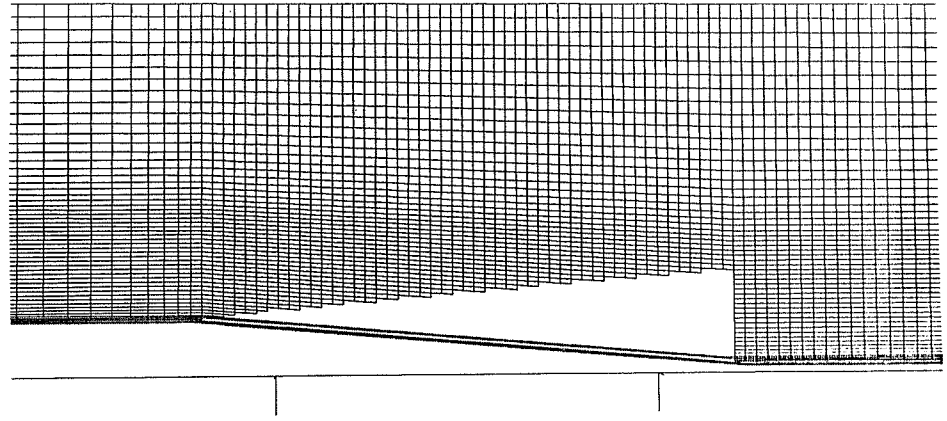

b. Injector grid blanking detail

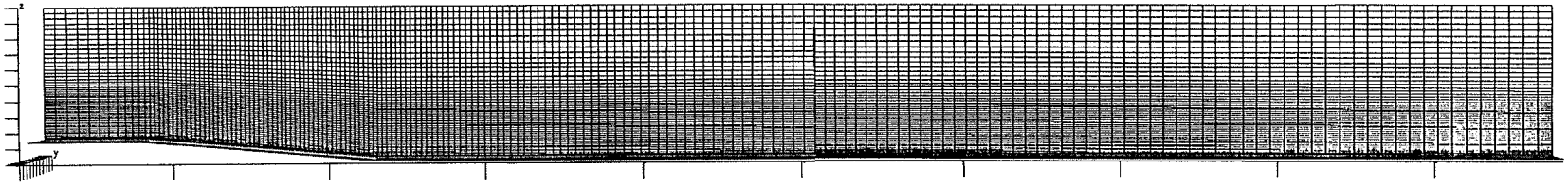

c. Longitudinal plane, $\overline{x}$ = -9 to $\overline{x}$ = 30

Figure 22. Computational grid for wide injector spacing geometries: 175 x 29 x 51 (a. b. and c. are shown on different scales)

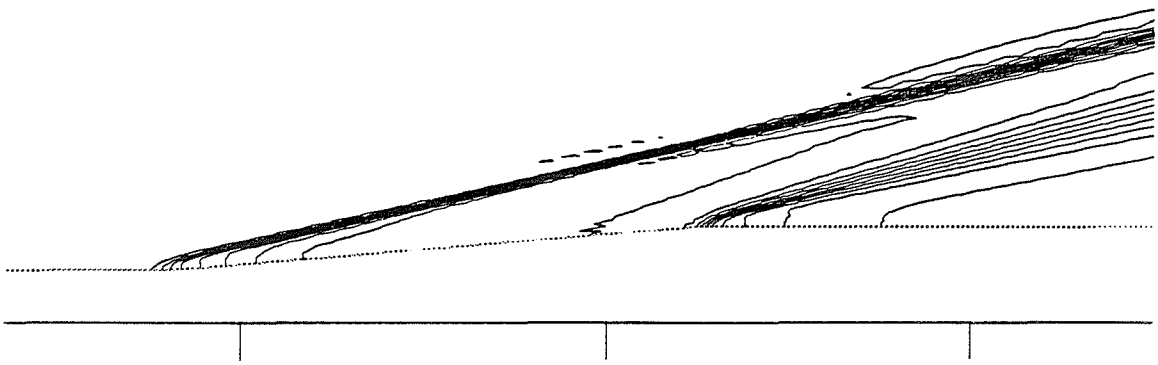

Figure 23. Shock development for two-dimensional smooth grid edge.

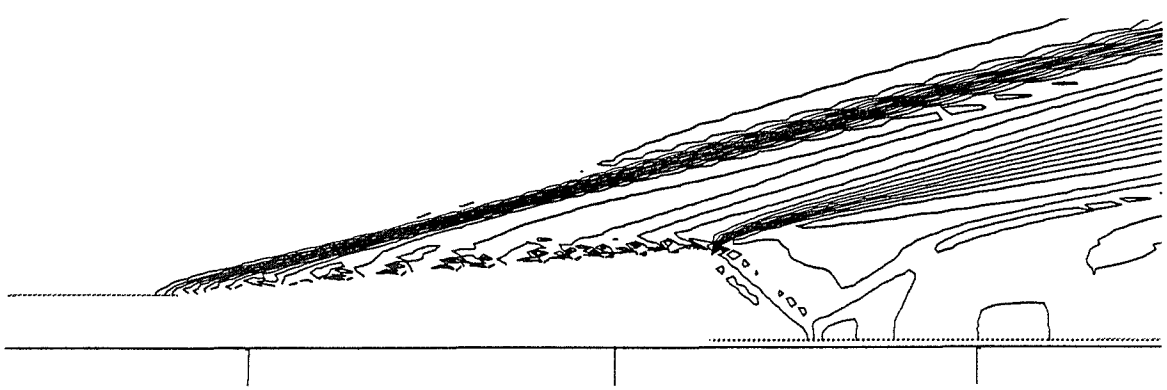

Figure 24. Shock development for two-dimensional rough grid edge.

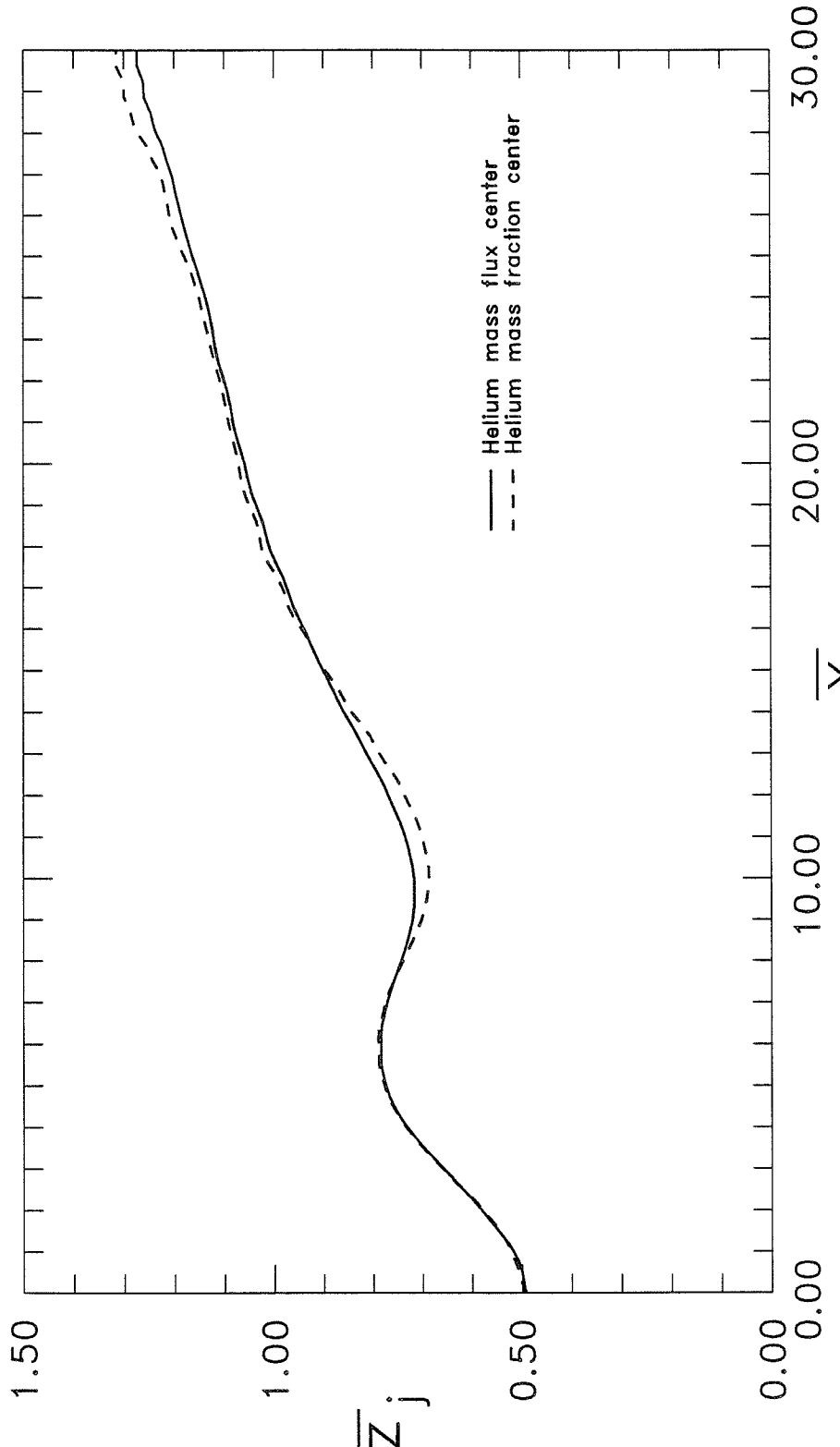

Figure 25. Comparison of calculation methods for jet lift-off height. Wide spacing, $\overline{\delta} = 0.20$, $\overline{p} = 1.0$, $\overline{v} = 1.0$, $\alpha_c = \alpha_e = 4.76^o$ (computational).

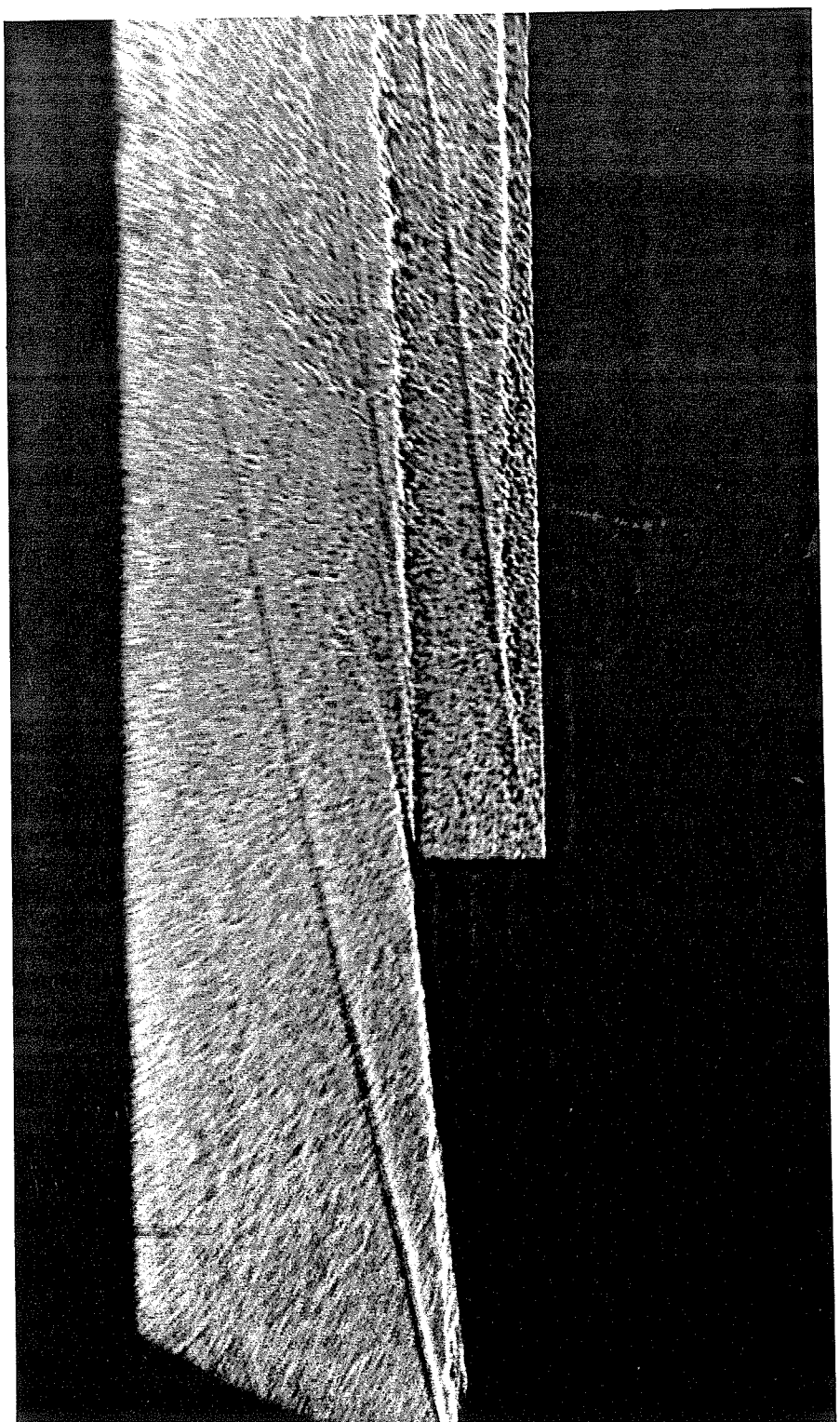

Figure 26. Shadowgraph of injector flowfield. Wide spacing, $\bar{\delta} = 0.20$, $\bar{p} = 1.0$, $\bar{v} = 1.33$, $\alpha_c = \alpha_e = 4.76^o$

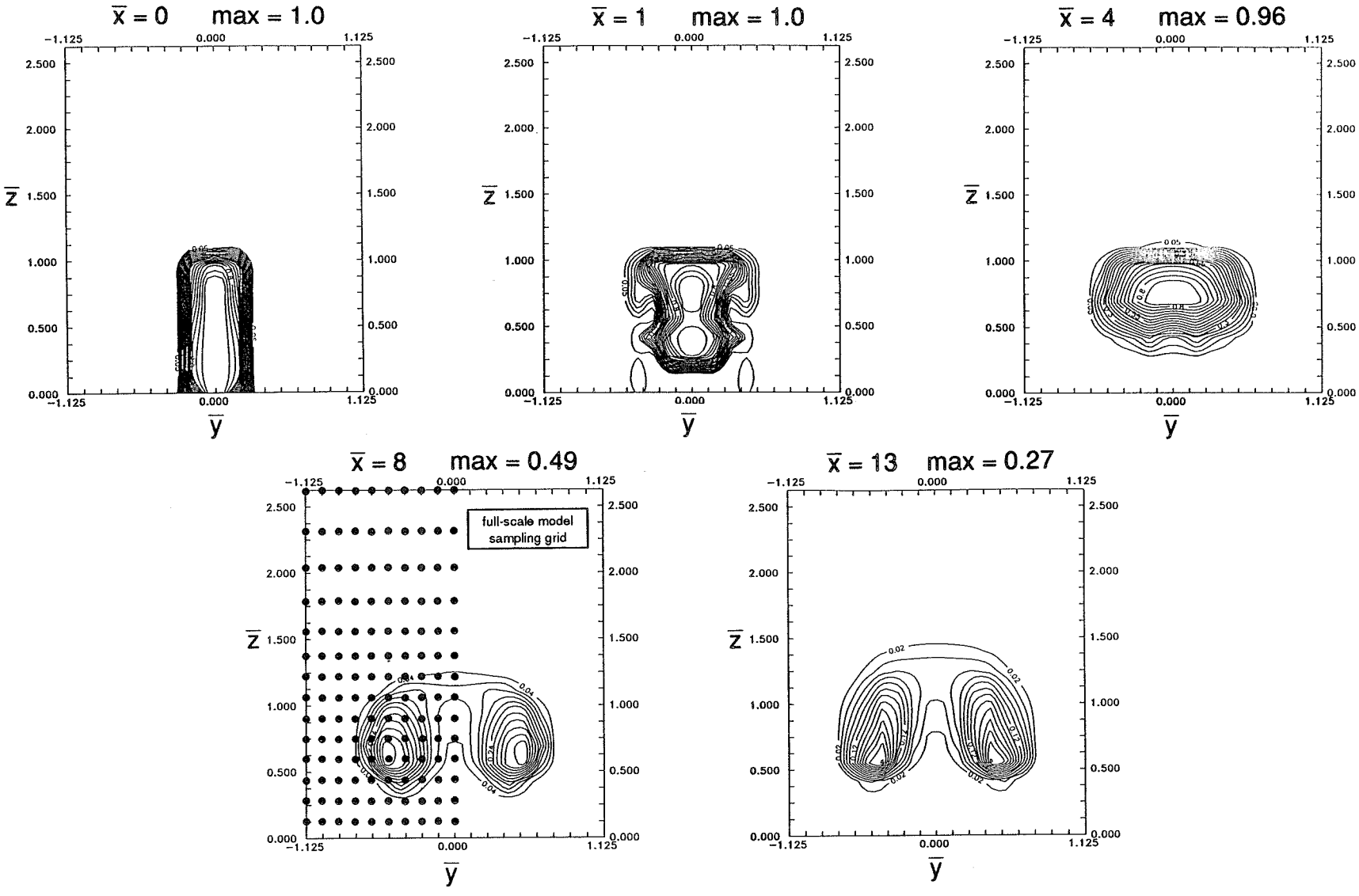

Figure 27. Helium mass fraction. Full-scale model, wide spacing, natural boundary layer, $\bar{\delta} = 0.20$, $\bar{p} = 1.0$, $\bar{v} = 1.33$ (experimental).

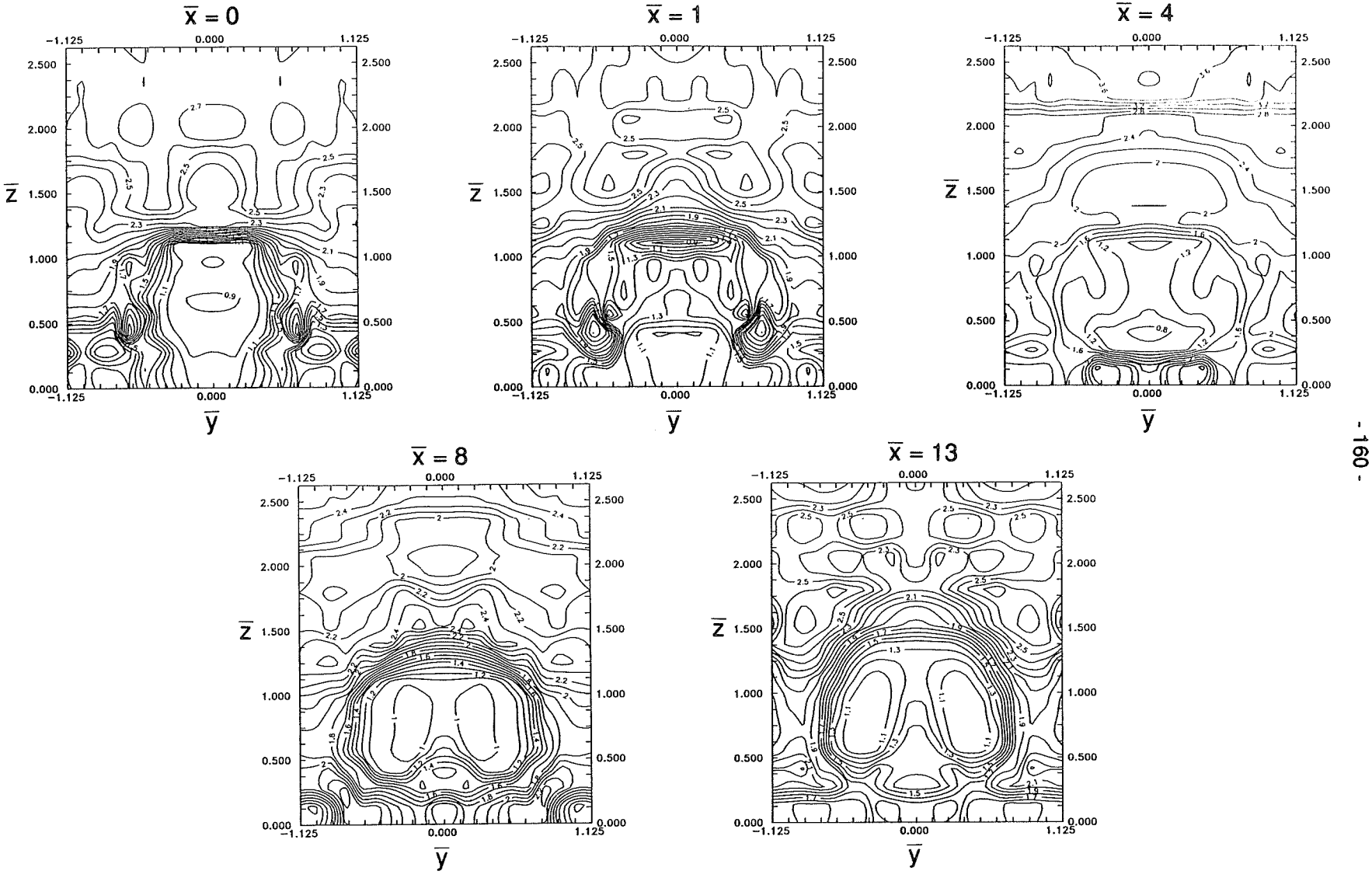

Figure 28. Cone static pressure (psia). Full-scale model, wide spacing, natural boundary layer, $\bar{\delta} = 0.20$, $\bar{p} = 1.0$, $\bar{v} = 1.33$ (experimental).

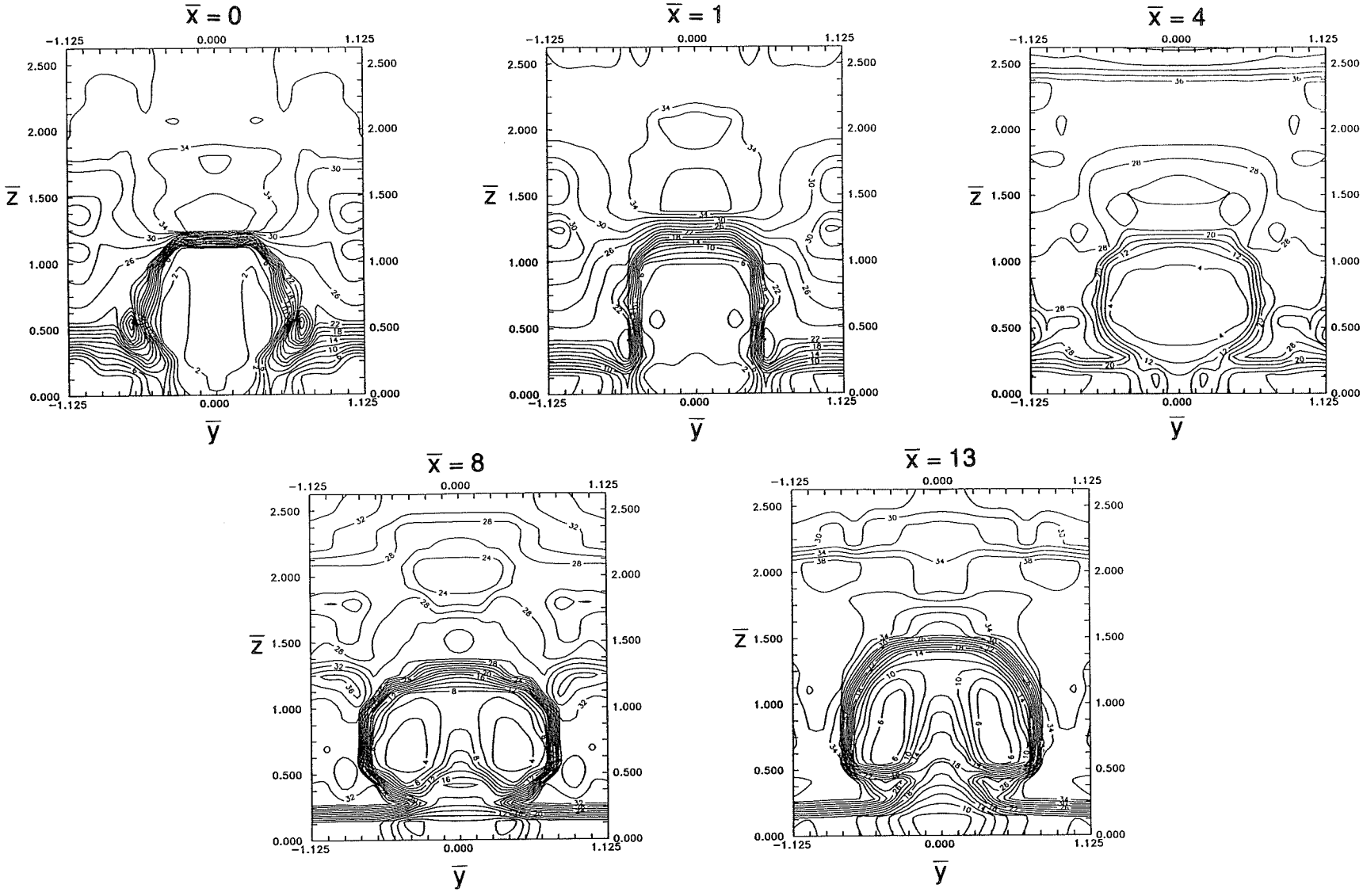

Figure 29. Pitot pressure (psia). Full-scale model, wide spacing, natural boundary layer, $\bar{\delta} = 0.20$, $\bar{p} = 1.0$, $\bar{v} = 1.33$ (experimental).

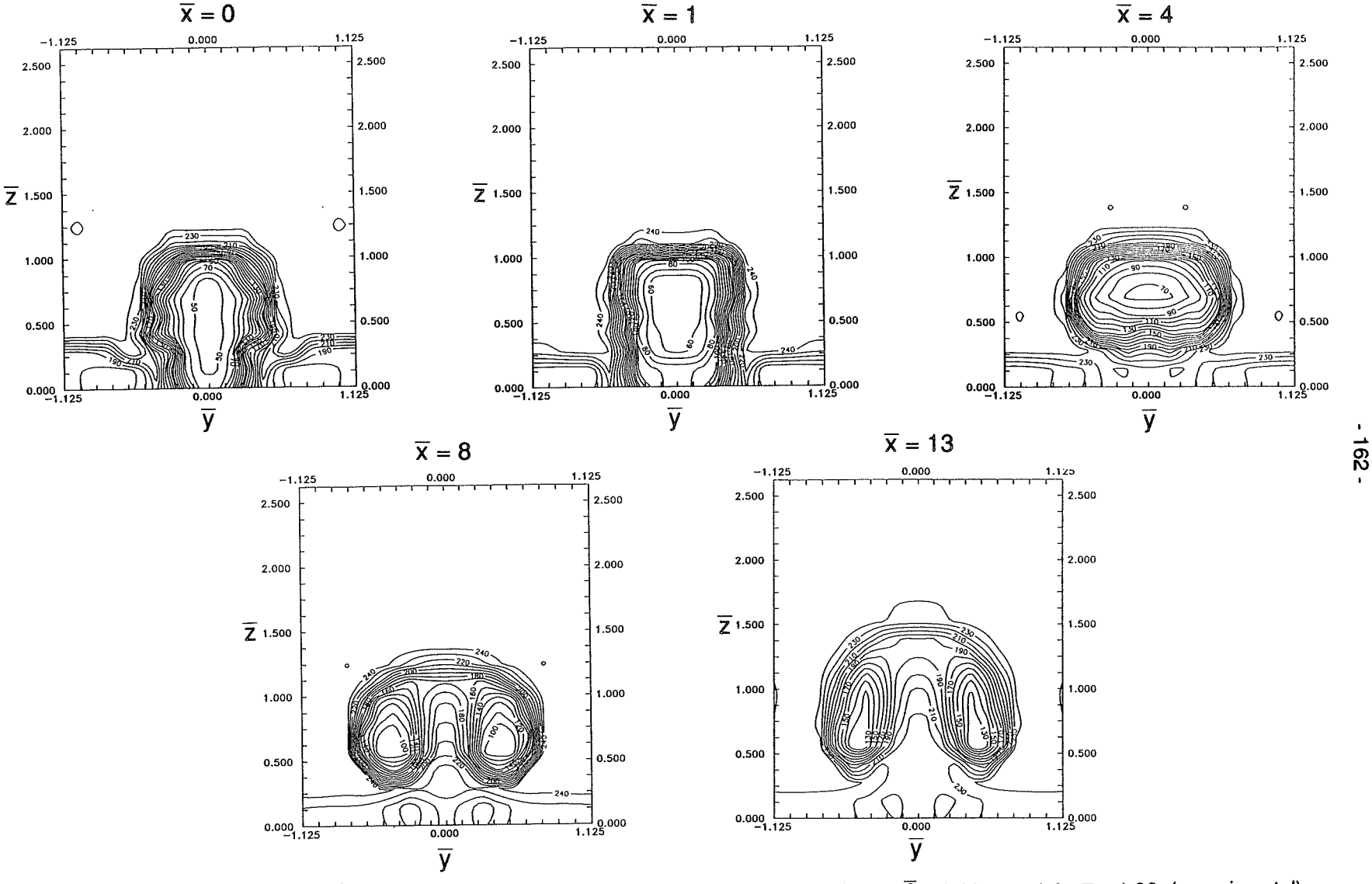

Figure 30. Total temperature (^{o}C). Full-scale model, wide spacing, natural boundary layer, $\bar{\delta} = 0.20$, $\bar{p} = 1.0$, $\bar{v} = 1.33$ (experimental).

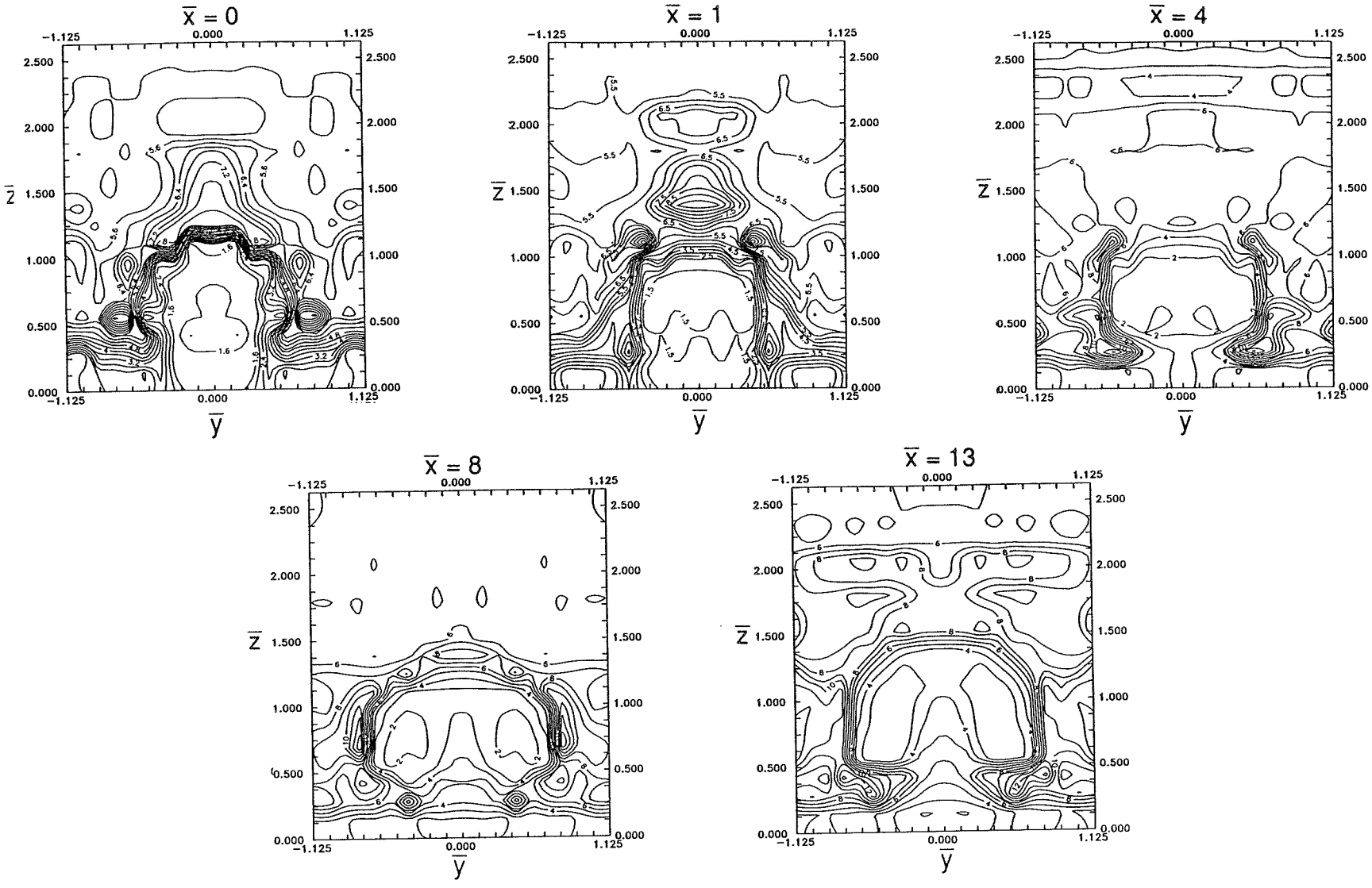

Figure 31. Mach number. Full-scale model, wide spacing, natural boundary layer, $\bar{\delta} = 0.20$, $\bar{p} = 1.0, \bar{v} = 1.33$ (experimental).

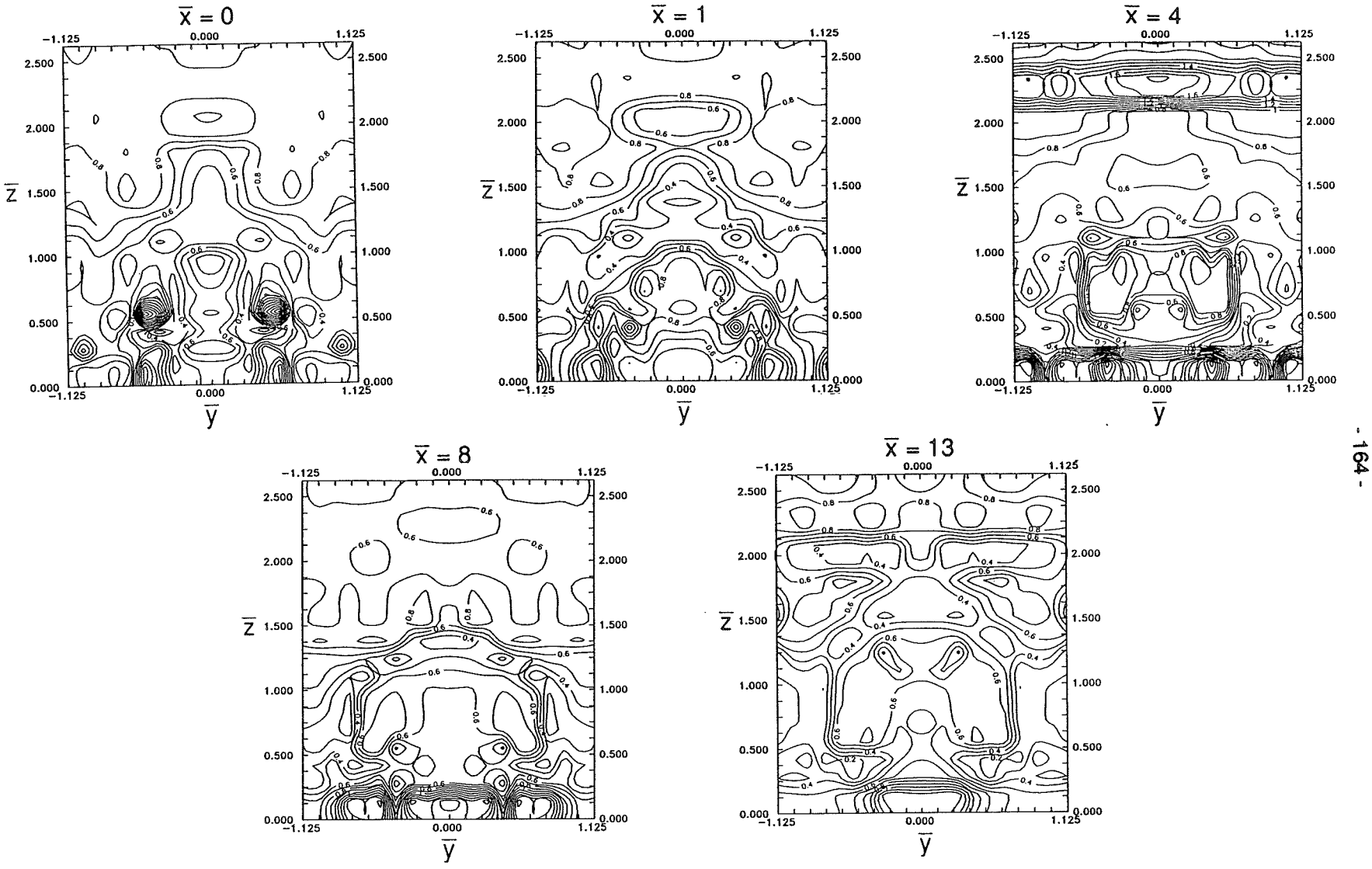

Figure 32. Static pressure (psia). Full-scale model, wide spacing, natural boundary layer, $\bar{\delta} = 0.20$, $\bar{p} = 1.0, \bar{v} = 1.33$ (experimental).

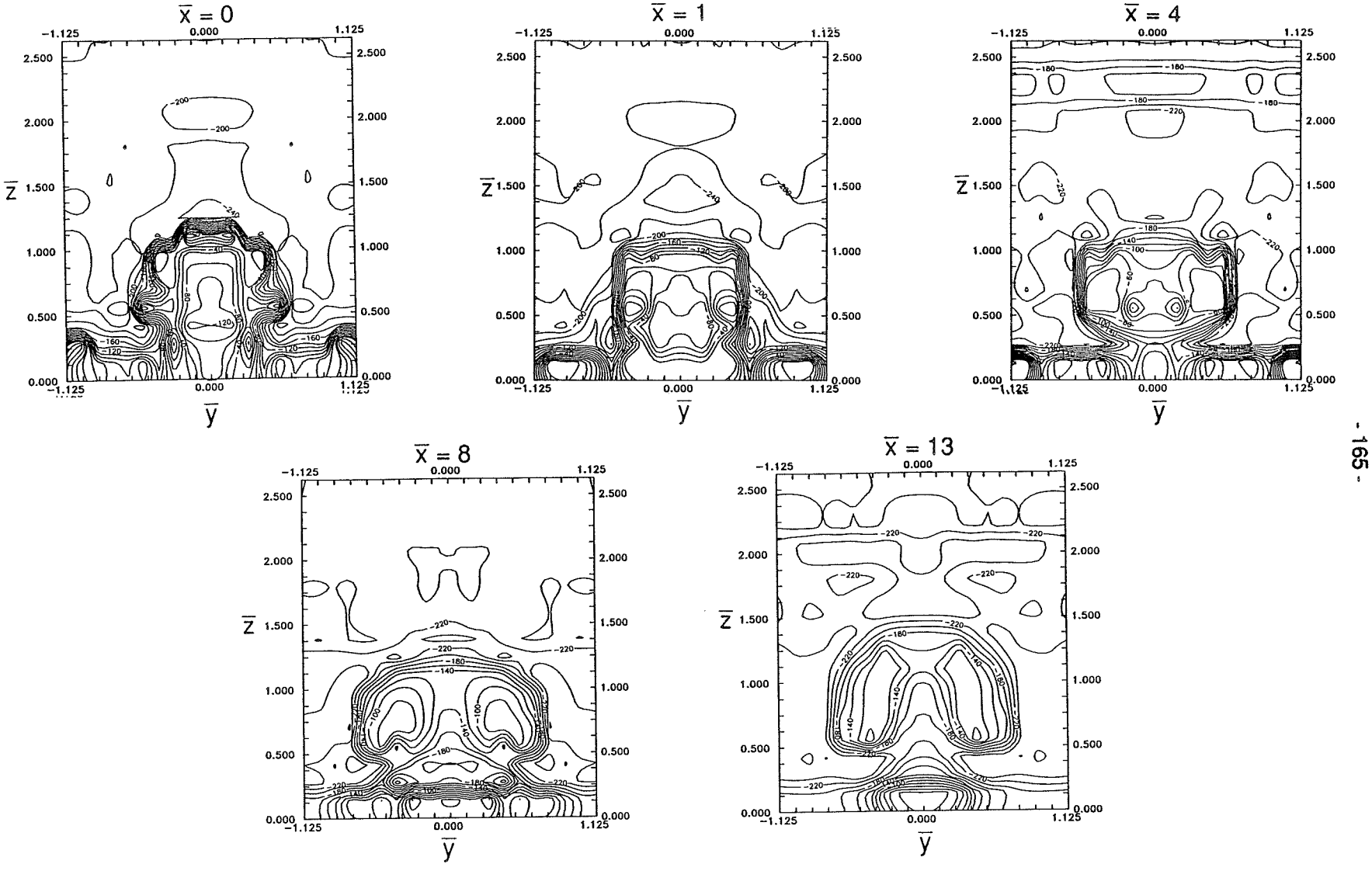

Figure 33. Static temperature (^{o}C). Full-scale model, wide spacing, natural boundary layer, $\bar{\delta} = 0.20$, $\bar{p} = 1.0, \bar{v} = 1.33$ (experimental).

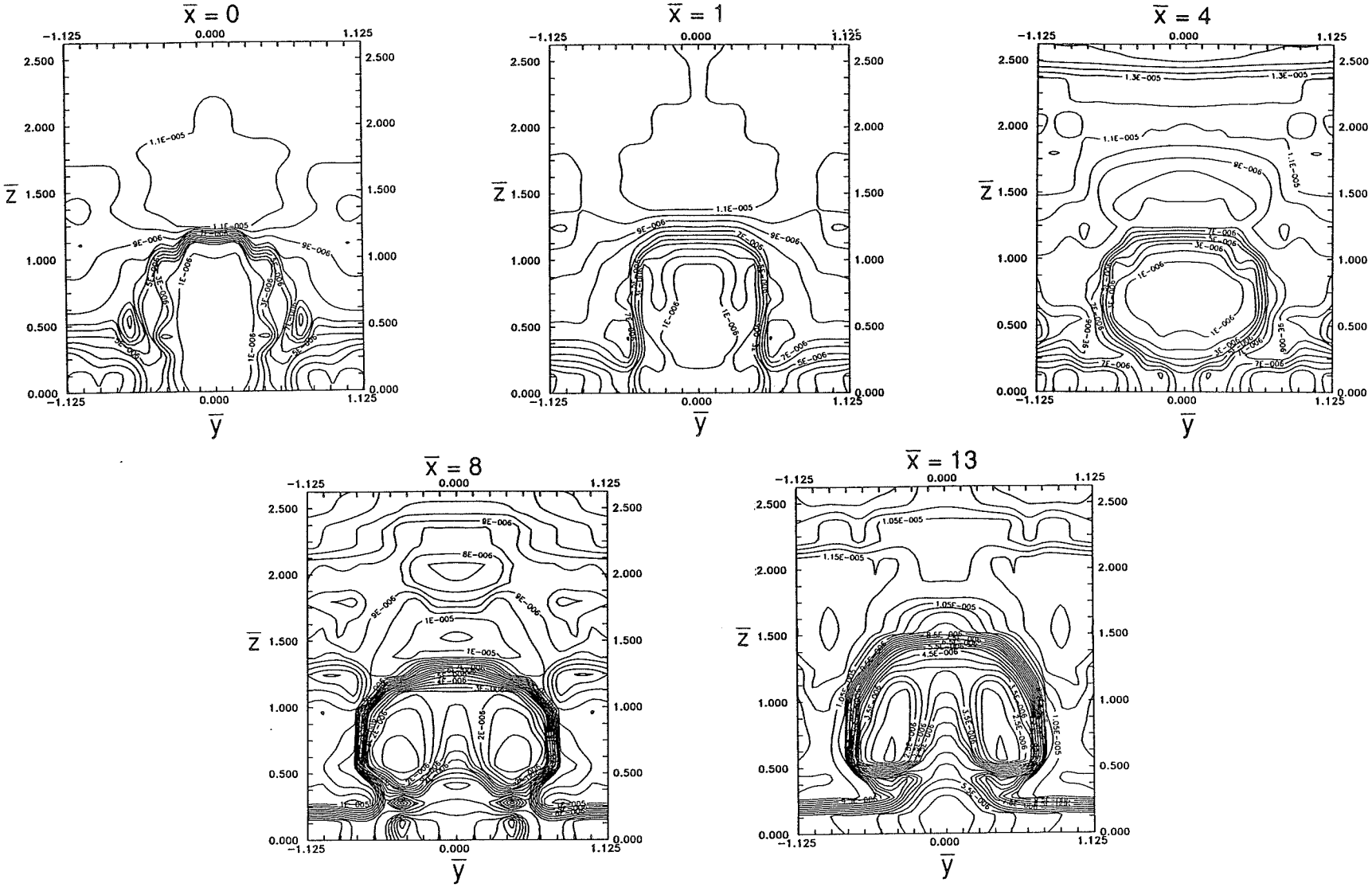

Figure 34. Density (lbm/in^3). Full-scale model, wide spacing, natural boundary layer, $\bar{\delta} = 0.20$, $\bar{p} = 1.0, \bar{v} = 1.33$ (experimental).

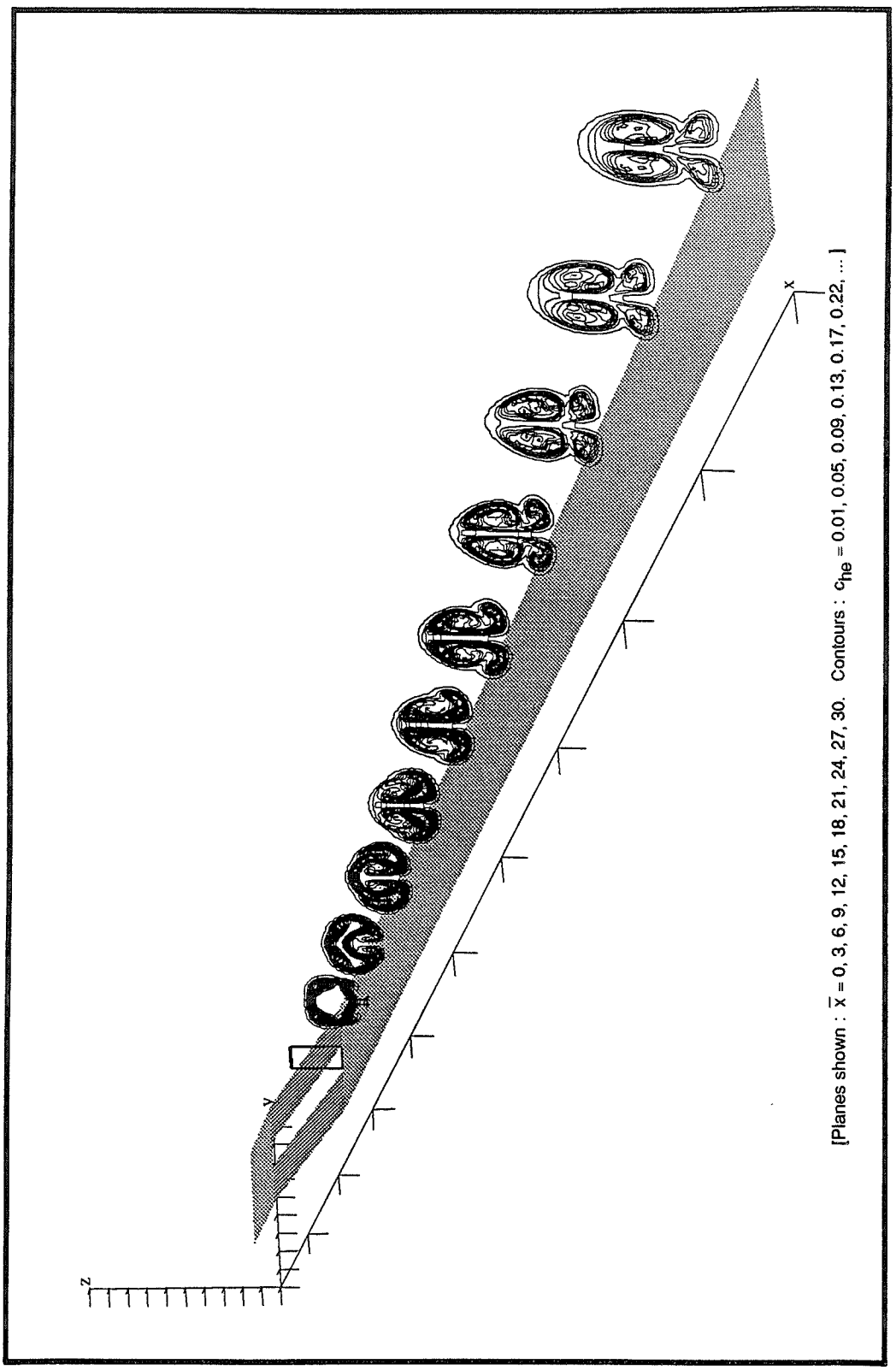

Figure 35. Contours of constant helium mass fraction.

Wide spacing, $\bar{\delta}$ = 0.20, $\bar{p}$ = 1.0, $\bar{v}$ = 1.0, $\alpha_c = \alpha_e = 4.76^o$ (computational).

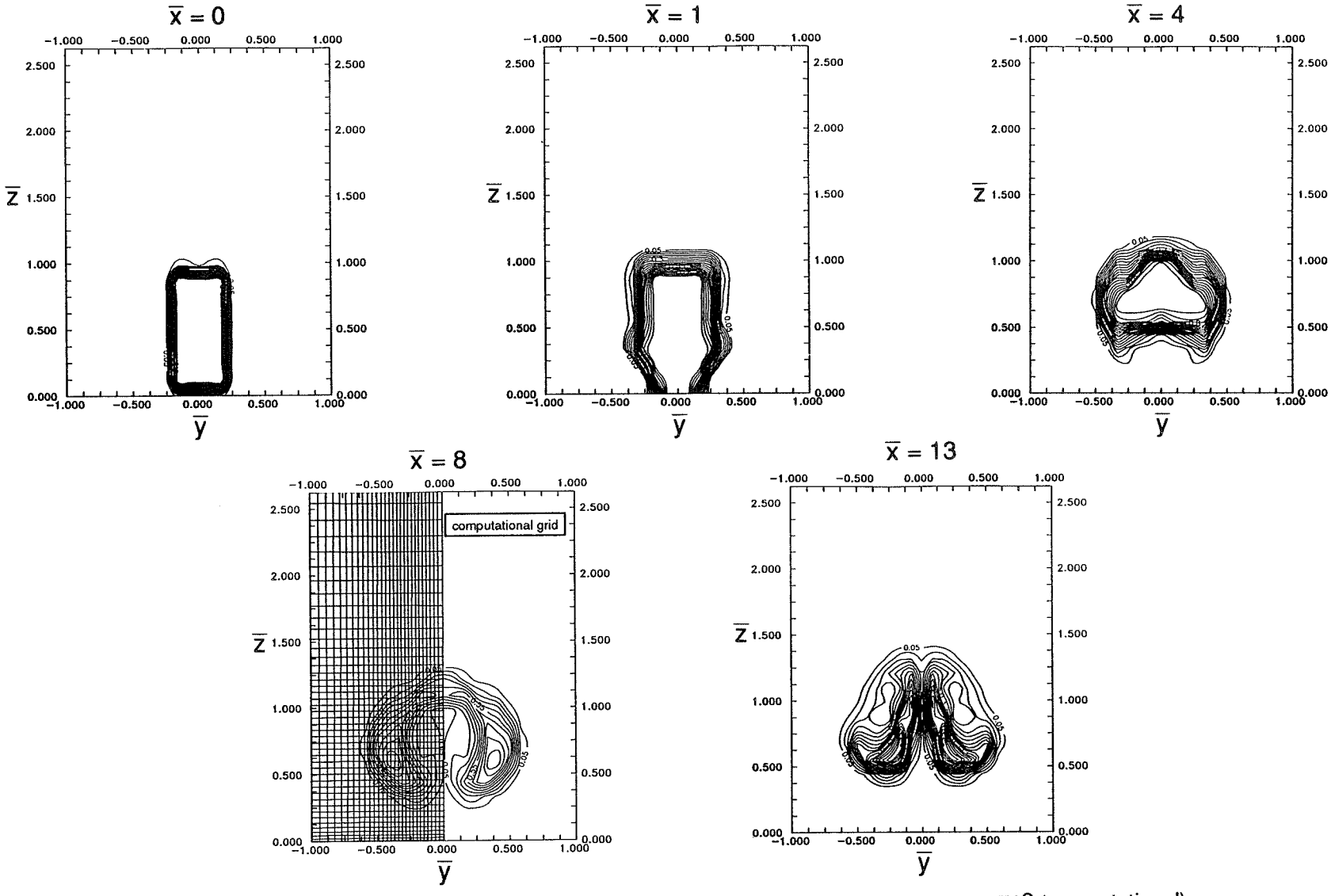

Figure 36. Helium mass fraction. Wide spacing, $\bar{\delta} = 0.20$, $\bar{p} = 1.0$, $\bar{v} = 1.0$, $\alpha_c = \alpha_e = 4.76^o$ (computational).

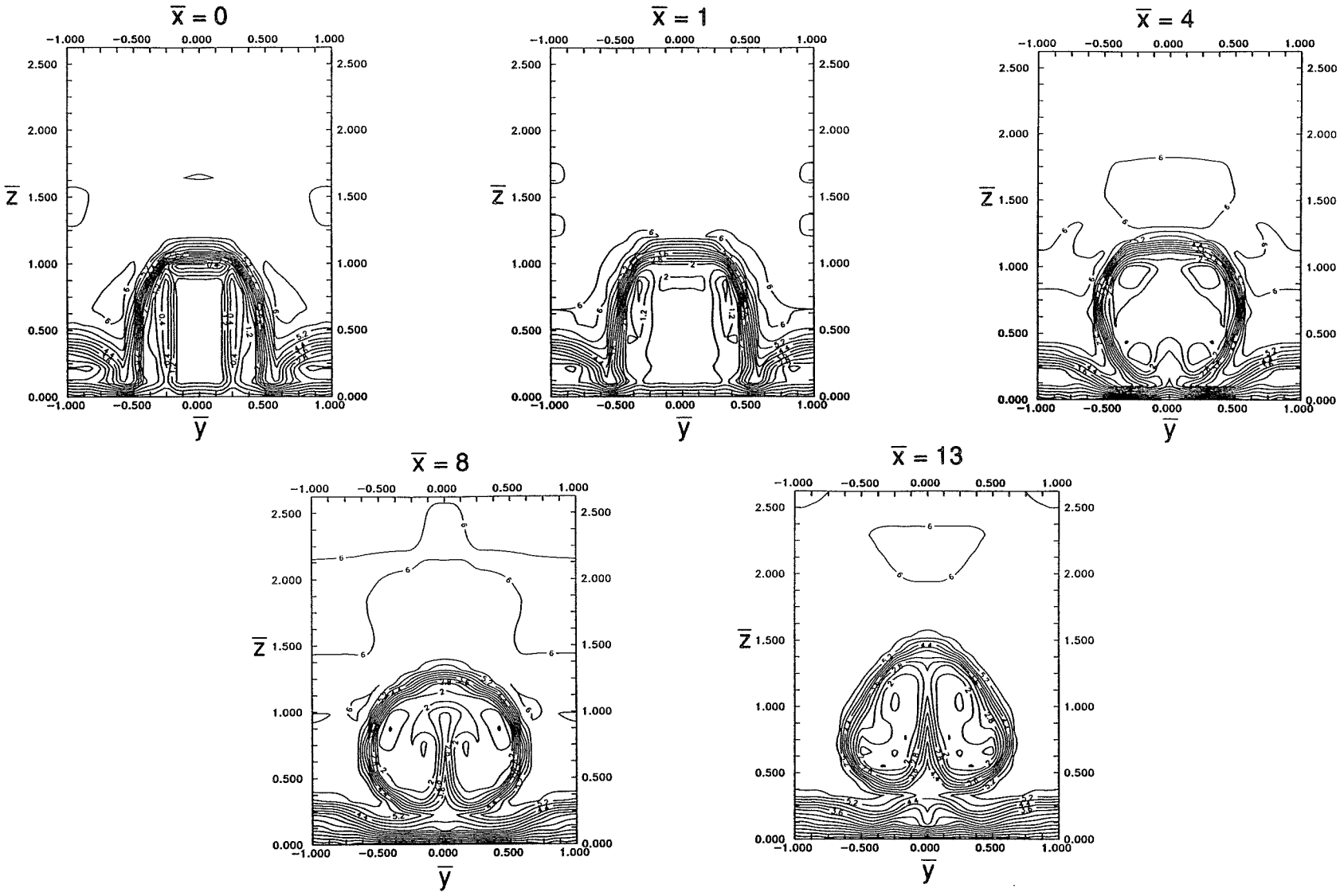

Figure 37. Mach number. Wide spacing, $\bar{\delta} = 0.20$, $\bar{p} = 1.0$, $\bar{v} = 1.0$, $\alpha_c = \alpha_e = 4.76^o$ (computational).

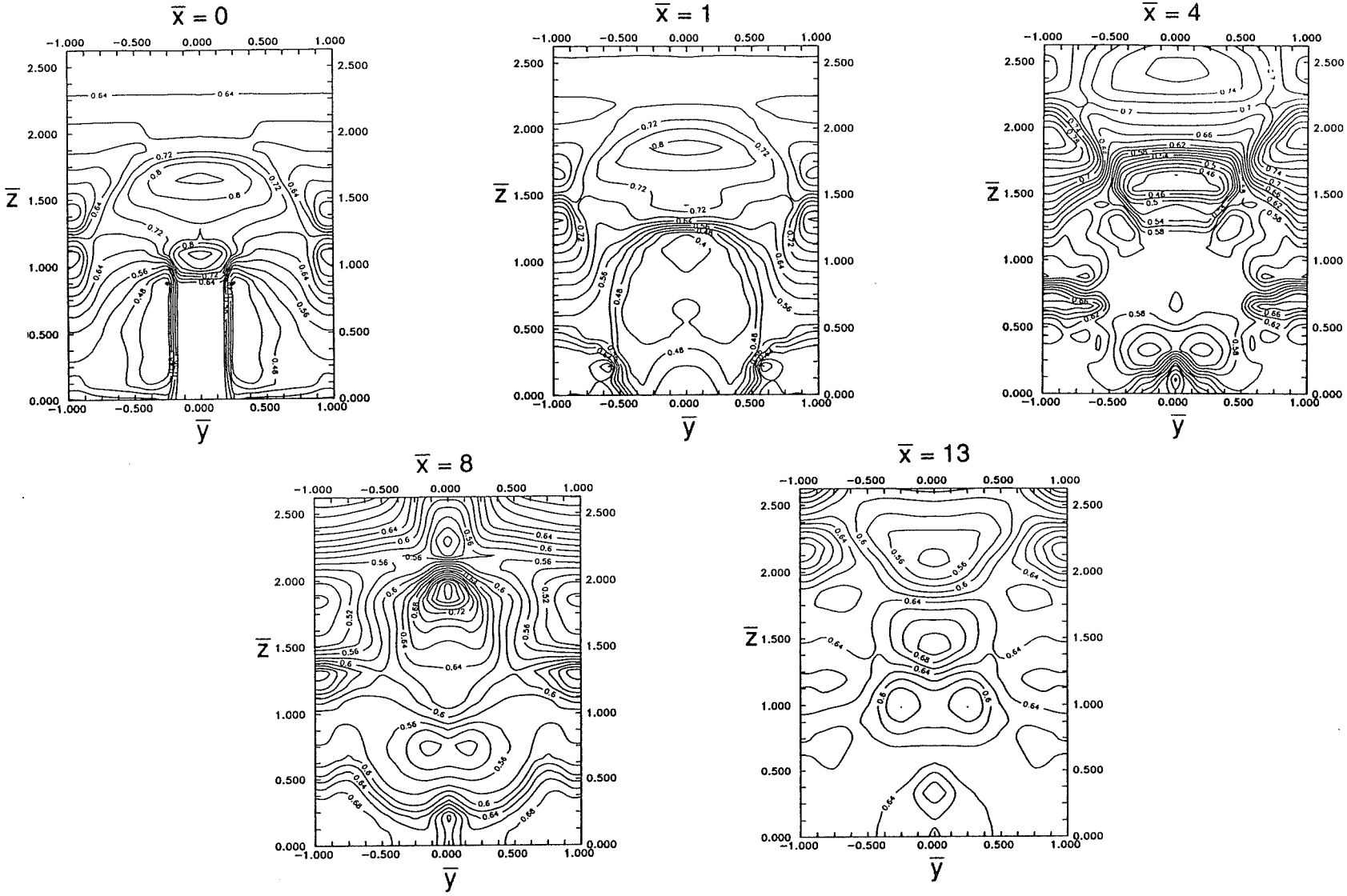

Figure 38. Static pressure (psia). Wide spacing, $\bar{\delta} = 0.20$, $\bar{p} = 1.0$, $\bar{v} = 1.0$, $\alpha_c = \alpha_e = 4.76^o$ (computational).

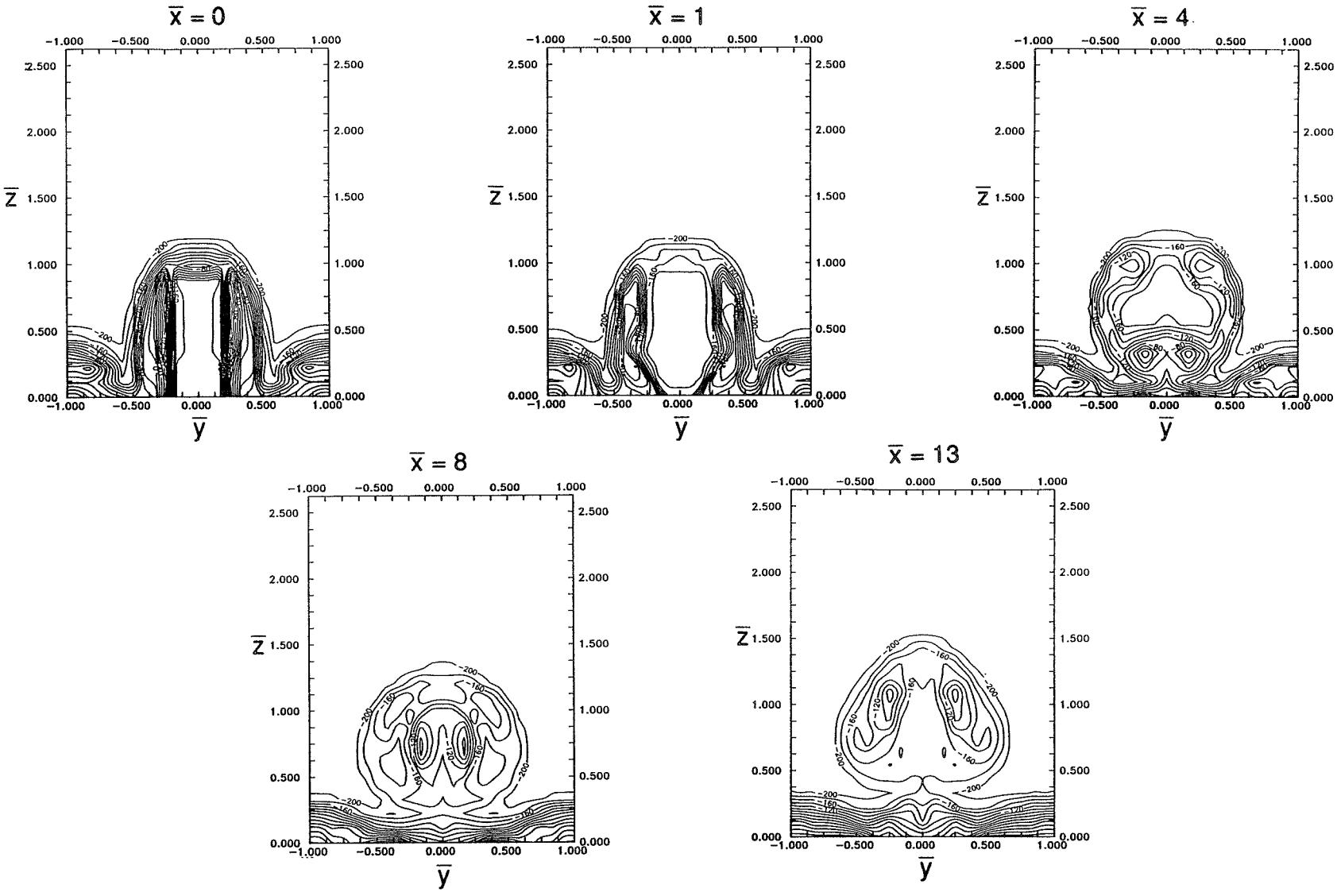

Figure 39. Static Temperature (^{o}C). Wide spacing, $\bar{\delta}$ = 0.20, $\bar{p}$ = 1.0, $\bar{v}$ = 1.0, $\alpha_c = \alpha_e = 4.76^{o}$ (computational).

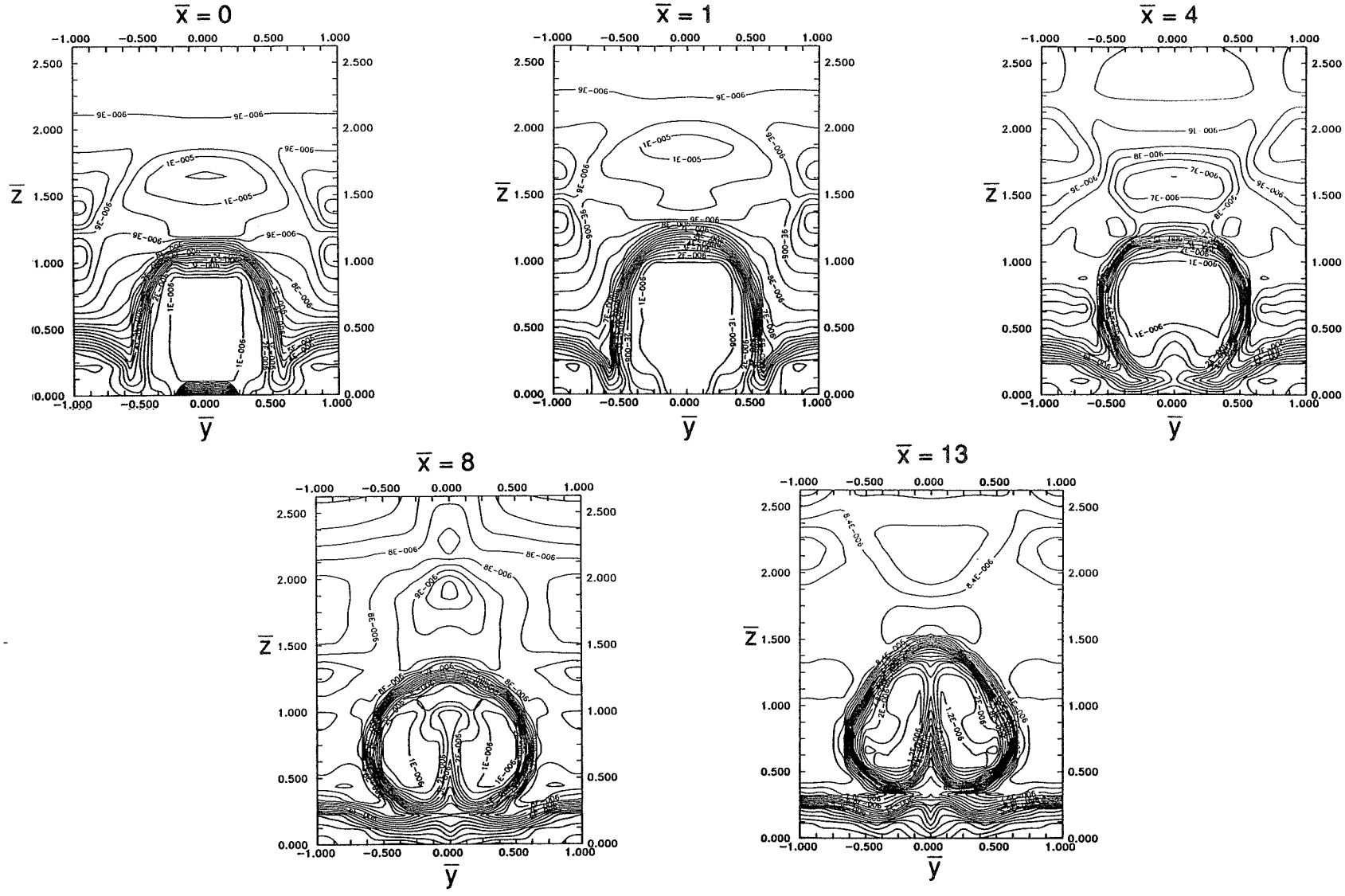

Figure 40. Density (lbm/in^3). Wide spacing, $\bar{\delta} = 0.20$, $\bar{p} = 1.0$, $\bar{v} = 1.0$, $\alpha_c = \alpha_e = 4.76^o$ (computational).

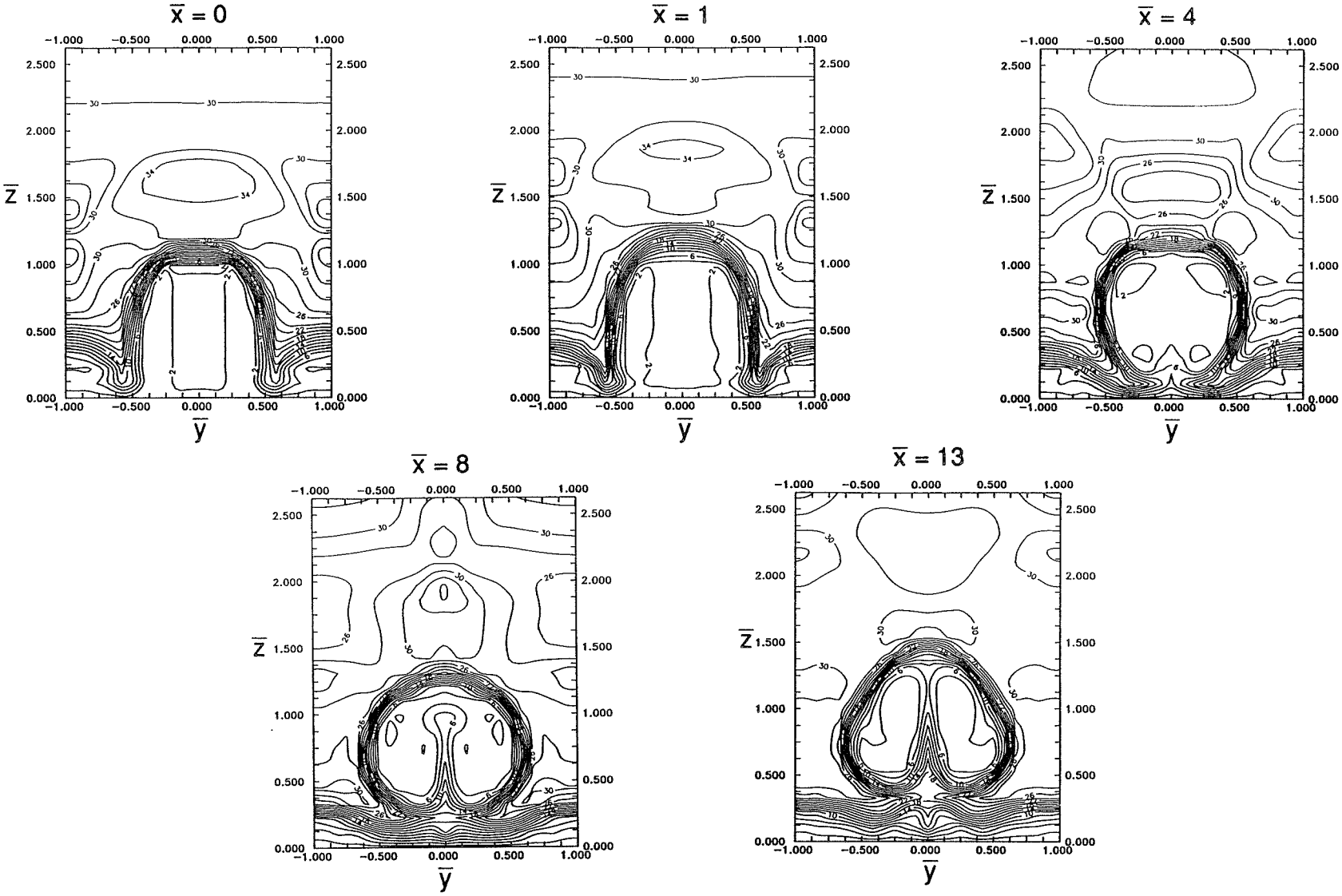

Figure 41. Pitot pressure (psia). Wide spacing, $\bar{\delta} = 0.20$, $\bar{p} = 1.0$, $\bar{v} = 1.0$, $\alpha_c = \alpha_e = 4.76^o$ (computational).

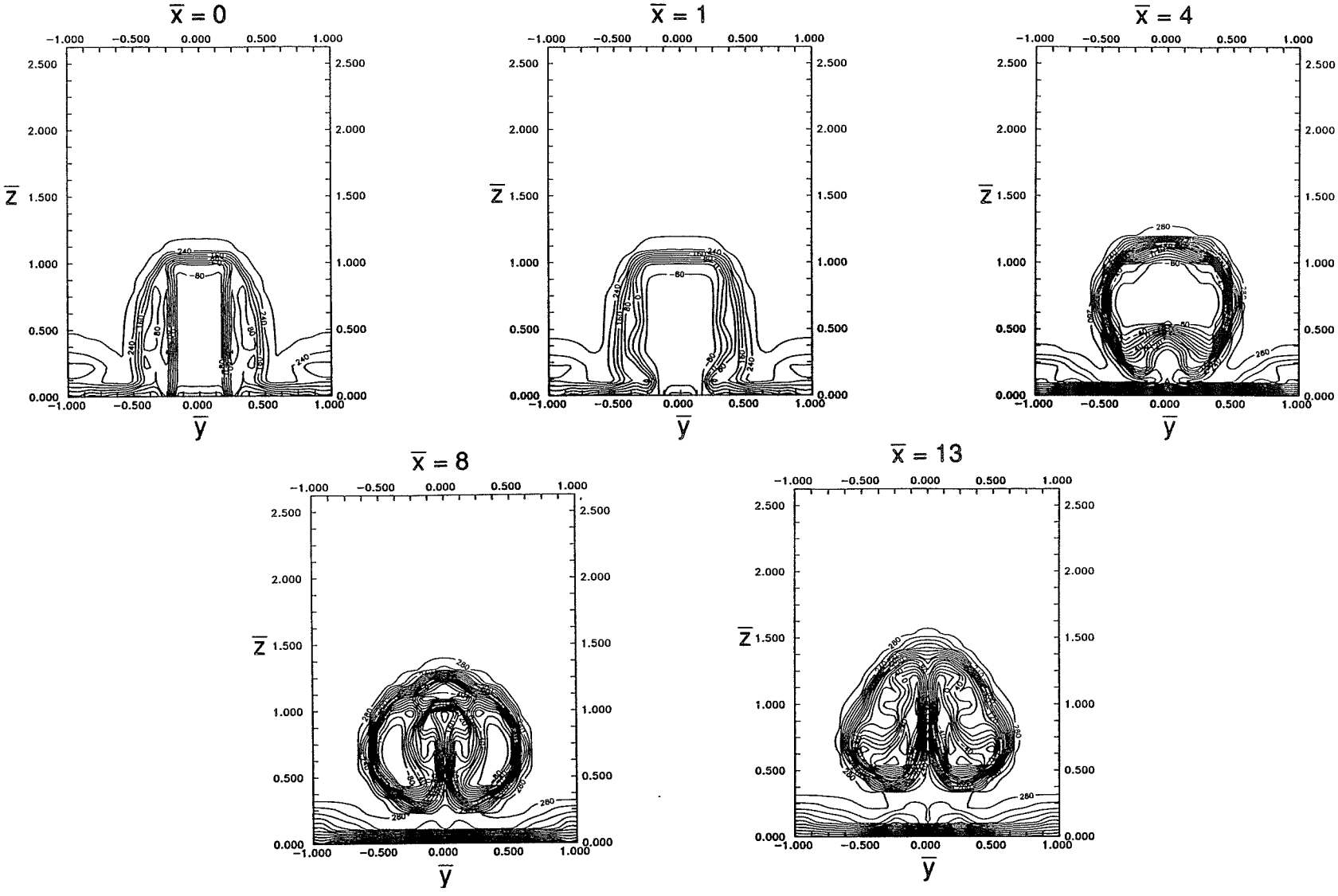

Figure 42. Total temperature (^{o}C). Wide spacing, $\bar{\delta}$ = 0.20, $\bar{p}$ = 1.0, $\bar{v}$ = 1.0, $\alpha_c = \alpha_e = 4.76^{o}$ (computational).

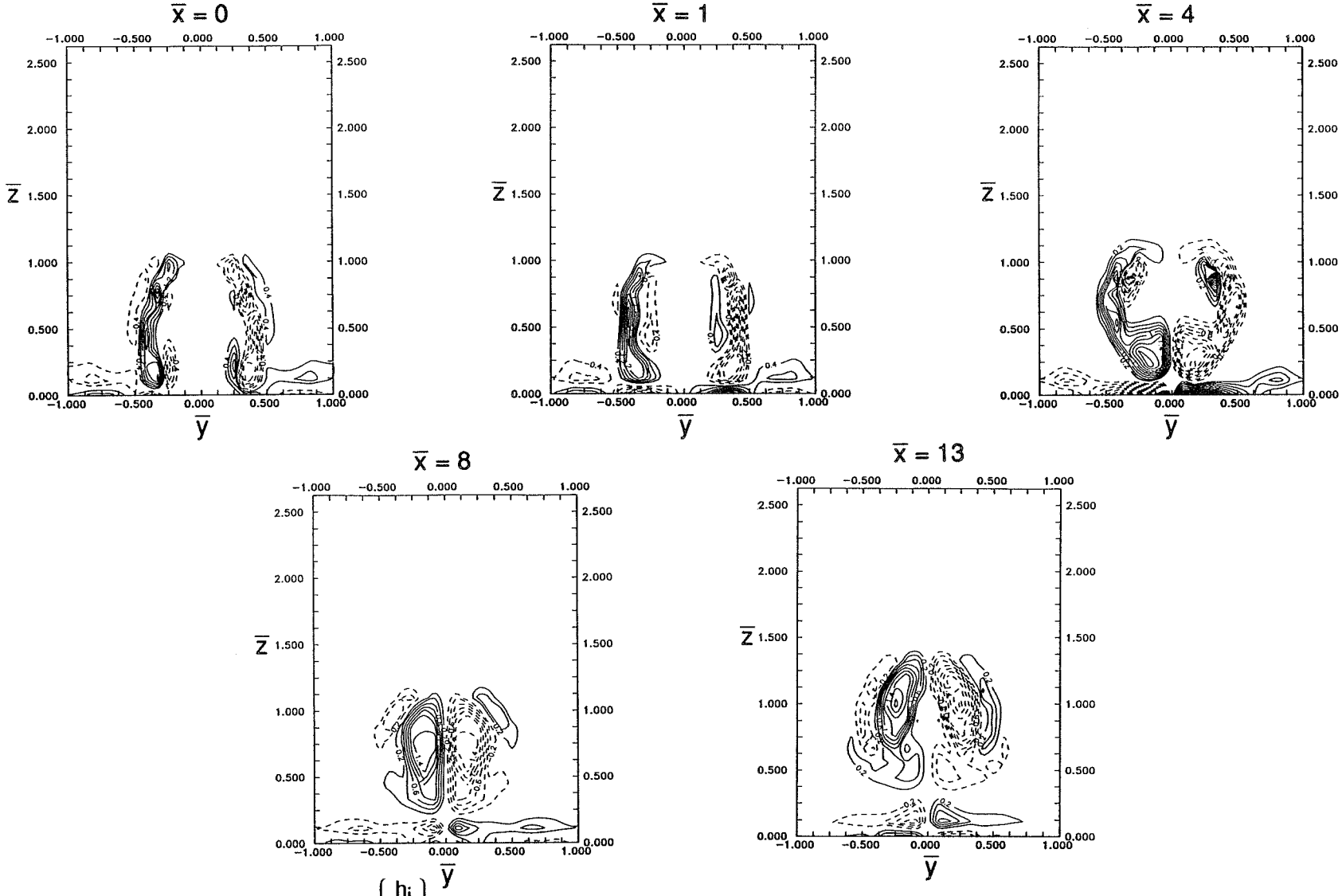

Figure 43. Vorticity, $\omega_x \left(\frac{h_i}{U_\infty} \right)$. Wide spacing, $\bar{\delta} = 0.20$, $\bar{p} = 1.0$, $\bar{v} = 1.0$, $\alpha_c = \alpha_e = 4.76^o$ (computational).

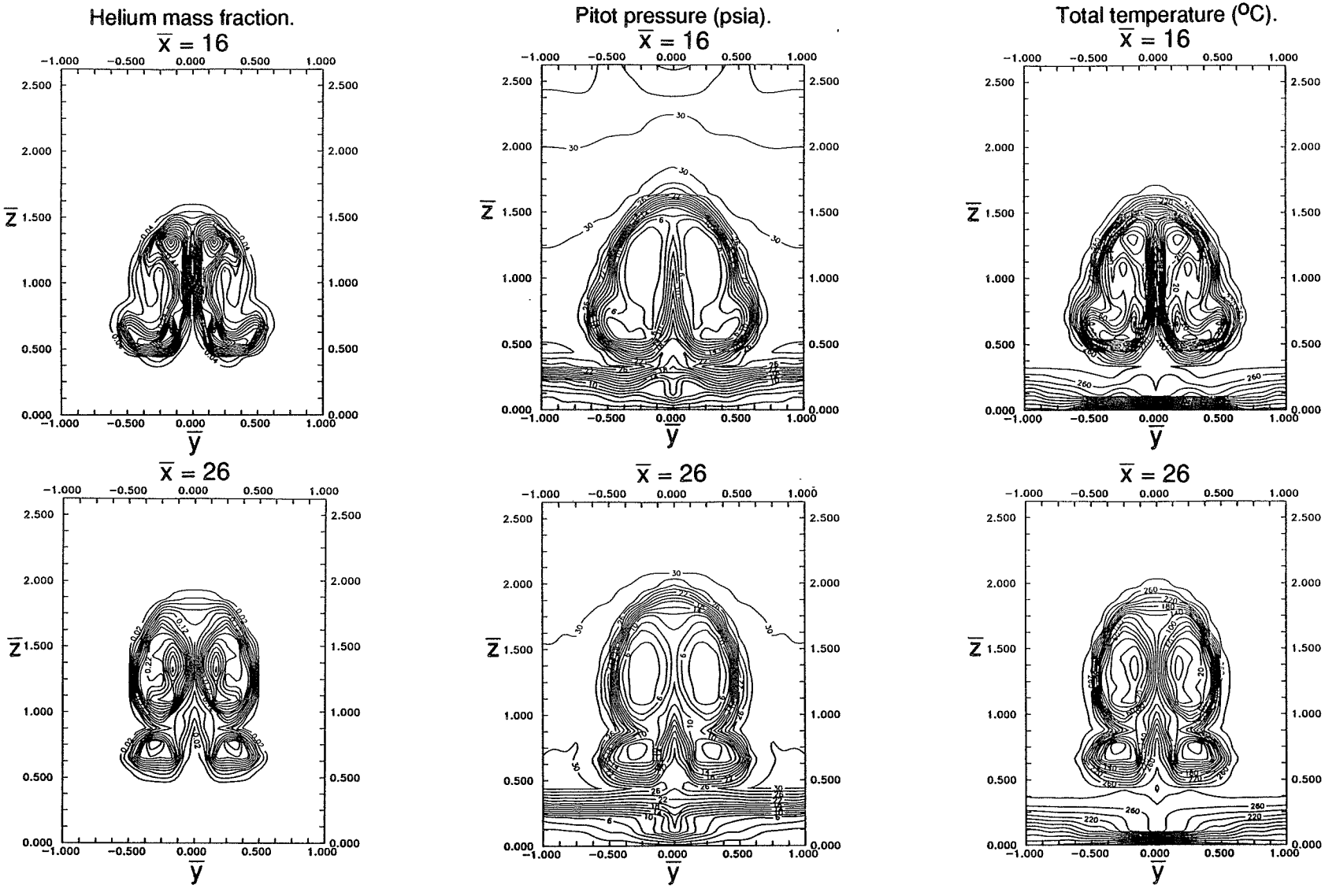

Figure 44. Wide spacing, $\bar{\delta} = 0.20$, $\bar{p} = 1.0$, $\bar{v} = 1.0$, $\alpha_c = \alpha_e = 4.76^o$ (computational).

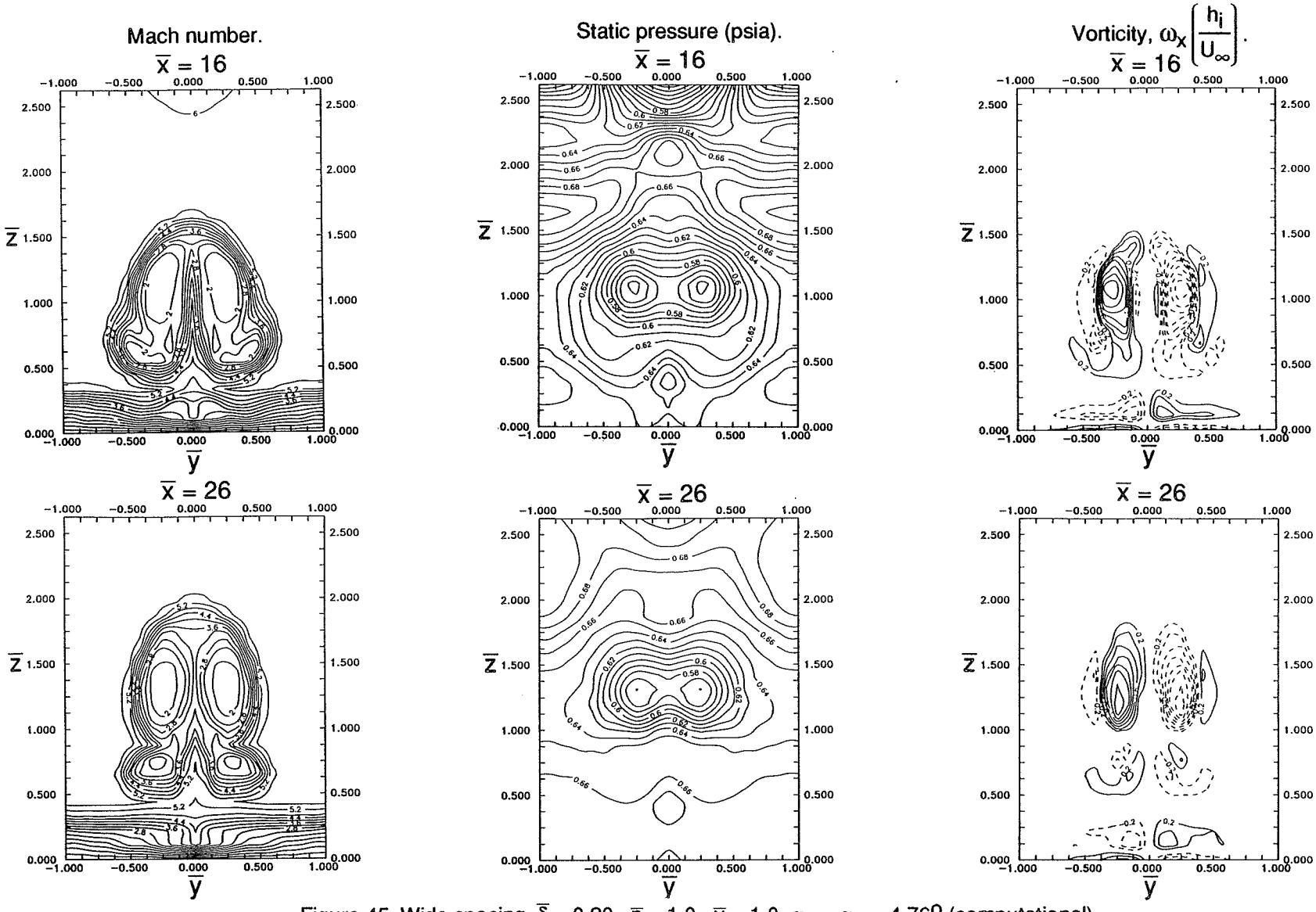

Figure 45. Wide spacing, $\overline{\delta}$ = 0.20, $\overline{p}$ = 1.0, $\overline{v}$ = 1.0, $\alpha_c = \alpha_e = 4.76^o$ (computational).

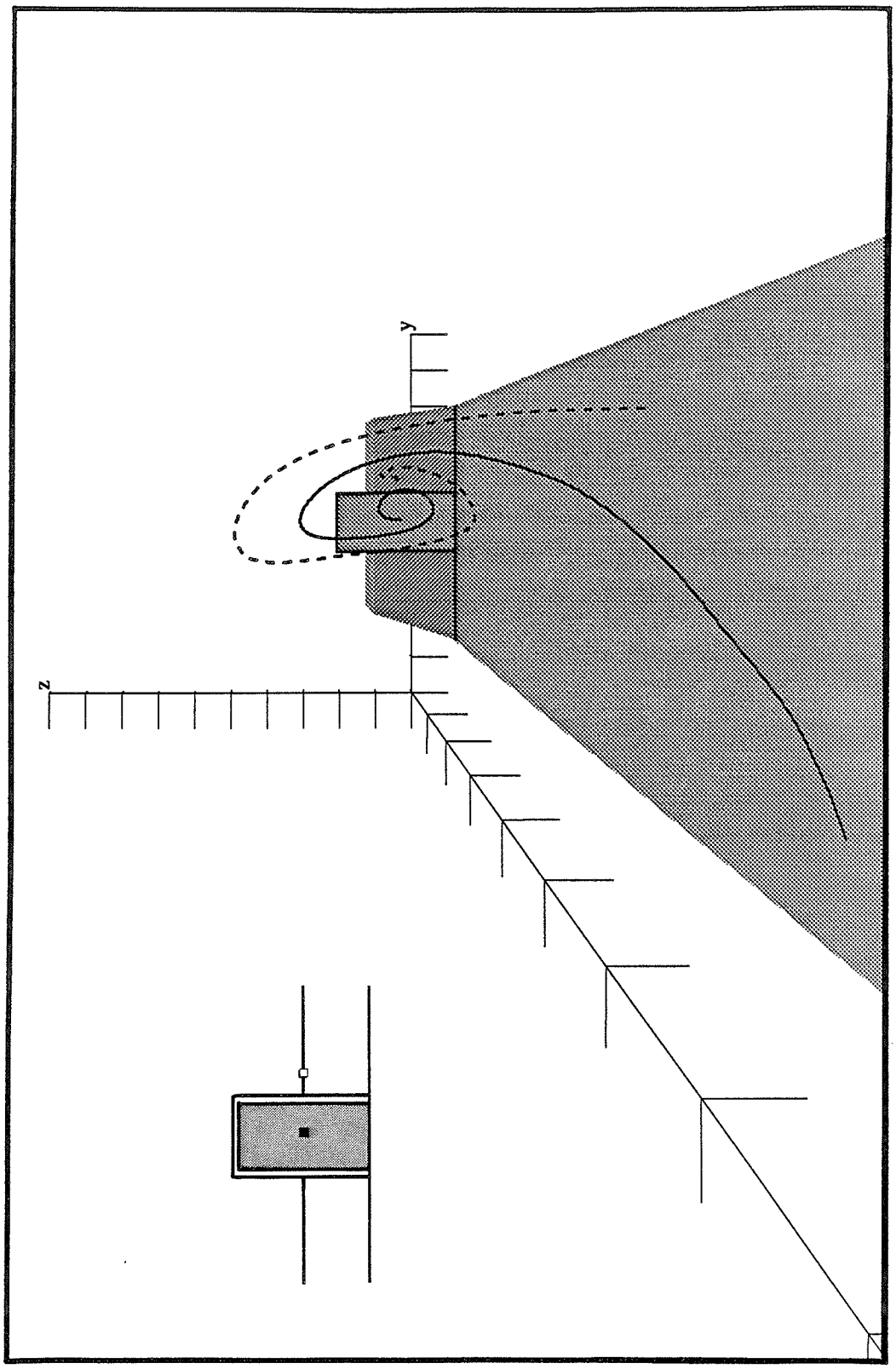

Figure 46. Particle traces.

Wide spacing, $\bar{\delta} = 0.20$, $\bar{p} = 1.0$, $\bar{v} = 1.0$, $\alpha_c = \alpha_e = 4.76^o$ (computational).

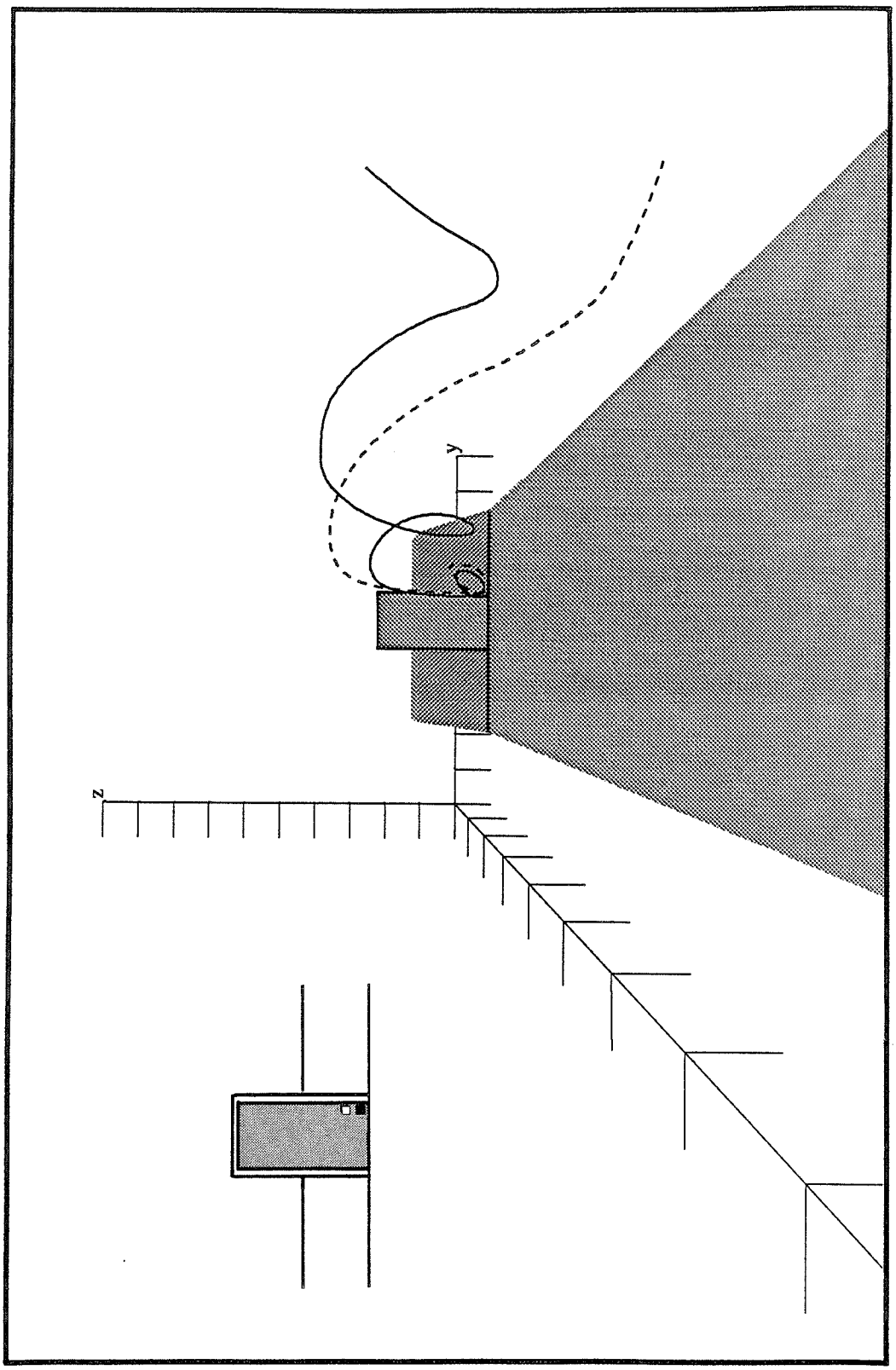

Figure 47. Particle traces.

Wide spacing, $\bar{\delta} = 0.20$, $\bar{p} = 1.0$, $\bar{v} = 1.0$, $\alpha_c = \alpha_e = 4.76^o$ (computational).

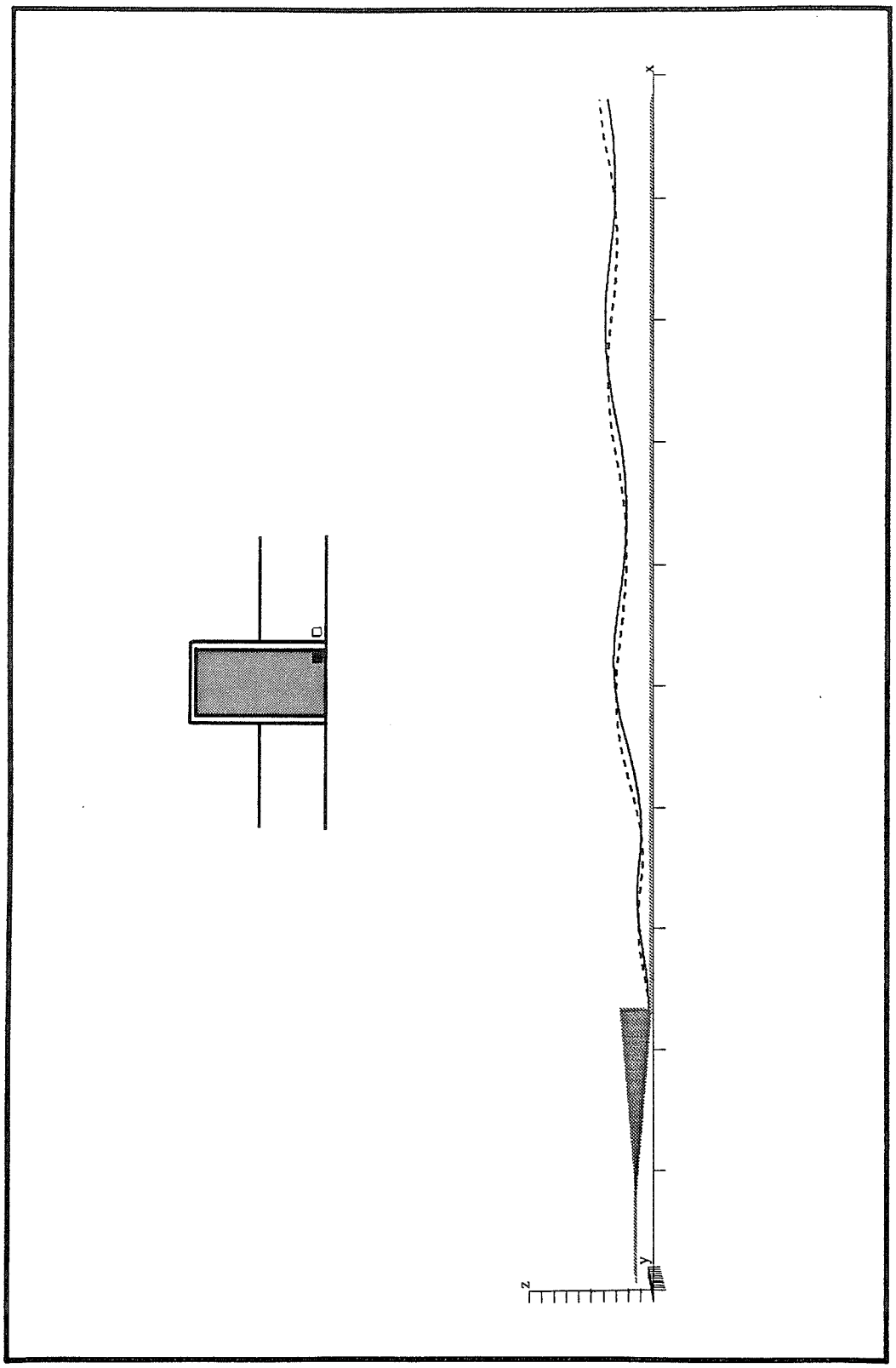

Figure 48. Particle traces.

Wide spacing, $\overline{\delta} = 0.20$, $\overline{p} = 1.0$, $\overline{v} = 1.0$, $\alpha_c = \alpha_e = 4.76^o$ (computational).

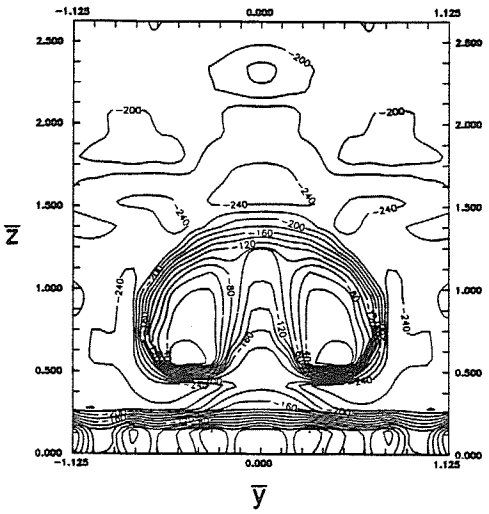

a. static temperature (°C)

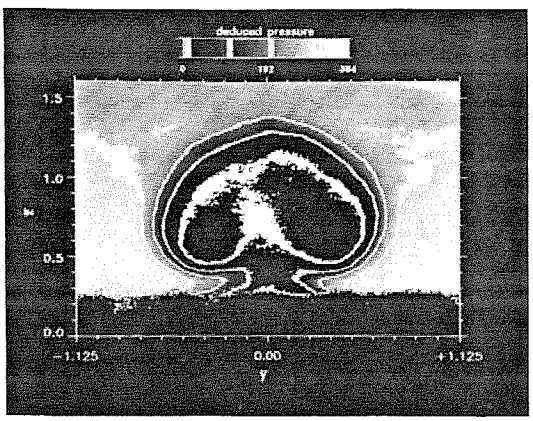

b. mean of 22 Rayleigh images

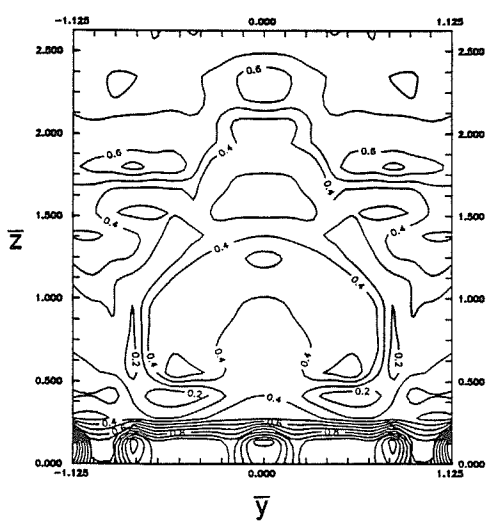

c. static pressure (psia)

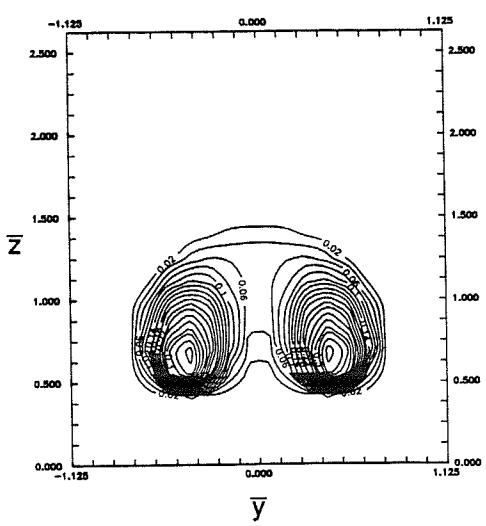

d. helium mass fraction

Figure 49. Comparison of mean survey data with mean of 22 planar Rayleigh images at $\bar{x} = 10$. Wide spacing, $\bar{\delta} = 0.20$, $\bar{p} = 1.0$, $\bar{v} = 1.33$, $\alpha_c = \alpha_e = 4.76^o$.

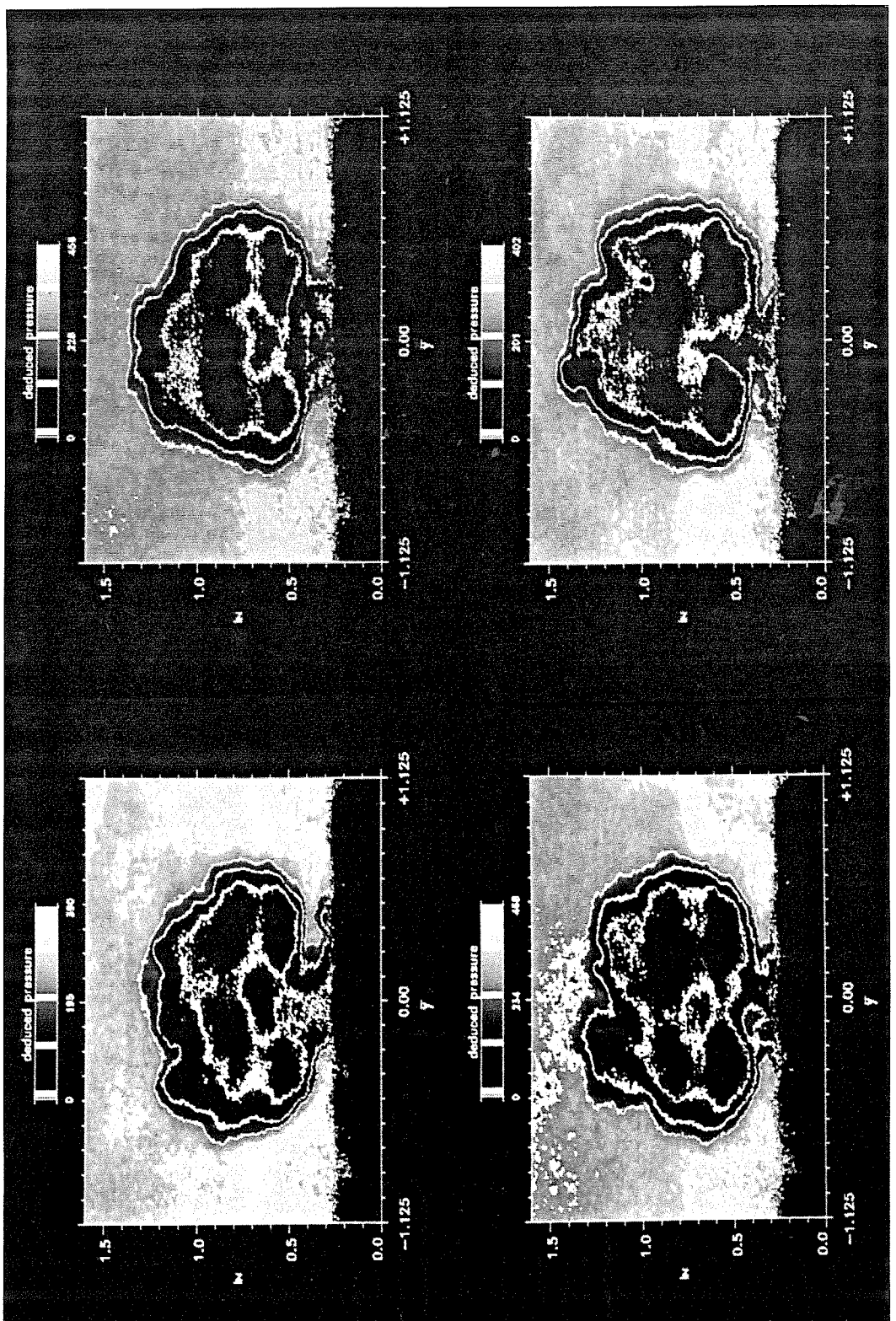

Figure 50. Instantaneous planar Rayleigh images at $\overline{x} = 10$. Wide spacing, $\overline{\delta} = 0.20$, $\overline{p} = 1.0$, $\overline{v} = 1.33$, $\alpha_c = \alpha_e = 4.76^o$.

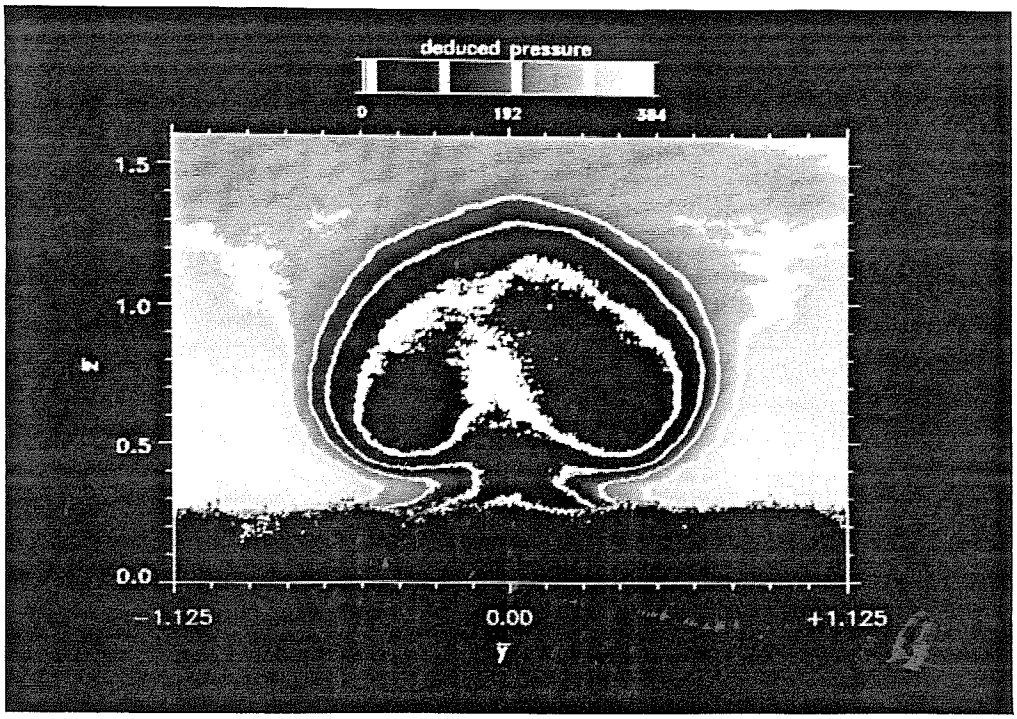

Figure 51. Mean of 22 planar Rayleigh images at $\overline{x} = 10$.

Wide spacing, $\overline{\delta} = 0.20$, $\overline{p} = 1.0$, $\overline{v} = 1.33$, $\alpha_c = \alpha_e = 4.76^o$.

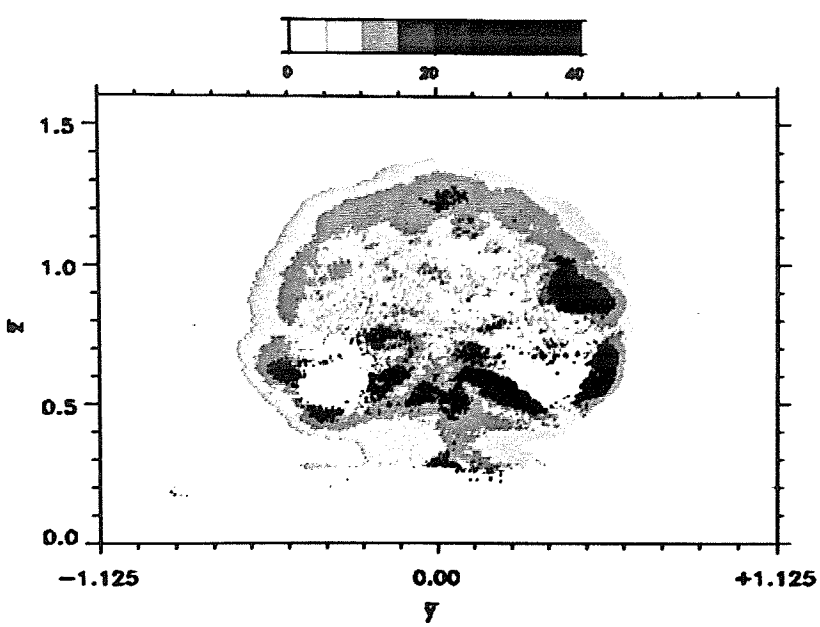

Figure 52. Standard deviation (%mean) about the mean for planar Rayleigh images at $\overline{x} = 10$.

Wide spacing, $\overline{\delta} = 0.20$, $\overline{p} = 1.0$, $\overline{v} = 1.33$, $\alpha_c = \alpha_e = 4.76^o$.

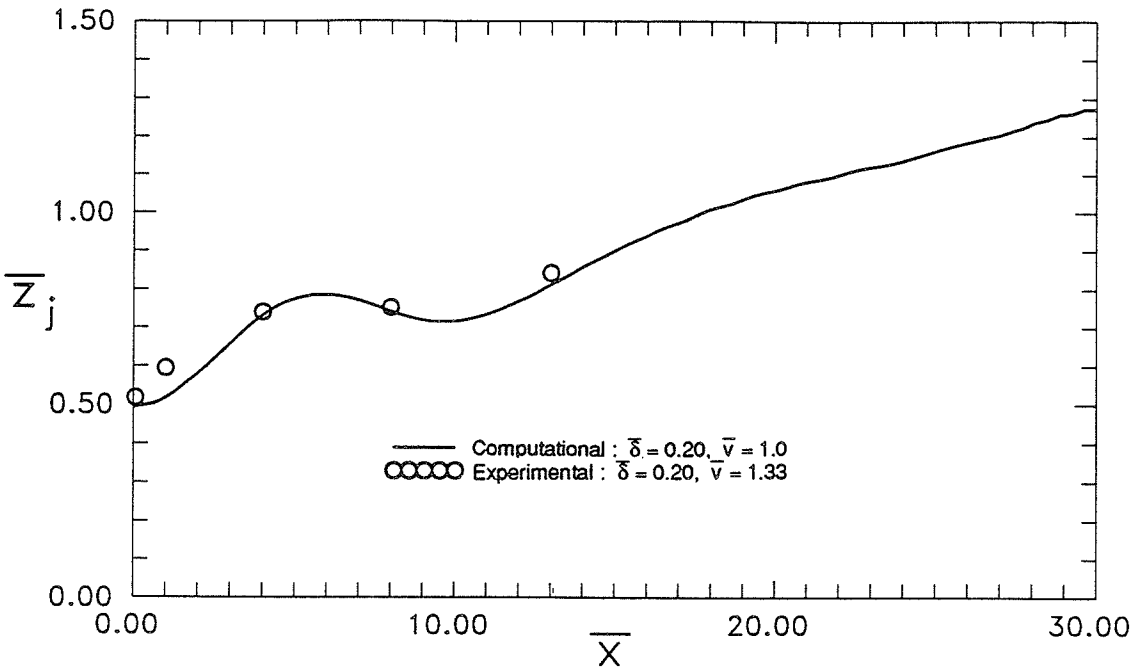

Figure 53. Jet lift-off. Wide spacing, thin boundary layer, $\overline{p}$ = 1.0, $\alpha_c = \alpha_e = 4.76^o$.

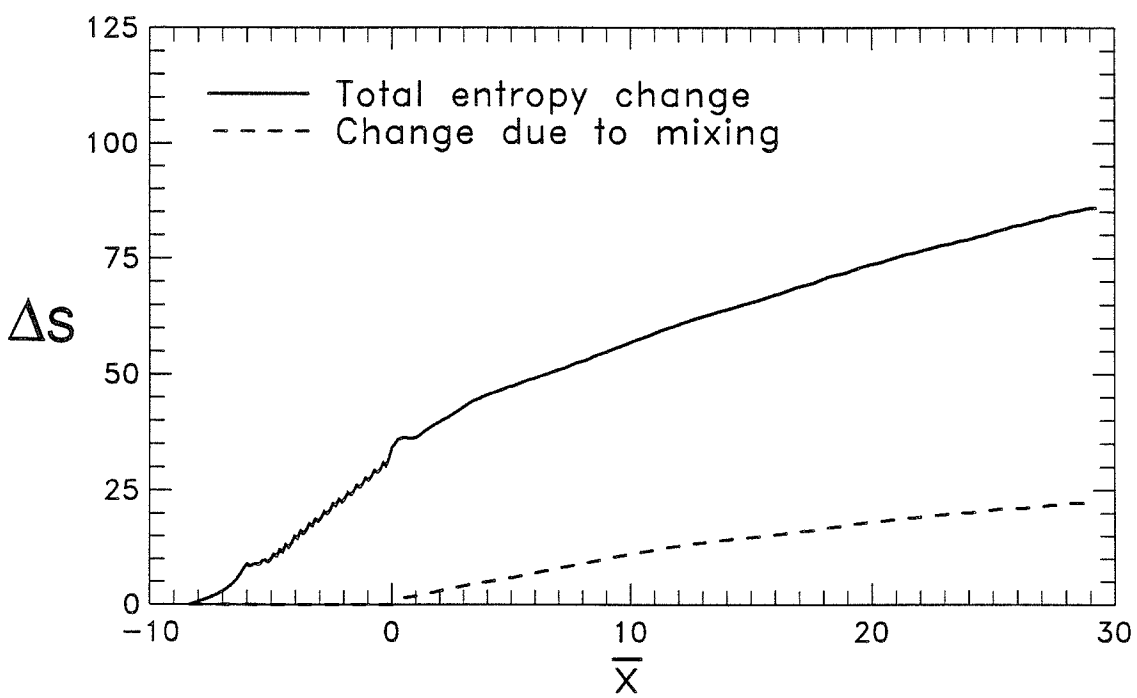

Figure 54. Entropy measure. Wide spacing, $\overline{\delta}$ = 0.20, $\overline{p}$ = 1.0, $\overline{v}$ = 1.0, $\alpha_c = \alpha_e = 4.76^o$

(computational).

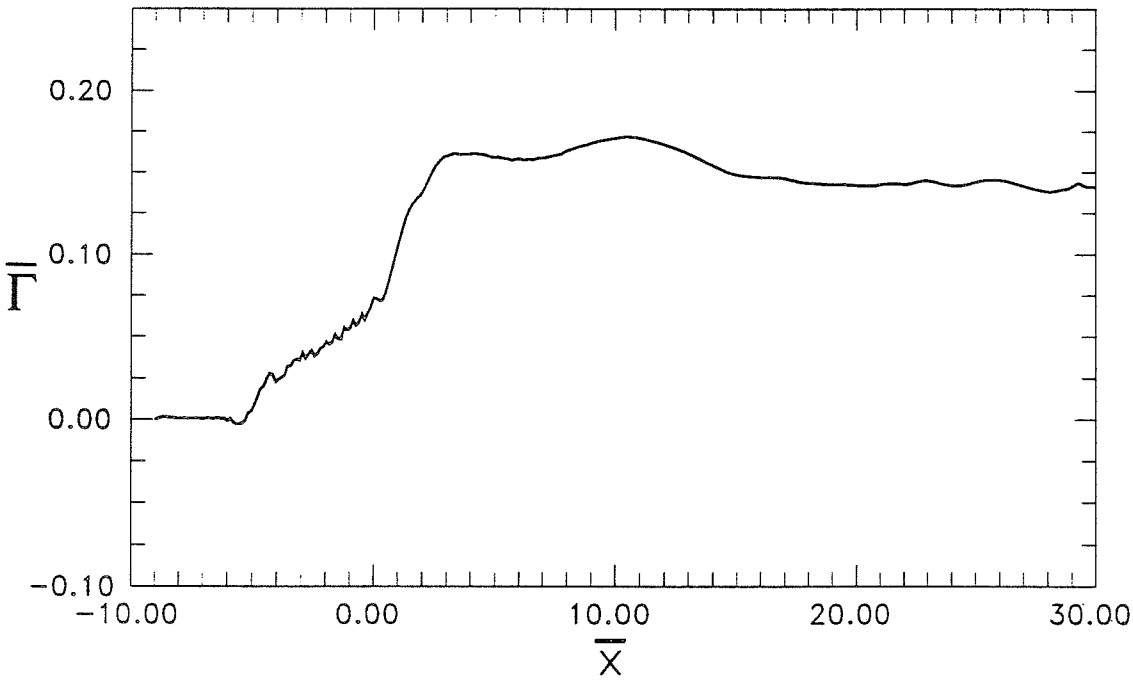

Figure 55. Circulation. Wide spacing, $\bar{\delta} = 0.20$, $\bar{p} = 1.0$, $\bar{v} = 1.0$, $\alpha_c = \alpha_e = 4.76^o$ (computational).

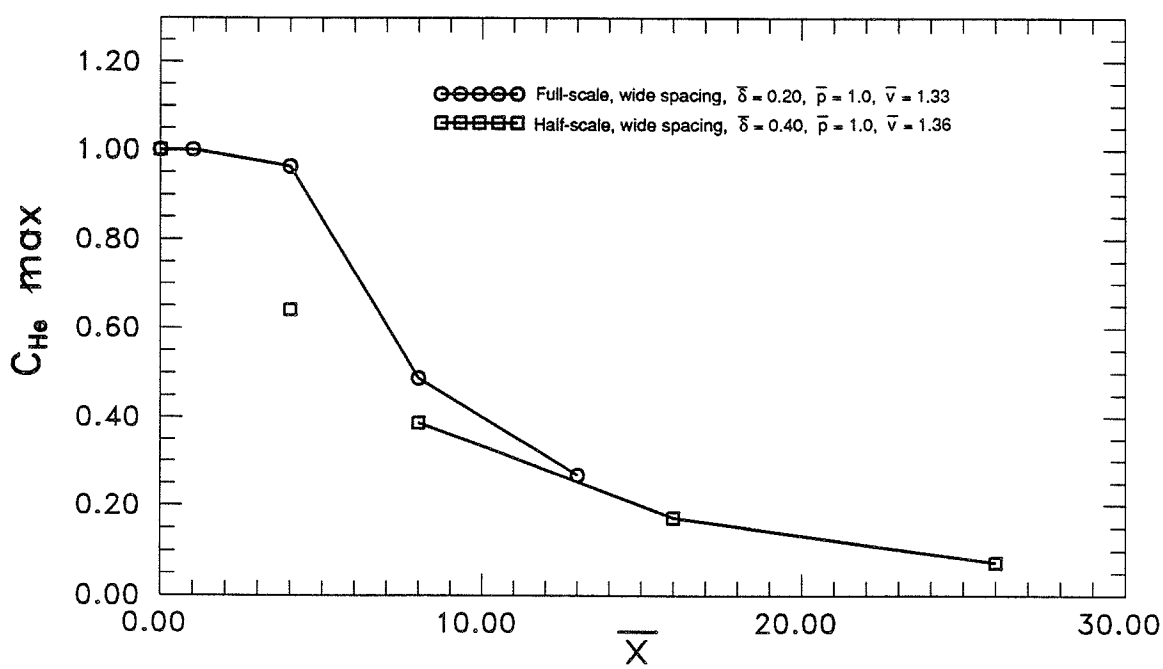

Figure 56. Decay of maximum helium mass fraction. Wide spacing, thin boundary layer, $\bar{p} = 1.0$, $\alpha_c = \alpha_e = 4.76^o$ (experimental).

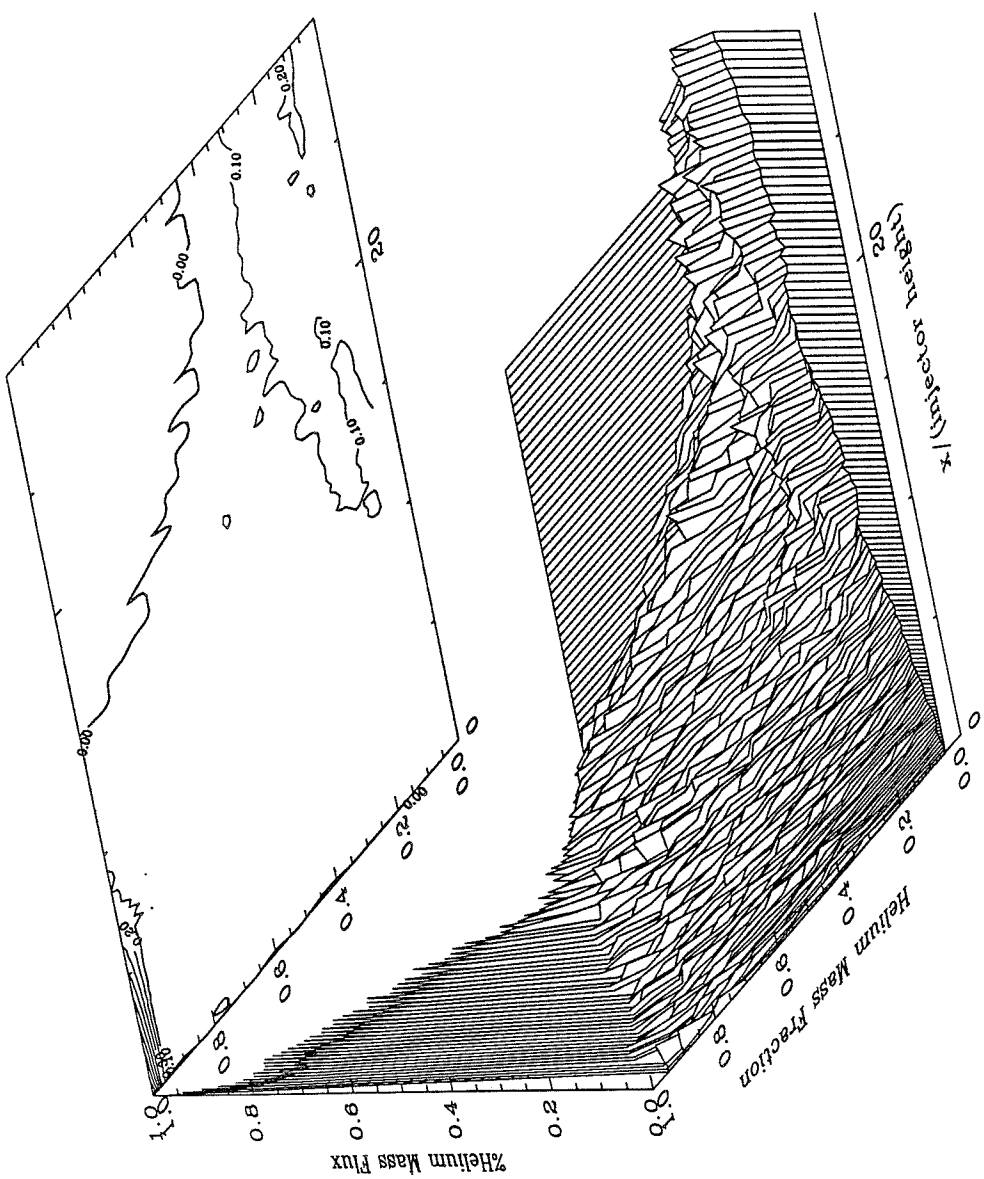

Figure 57. Mixedness Measure. Wide spacing, $\bar{\delta} = 0.20$, $\bar{p} = 1.0$, $\bar{v} = 1.0$, $\alpha_C = \alpha_e = 4.76^O$ (computational).

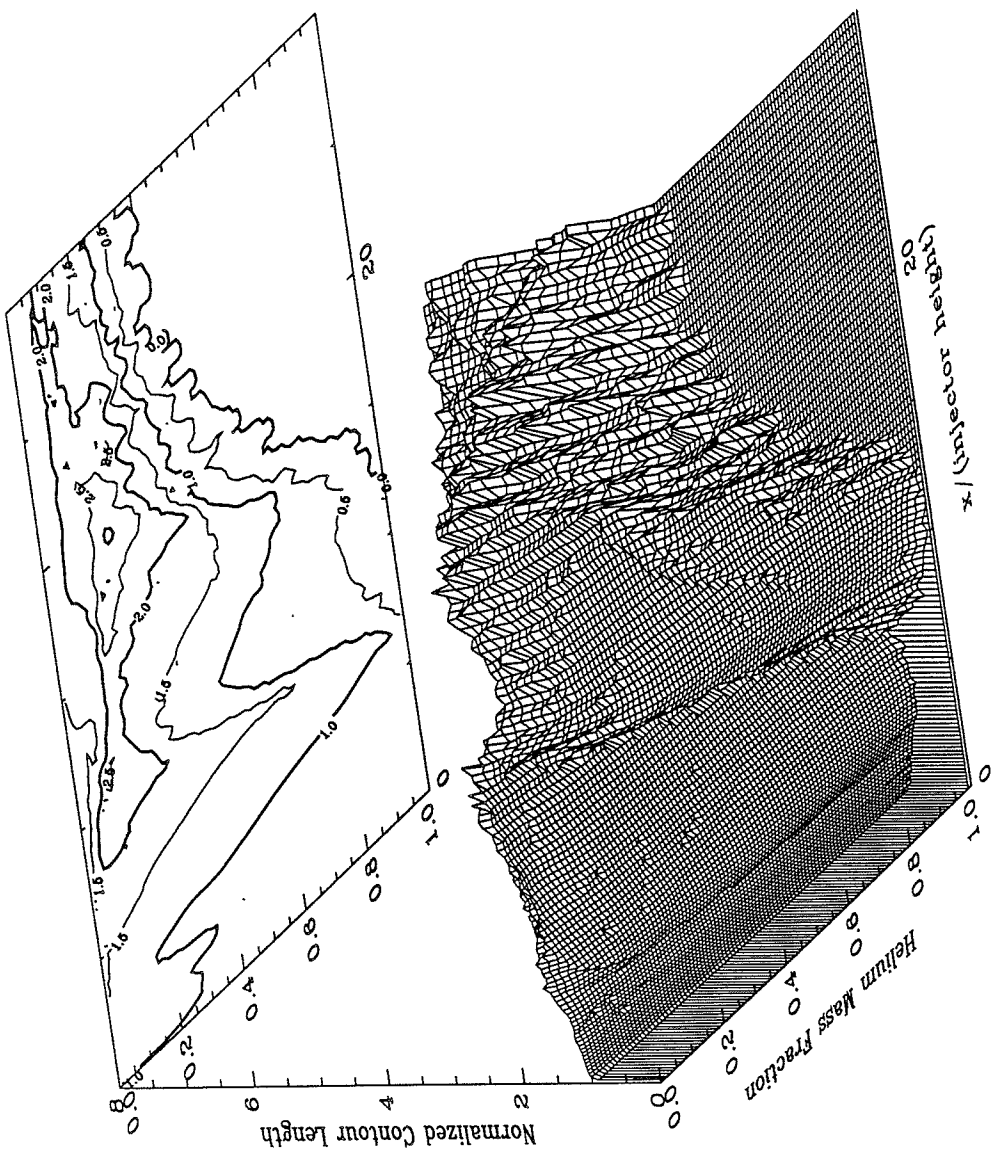

Figure 58. Length of contours of constant mass fraction. Wide spacing, $\overline{\delta} = 0.20$, $\overline{p} = 1.0$, $\overline{v} = 1.0$, $\alpha_c = \alpha_e = 4.76^o$ (computational).

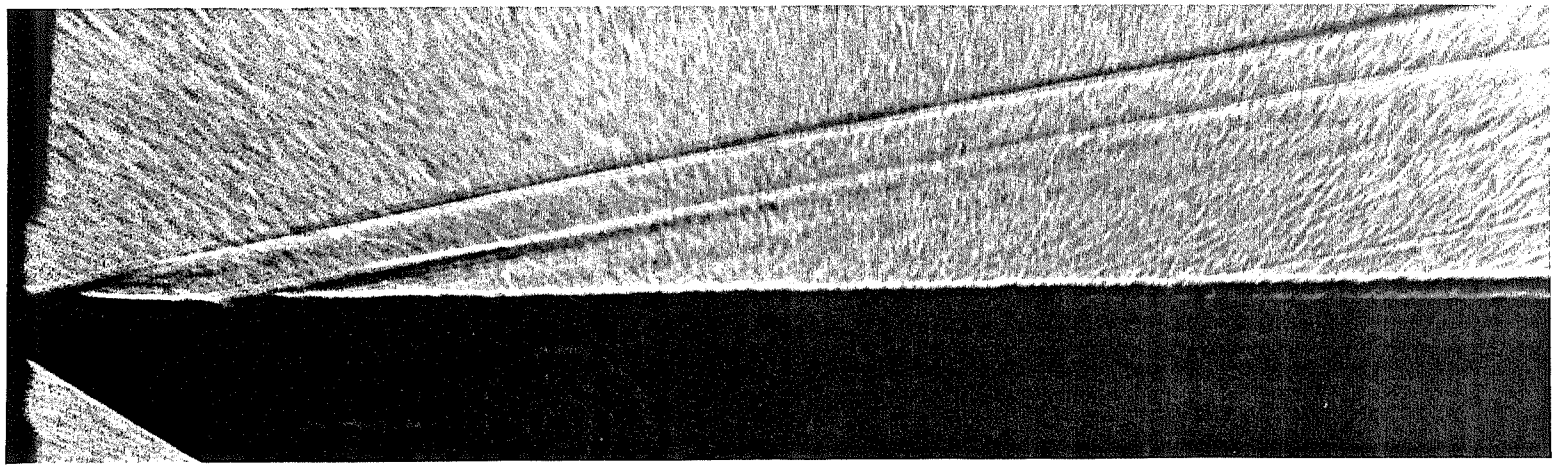

Figure 59. Shadowgraph of 'natural' boundary layer. $R_e = 15 \times 10^6$ /ft.

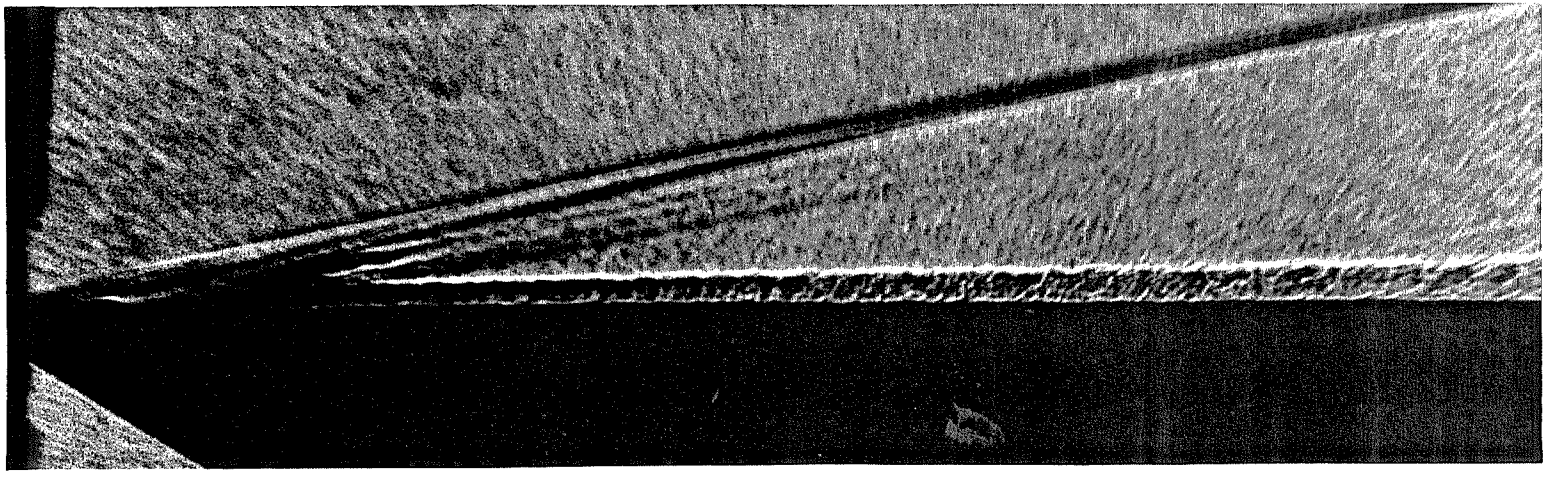

Figure 60. Shadowgraph of tripped boundary layer. $R_e = 15 \times 10^6$ /ft.

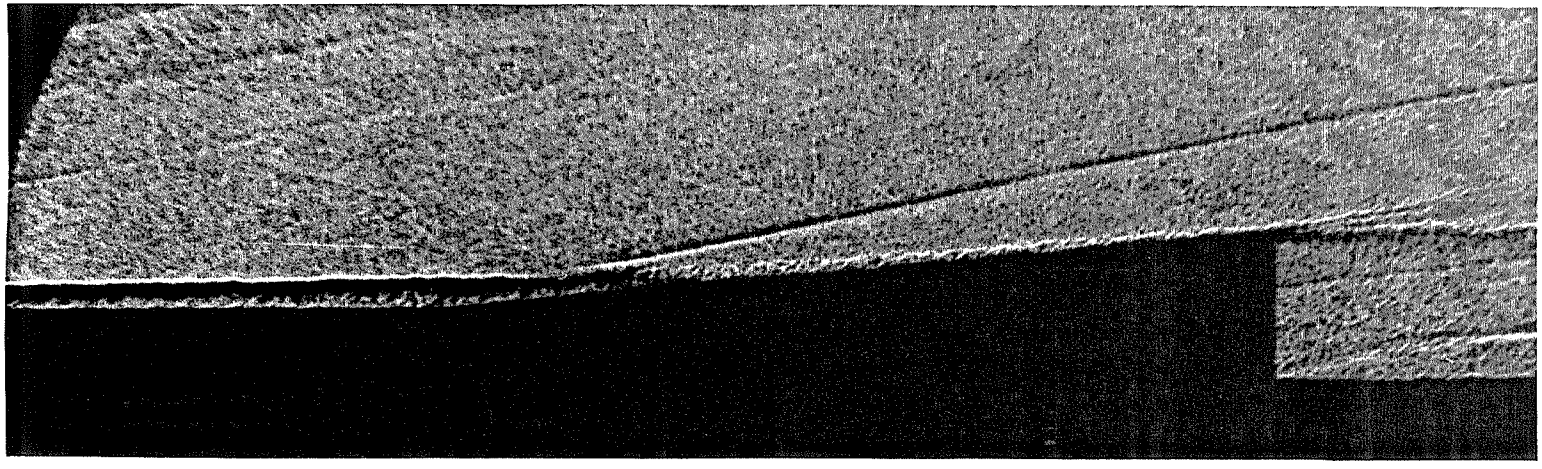

Figure 61. Shadowgraph of 'natural' boundary layer entering injector ramps. $R_e = 15x10^6$ /ft.

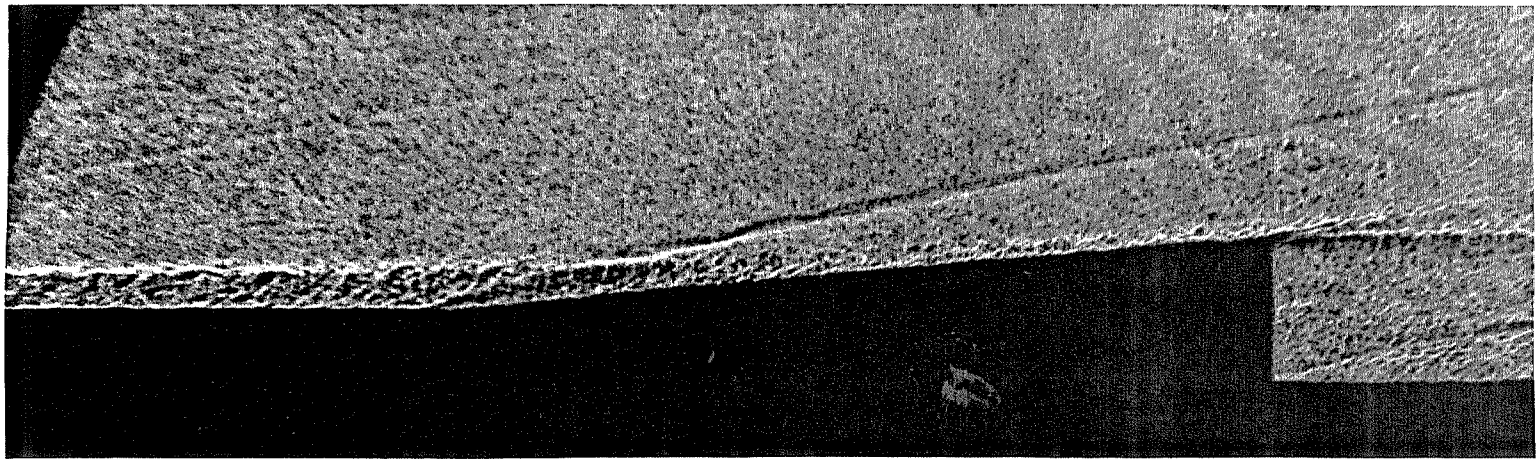

Figure 62. Shadowgraph of tripped boundary layer entering injector ramps. $R_e = 15x10^6$ /ft.

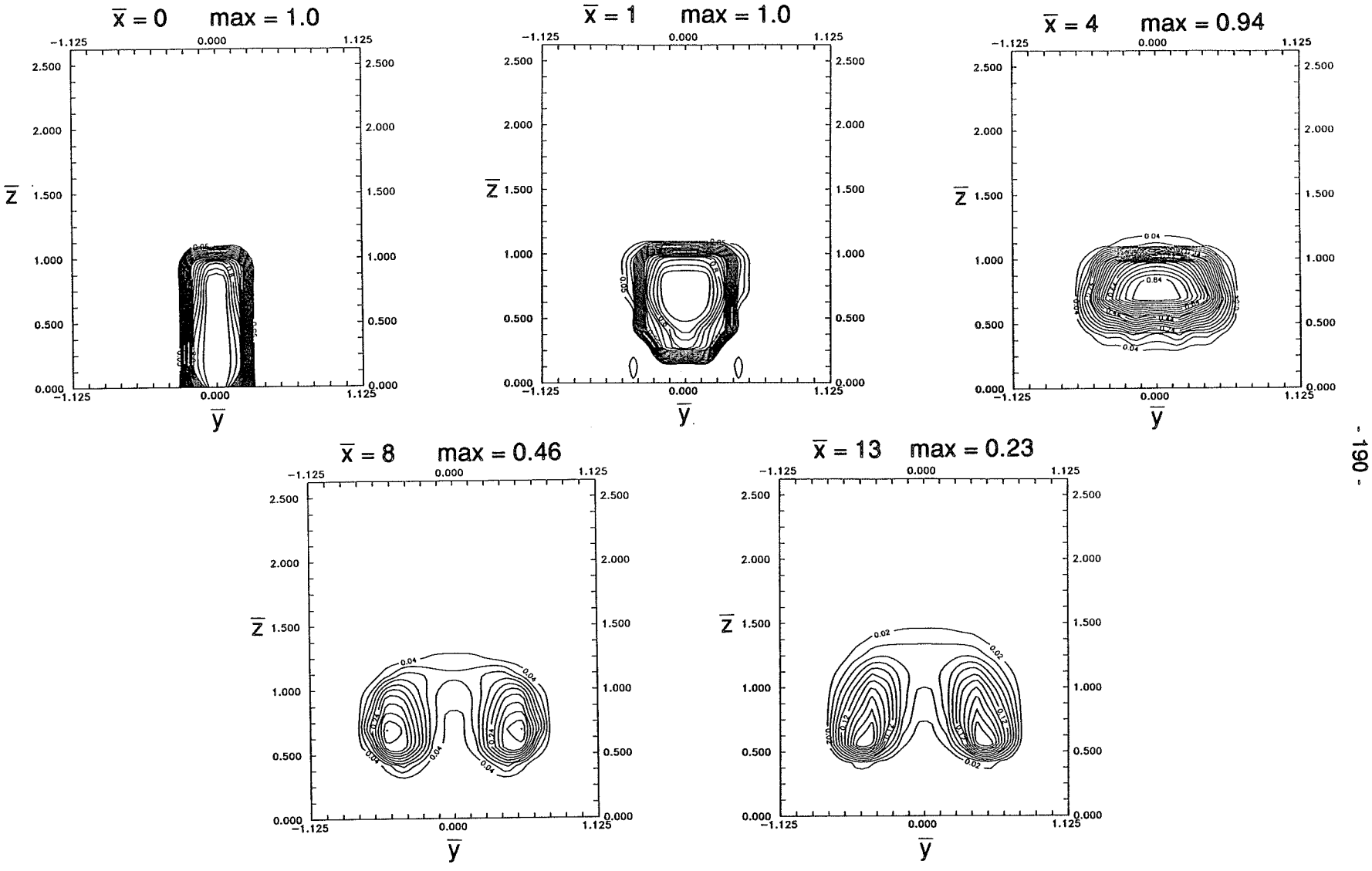

Figure 63. Helium mass fraction. Full-scale model, wide spacing, tripped boundary layer, $\bar{\delta} = 0.35$, $\bar{p} = 1.0$, $\bar{v} = 1.33$ (experimental).

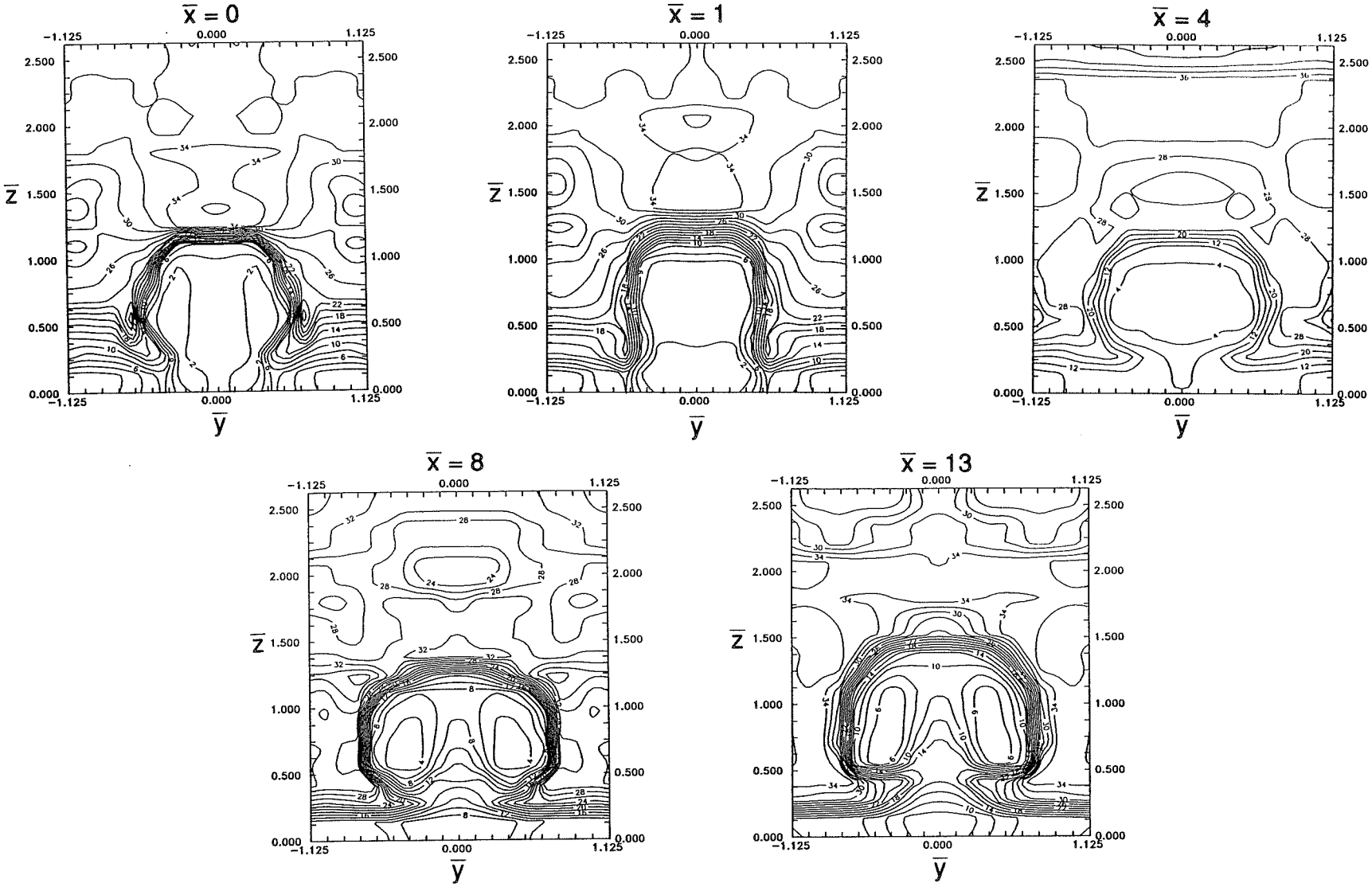

Figure 64. Pitot pressure (psia). Full-scale model, wide spacing, tripped boundary layer, $\bar{\delta} = 0.35$, $\bar{p} = 1.0$, $\bar{v} = 1.33$ (experimental).

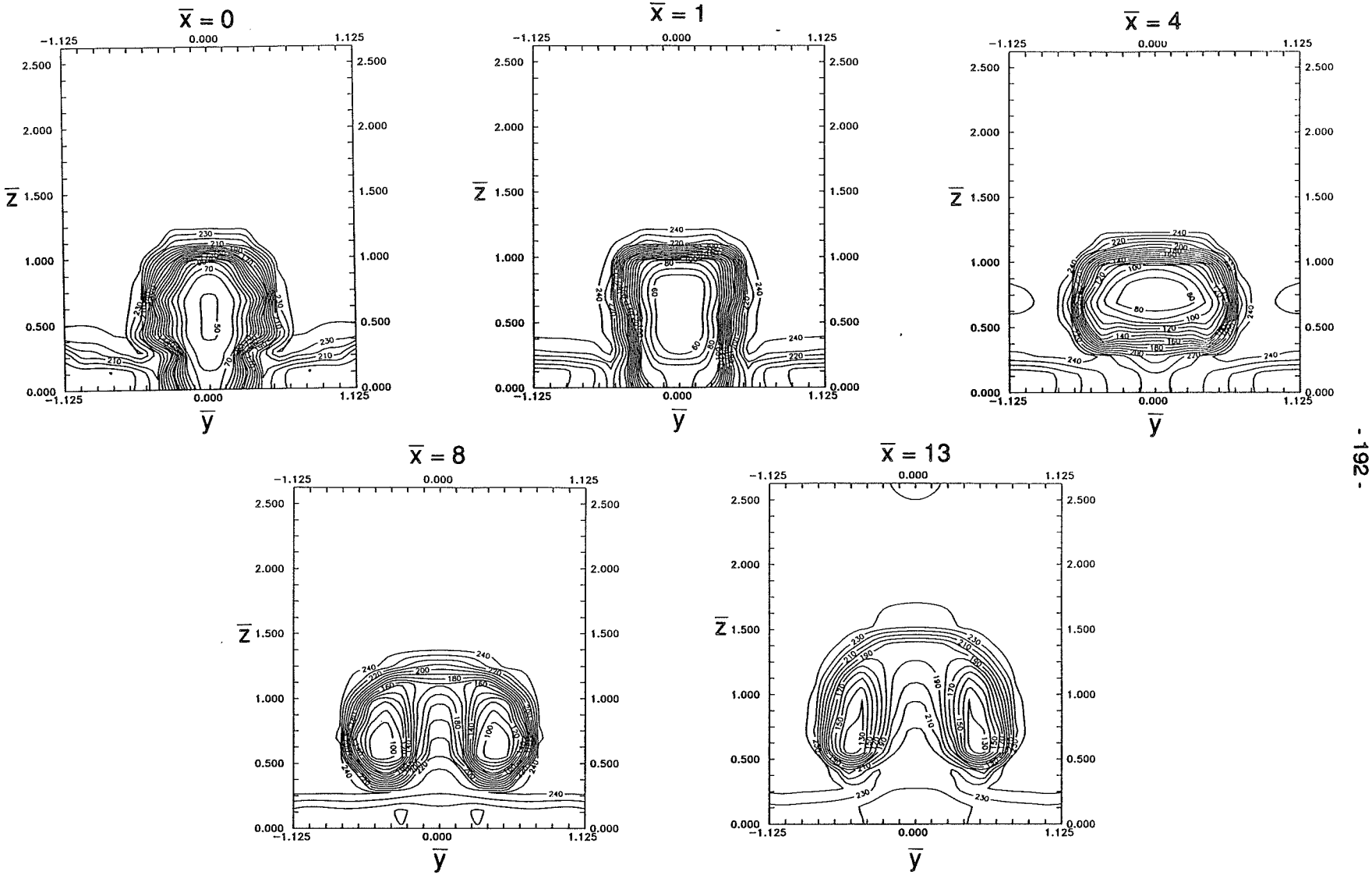

Figure 65. Total temperature (^{o}C). Full-scale model, wide spacing, tripped boundary layer, $\bar{\delta} = 0.35$, $\bar{p} = 1.0$, $\bar{v} = 1.33$ (experimental).

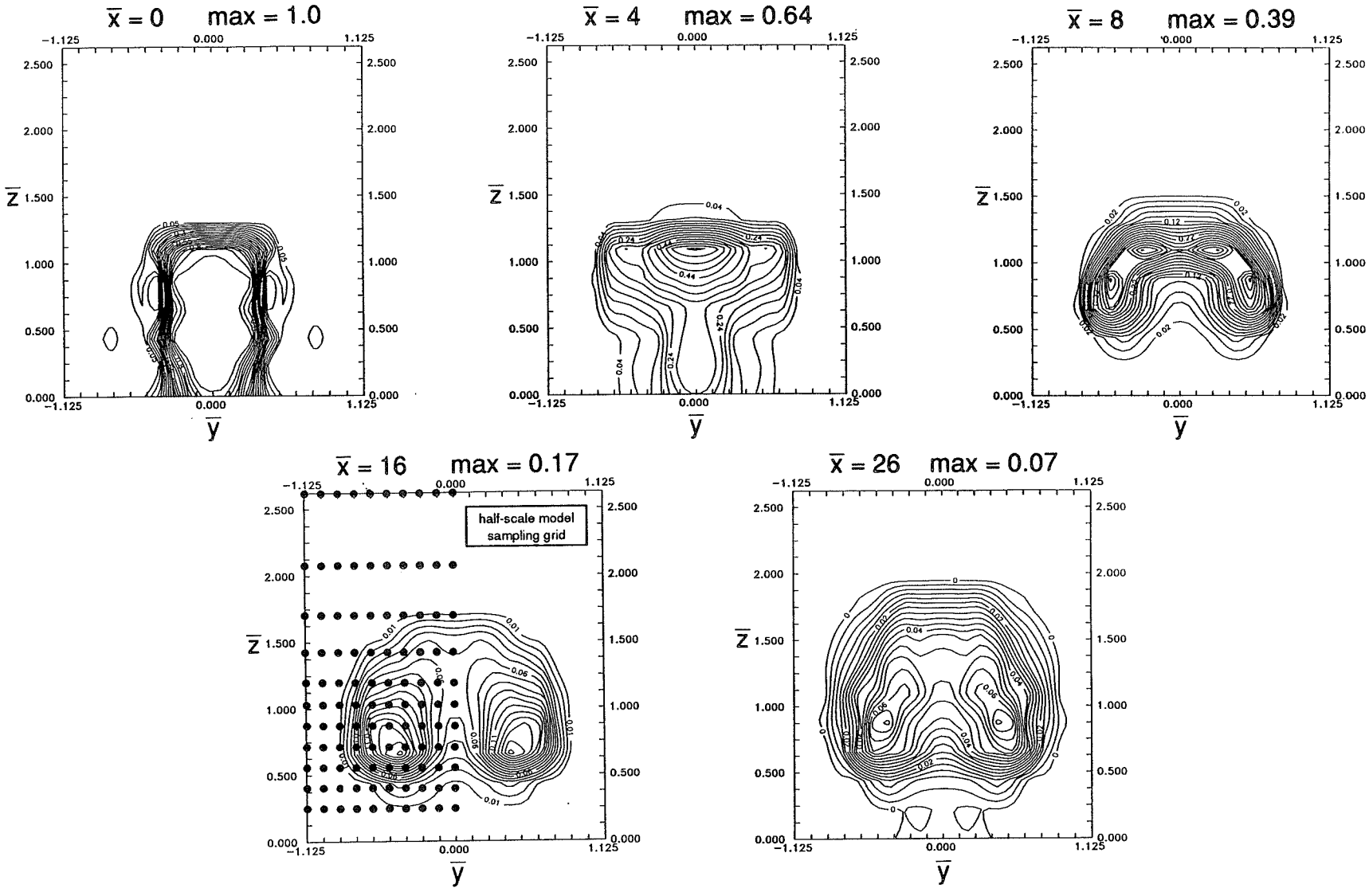

Figure 66. Helium mass fraction. Half-scale model, wide spacing, natural boundary layer, $\bar{\delta} = 0.40$, $\bar{p} = 1.0$, $\bar{v} = 1.36$ (experimental).

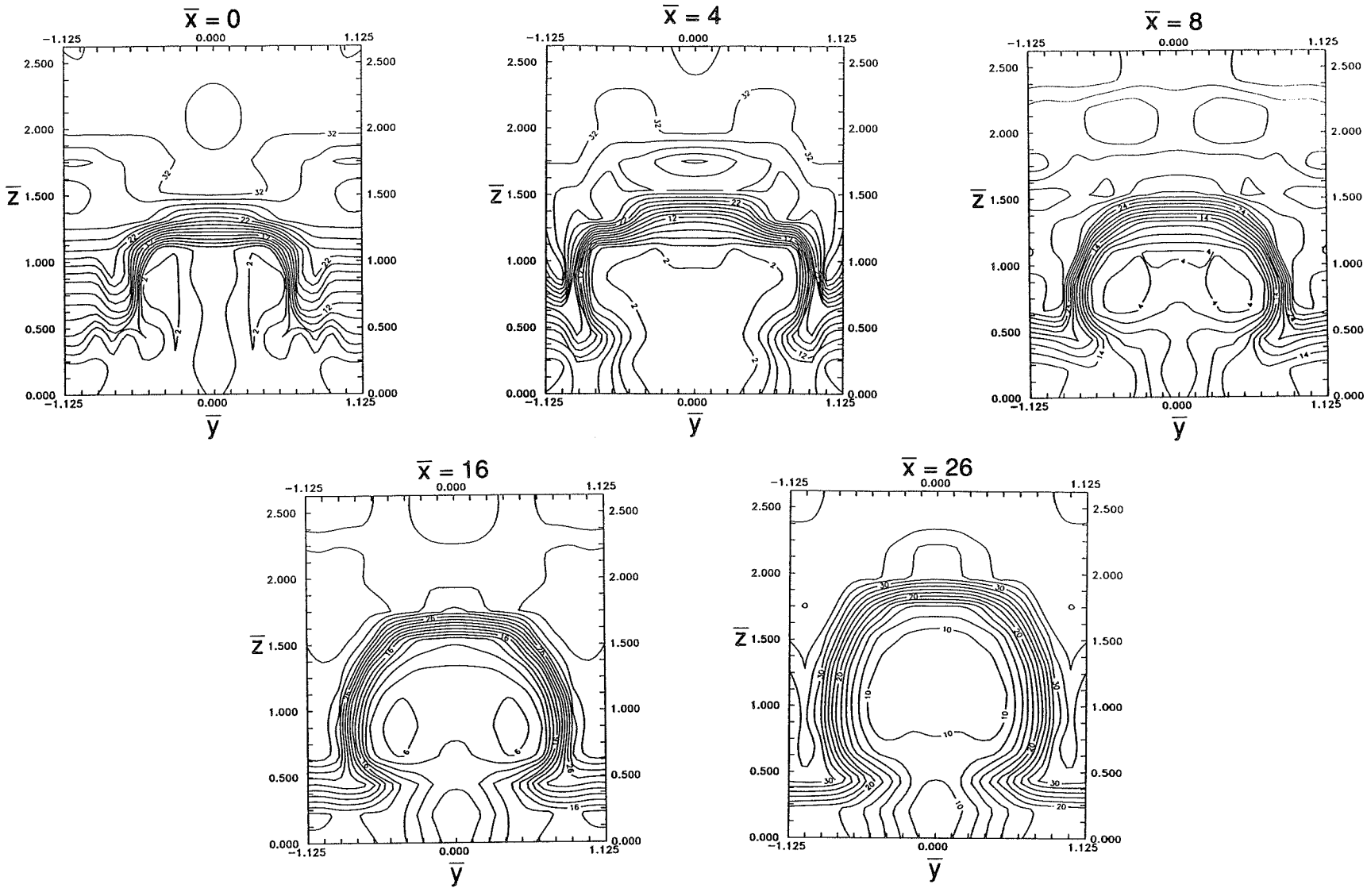

Figure 67. Pitot pressure (psia). Half-scale model, wide spacing, natural boundary layer, $\bar{\delta} = 0.40$, $\bar{p} = 1.0$, $\bar{v} = 1.36$ (experimental).

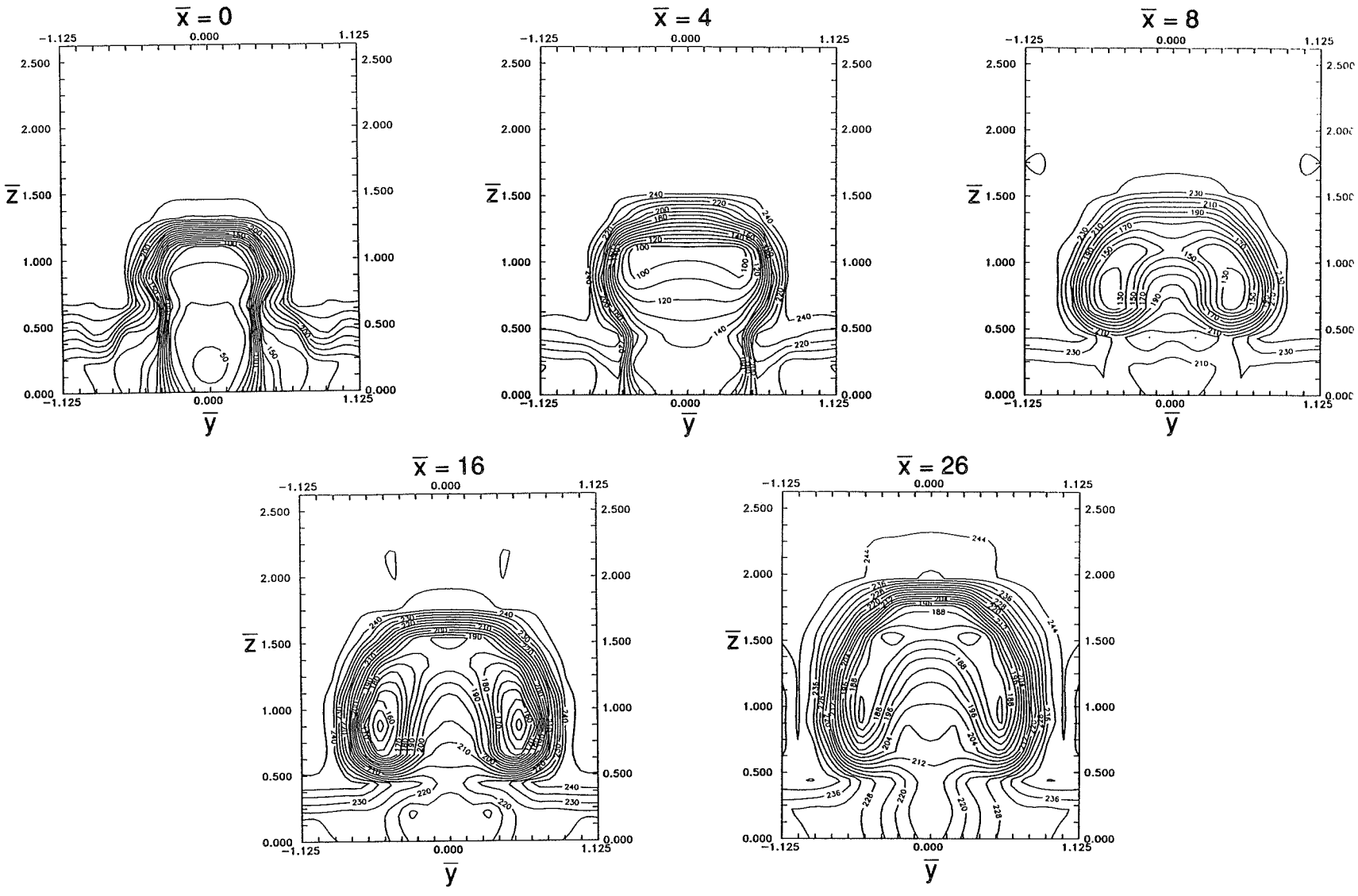

Figure 68. Total temperature (^{o}C). Half-scale model, wide spacing, natural boundary layer, $\bar{\delta} = 0.40$, $\bar{p} = 1.0$, $\bar{v} = 1.36$ (experimental).

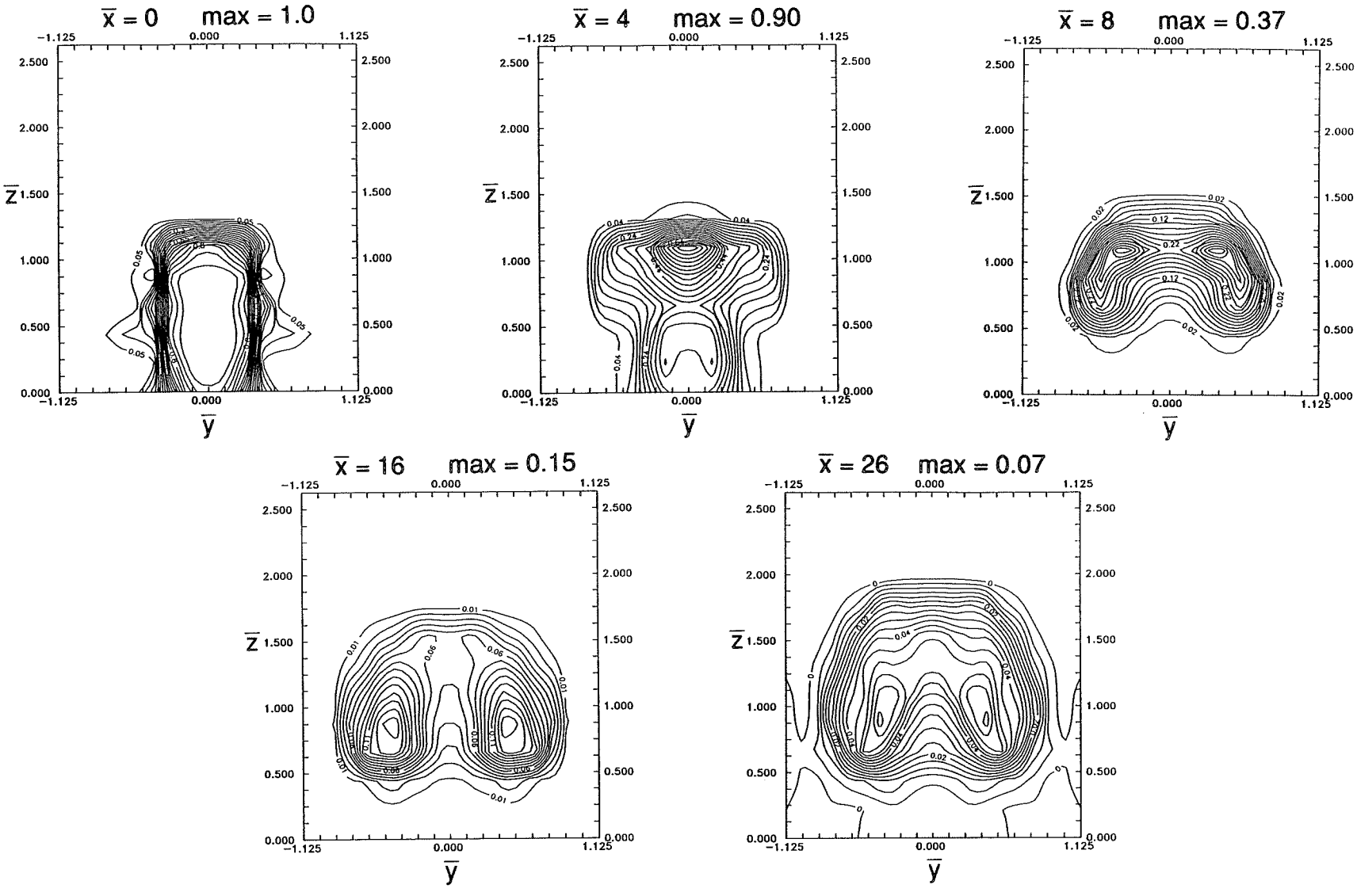

Figure 69. Helium mass fraction. Half-scale model, wide spacing, tripped boundary layer, $\bar{\delta} = 0.70$, $\bar{p} = 1.0$, $\bar{v} = 1.36$ (experimental).

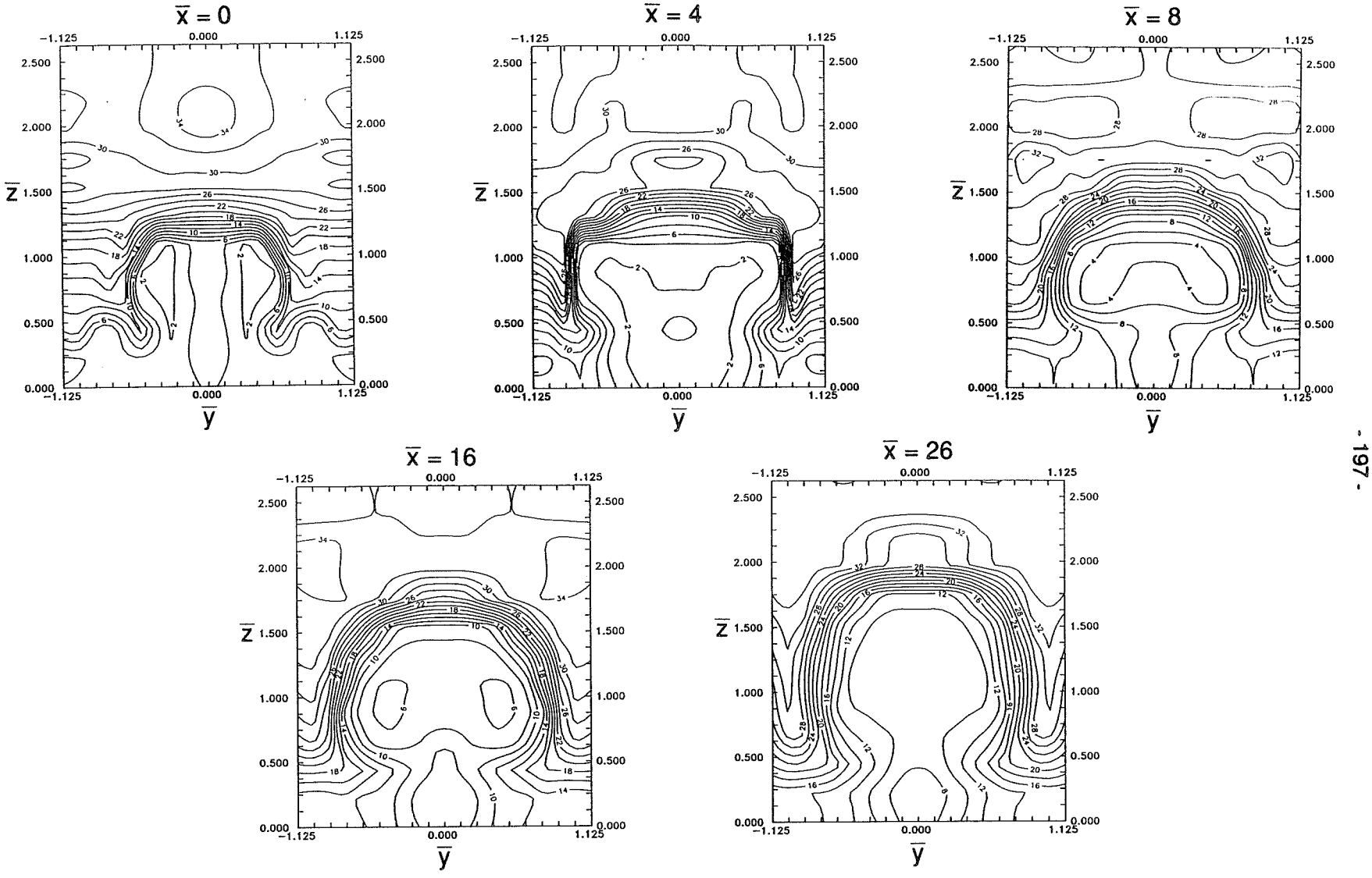

Figure 70. Pitot pressure (psia). Half-scale model, wide spacing, tripped boundary layer, $\bar{\delta} = 0.70$, $\bar{p} = 1.0$, $\bar{v} = 1.36$ (experimental).

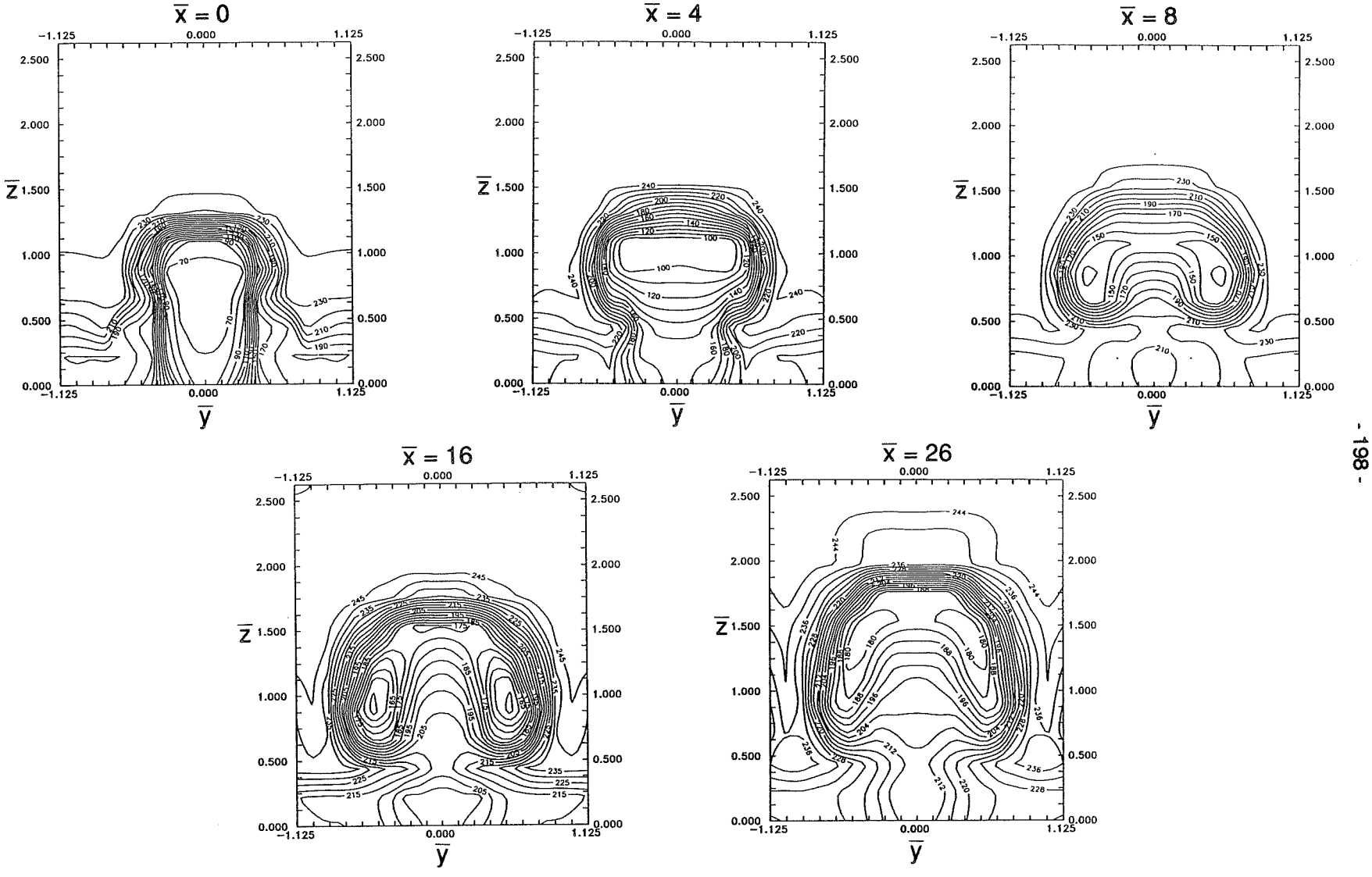

Figure 71. Total temperature (^{o}C). Half-scale model, wide spacing, tripped boundary layer, $\bar{\delta} = 0.70$, $\bar{p} = 1.0$, $\bar{v} = 1.36$ (experimental).

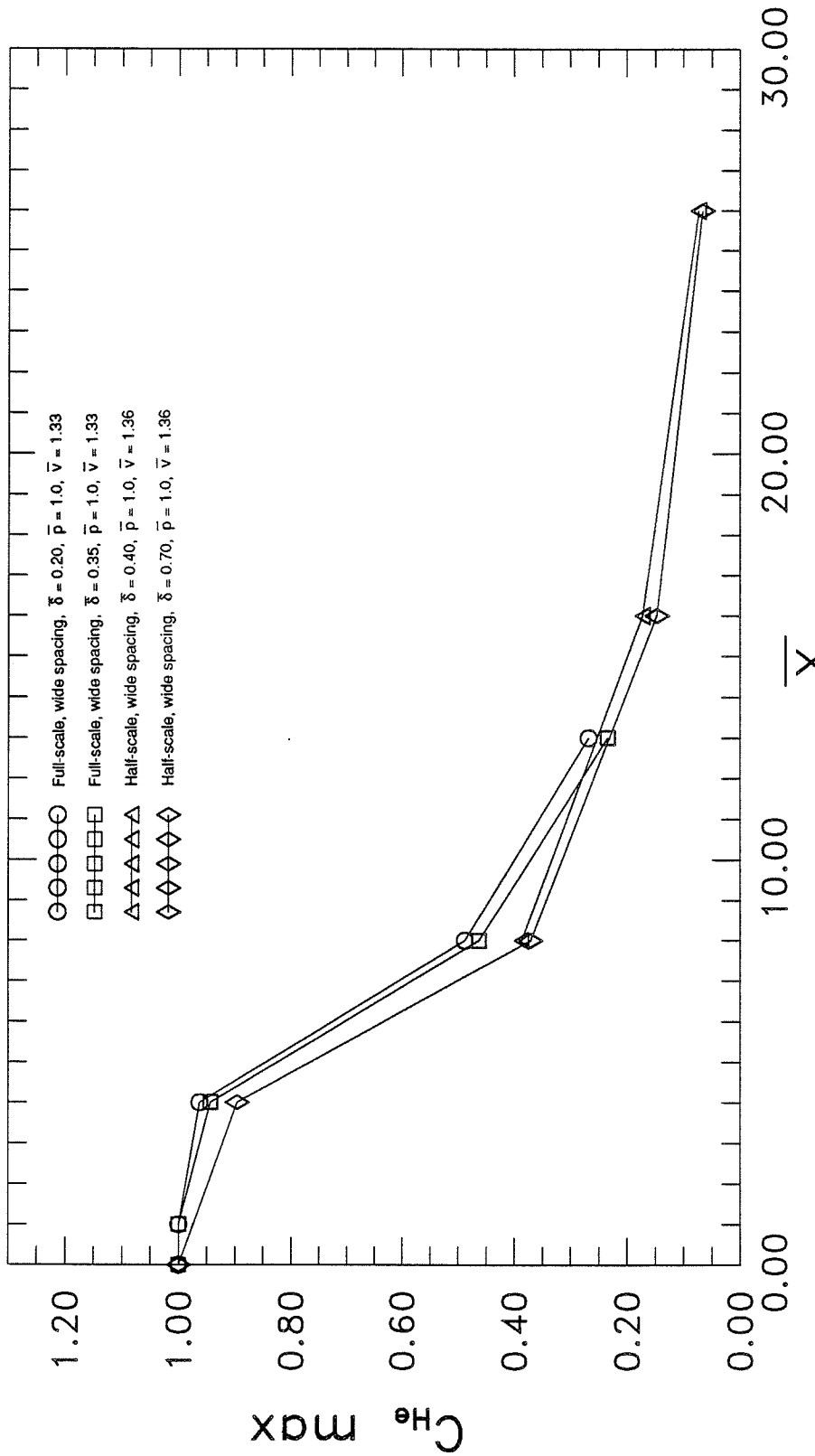

Figure 72. Decay of maximum helium mass fraction for wide spacing geometry with boundary layers of various heights (experimental).

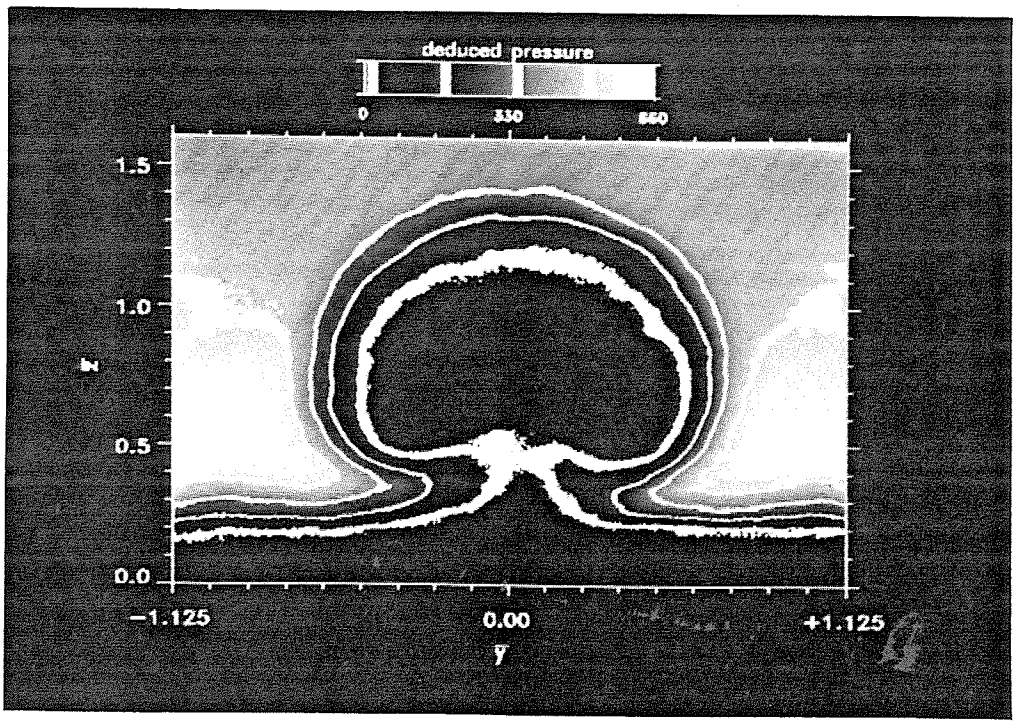

Figure 73. Mean of 22 planar Rayleigh images at $\bar{x}$ = 10.

Wide spacing, $\bar{\delta}$ = 0.35, $\bar{p}$ = 1.0, $\bar{v}$ = 1.33, $\alpha_c = \alpha_e = 4.76^o$.

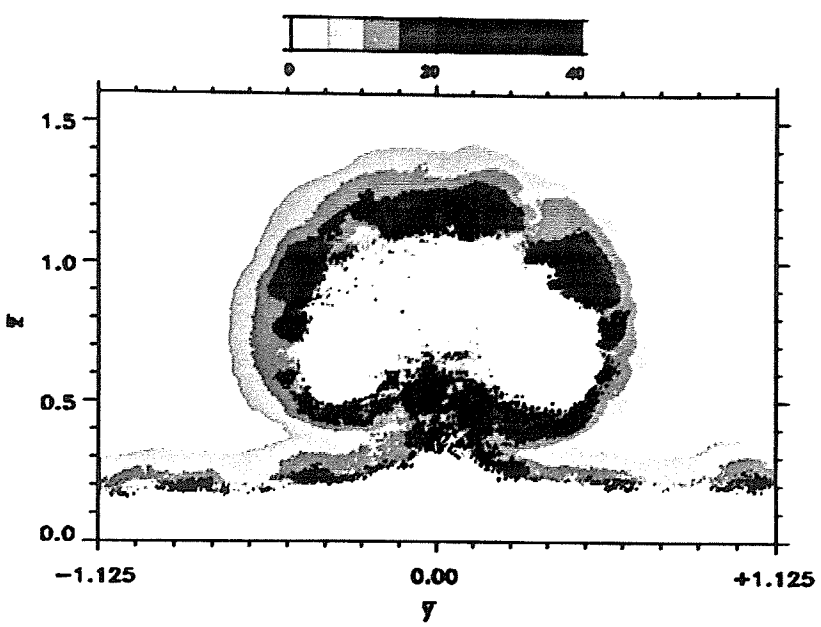

Figure 74. Standard deviation (%mean) about the mean for planar Rayleigh images at $\bar{x}$ = 10.

Wide spacing, $\bar{\delta}$ = 0.35, $\bar{p}$ = 1.0, $\bar{v}$ = 1.33, $\alpha_c = \alpha_e = 4.76^o$.

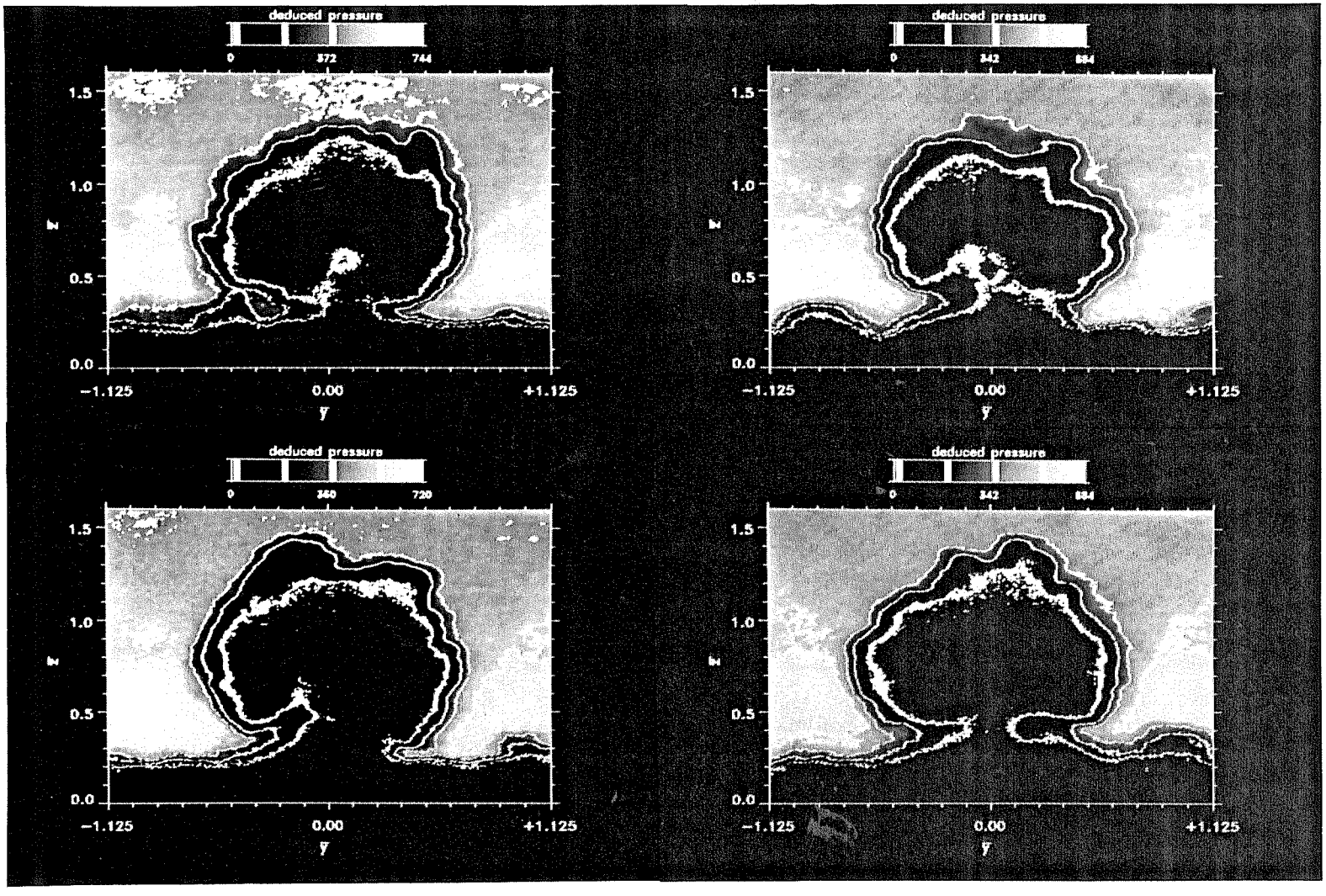

Figure 75. Instantaneous planar Rayleigh images at $\overline{x} = 10$. Wide spacing, $\overline{\delta} = 0.35$, $\overline{p} = 1.0$, $\overline{v} = 1.33$, $\alpha_c = \alpha_e = 4.76^o$.

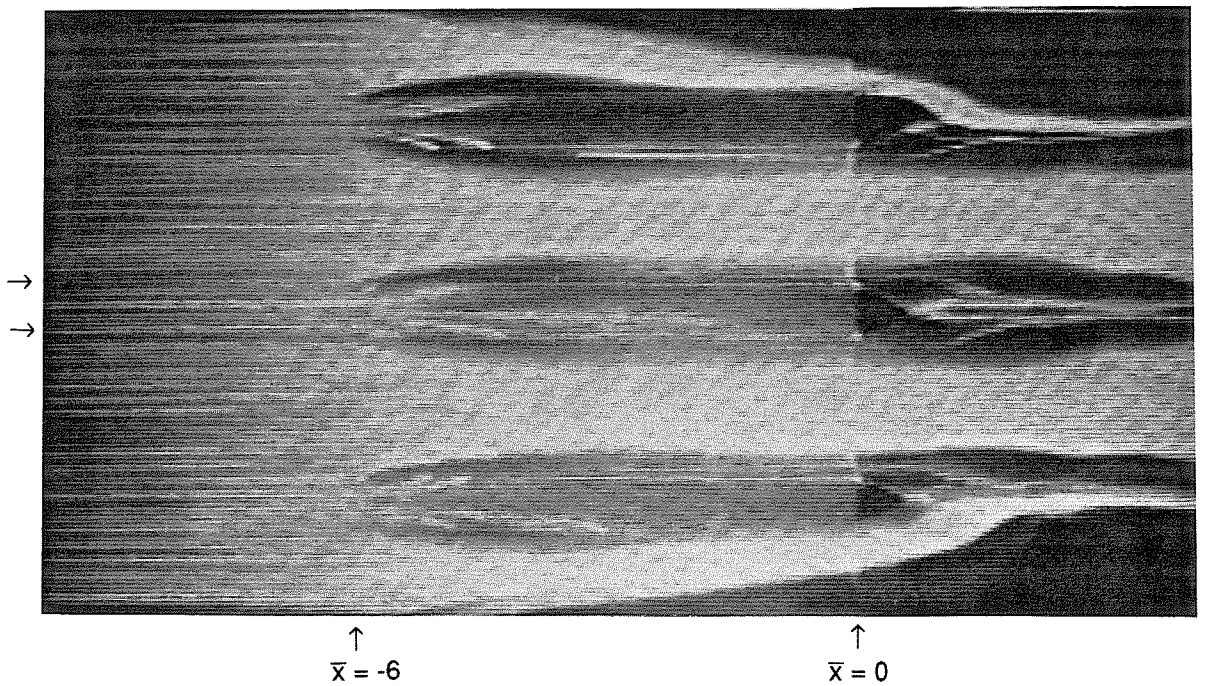

Figure 76. Surface oil flow photograph.

Full-scale model, wide spacing, $\overline{\delta}$ = 0.20, $\overline{p}$ = 1.0, $\alpha_c = \alpha_e = 4.76^o$.

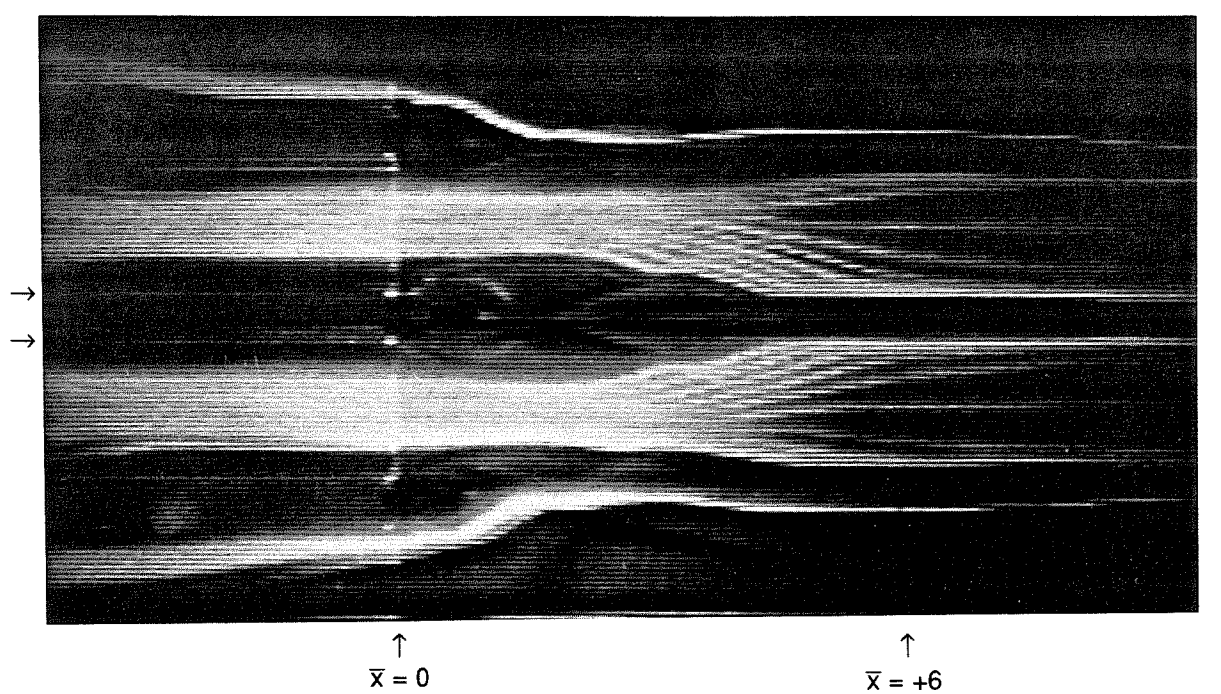

Figure 77. Surface oil flow photograph.

Full-scale model, wide spacing, $\overline{\delta}$ = 0.20, underexpanded jet, $\alpha_c = \alpha_e = 4.76^o$.

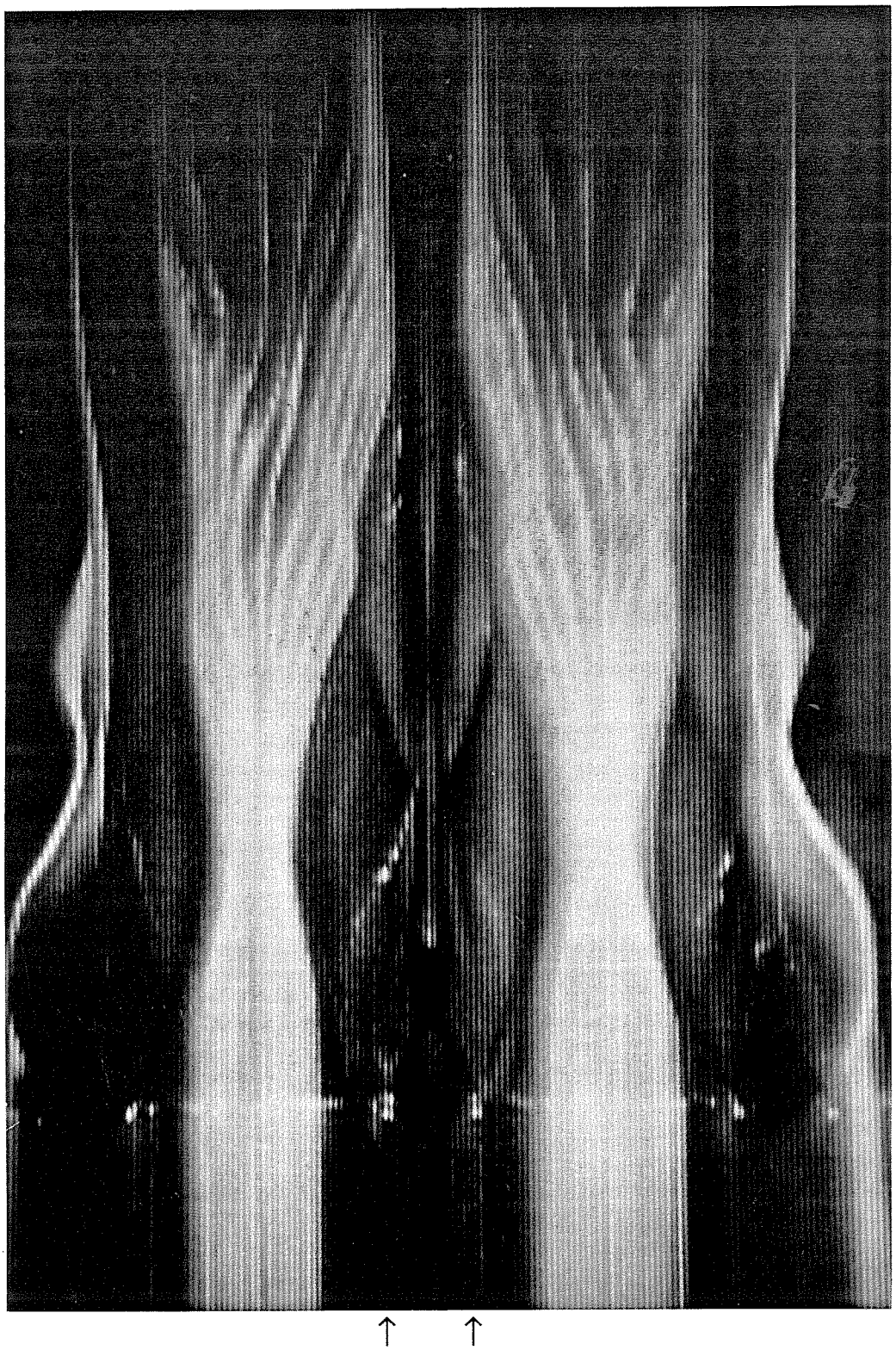

Figure 78. Surface oil flow photograph. Full-scale model, wide spacing, $\bar{\delta} = 0.20$, underexpanded jet, $\alpha_c = \alpha_e = 4.76^o$.

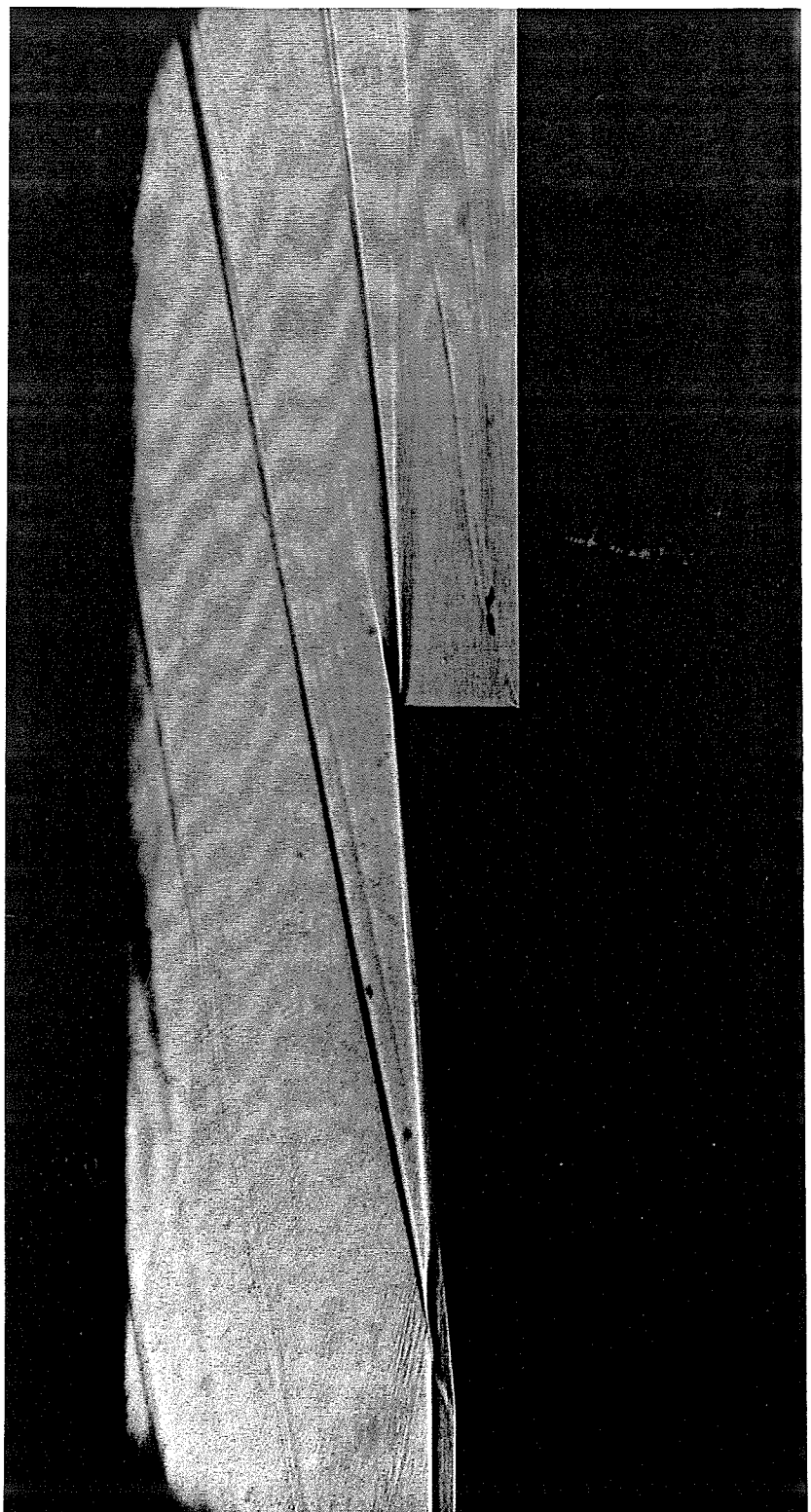

Figure 79. Schlieren photograph. Full-scale model, narrow spacing, $\bar{\delta} = 0.20$, $\bar{p} = 1.0$, $\alpha_c = \alpha_e = 4.76^o$.

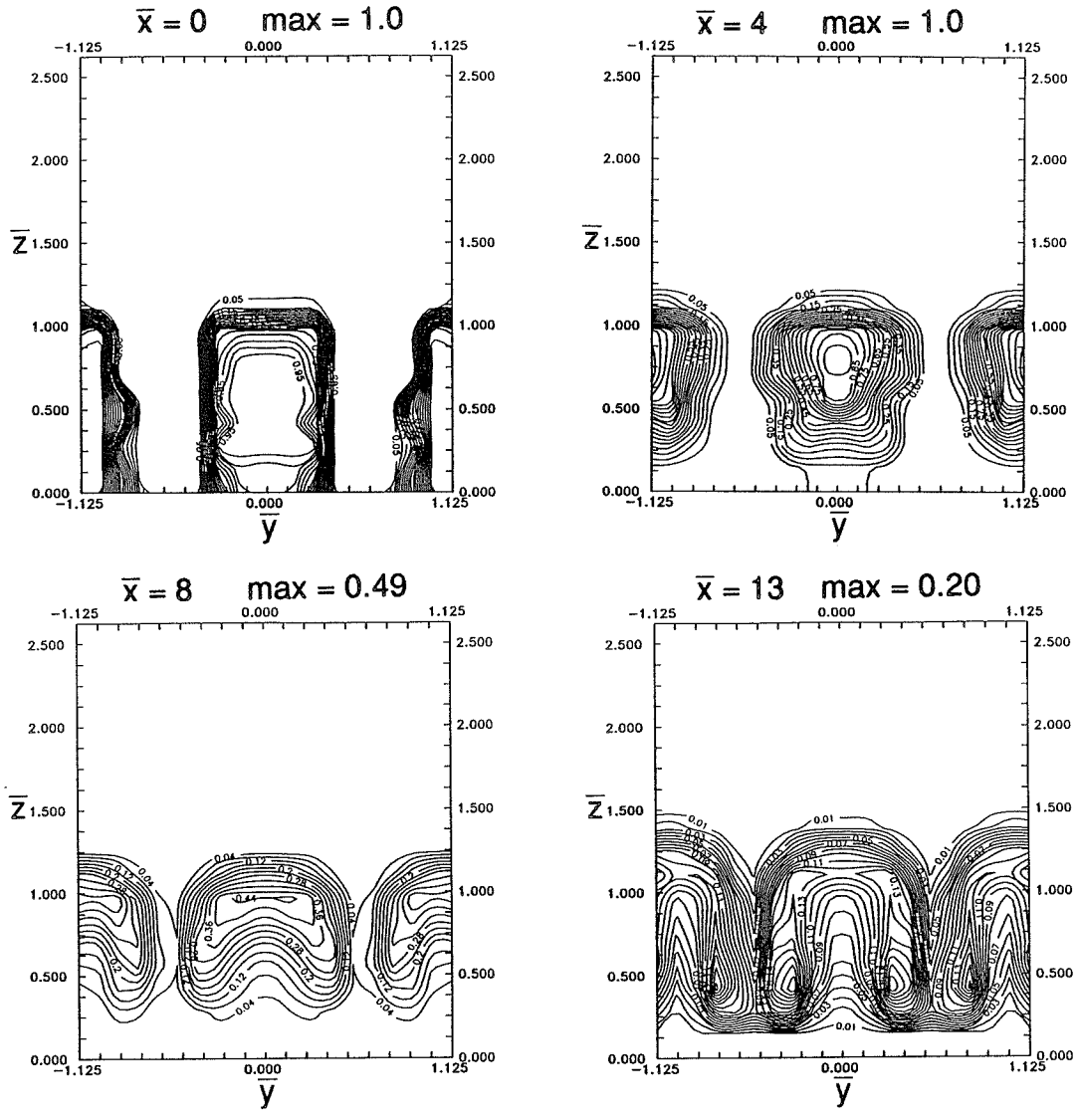

Figure 80. Helium mass fraction. Full-scale model, narrow spacing, natural boundary layer, $\bar{\delta} = 0.20$, $\bar{p} = 1.0$, $\bar{v} = 1.28$ (experimental).

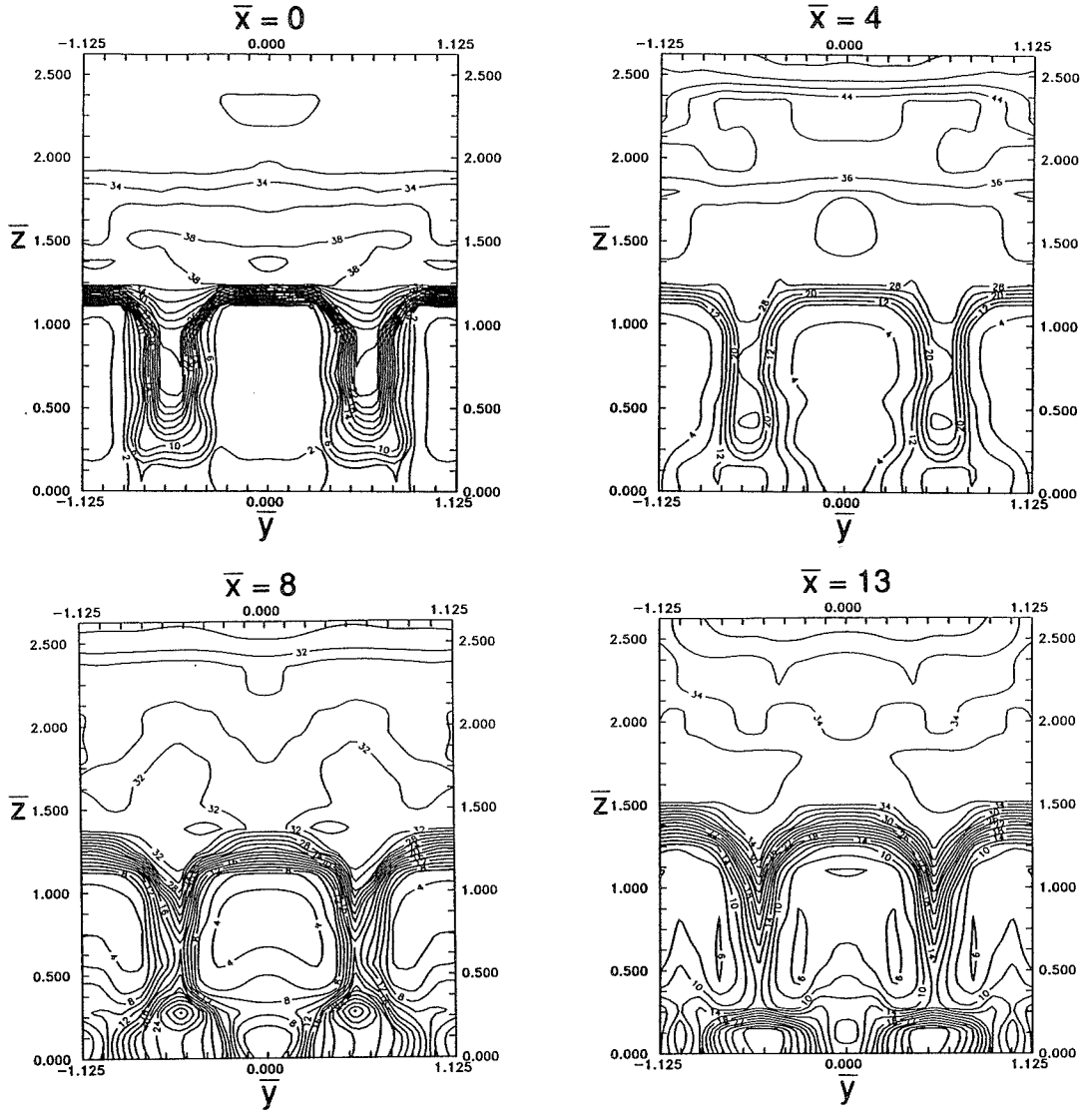

Figure 81. Pitot pressure (psia). Full-scale model, narrow spacing, natural boundary layer, $\bar{\delta} = 0.20$, $\bar{p} = 1.0$, $\bar{v} = 1.28$ (experimental).

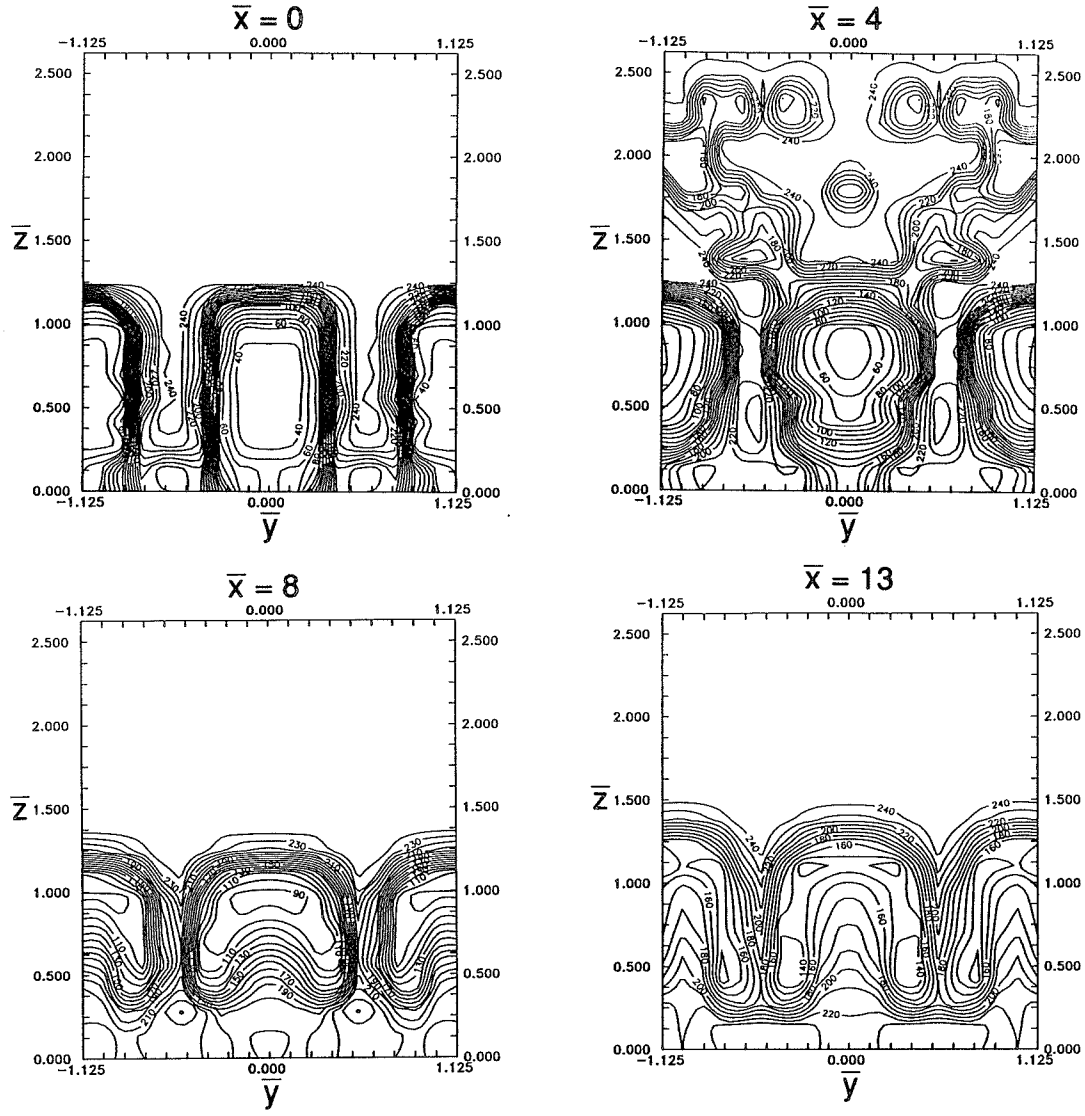

Figure 82. Total temperature (^{o}C). Full-scale model, narrow spacing, natural boundary layer, $\bar{\delta} = 0.20$, $\bar{p} = 1.0$, $\bar{v} = 1.28$ (experimental).

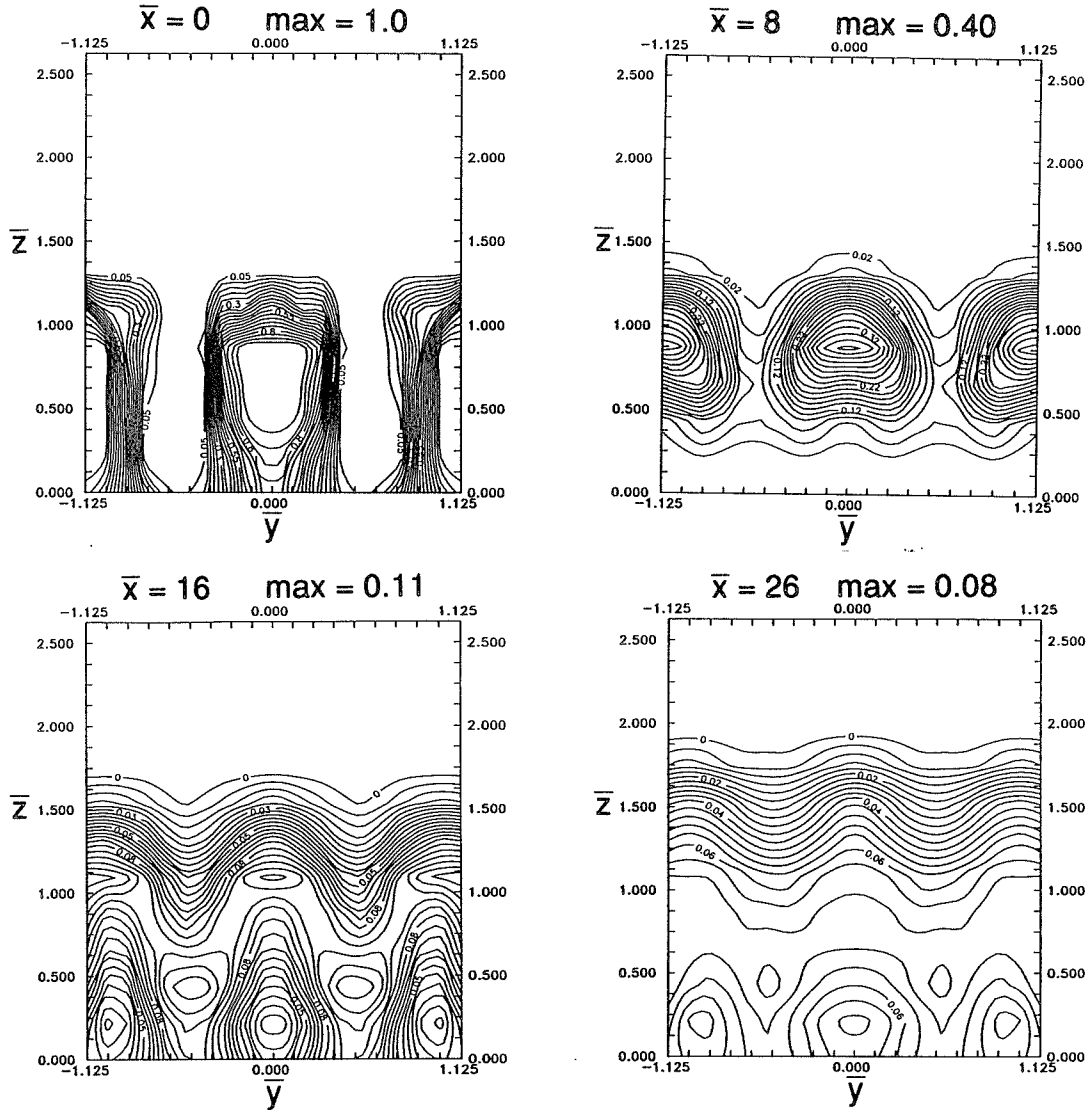

Figure 83. Helium mass fraction. Half-scale model, narrow spacing, tripped boundary layer, $\bar{\delta} = 0.70$, $\bar{p} = 1.0$, $\bar{v} = 1.35$ (experimental).

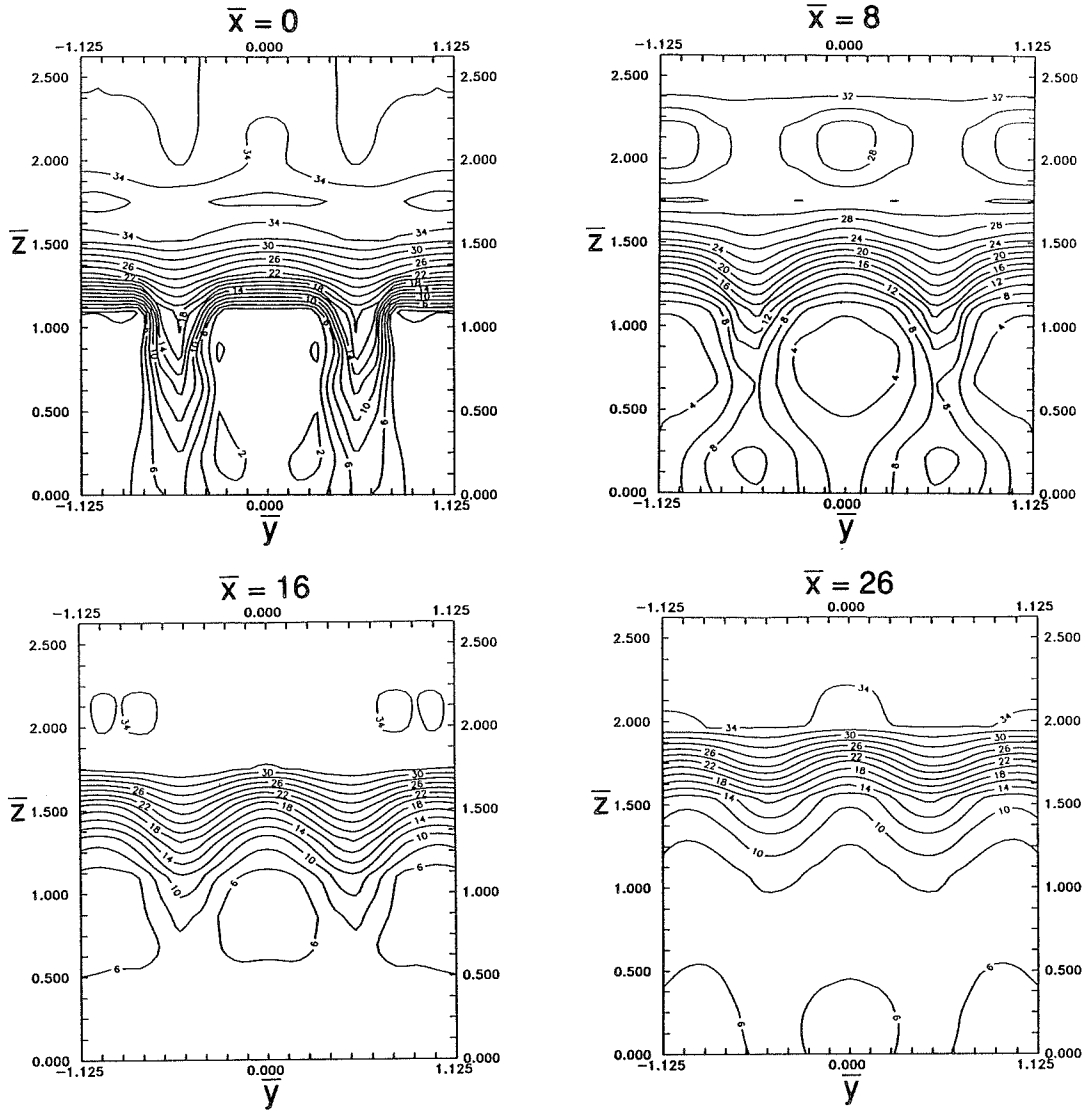

Figure 84. Pitot pressure (psia). Half-scale model, narrow spacing, tripped boundary layer, $\bar{\delta} = 0.70$, $\bar{p} = 1.0$, $\bar{v} = 1.35$ (experimental).

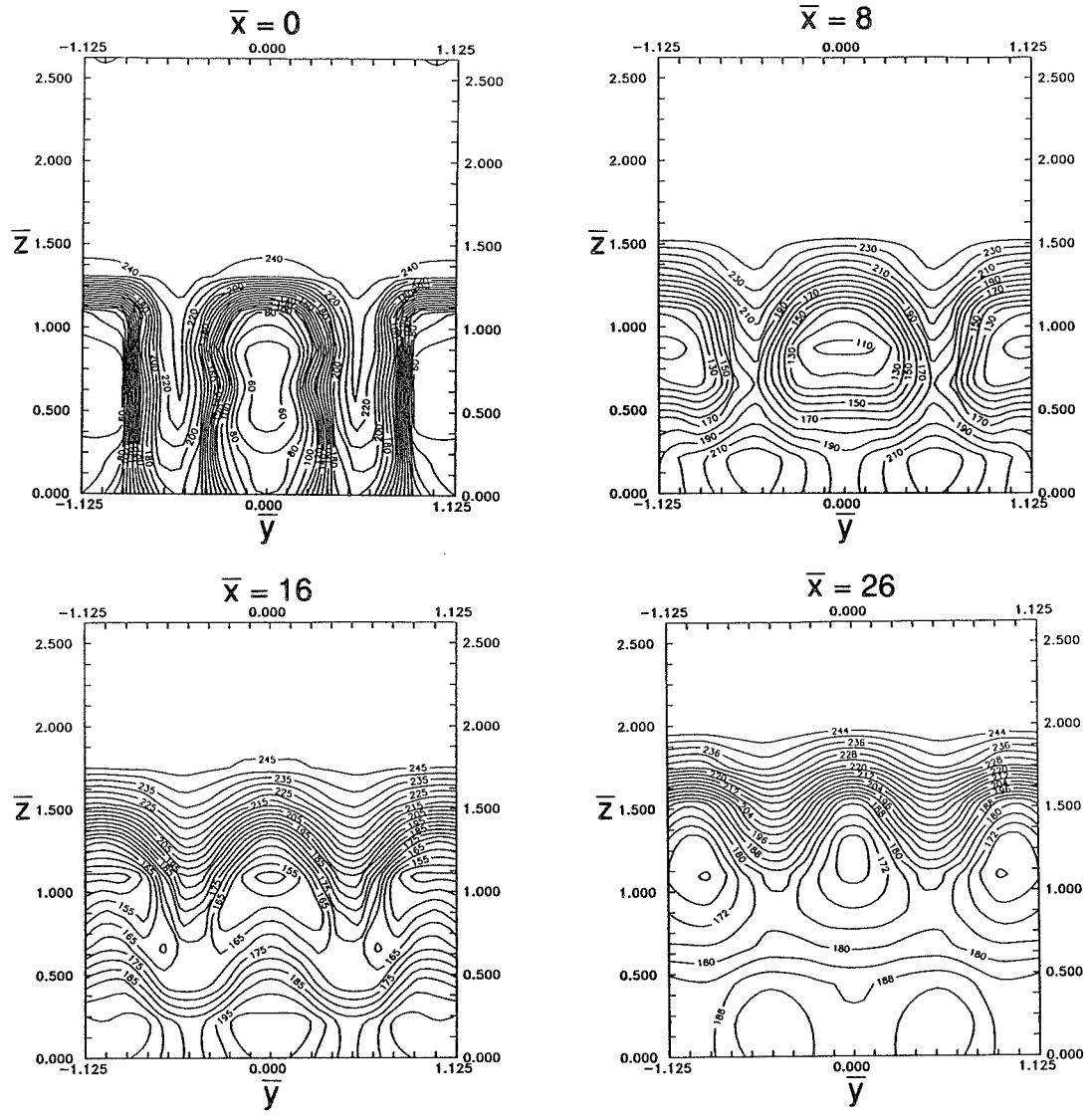

Figure 85. Total temperature (^{o}C). Half-scale model, narrow spacing, tripped boundary layer, $\bar{\delta} = 0.70$, $\bar{p} = 1.0$, $\bar{v} = 1.35$ (experimental).

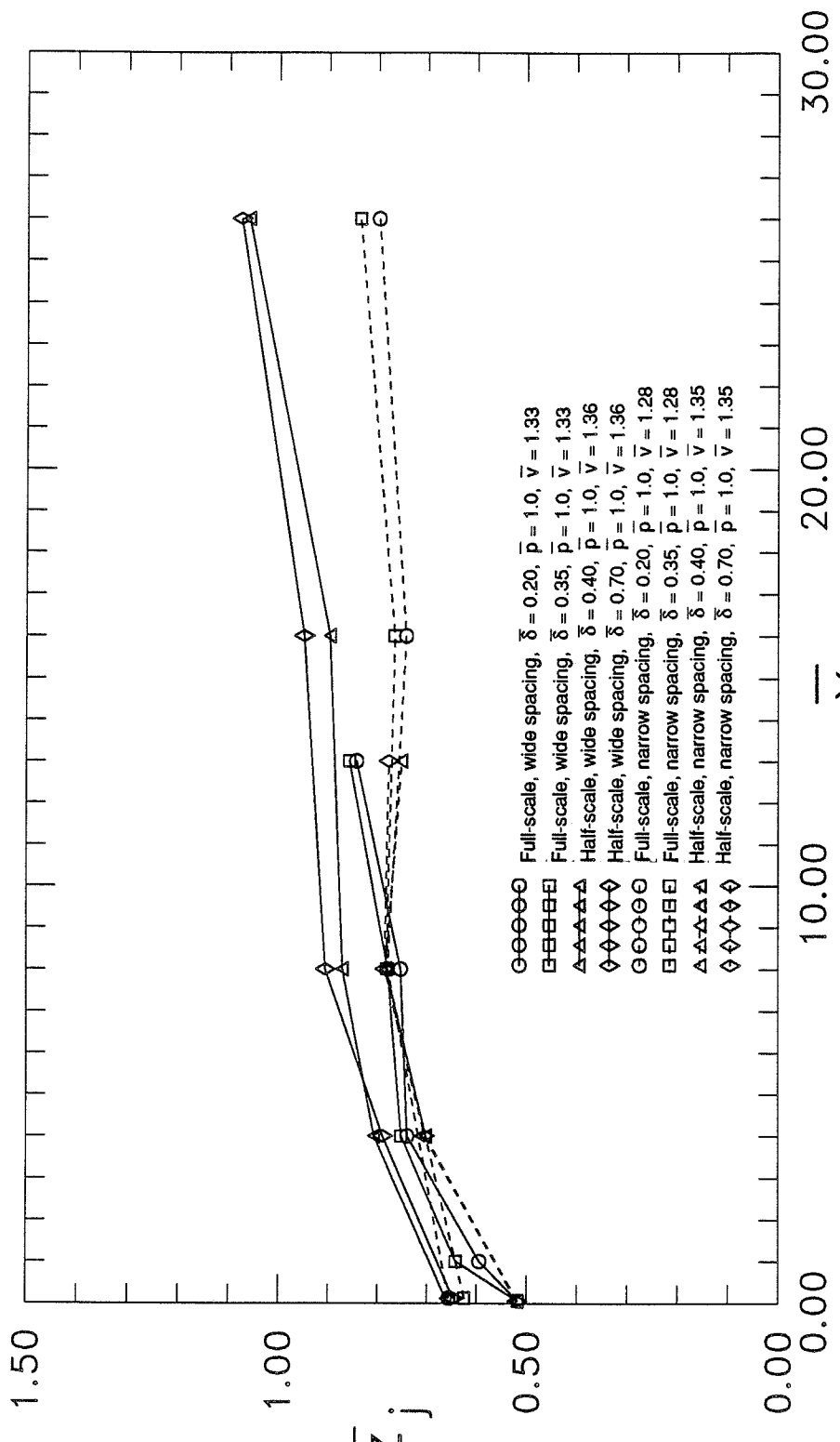

Figure 86. Jet lift-off : Boundary layer and injector spacing effects (experimental).

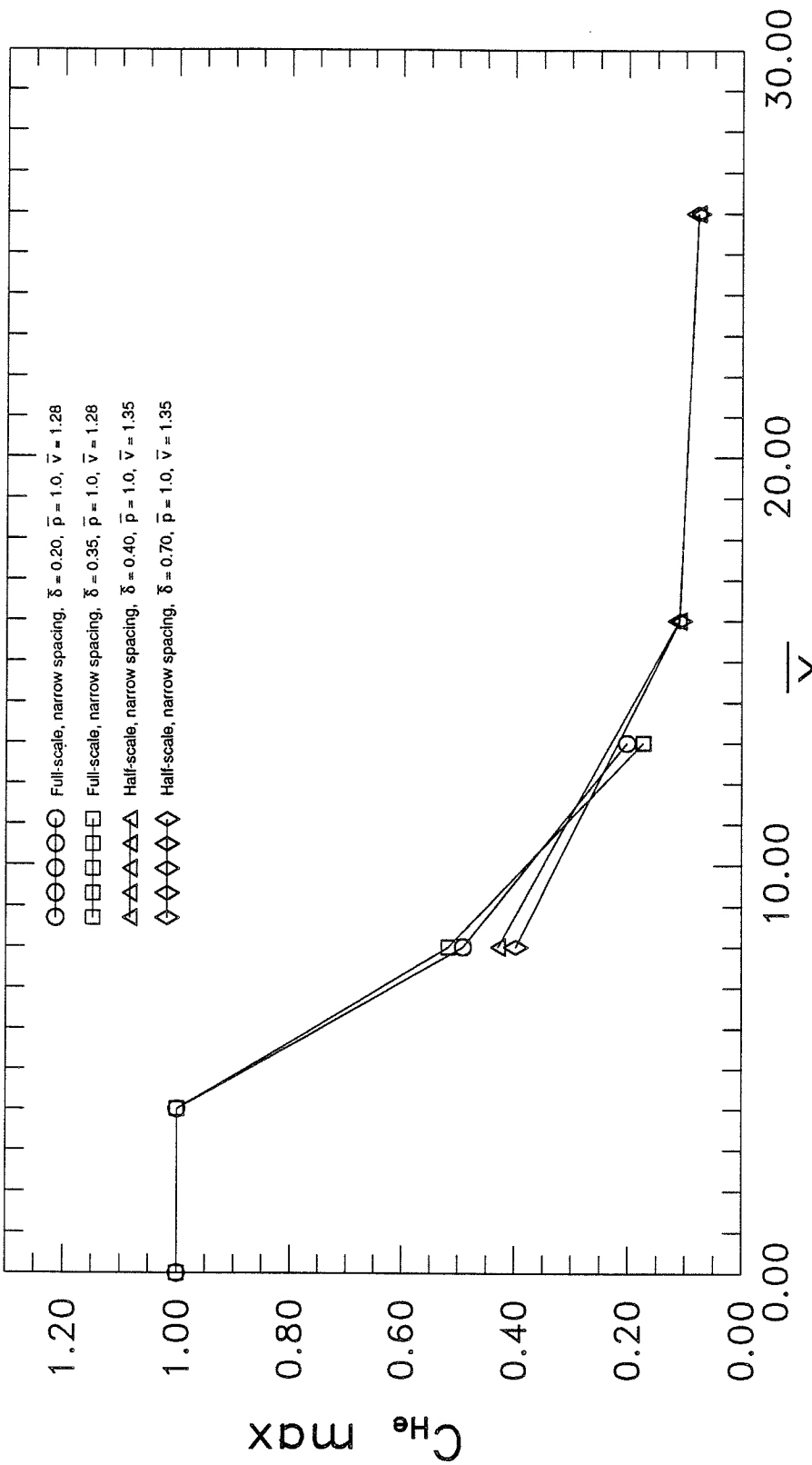

Figure 87. Decay of maximum helium mass fraction for narrow spacing geometry with boundary layers of various heights (experimental).

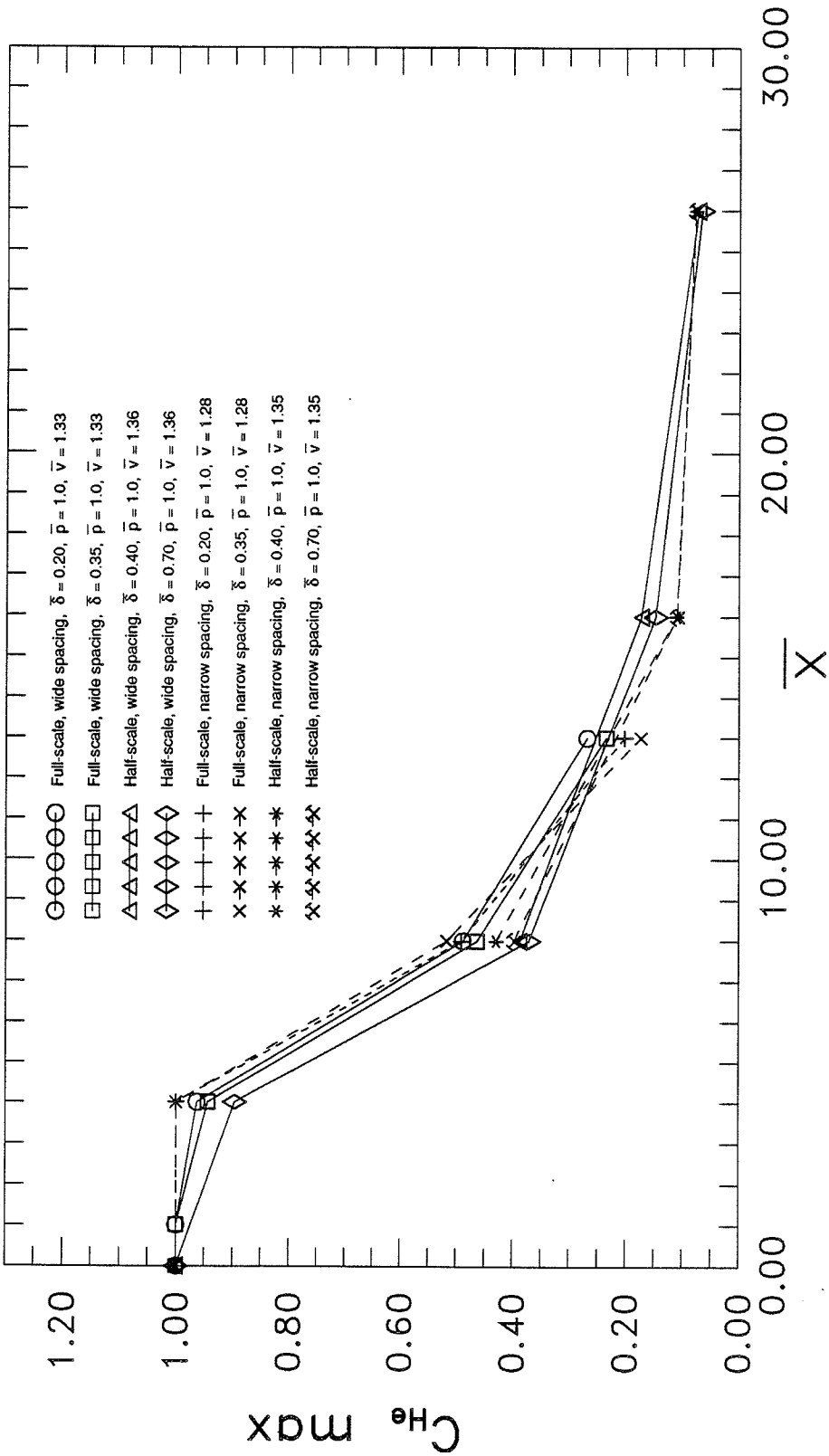

Figure 88. Decay of maximum helium mass fraction for various spacings and boundary layer thicknesses (experimental).

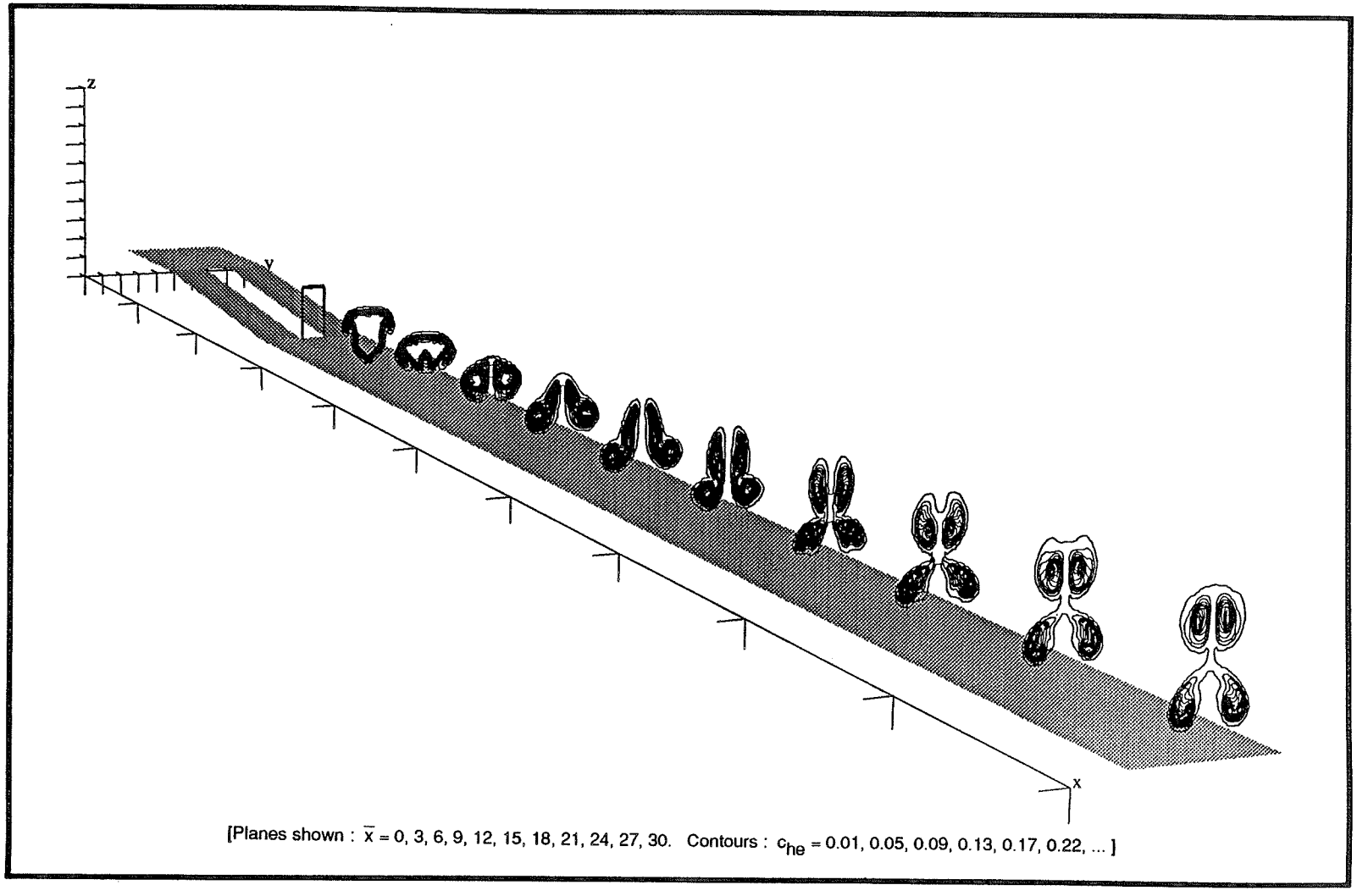

Figure 89. Contours of constant helium mass fraction.

Wide spacing, $\bar{\delta}$ = 0 (inviscid b.c.), $\bar{p}$ = 1.0, $\bar{v}$ = 1.0, $\alpha_c = \alpha_e = 4.76^o$ (computational).

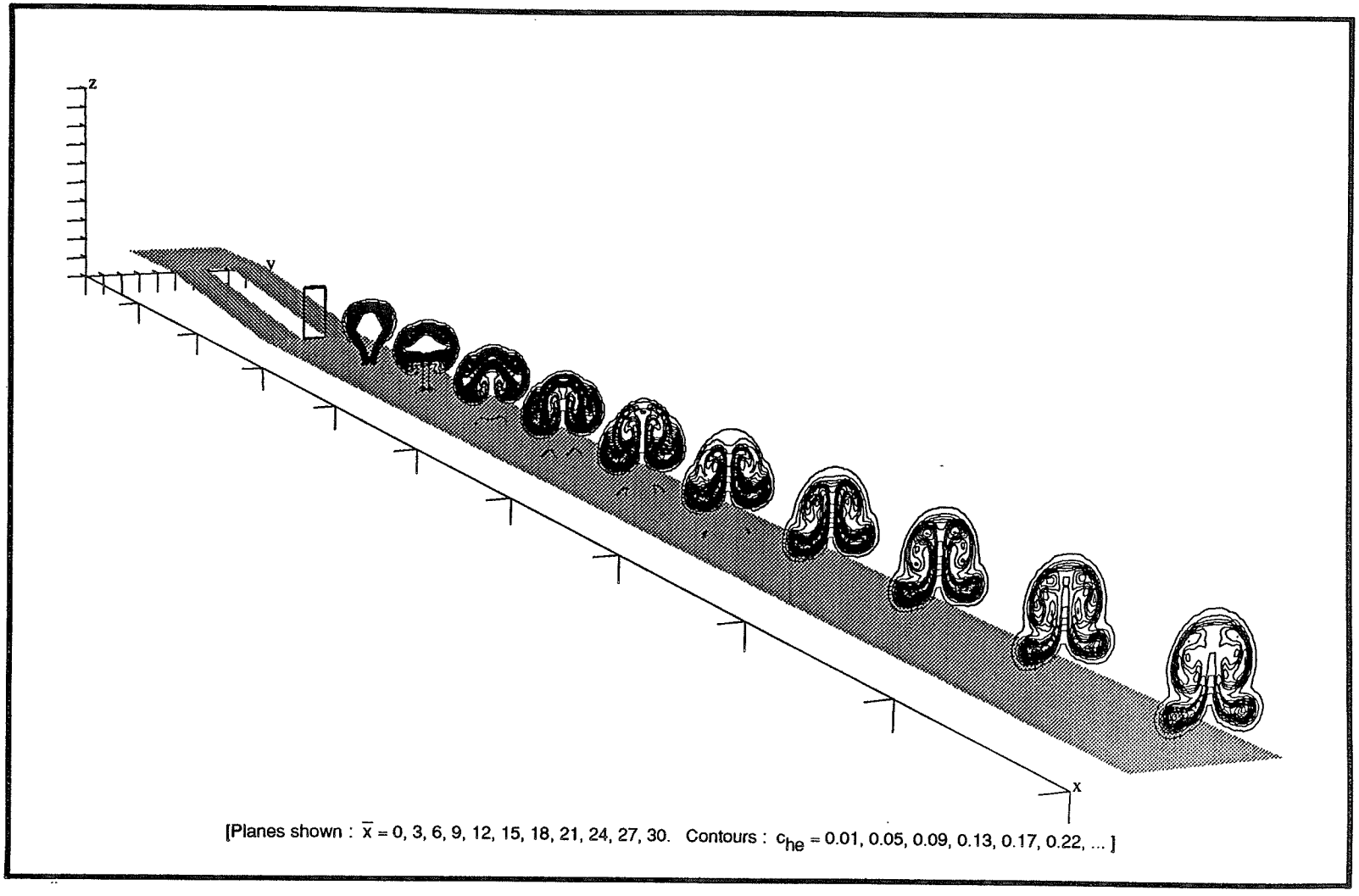

Figure 90. Contours of constant helium mass fraction.

Wide spacing, $\bar{\delta}$ = 1.0, $\bar{p}$ = 1.0, $\bar{v}$ = 1.0, $\alpha_c = \alpha_e = 4.76^o$ (computational).

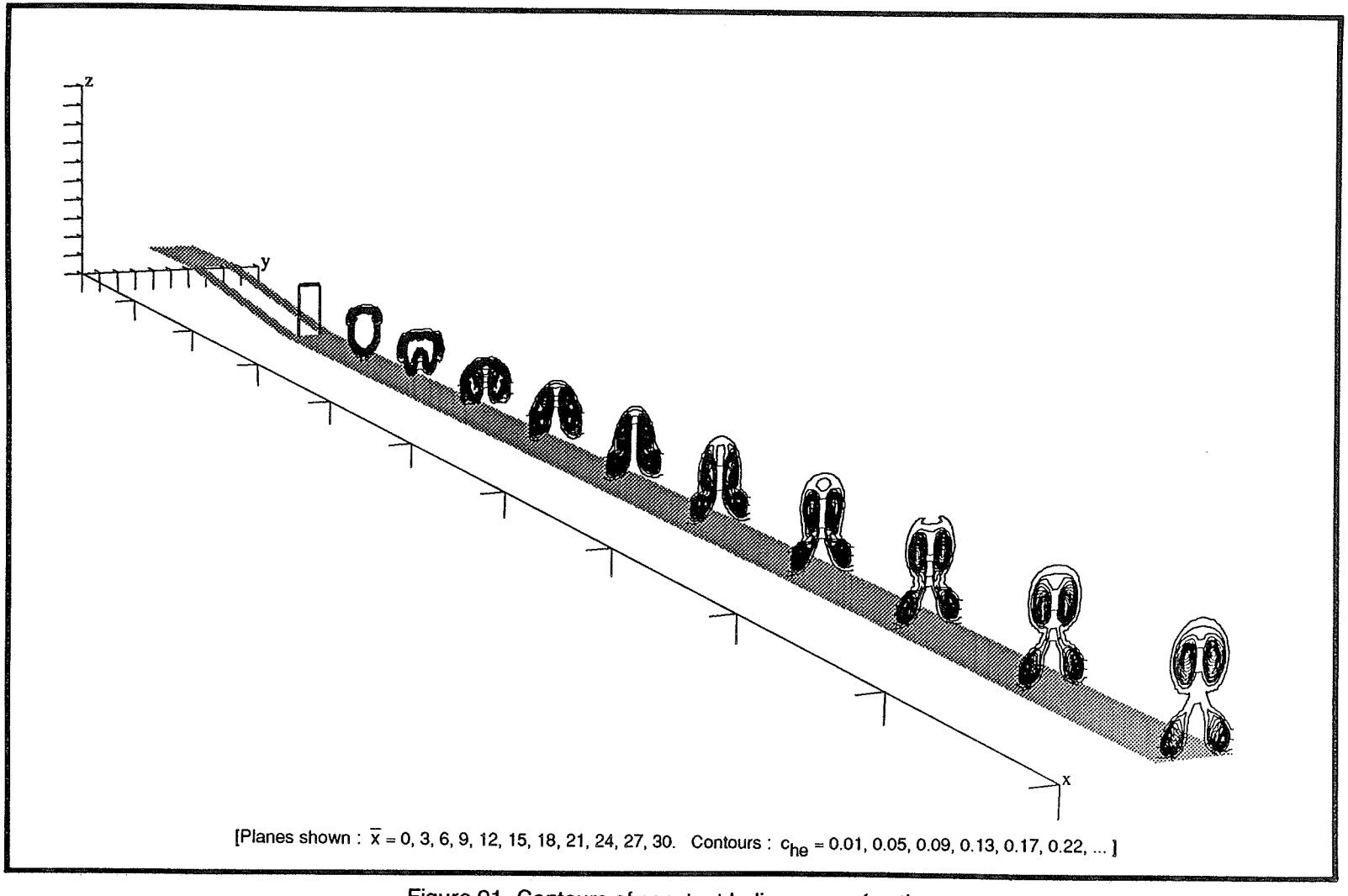

Figure 91. Contours of constant helium mass fraction.

Narrow spacing, $\bar{\delta}$ = 0 (inviscid b.c.), $\bar{p}$ = 1.0, $\bar{v}$ = 1.0, $\alpha_c = \alpha_e = 4.76^o$ (computational).

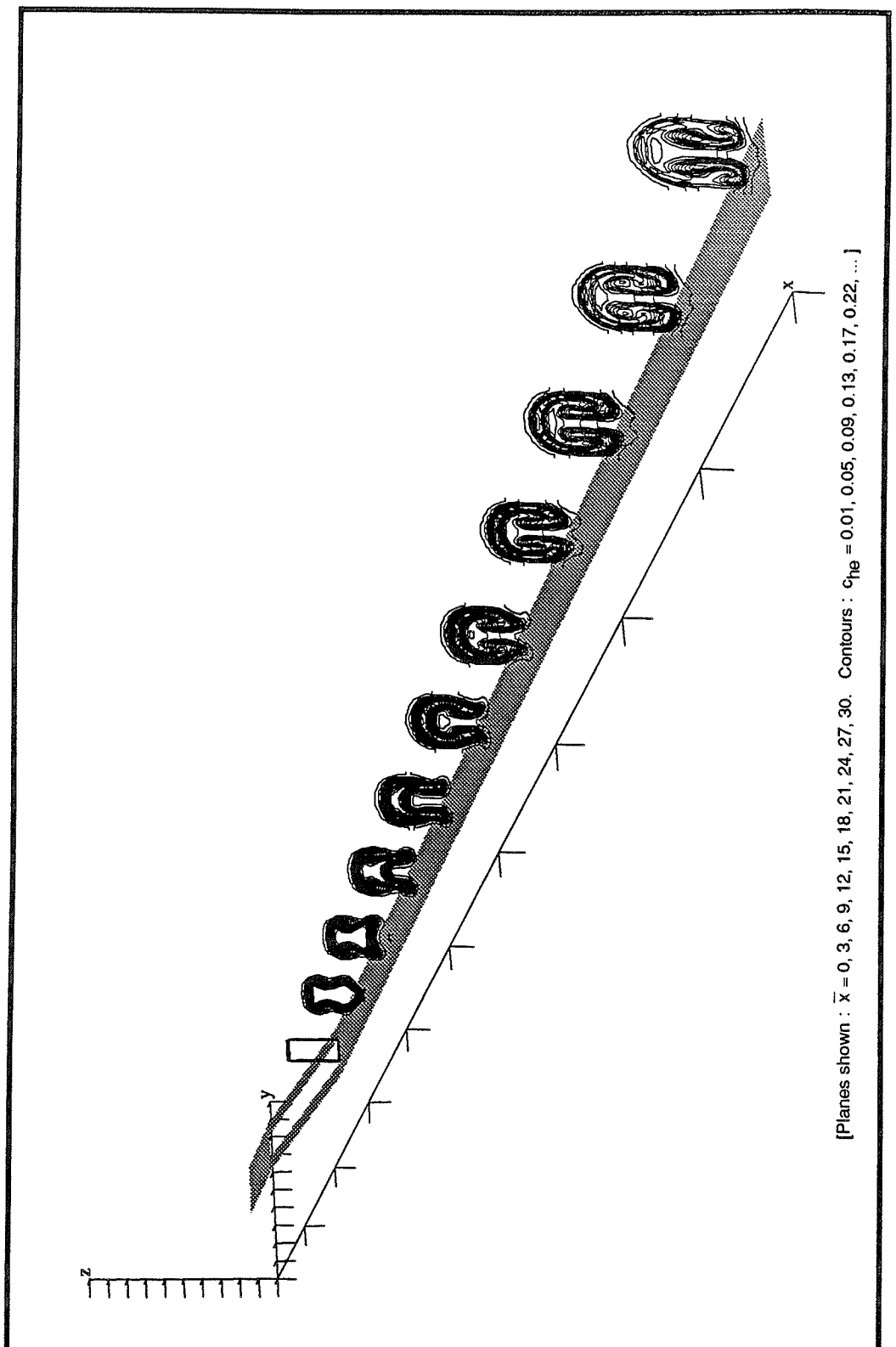

Figure 92. Contours of constant helium mass fraction.

Narrow spacing, $\bar{\delta}$ = 0.20, $\bar{p}$ = 1.0, $\bar{v}$ = 1.0, $\alpha_c = \alpha_e = 4.76^o$ (computational).

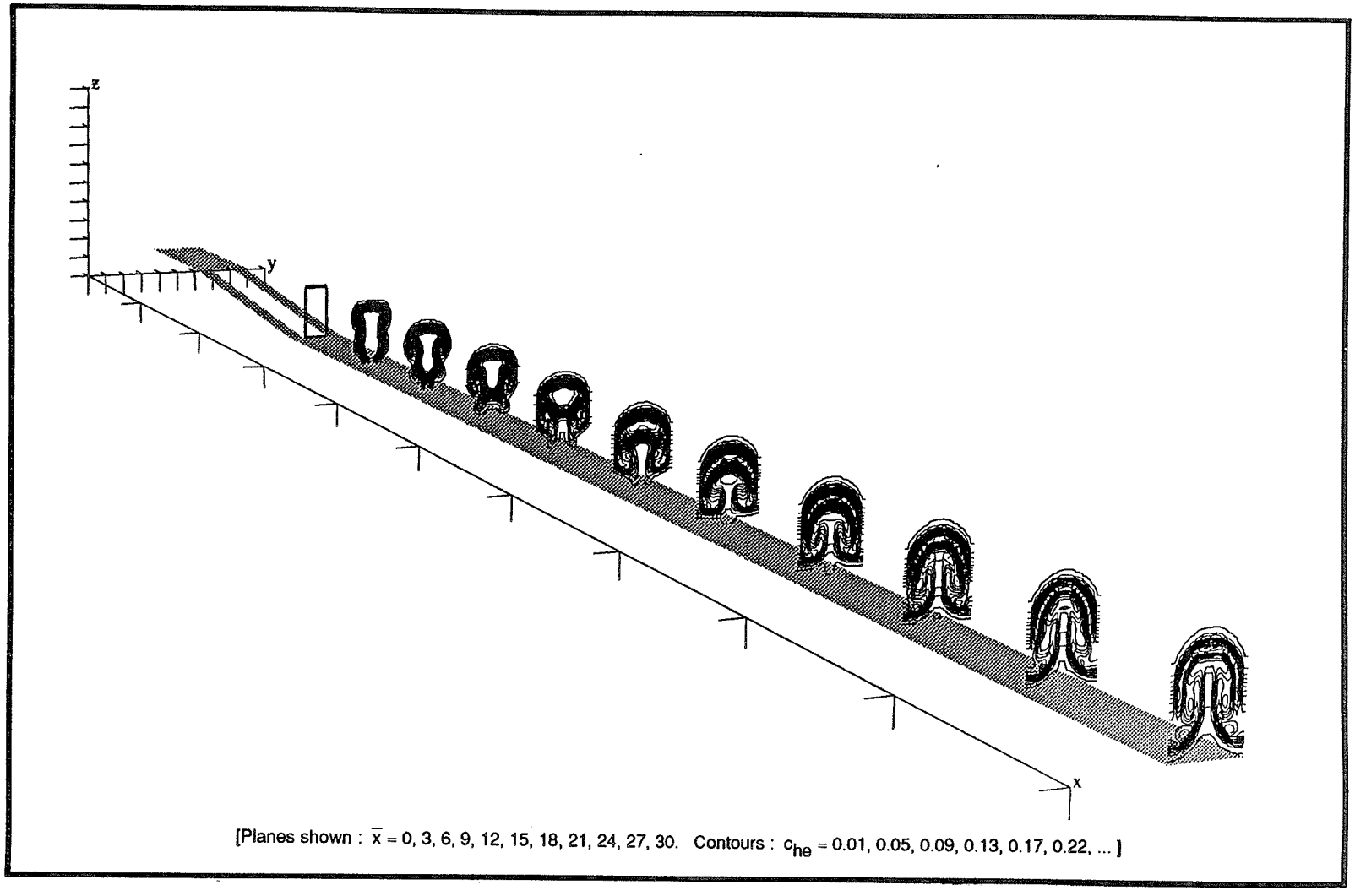

Figure 93. Contours of constant helium mass fraction.

Narrow spacing, $\bar{\delta}$ = 1.0, $\bar{p}$ = 1.0, $\bar{v}$ = 1.0, $\alpha_c = \alpha_e = 4.76^o$ (computational).

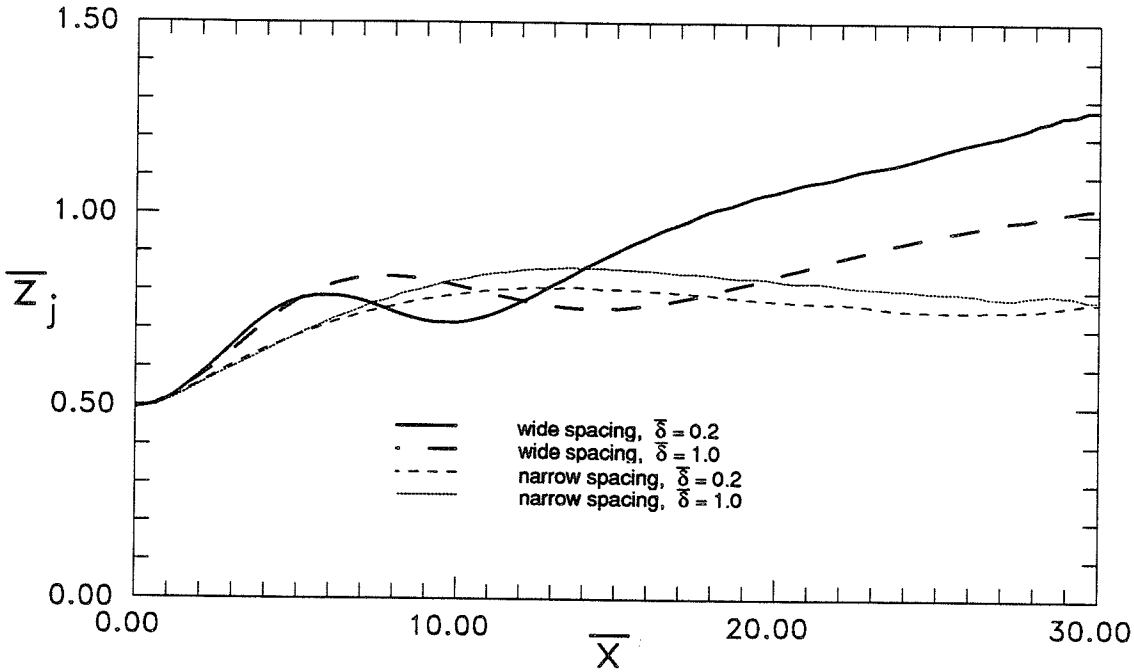

a. finite thickness boundary layers

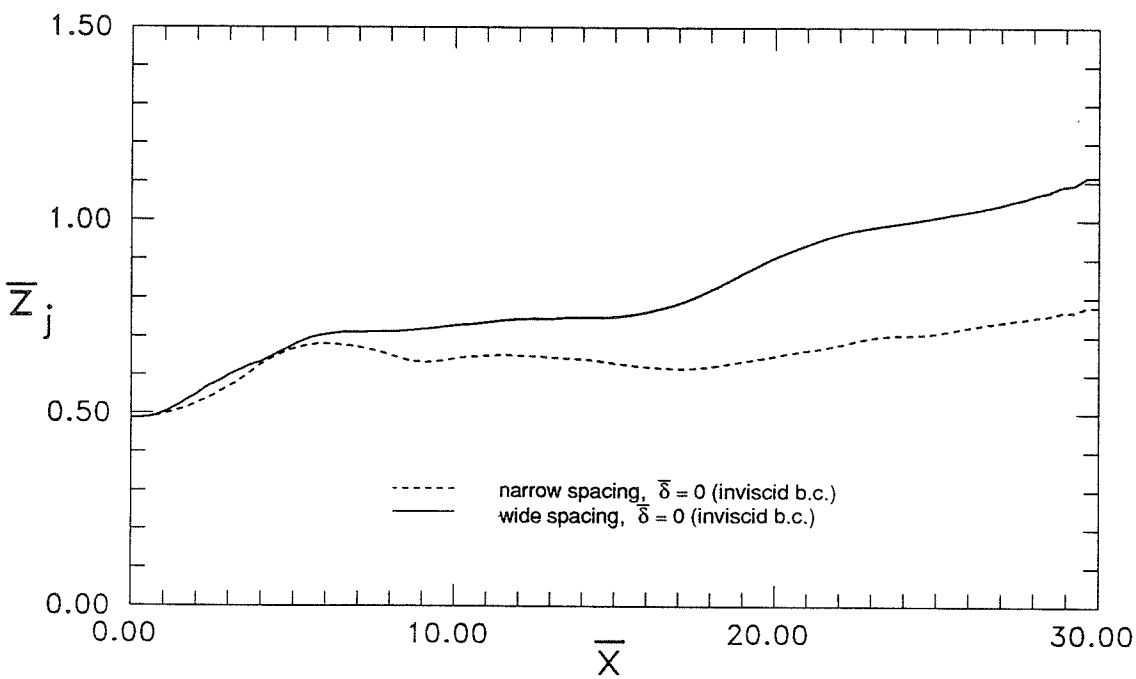

b. inviscid boundary conditions

Figure 94. Jet lift-off : Boundary layer and injector spacing effects.

$\overline{p}$ = 1.0, $\overline{v}$ = 1.0, $\alpha_c = \alpha_e = 4.76^o$ (computational).

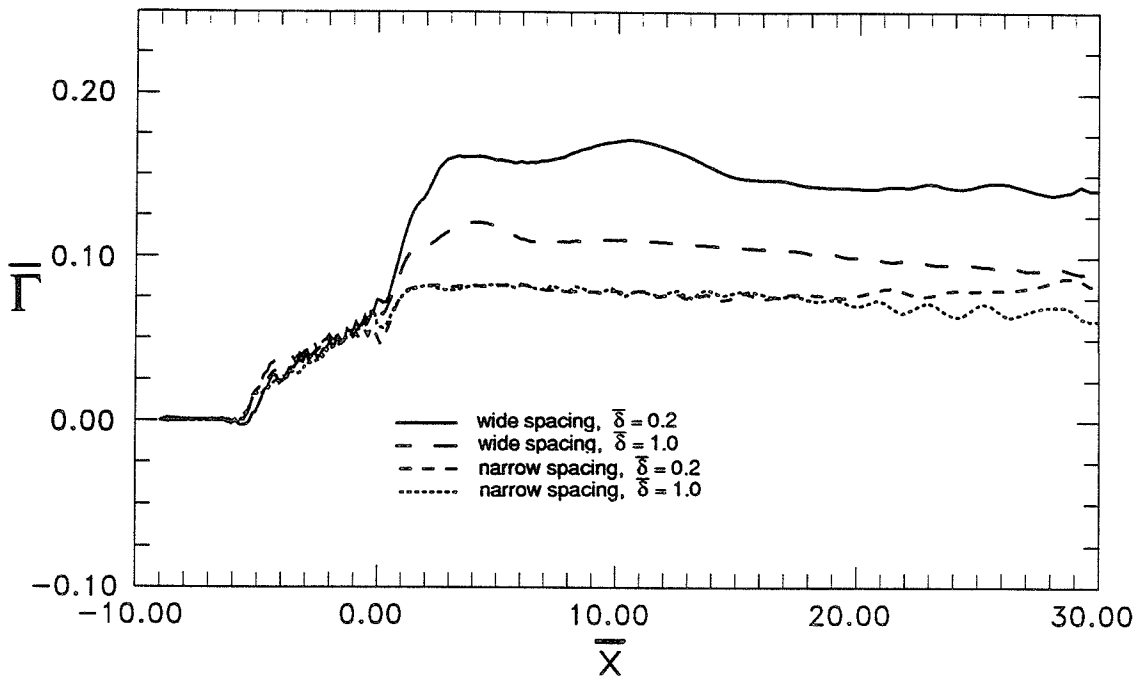

a. finite thickness boundary layers

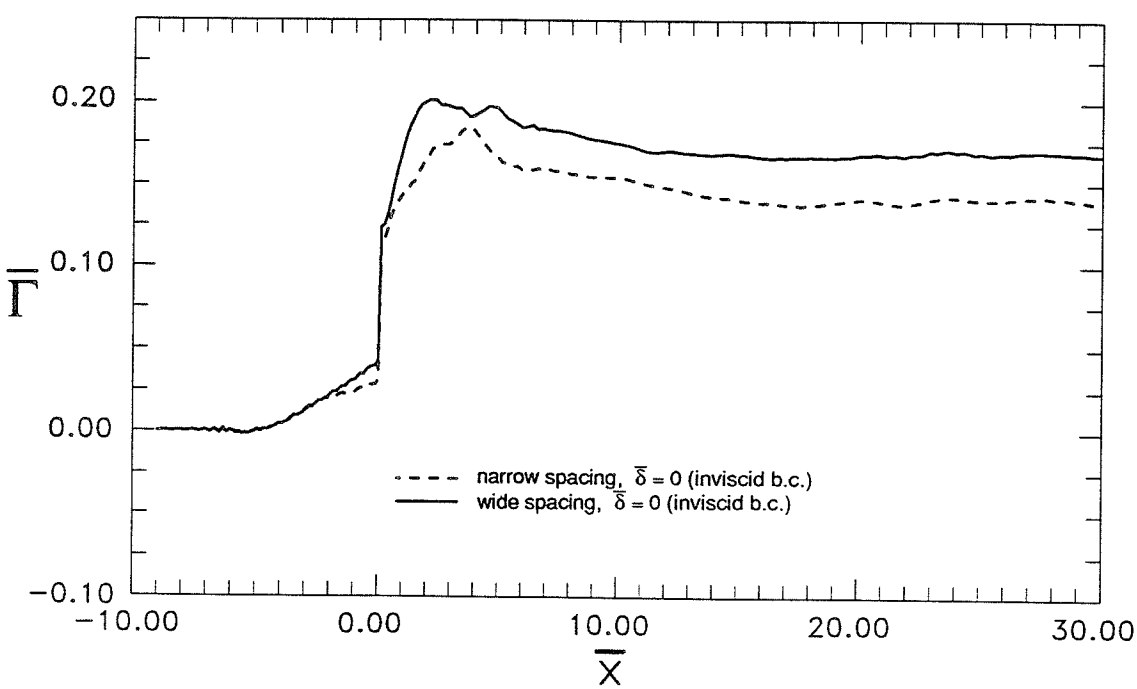

b. inviscid boundary conditions

Figure 95. Circulation : Boundary layer and injector spacing effects.

$\overline{p}$ = 1.0, $\overline{v}$ = 1.0, $\alpha_c = \alpha_e = 4.76^o$ (computational).

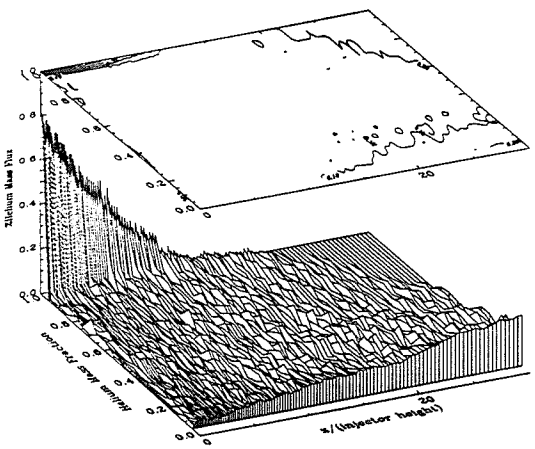

a. Wide spacing, $\overline{\delta} = 0$ (inviscid b.c.)

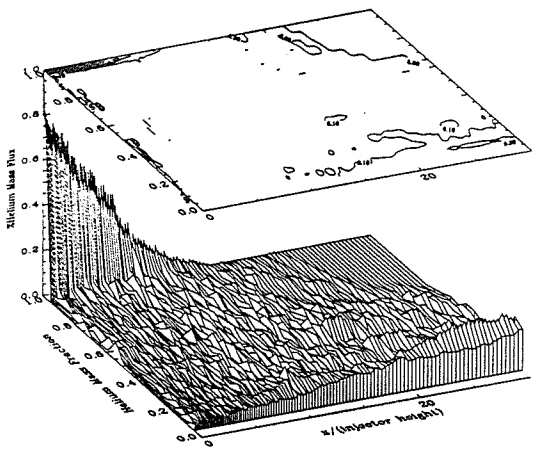

d. Narrow spacing, $\overline{\delta} = 0$ (inviscid b.c.)

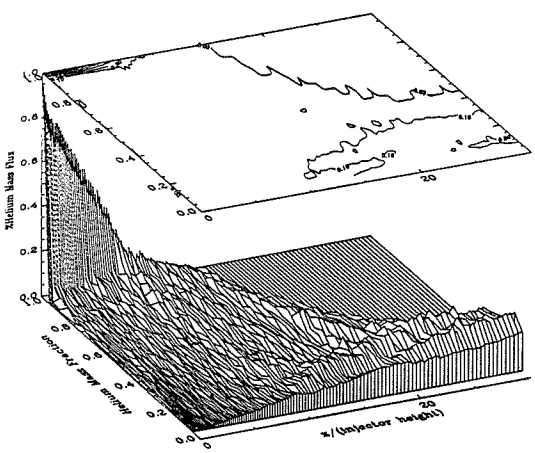

b. Wide spacing, $\overline{\delta} = 0.2$

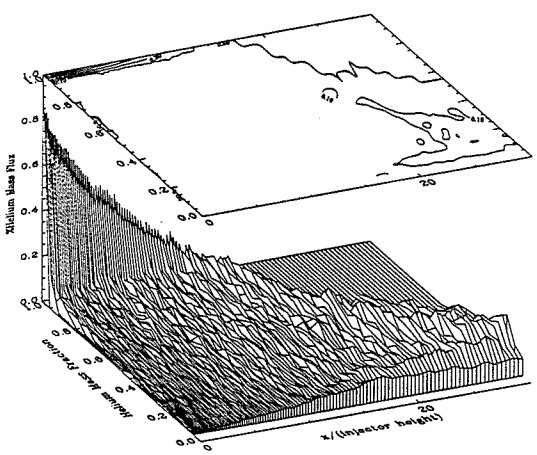

e. Narrow spacing, $\overline{\delta} = 0.2$

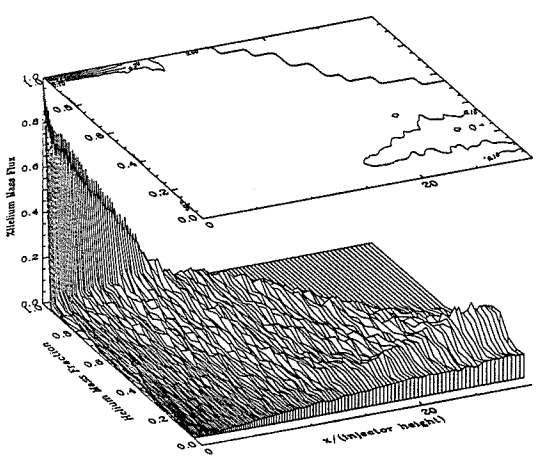

c. Wide spacing, $\overline{\delta} = 1.0$

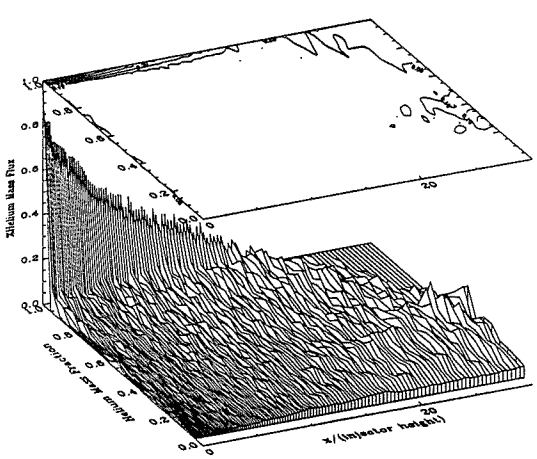

f. Narrow spacing, $\overline{\delta} = 1.0$

Figure 96. Mixedness Measure for various spacings and boundary layer thicknesses, $\overline{\rho} = 1.0$, $\overline{v} = 1.0$, $\alpha_c = 4.76^o$, $\alpha_e = 4.76^o$ (computational).

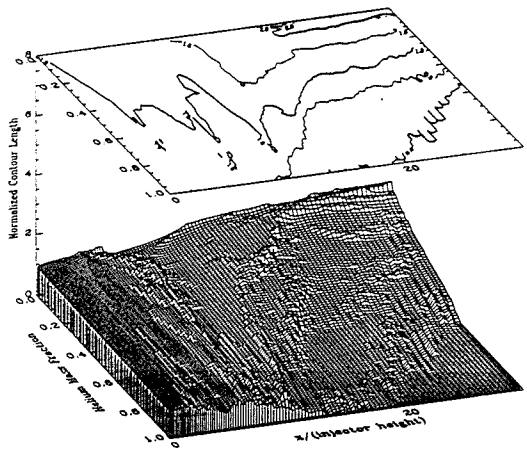

a. Wide spacing, $\overline{\delta} = 0$ (inviscid b.c.)

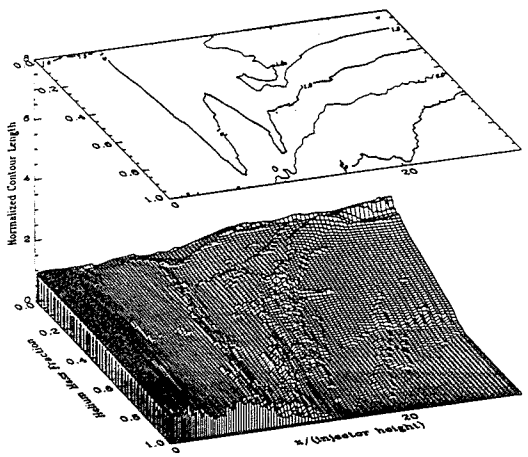

d. Narrow spacing, $\overline{\delta} = 0$ (inviscid b.c.)

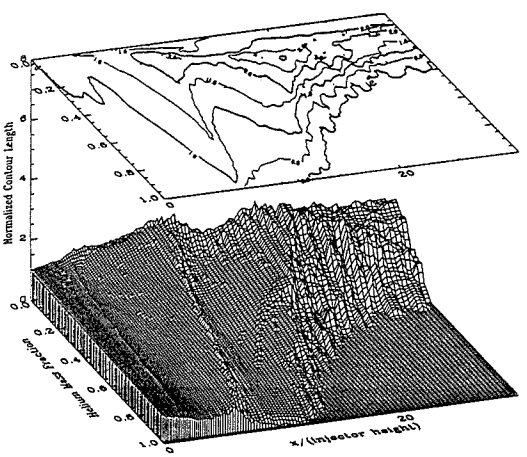

b. Wide spacing, $\overline{\delta} = 0.2$

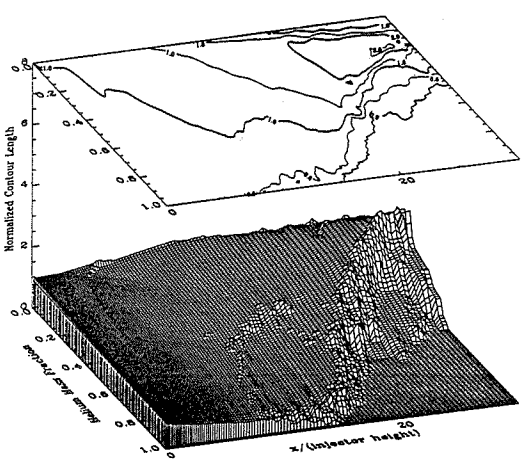

e. Narrow spacing, $\overline{\delta} = 0.2$

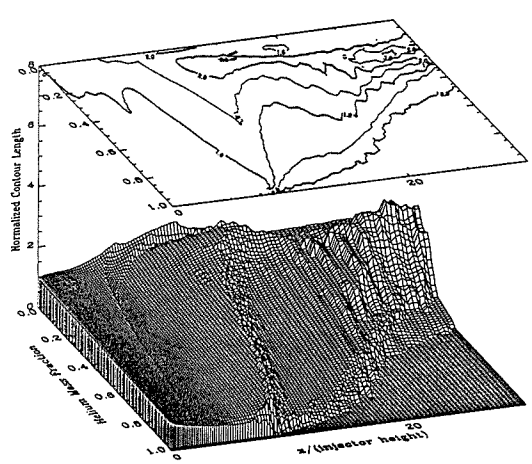

c. Wide spacing, $\overline{\delta} = 1.0$

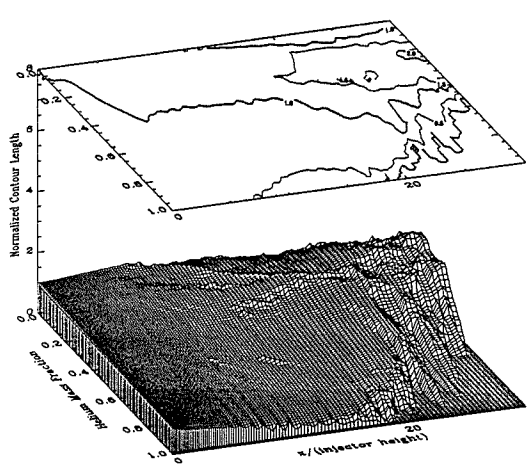

f. Narrow spacing, $\overline{\delta} = 1.0$

Figure 97. Length of contours of constant mass fraction for various spacings and boundary layer thicknesses, $\overline{p} = 1.0$, $\overline{v} = 1.0$, $\alpha_c = 4.76^o$, $\alpha_e = 4.76^o$ (computational).

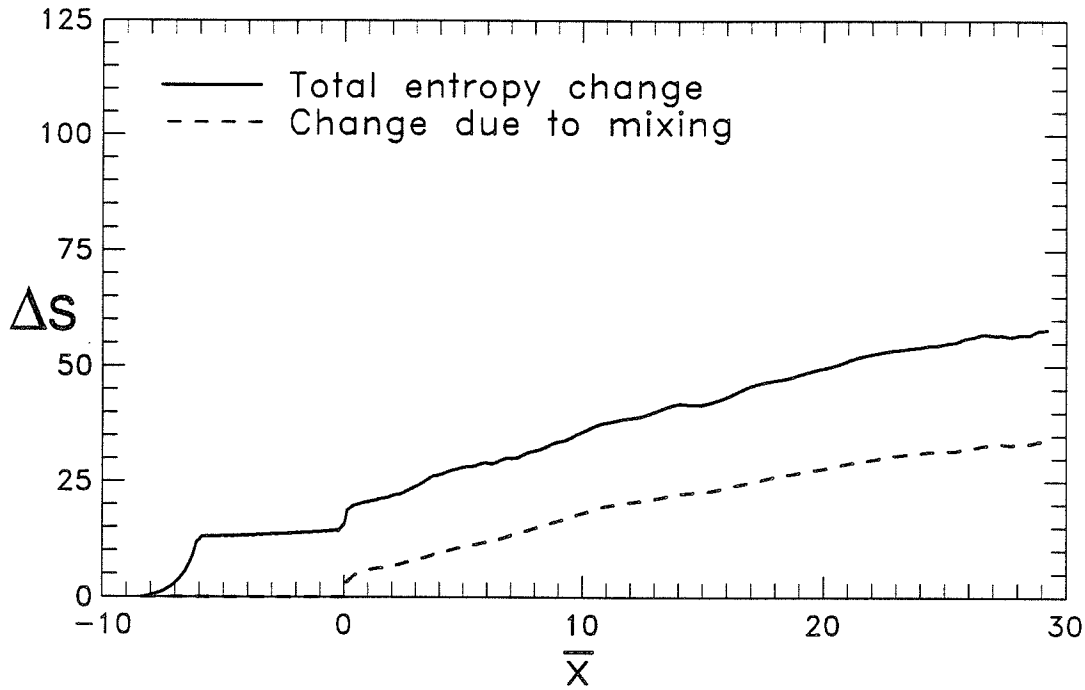

a. narrow spacing

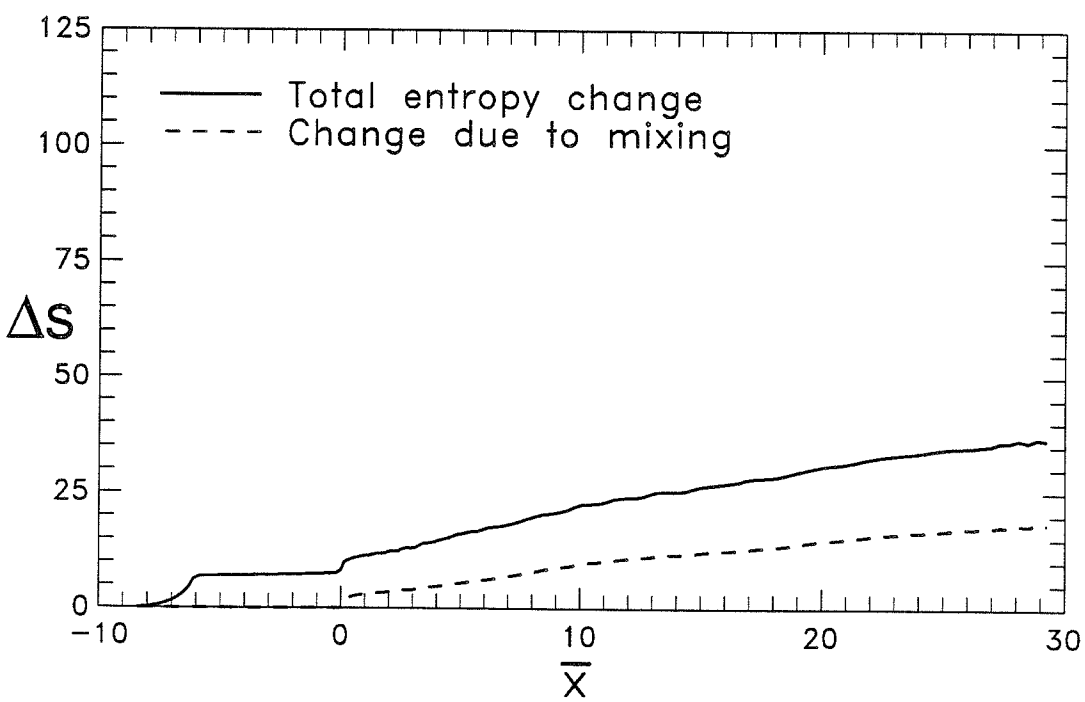

b. wide spacing

Figure 98. Entropy measure for wide and narrow spacing, $\overline{\delta} = 0$ (inviscid b.c.), $\overline{p} = 1.0$, $\overline{v} = 1.0$, $\alpha_c = \alpha_a = 4.76^o$ (computational).

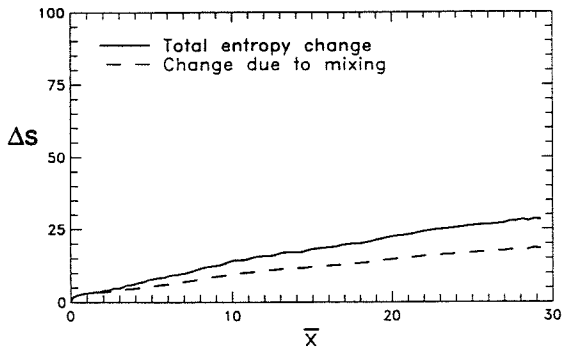

a. Wide spacing, $\bar{\delta} = 0$ (inviscid b.c.)

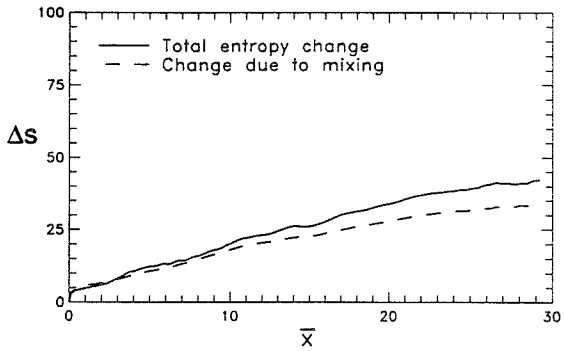

d. Narrow spacing, $\bar{\delta} = 0$ (inviscid b.c.)

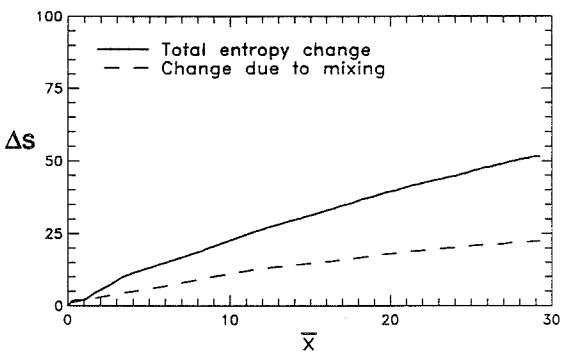

b. Wide spacing, $\bar{\delta} = 0.2$

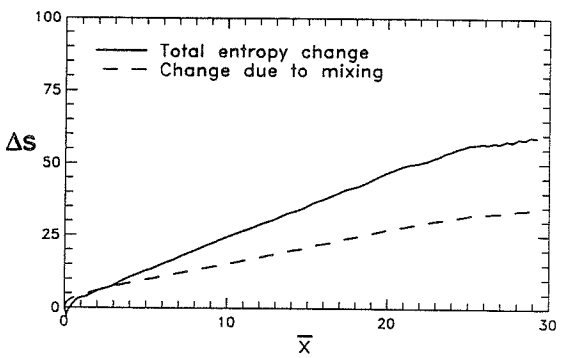

e. Narrow spacing, $\bar{\delta} = 0.2$

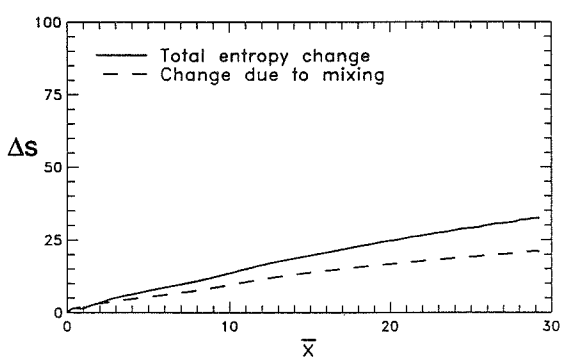

c. Wide spacing, $\bar{\delta} = 1.0$

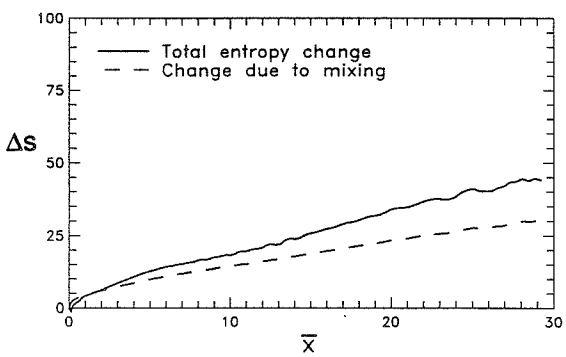

f. Narrow spacing, $\bar{\delta} = 1.0$

Figure 99. Entropy Measure for various spacings and boundary layer thicknesses, $\bar{p} = 1.0$, $\bar{v} = 1.0$, $\alpha_c = 4.76^o$, $\alpha_e = 4.76^o$ (computational).

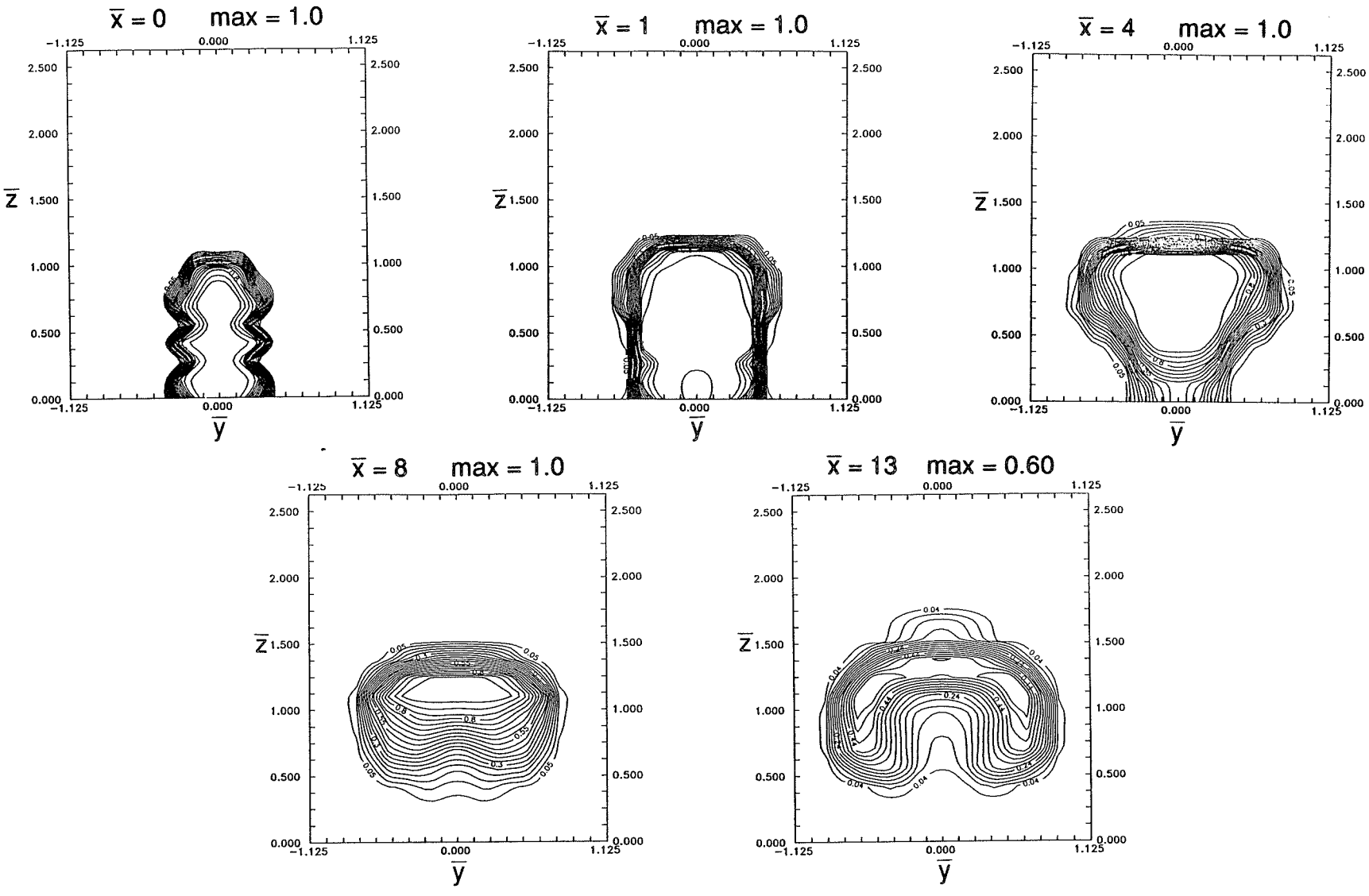

Figure 100. Helium mass fraction. Full-scale model, wide spacing, natural boundary layer, $\bar{\delta} = 0.20$, $\bar{p} = 4.0$, $\bar{v} = 1.27$ (experimental).

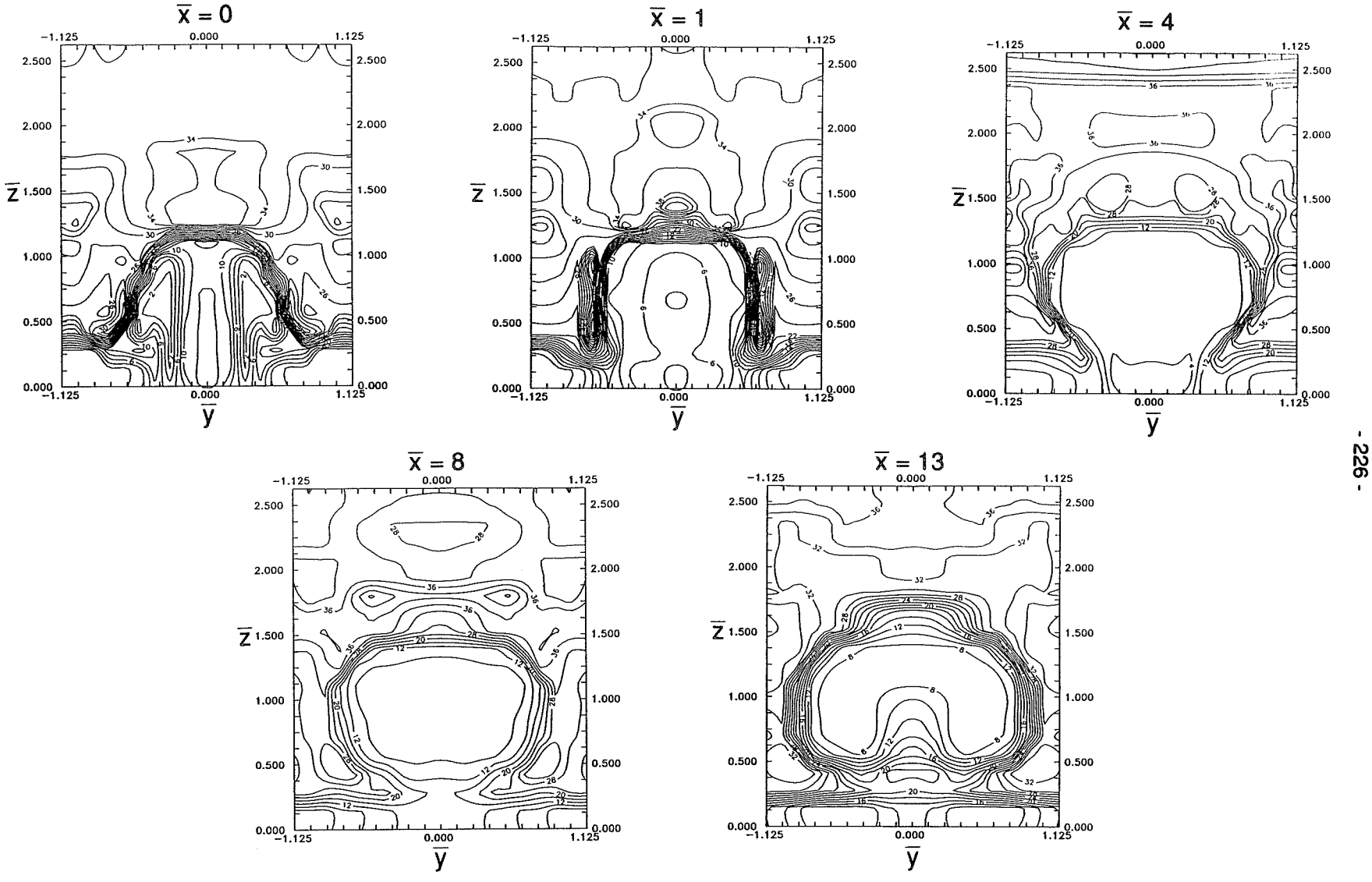

Figure 101. Pitot pressure (psia). Full-scale model, wide spacing, natural boundary layer, $\bar{\delta} = 0.20$, $\bar{p} = 4.0$, $\bar{v} = 1.27$ (experimental).

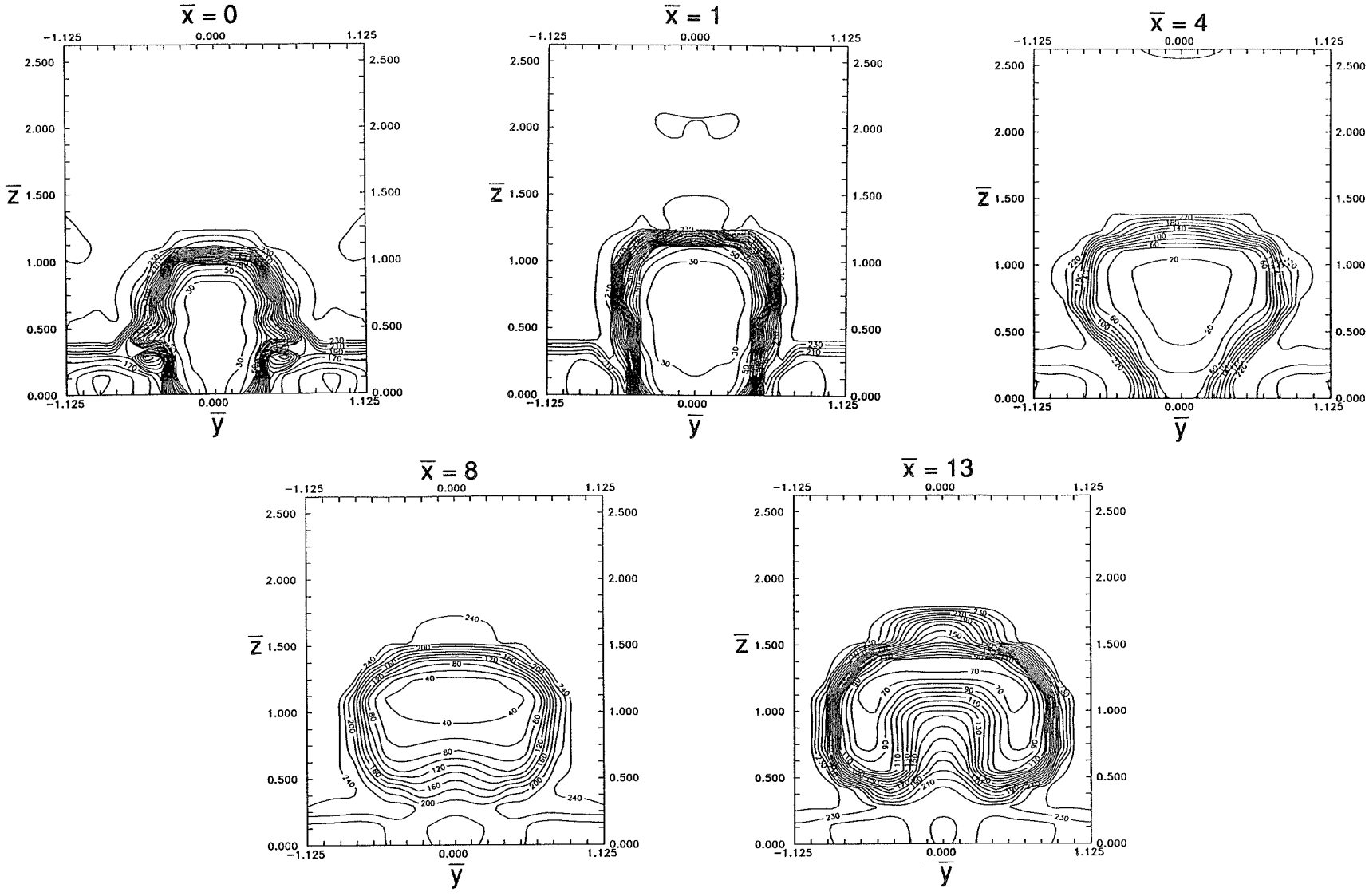

Figure 102. Total temperature (°C). Full-scale model, wide spacing, natural boundary layer, $\bar{\delta} = 0.20$, $\bar{p} = 4.0$, $\bar{v} = 1.27$ (experimental).

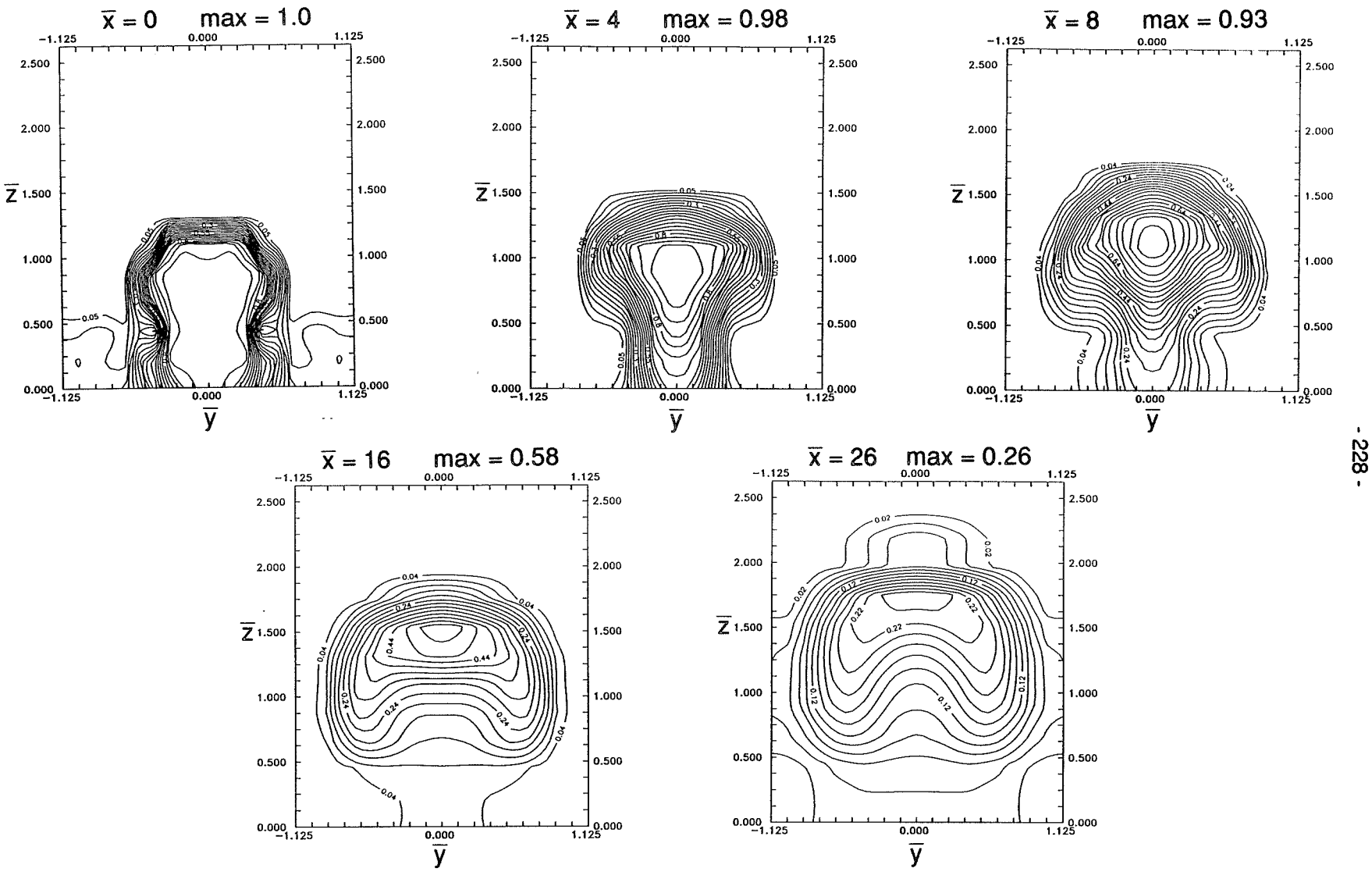

Figure 103. Helium mass fraction. Half-scale model, wide spacing, natural boundary layer, $\bar{\delta} = 0.40$, $\bar{p} = 4.0$, $\bar{v} = 1.30$ (experimental).

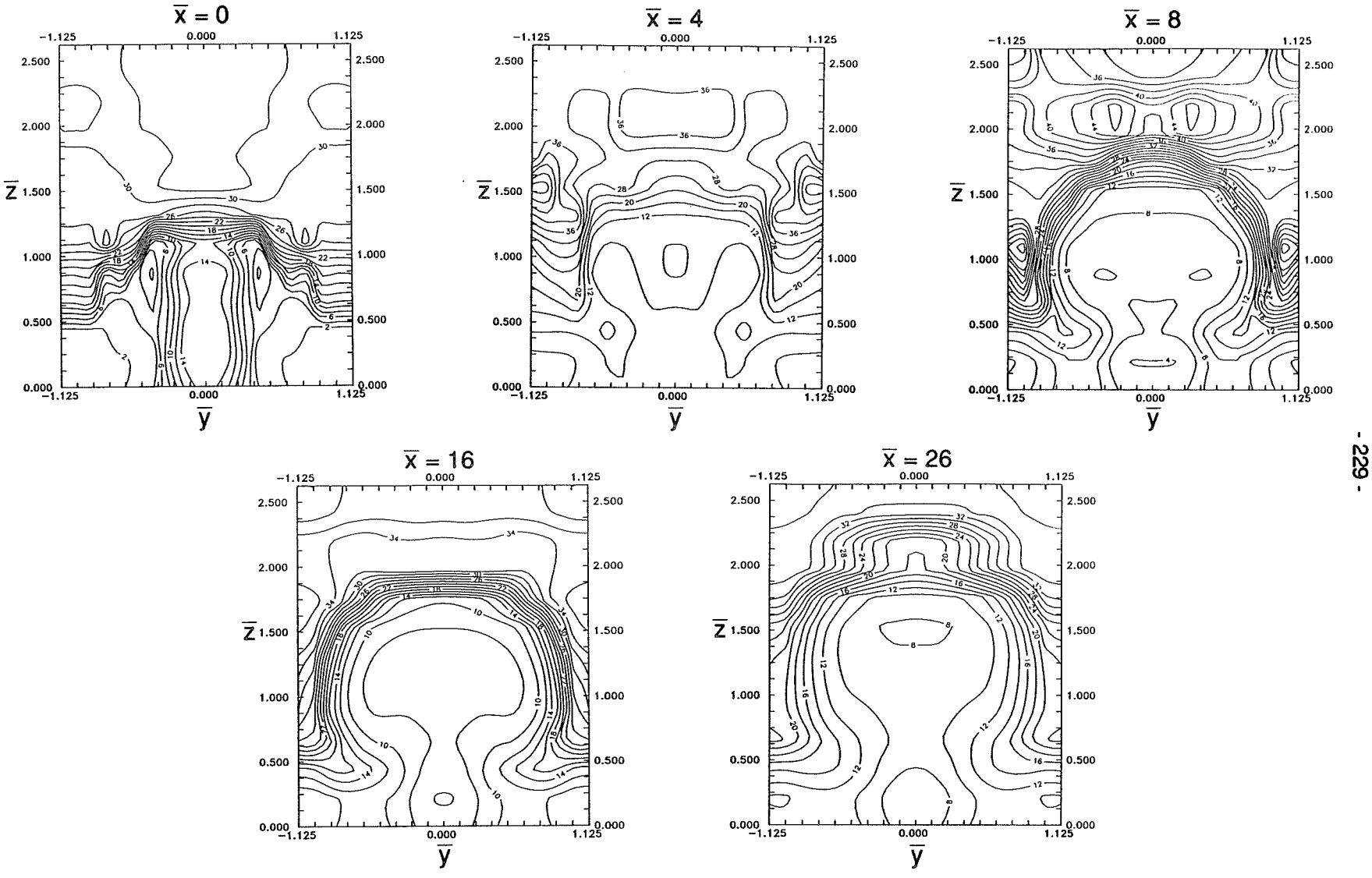

Figure 104. Pitot pressure (psia). Half-scale model, wide spacing, natural boundary layer, $\bar{\delta} = 0.40$, $\bar{p} = 4.0$, $\bar{v} = 1.30$ (experimental).

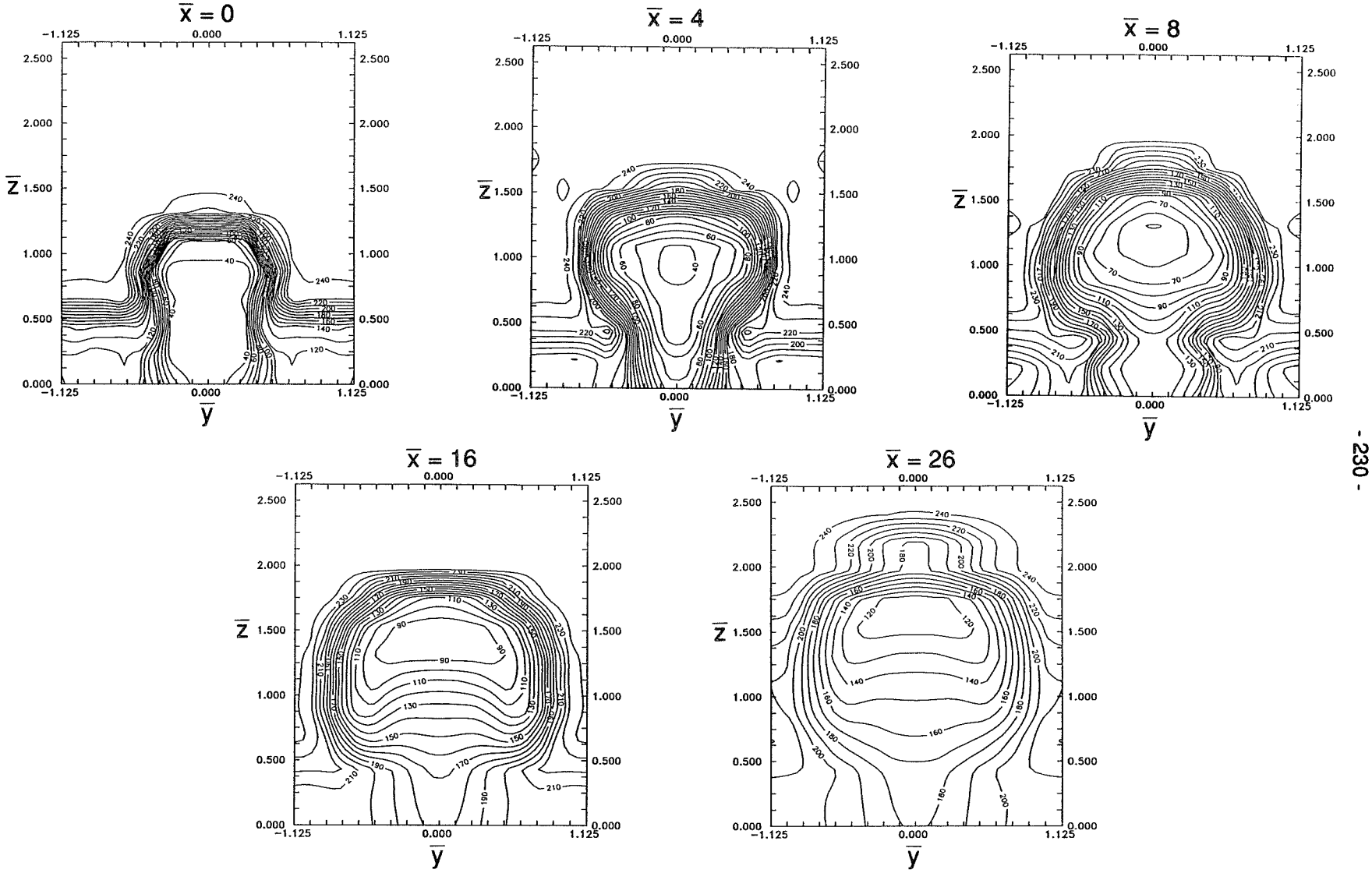

Figure 105. Total temperature (^{o}C). Half-scale model, wide spacing, natural boundary layer, $\bar{\delta} = 0.40$, $\bar{p} = 4.0$, $\bar{v} = 1.30$ (experimental).

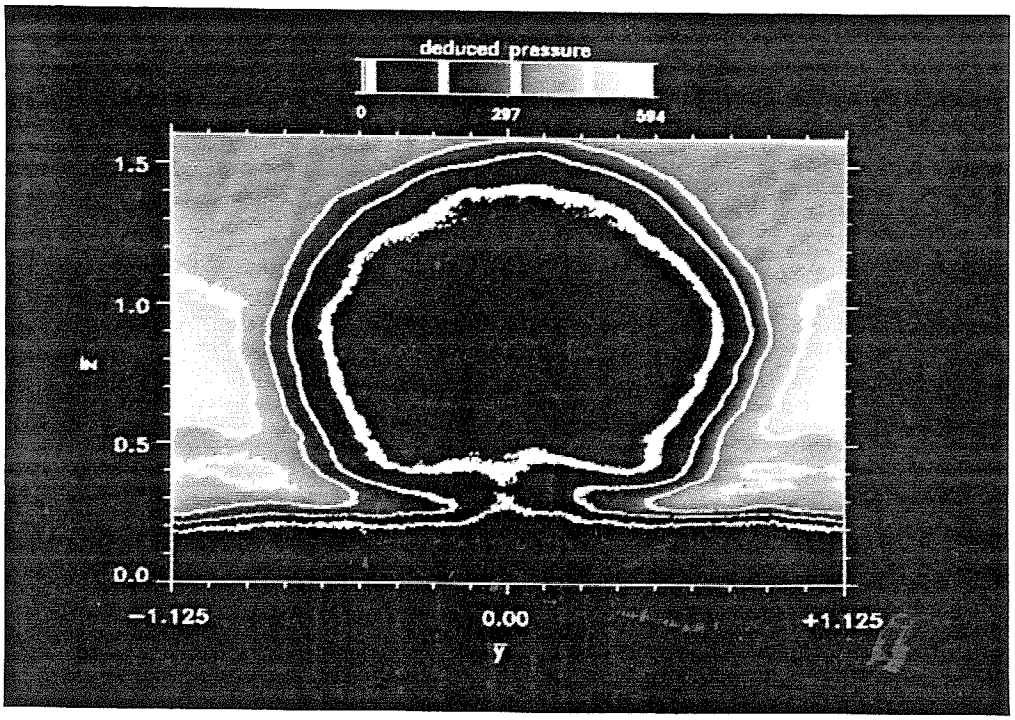

Figure 106. Mean of 22 planar Rayleigh images at $\overline{x}$ = 10.

Wide spacing, $\overline{\delta}$ = 0.20, $\overline{p}$ = 4.0, $\overline{v}$ = 1.28, $\alpha_c = \alpha_e = 4.76^o$.

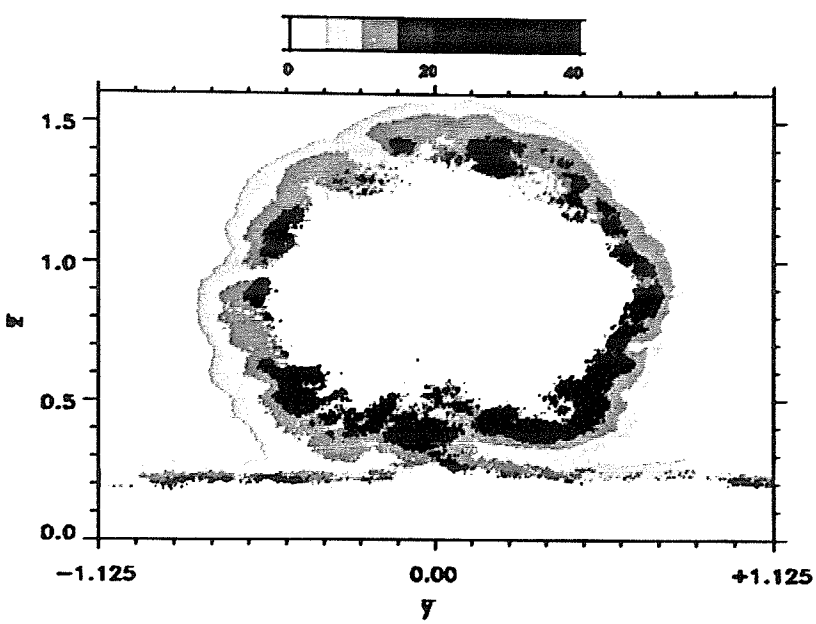

Figure 107. Standard deviation (%mean) about the mean for planar Rayleigh images at $\overline{x}$ = 10.

Wide spacing, $\overline{\delta}$ = 0.20, $\overline{p}$ = 4.0, $\overline{v}$ = 1.28, $\alpha_c = \alpha_e = 4.76^o$.

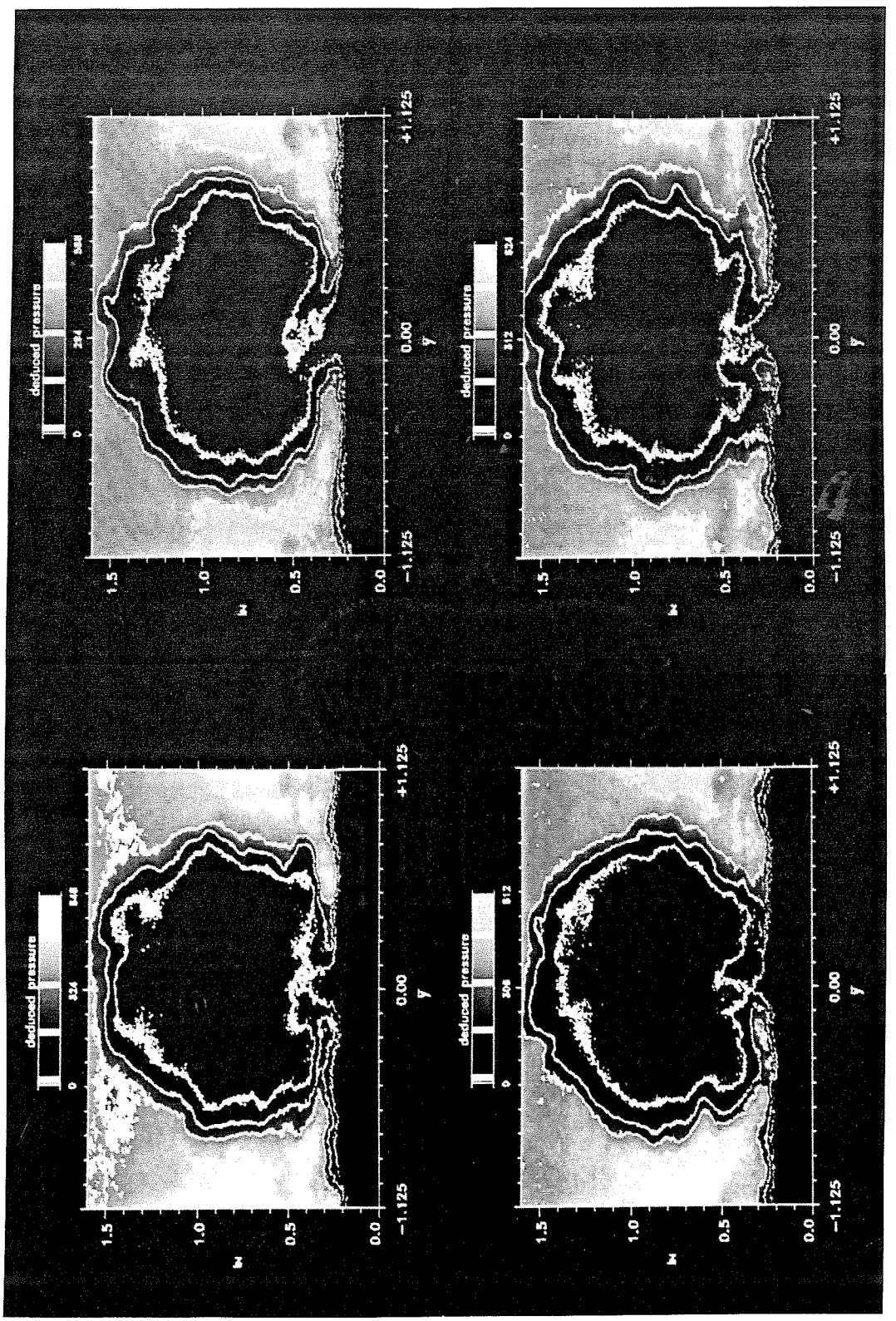

Figure 108. Instantaneous planar Rayleigh images at $\bar{x} = 10$. Wide spacing, $\bar{\delta} = 0.20$, $\bar{p} = 4.0$, $\bar{v} = 1.28$, $\alpha_c = \alpha_e = 4.76^o$.

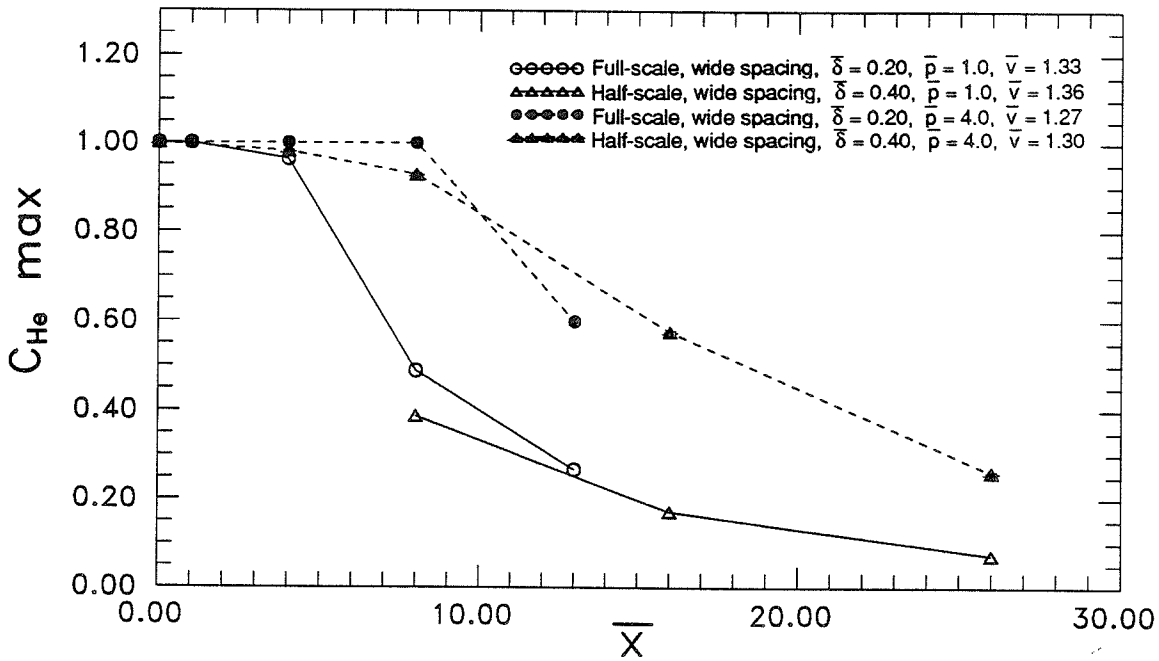

Figure 109. Decay of maximum helium mass fraction: Pressure ratio effects (experimental).

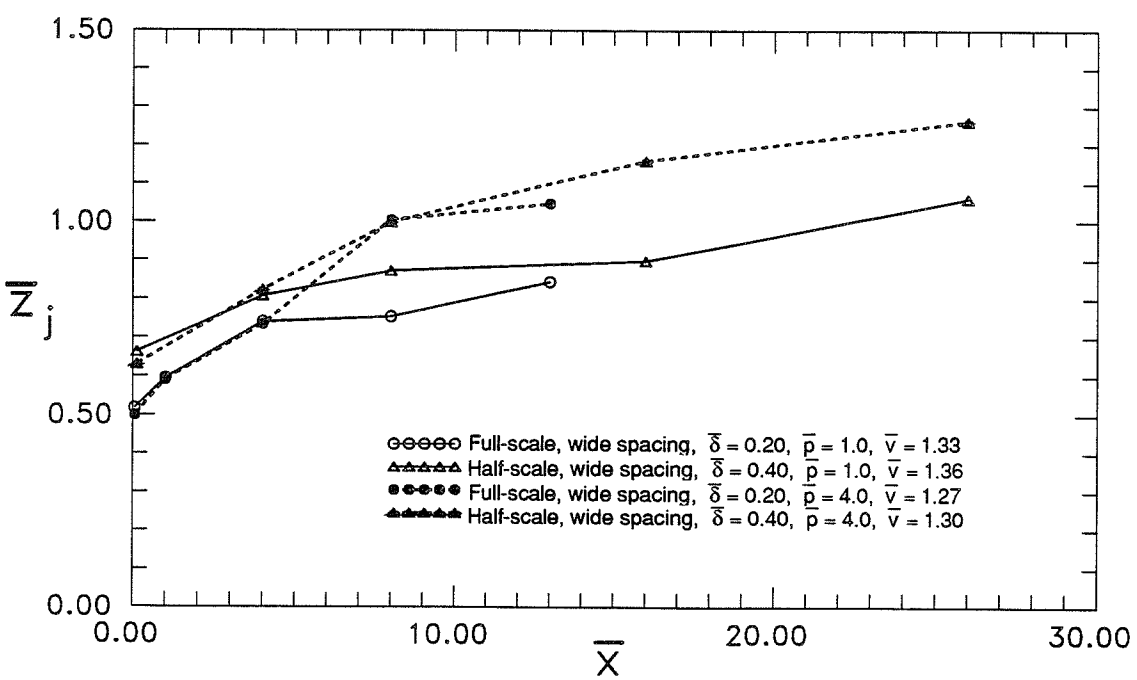

Figure 110. Jet lift-off : Pressure ratio effects (experimental).

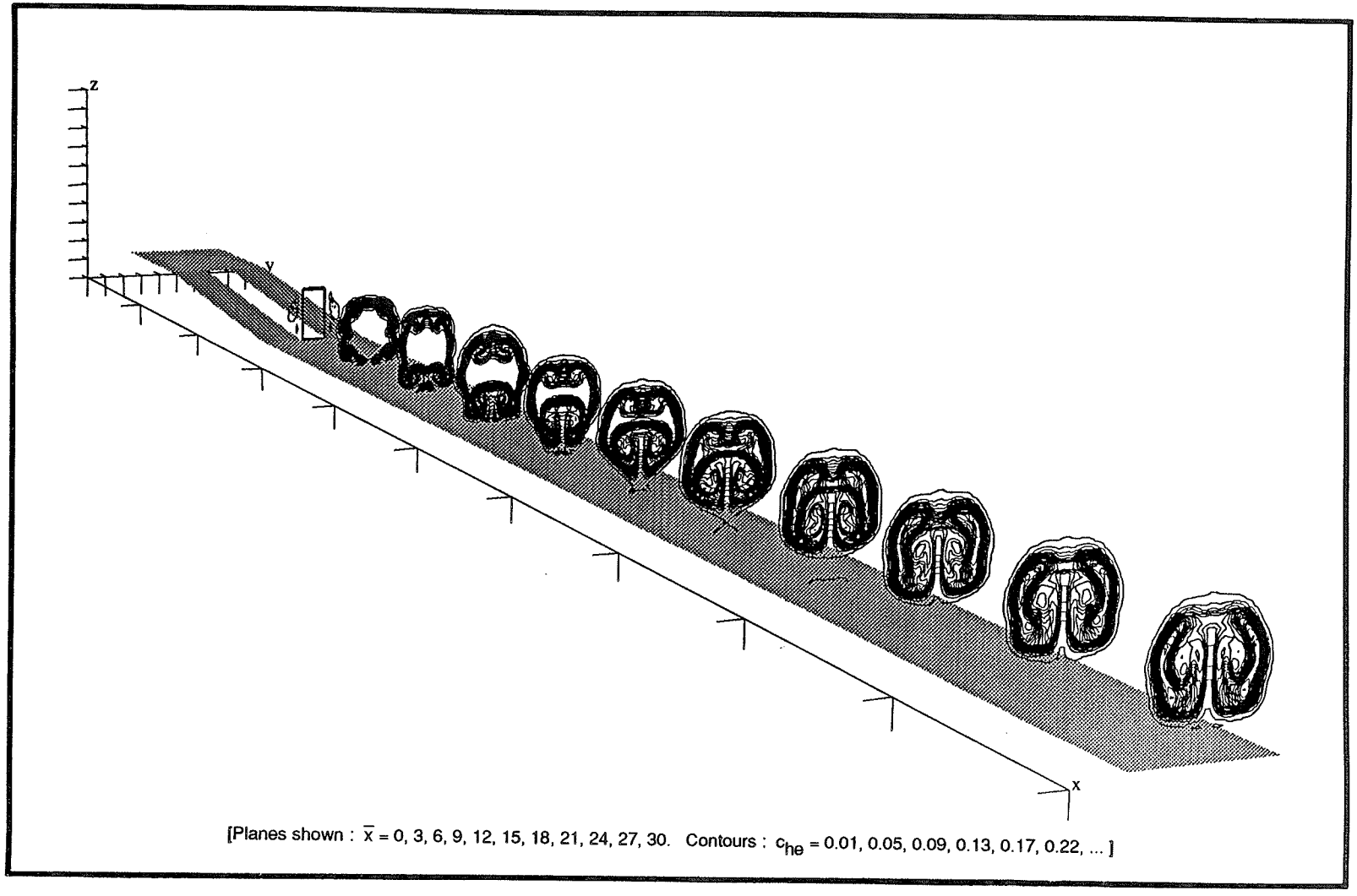

Figure 111. Contours of constant helium mass fraction.

Wide spacing, $\overline{\delta}$ = 0.20, $\overline{p}$ = 4.0, $\overline{v}$ = 1.0, $\alpha_c = \alpha_e = 4.76^o$ (computational).

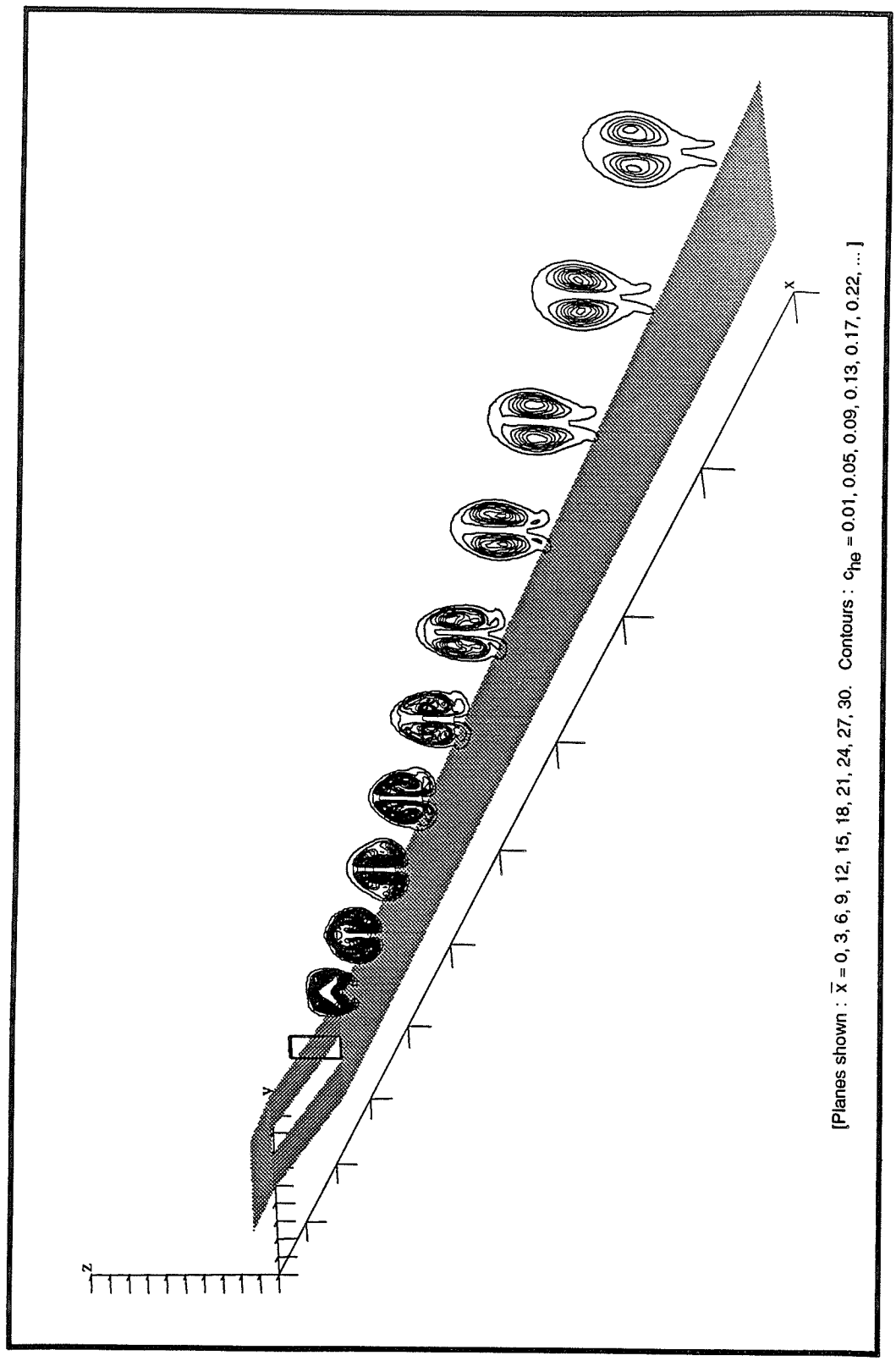

Figure 112. Contours of constant helium mass fraction.

Wide spacing, $\bar{\delta}$ = 0.20, $\bar{p}$ = 0.4, $\bar{v}$ = 1.0, $\alpha_c = \alpha_e$ = 4.76^o (computational).

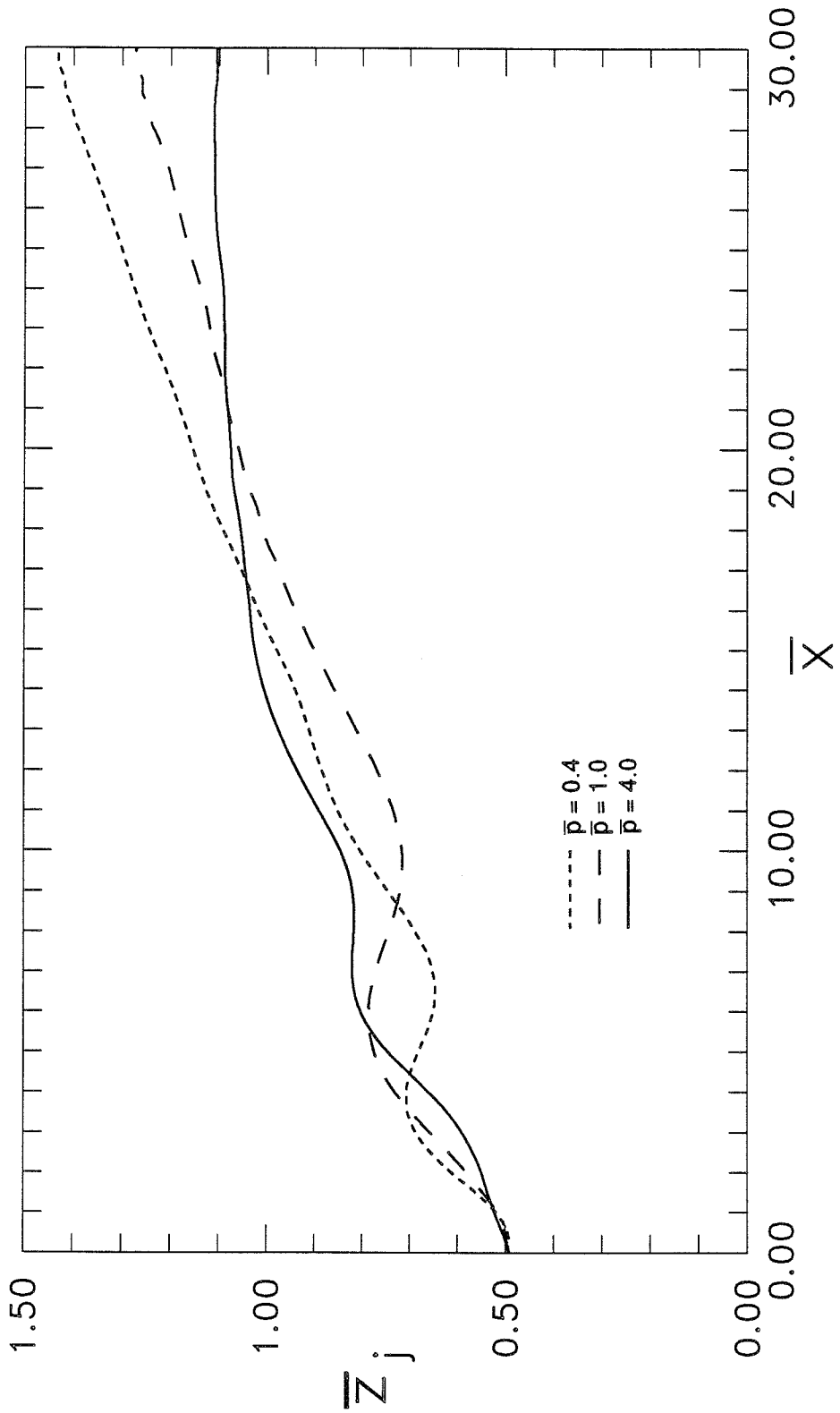

Figure 113. Jet lift-off : Pressure ratio effects. Wide spacing, $\overline{\delta} = 0.20$, $\overline{v} = 1.0$, $\alpha_c = \alpha_e = 4.76^o$ (computational).

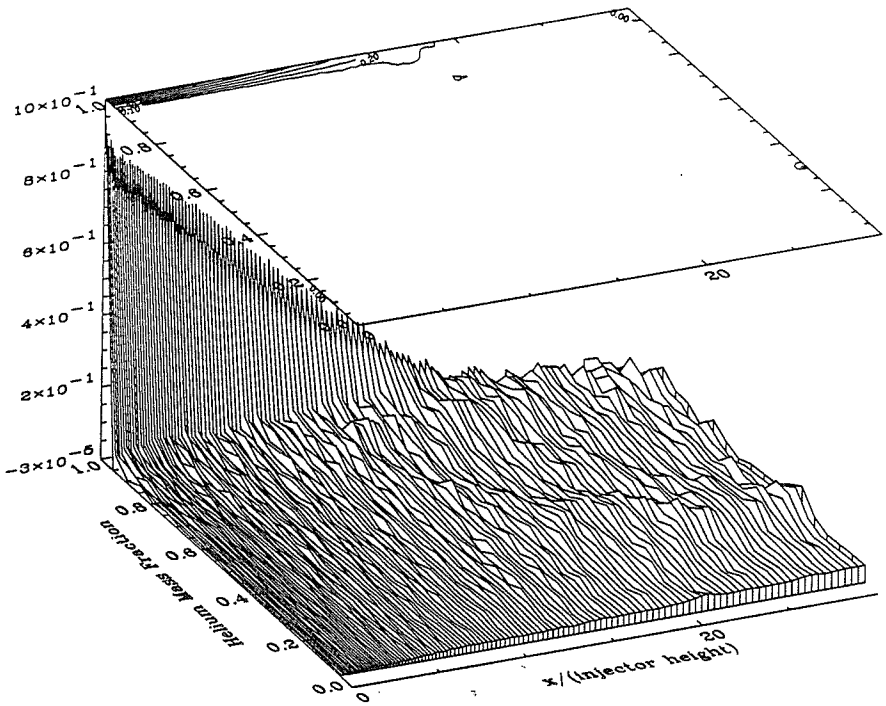

a. $\overline{p} = 4.0$

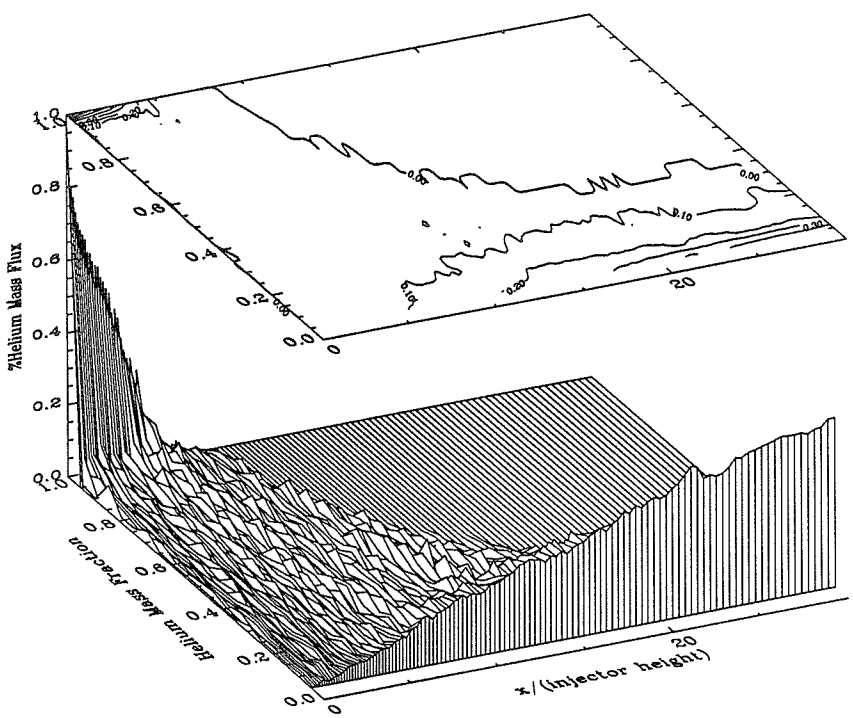

b. $\overline{p} = 0.4$

Figure 114. Mixedness Measure for high and low injectant to freestream pressure ratios, wide spacing, $\overline{\delta} = 0.2$, $\overline{v} = 1.0$, $\alpha_c = 4.76^o$, $\alpha_e = 4.76^o$ (computational).

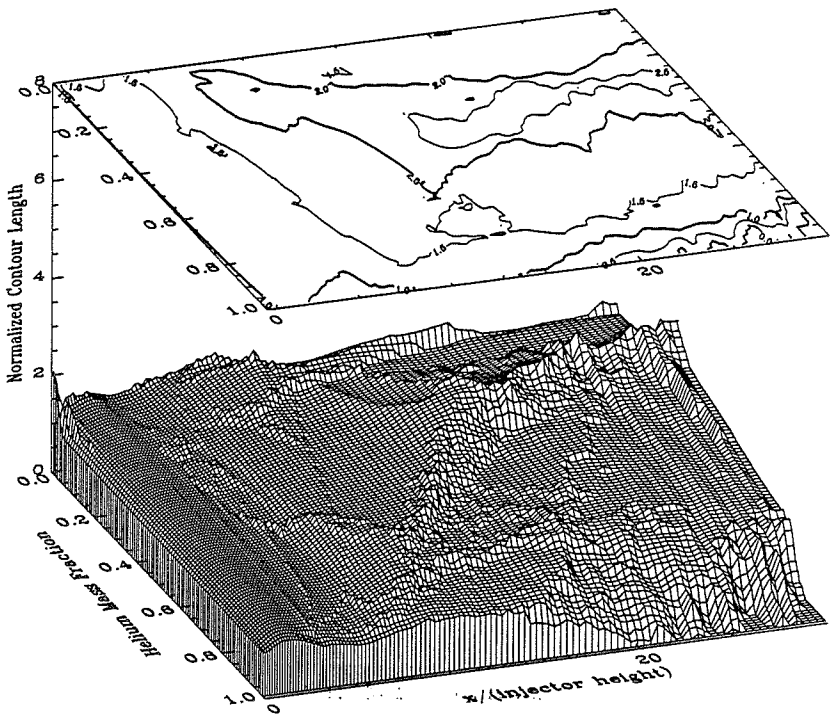

a. $\overline{p} = 4.0$

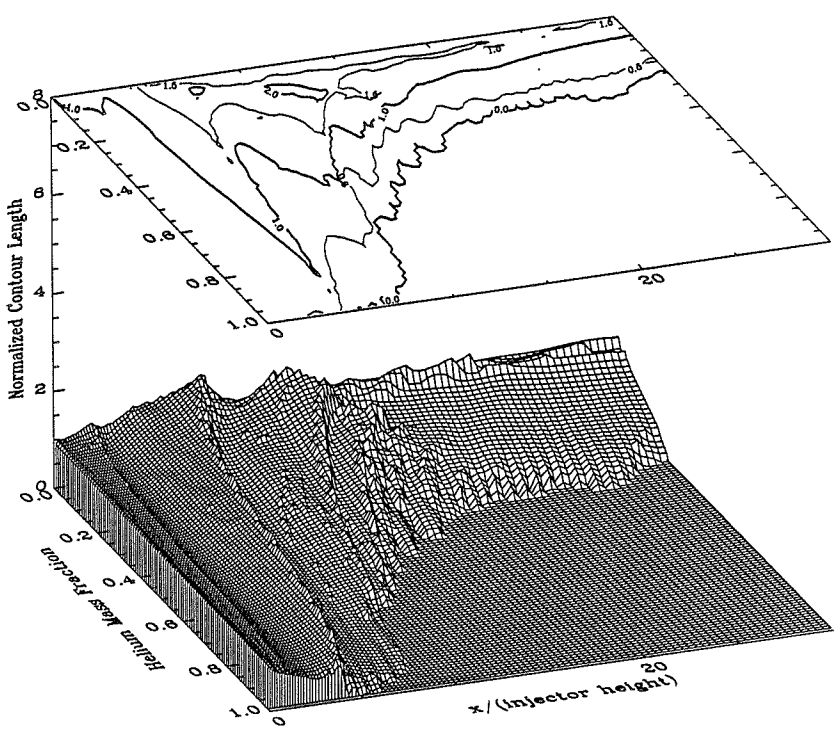

b. $\overline{p} = 0.4$

Figure 115. Length of contours of constant mass fraction for high and low injectant to freestream pressure ratios, wide spacing, $\overline{\delta} = 0.2$, $\overline{v} = 1.0$, $\alpha_c = 4.76^o$, $\alpha_e = 4.76^o$ (computational).

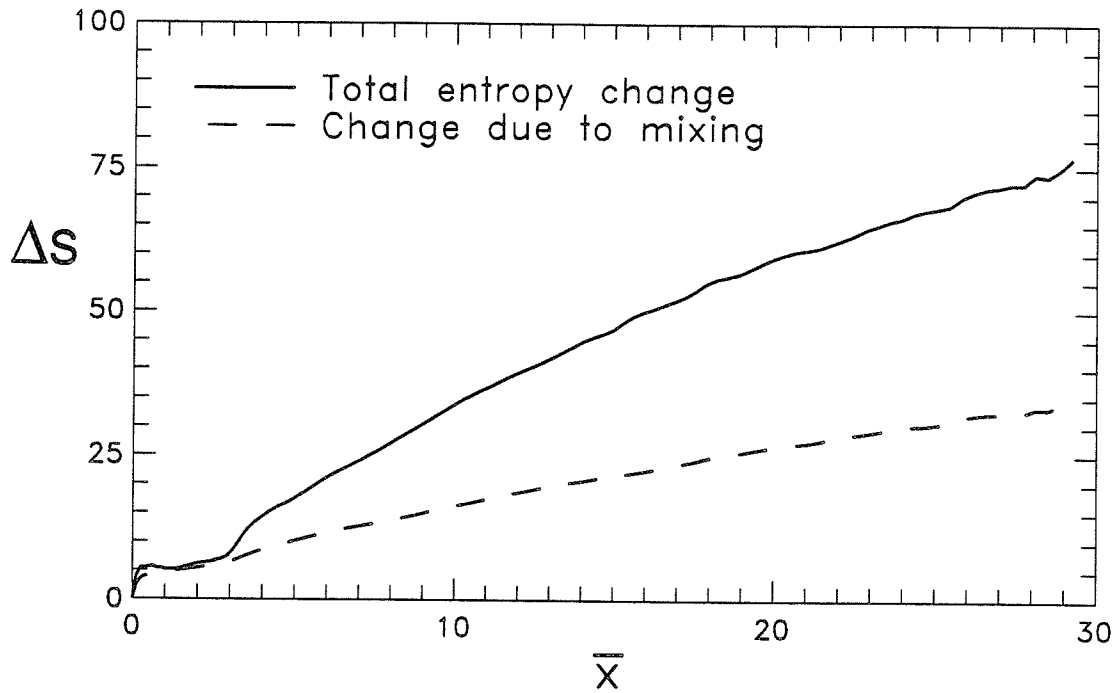

a. $\bar{p} = 4.0$

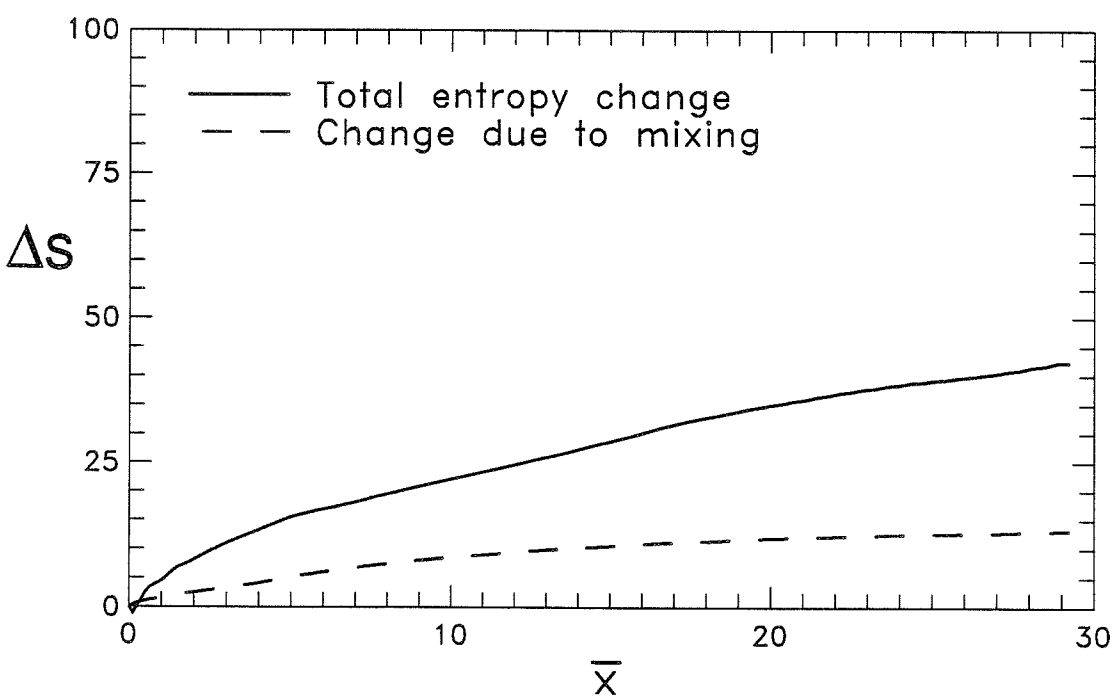

b. $\bar{p} = 0.4$

Figure 116. Entropy measure variations with pressure ratio. Wide spacing, $\bar{\delta} = 0.2$, $\bar{v} = 1.0$, $\alpha_c = \alpha_e = 4.76^o$ (computational).

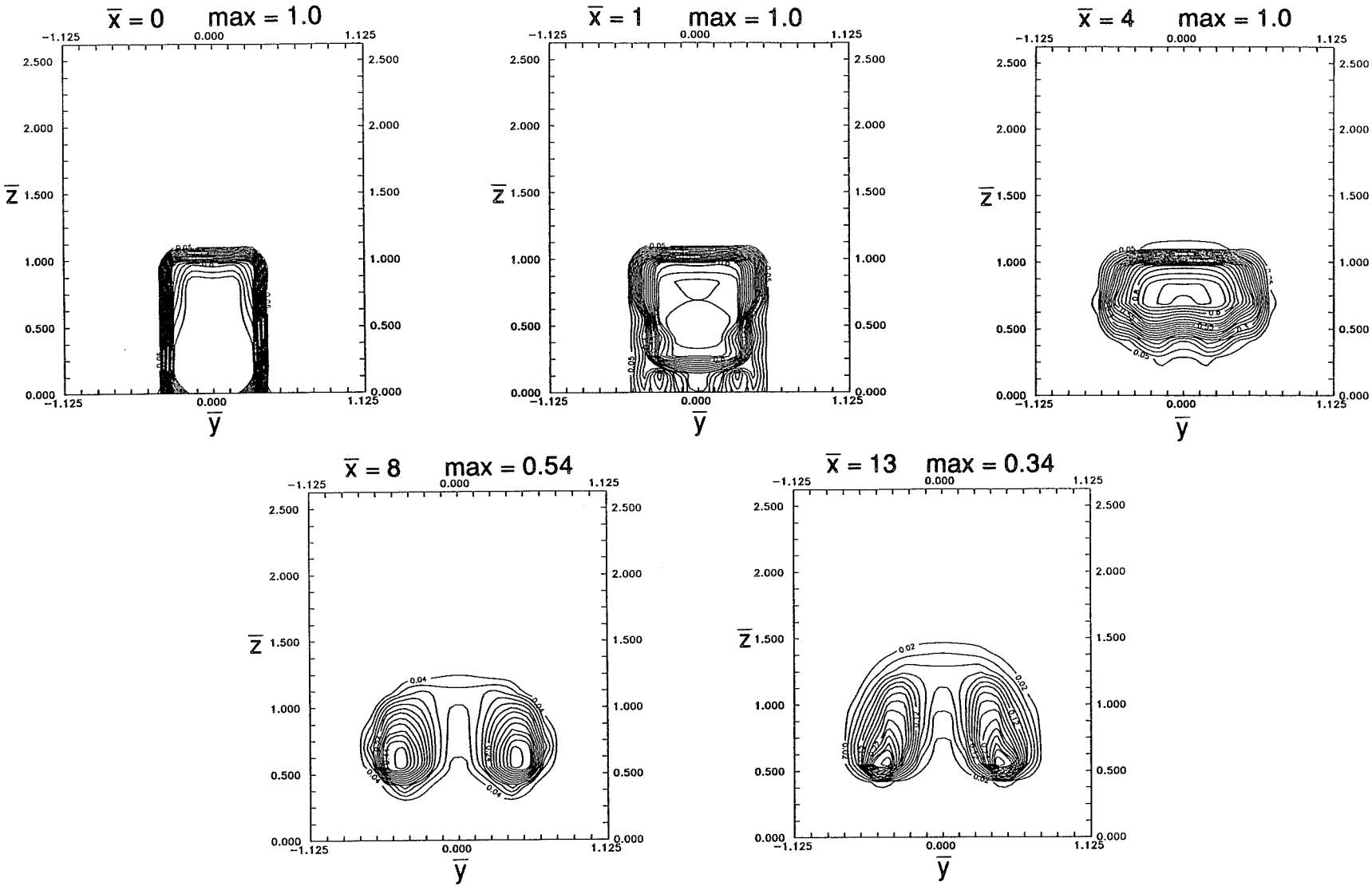

Figure 117. Helium mass fraction. Full-scale model, wide spacing, natural boundary layer, $\bar{\delta} = 0.20$, $\bar{p} = 1.0$, $\bar{v} = 1.12$ (experimental).

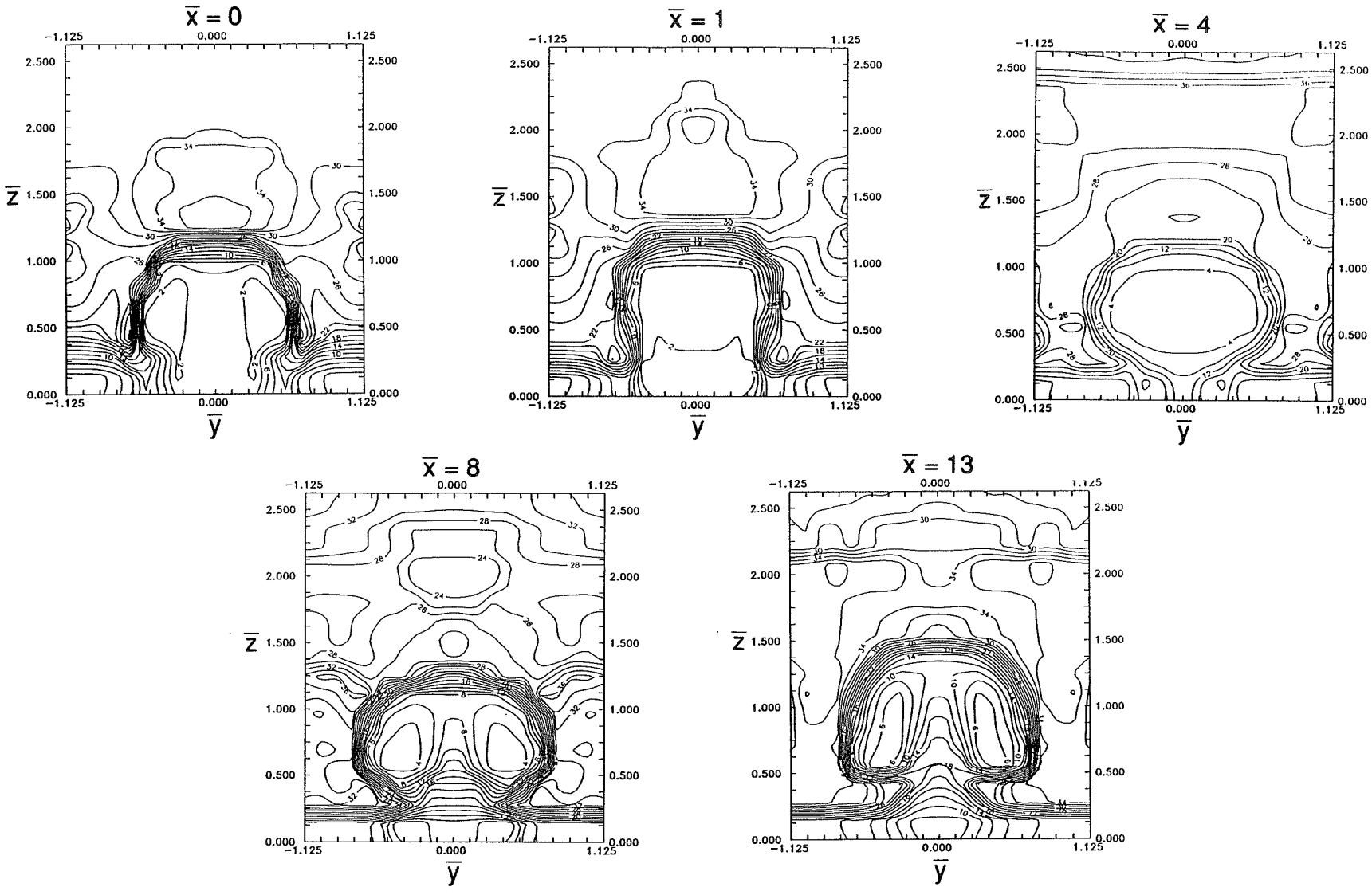

Figure 118. Pitot pressure (psia). Full-scale model, wide spacing, natural boundary layer, $\bar{\delta} = 0.20$, $\bar{p} = 1.0$, $\bar{v} = 1.12$ (experimental).

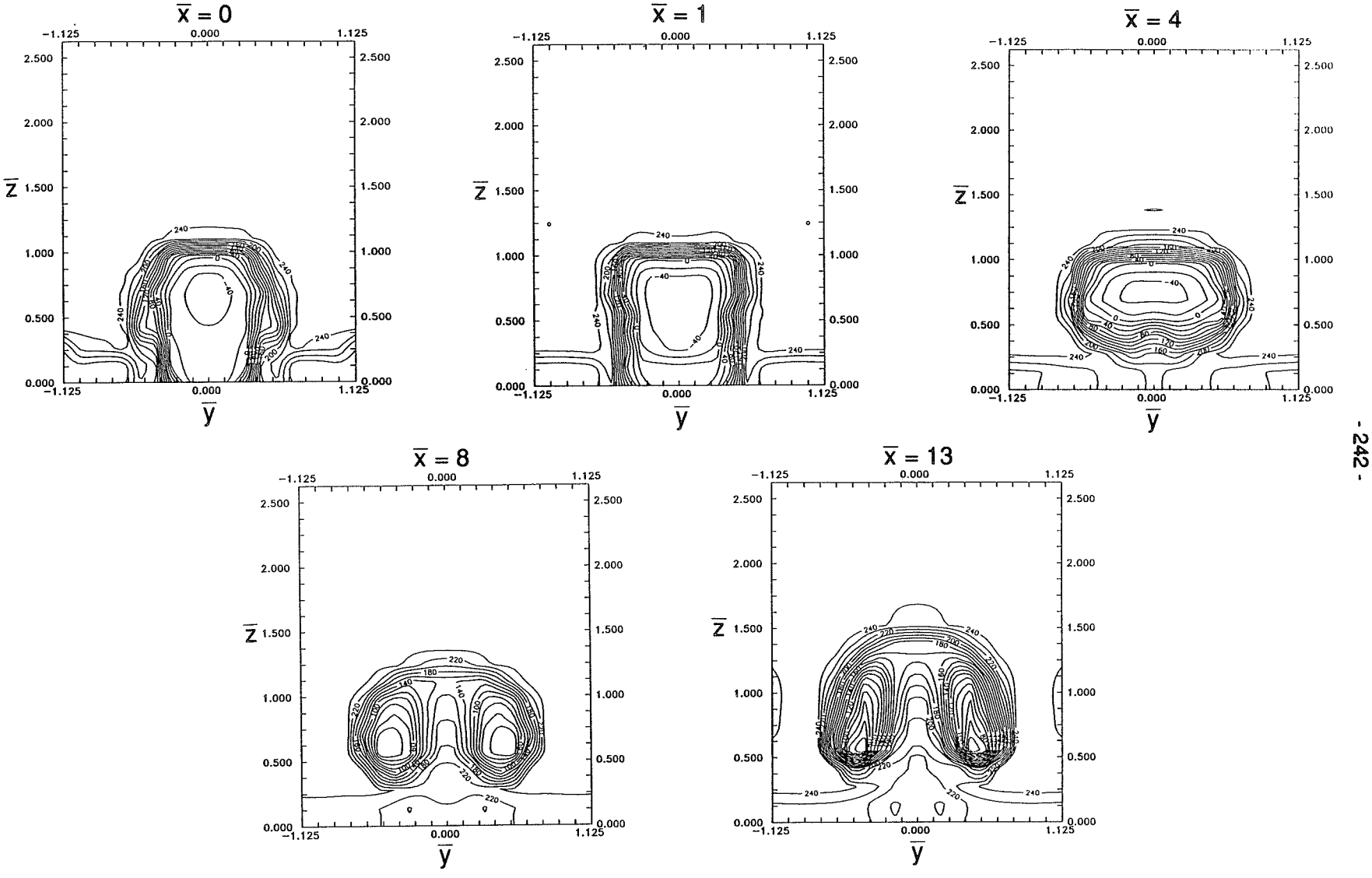

Figure 119. Total temperature (^{o}C). Full-scale model, wide spacing, natural boundary layer, $\bar{\delta} = 0.20$, $\bar{p} = 1.0$, $\bar{v} = 1.12$ (experimental).

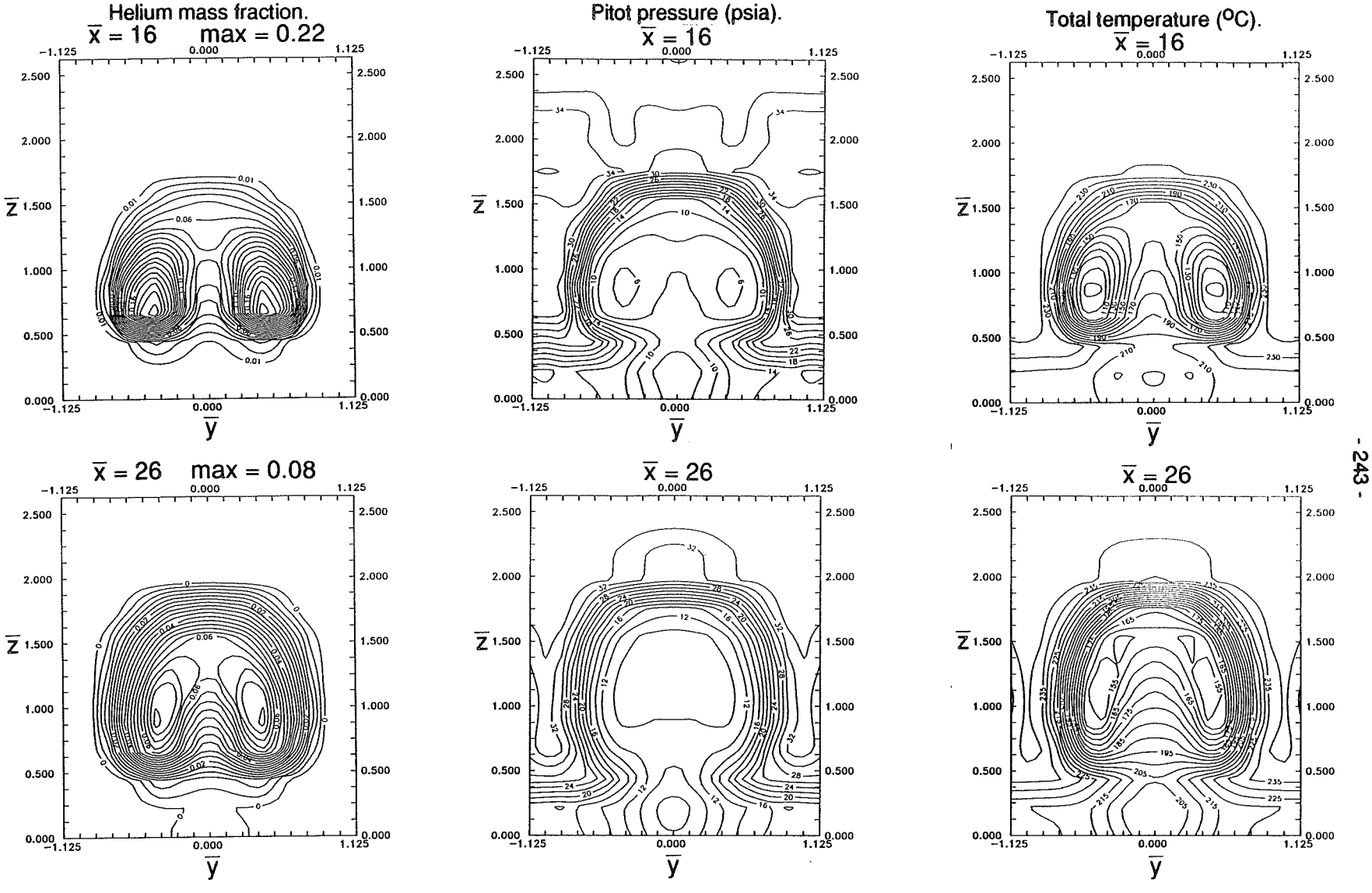

Figure 120. Half-scale model, wide spacing, natural boundary layer, $\bar{\delta} = 0.40$, $\bar{p} = 1.0$, $\bar{v} = 1.14$ (experimental).

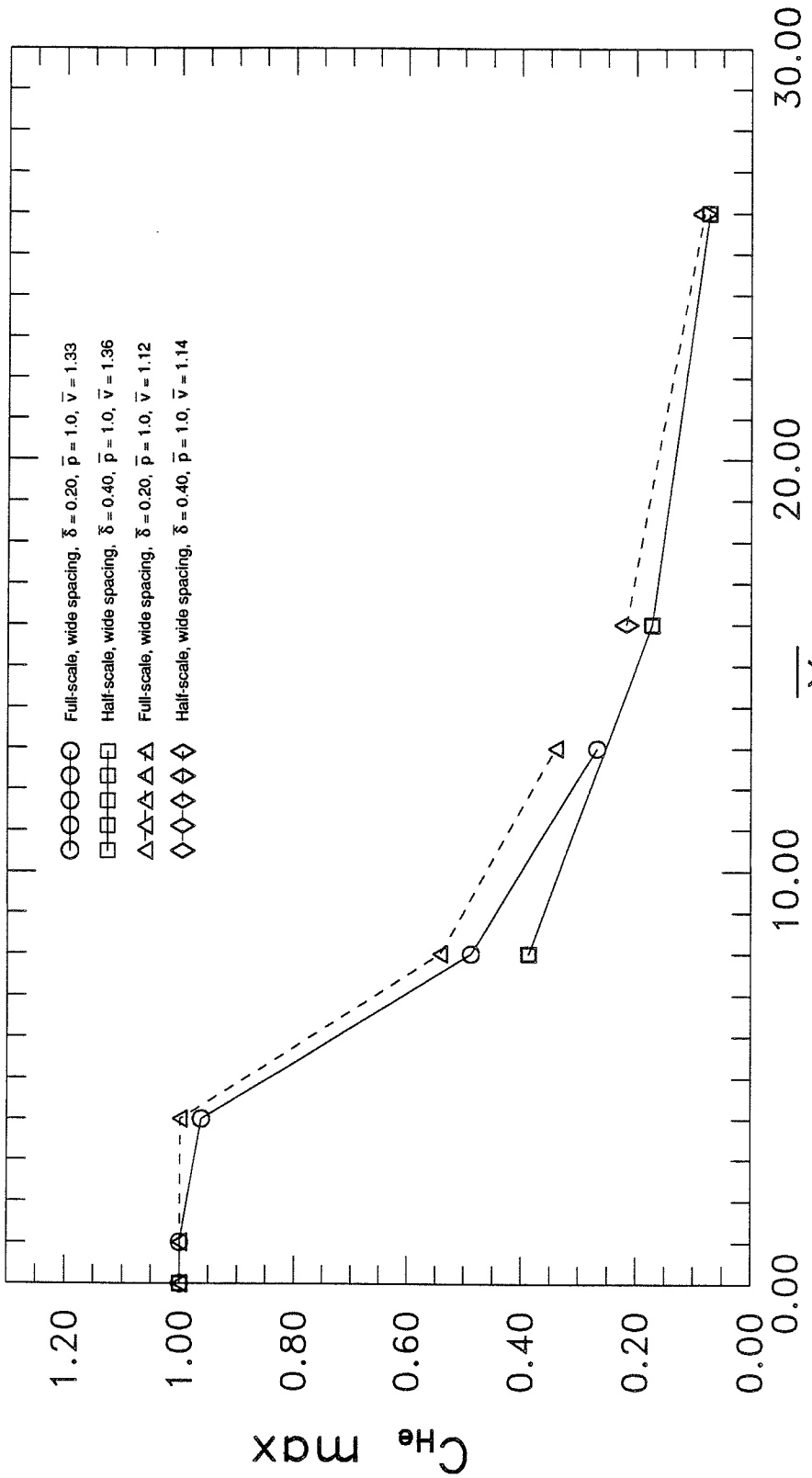

Figure 121. Decay of maximum helium mass fraction : Velocity ratio effects (experimental).

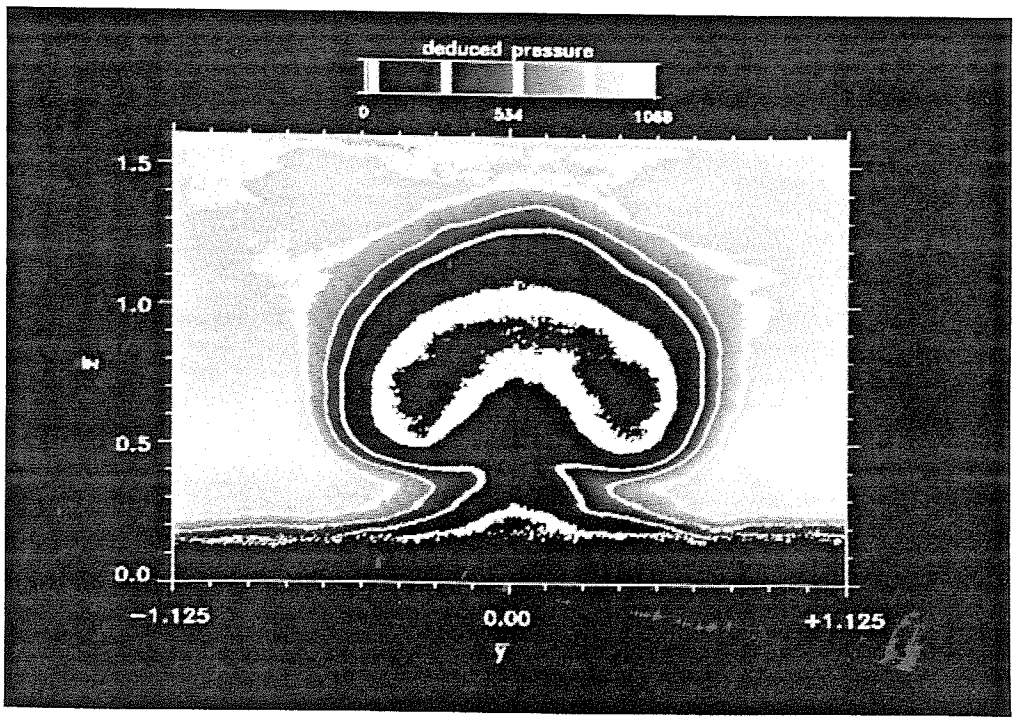

Figure 122. Mean of 22 planar Rayleigh images at $\overline{x}$ = 10.

Wide spacing, $\overline{\delta}$ = 0.20, $\overline{p}$ = 1.0, $\overline{v}$ = 1.12, $\alpha_c = \alpha_e = 4.76^o$.

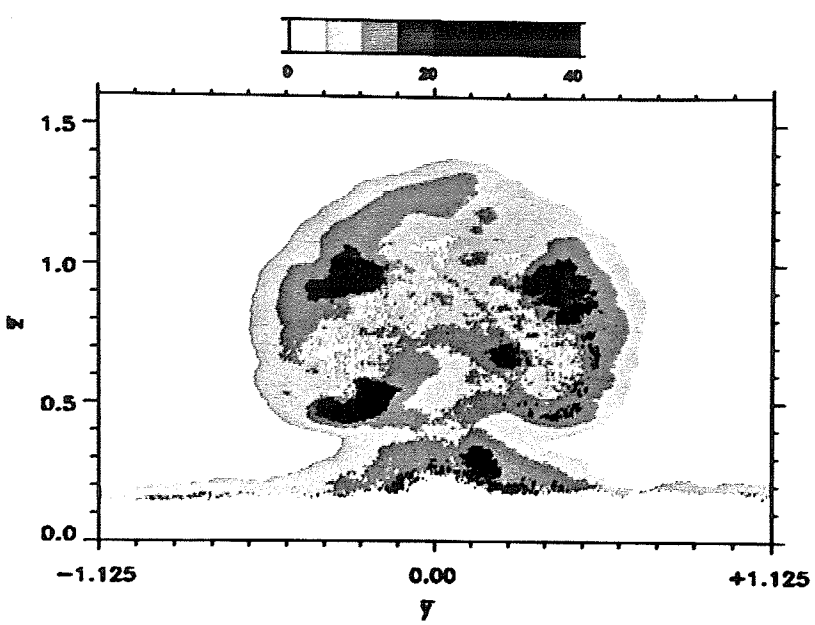

Figure 123. Standard deviation (%mean) about the mean for planar Rayleigh images at $\overline{x}$ = 10.

Wide spacing, $\overline{\delta}$ = 0.20, $\overline{p}$ = 1.0, $\overline{v}$ = 1.12, $\alpha_c = \alpha_e = 4.76^o$.

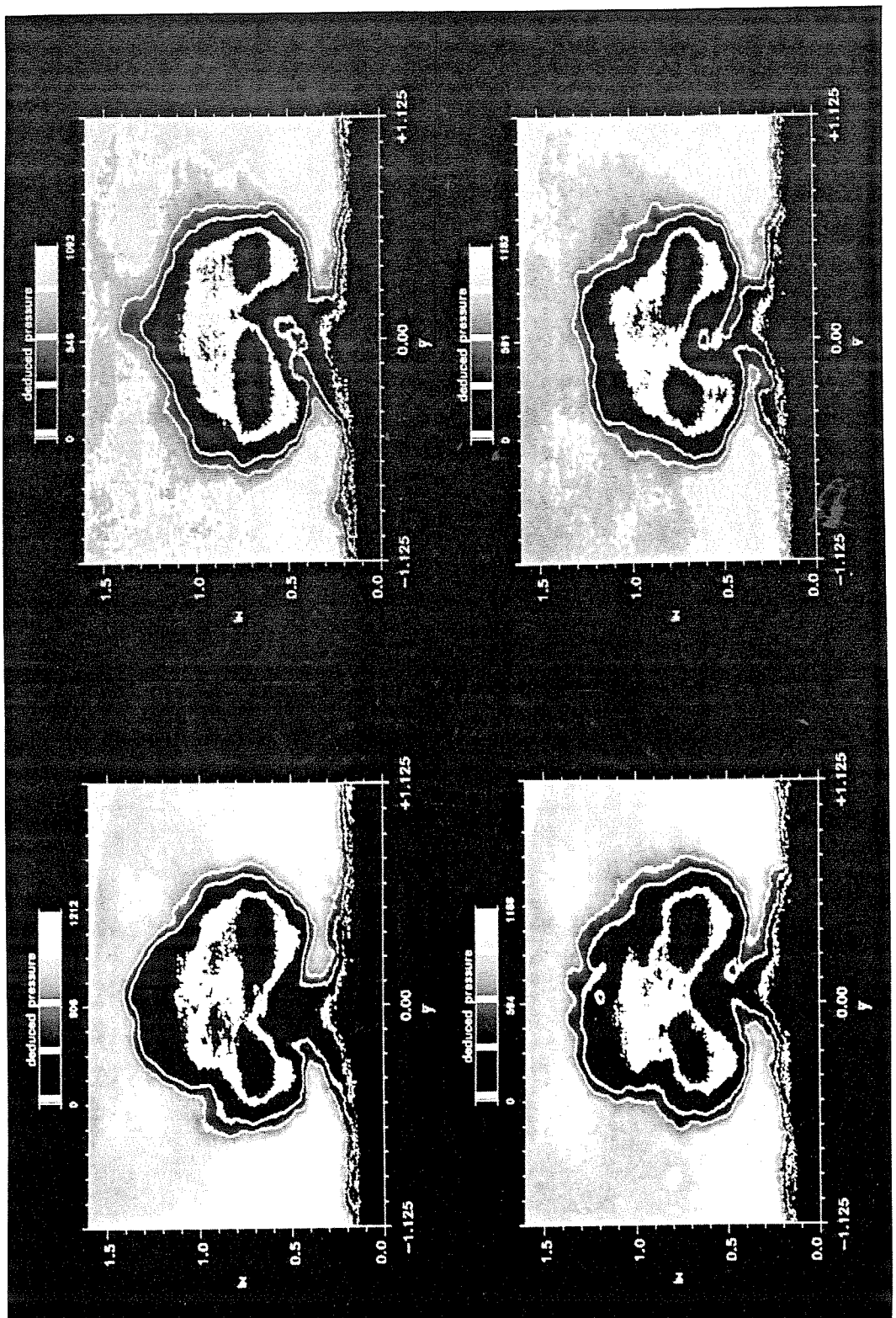

Figure 124. Instantaneous planar Rayleigh images at $\bar{x} = 10$. Wide spacing, $\bar{\delta} = 0.20$, $\bar{p} = 1.0$, $\bar{v} = 1.12$, $\alpha_c = \alpha_e = 4.76^o$.

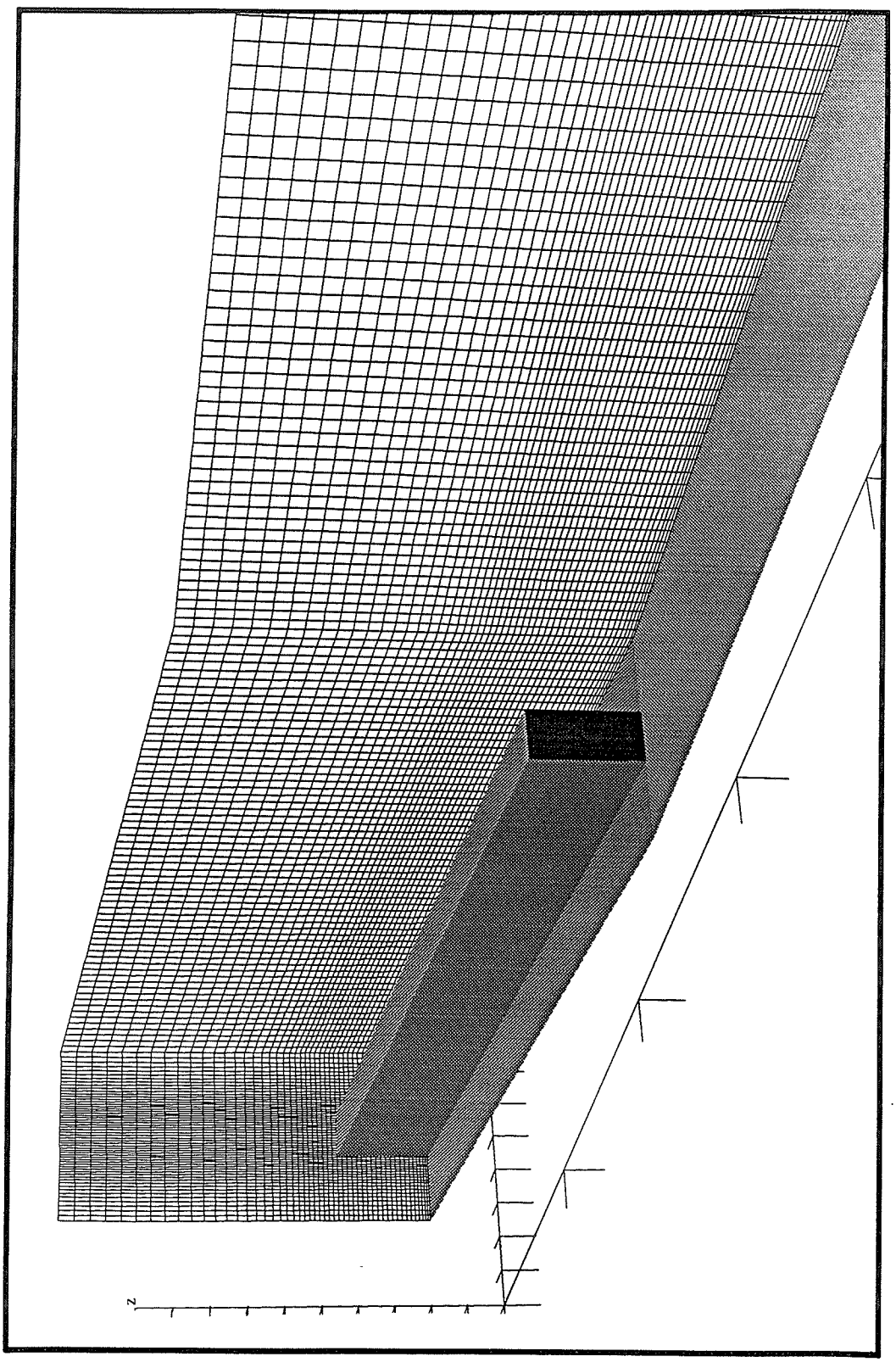

Figure 125. The all-shock geometry.

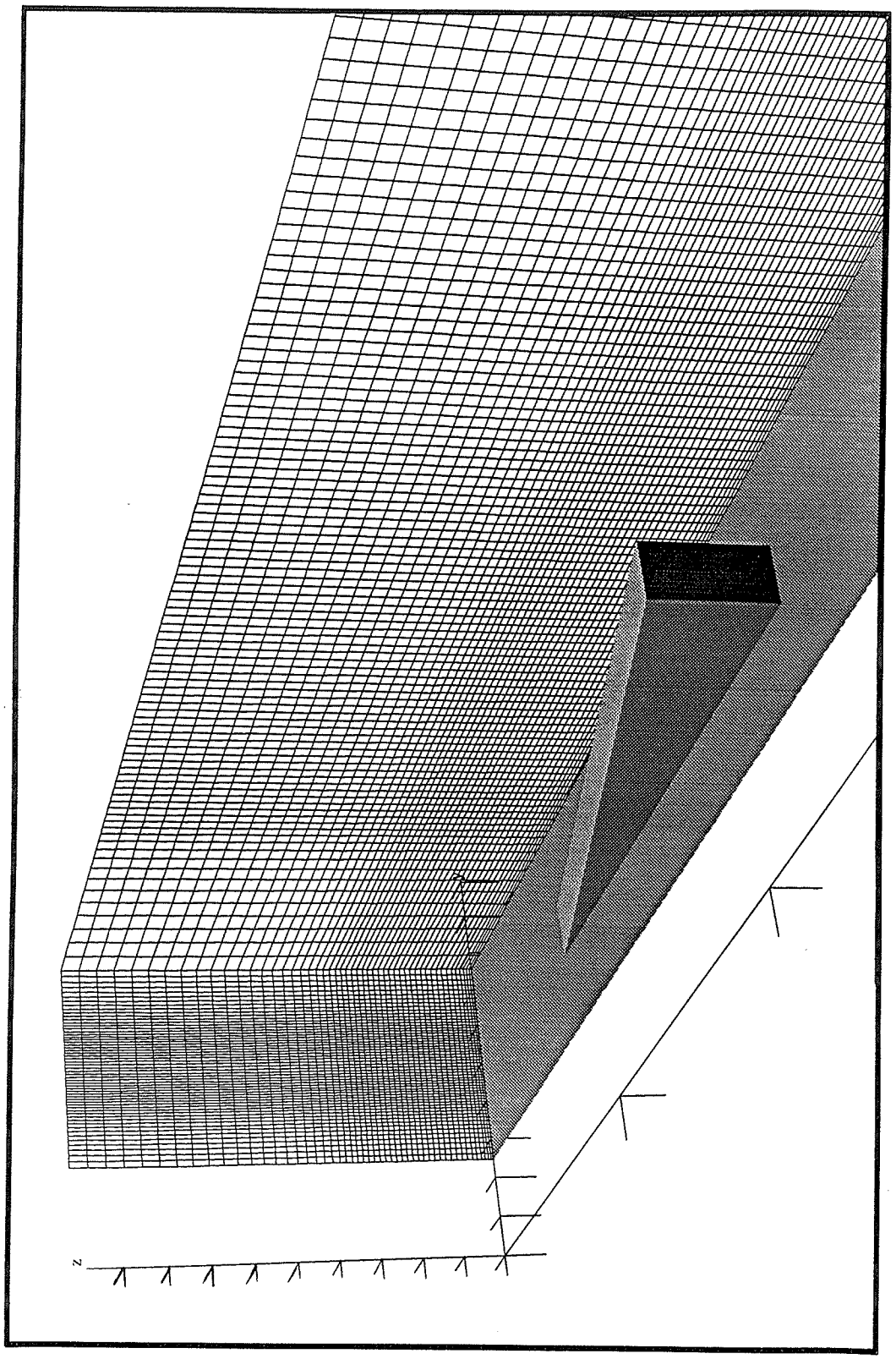

Figure 126. The no-shock geometry.

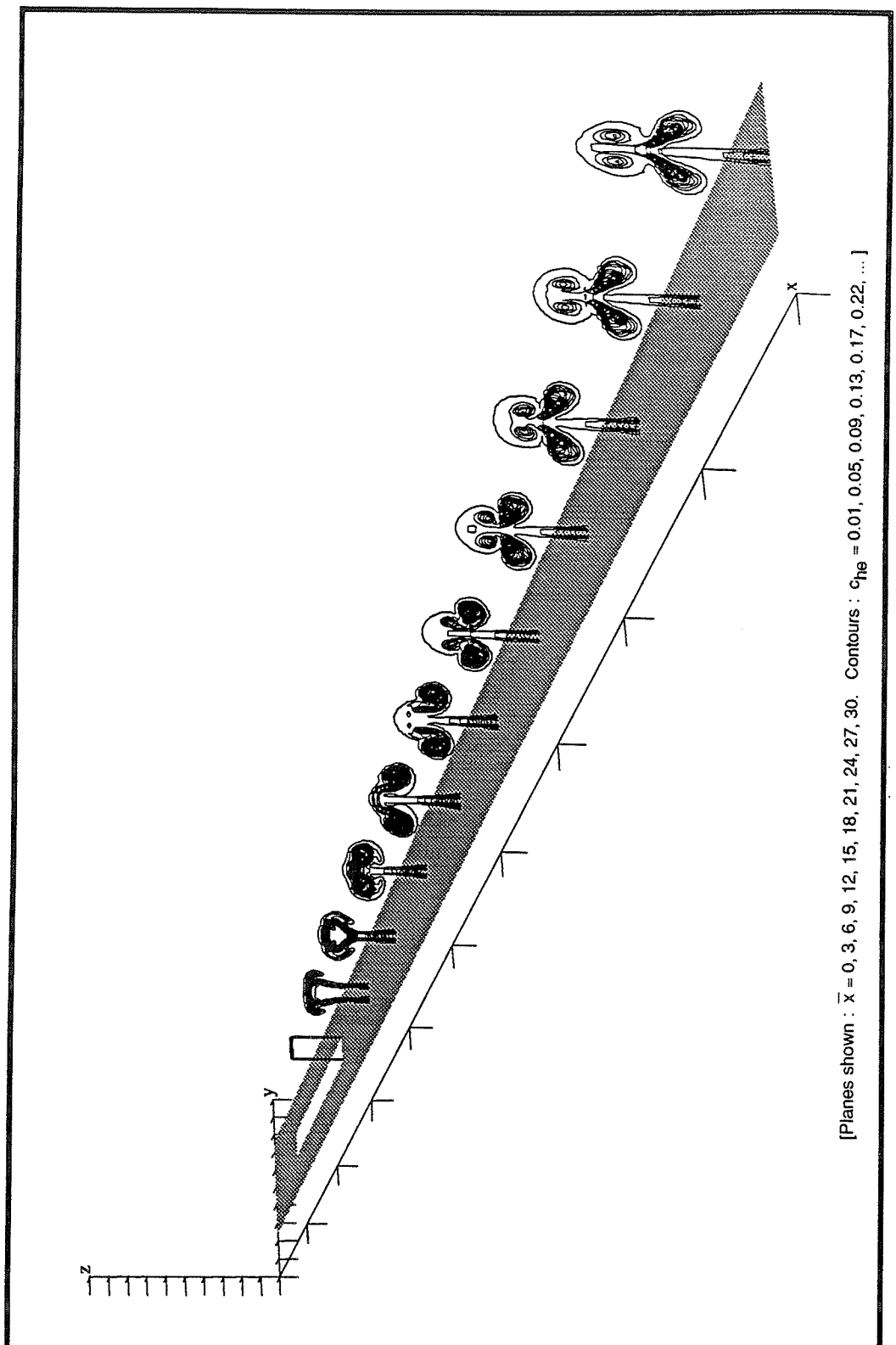

Figure 127. Contours of constant helium mass fraction.

Wide spacing, $\bar{\delta}$ = 0 (inviscid b.c.), $\bar{p}$ = 1.0, $\bar{v}$ = 1.0, $\alpha_c = 9.46^o$, $\alpha_e = 0^o$ (computational).

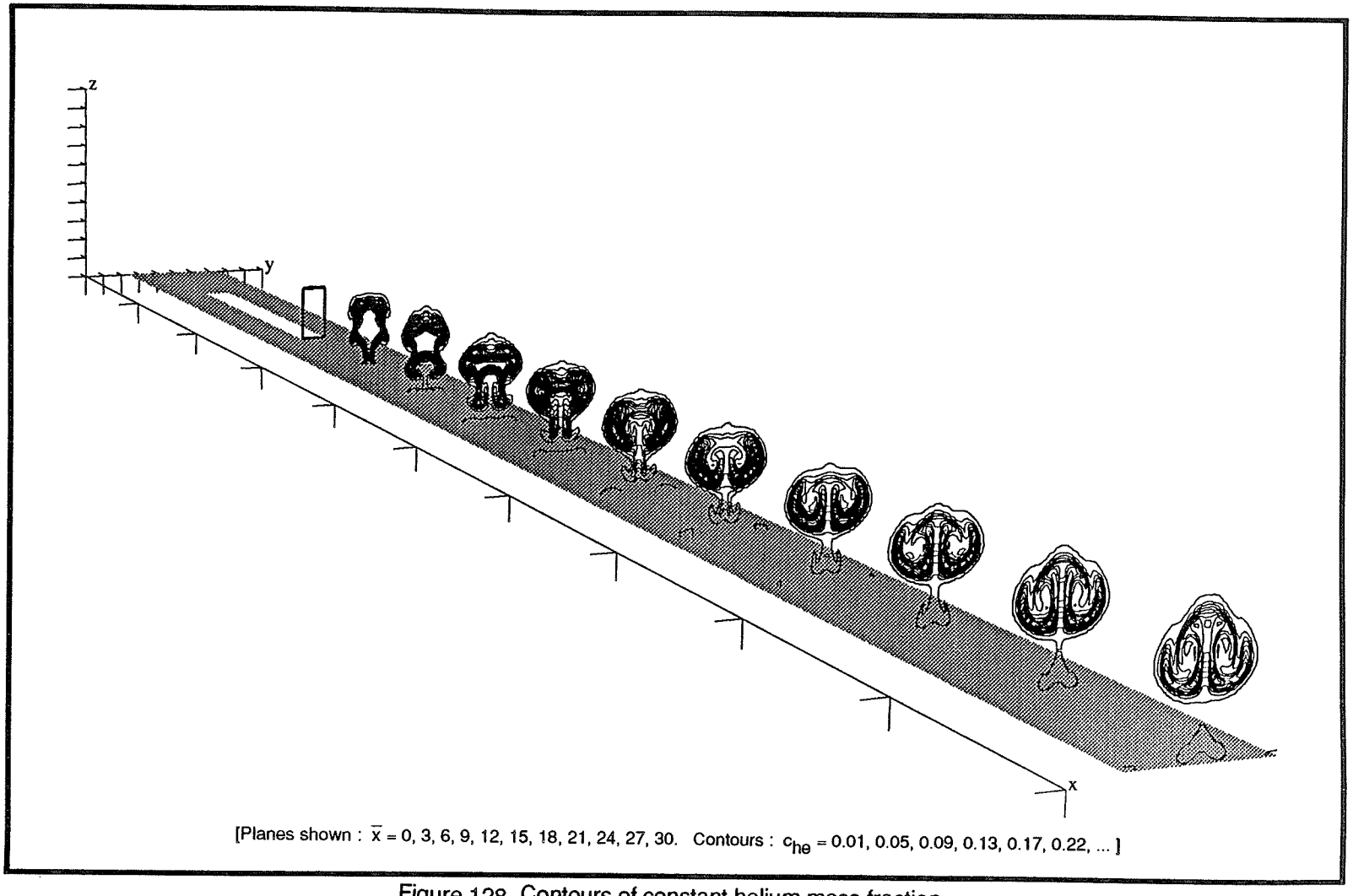

Figure 128. Contours of constant helium mass fraction.

Wide spacing, $\overline{\delta}$ = 0.20, $\overline{p}$ = 1.0, $\overline{v}$ = 1.0, $\alpha_c = 9.46^o$, $\alpha_e = 0^o$ (computational).

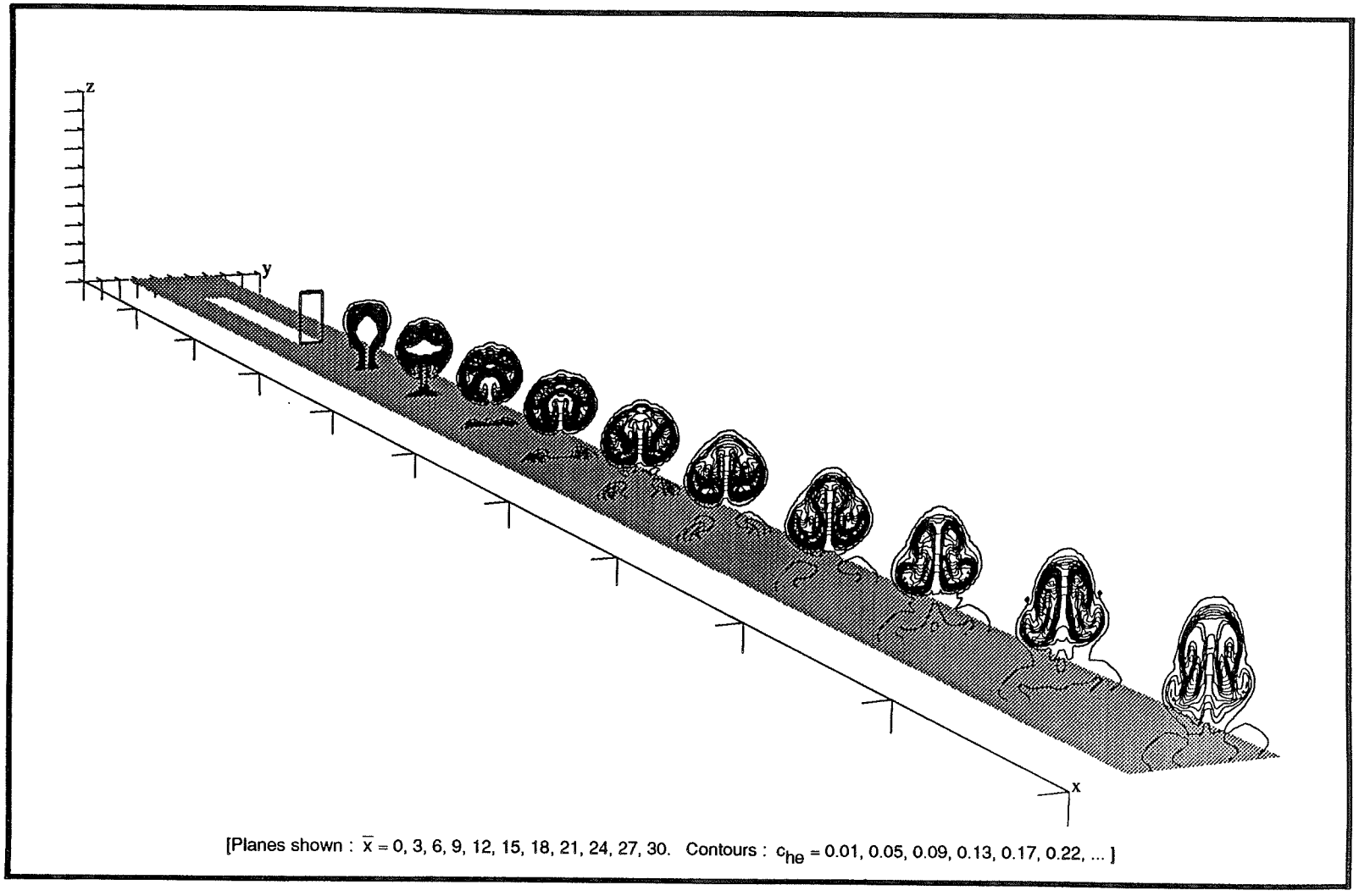

Figure 129. Contours of constant helium mass fraction.

Wide spacing, $\bar{\delta}$ = 1.0, $\bar{p}$ = 1.0, $\bar{v}$ = 1.0, $\alpha_c = 9.46^o$, $\alpha_e = 0^o$ (computational).

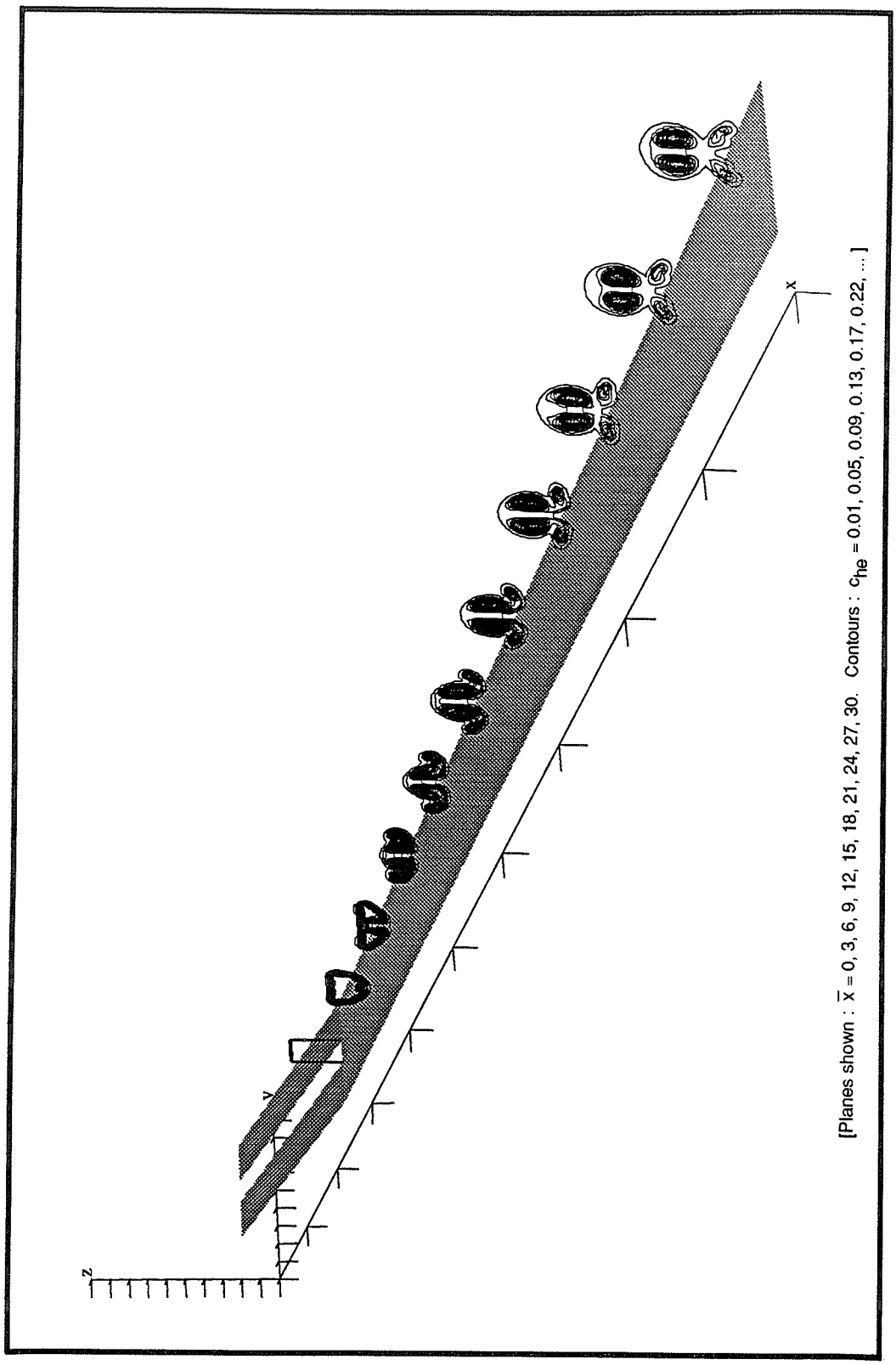

Figure 130. Contours of constant helium mass fraction.

Wide spacing, $\bar{\delta}$ = 0 (invisicd b.c.), $\bar{p}$ = 1.0, $\bar{v}$ = 1.0, all-shock geometry, $\alpha_e = 4.76^o$ (computational).

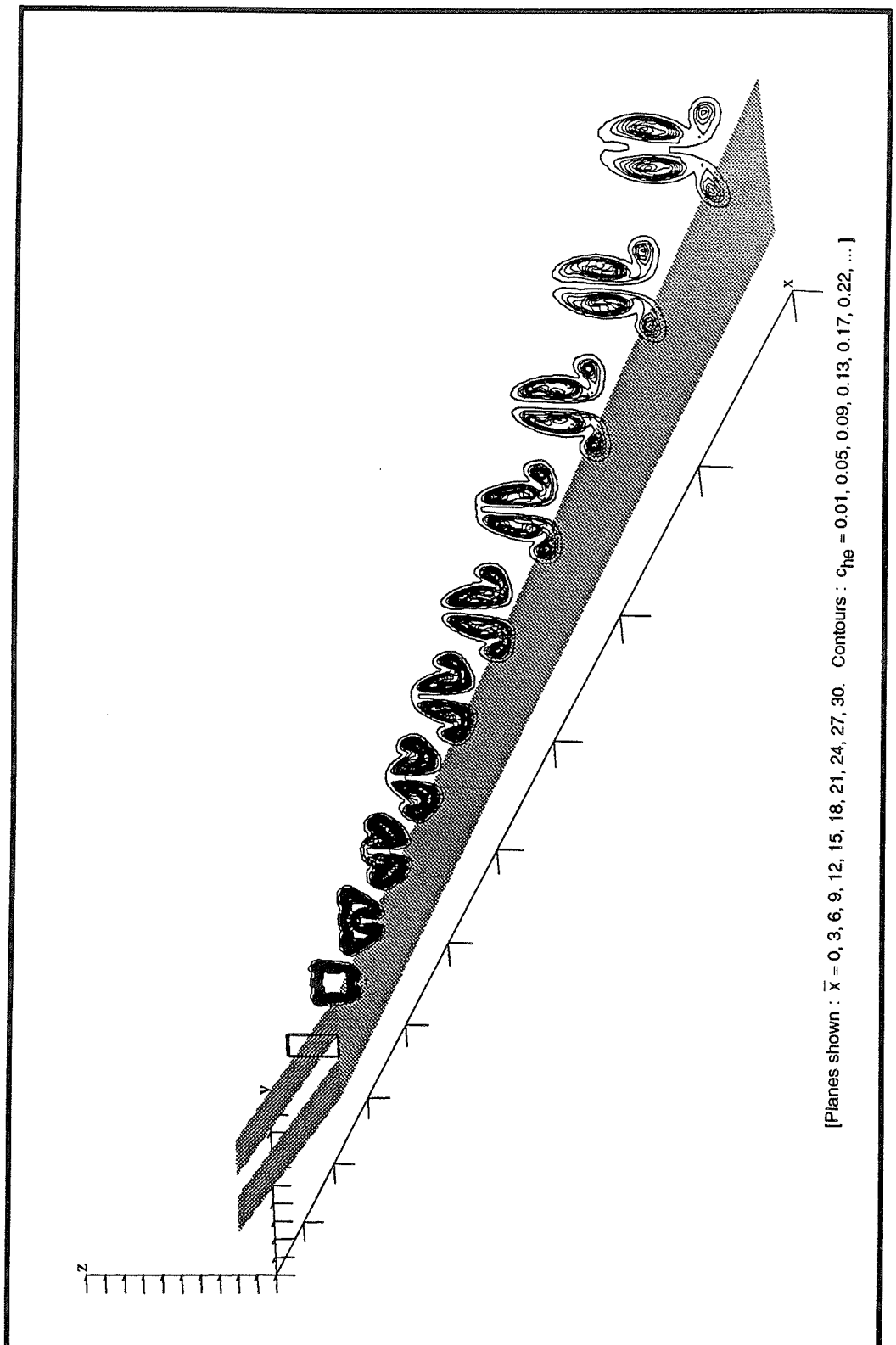

Figure 131. Contours of constant helium mass fraction.

Wide spacing, $\bar{\delta}$ = 0.20, $\bar{p}$ = 1.0, $\bar{v}$ = 1.0, all-shock geometry, $\alpha_e = 4.76^o$ (computational).

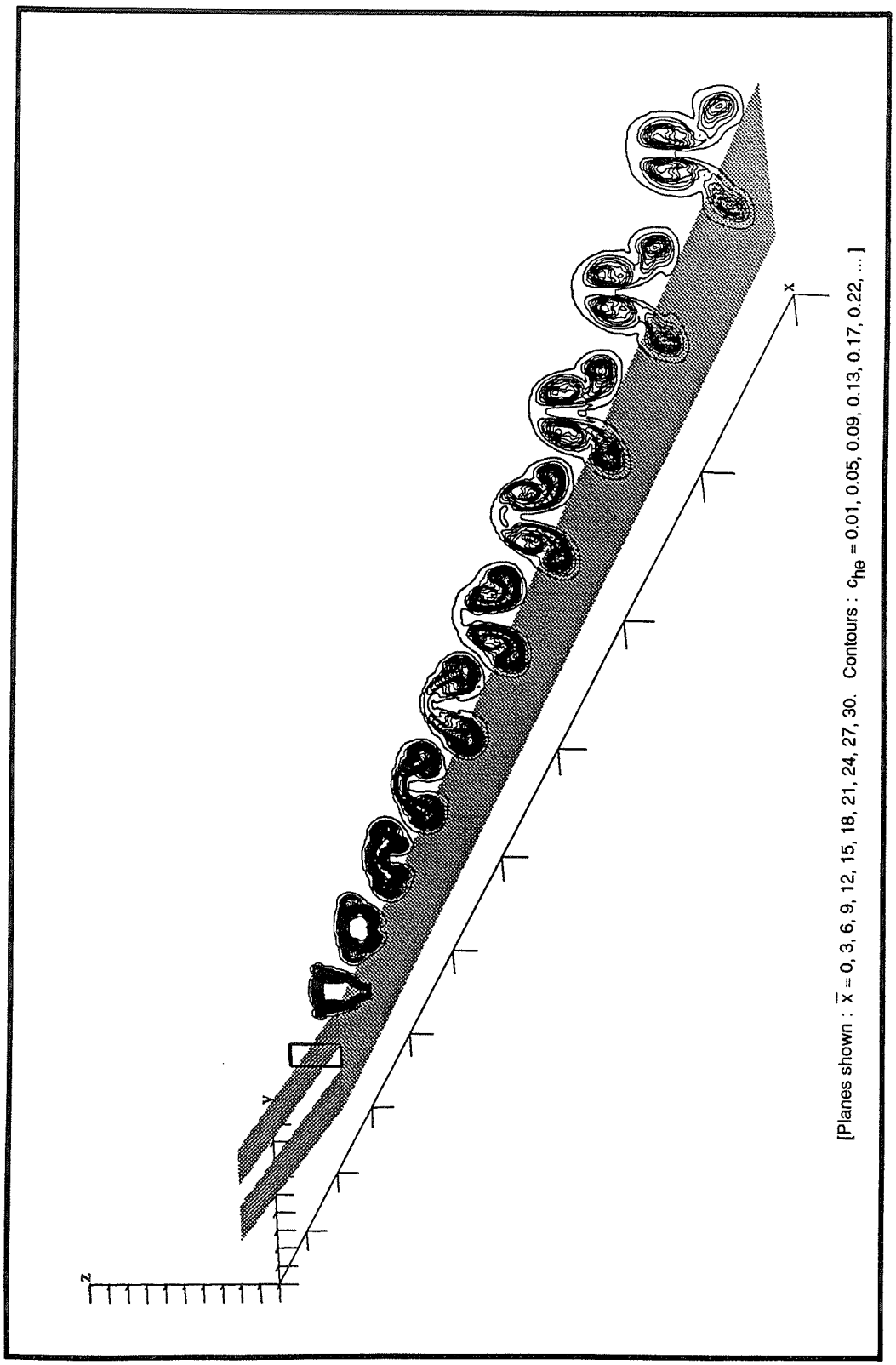

Figure 132. Contours of constant helium mass fraction.

Wide spacing, $\overline{\delta}$ = 1.0, $\overline{p}$ = 1.0, $\overline{v}$ = 1.0, all-shock geometry, $\alpha_e = 4.76^o$ (computational).

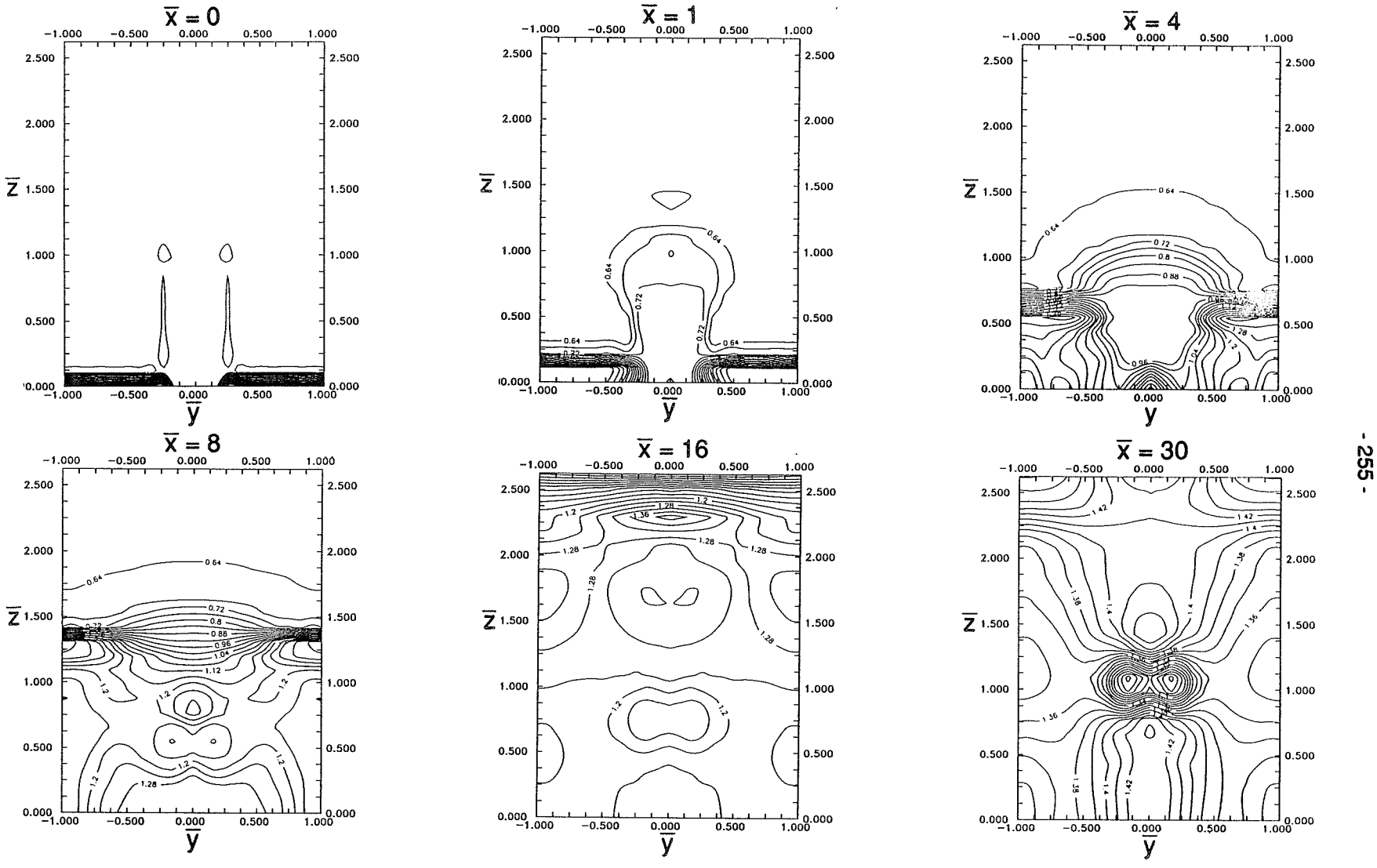

Figure 133. Static pressure (psia). Wide spacing, $\bar{\delta} = 0$ (inviscid b.c.), $\bar{p} = 1.0$, $\bar{v} = 1.0$, all-shock geometry, $\alpha_e = 4.76^o$ (computational).

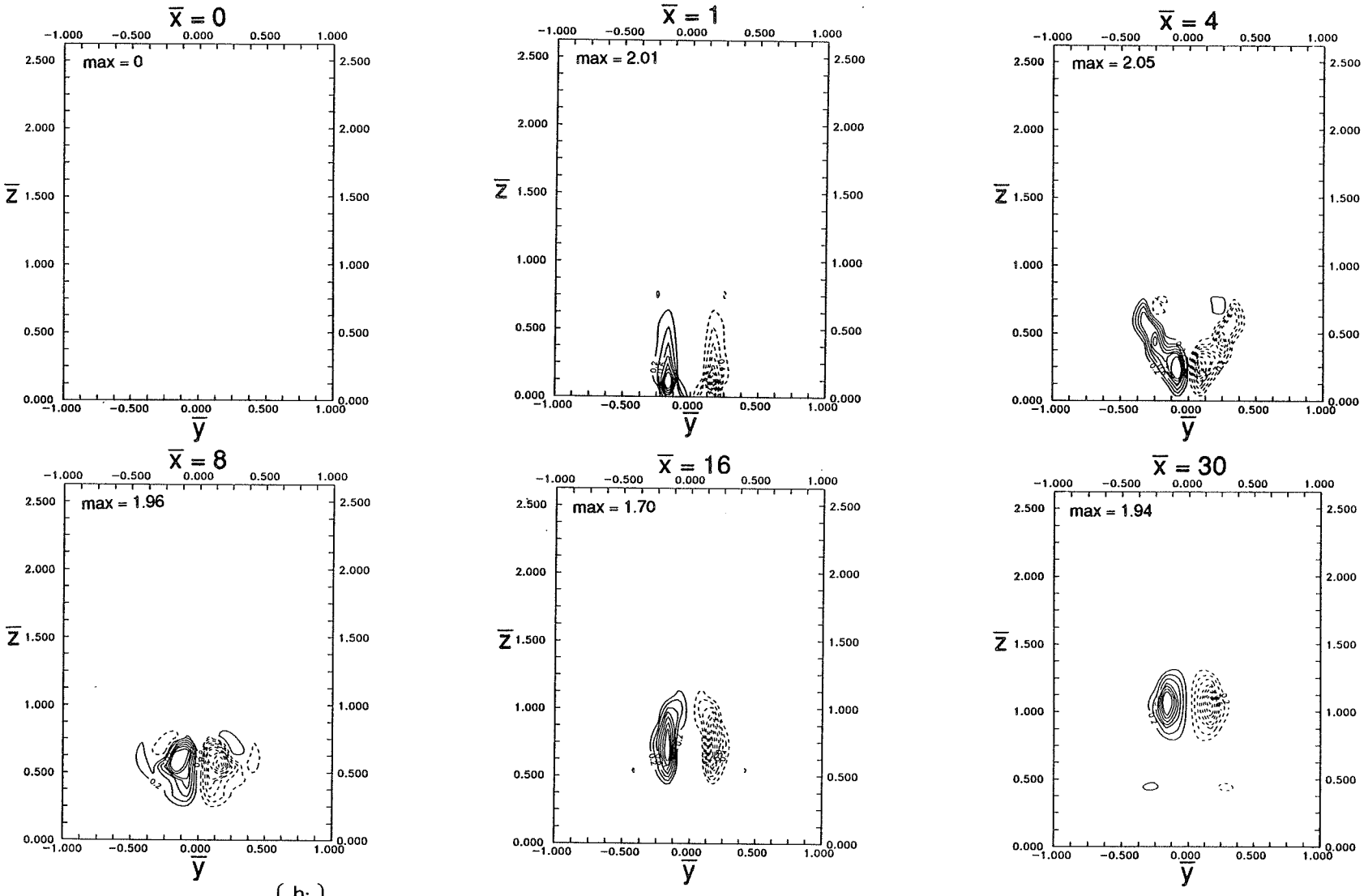

Figure 134. Vorticity, $\omega_x \left(\frac{h_i}{U_\infty} \right)$. Wide spacing, $\bar{\delta} = 0$ (inviscid b.c.), $\bar{p} = 1.0$, $\bar{v} = 1.0$, all-shock geometry, $\alpha_e = 4.76^o$ (computational).

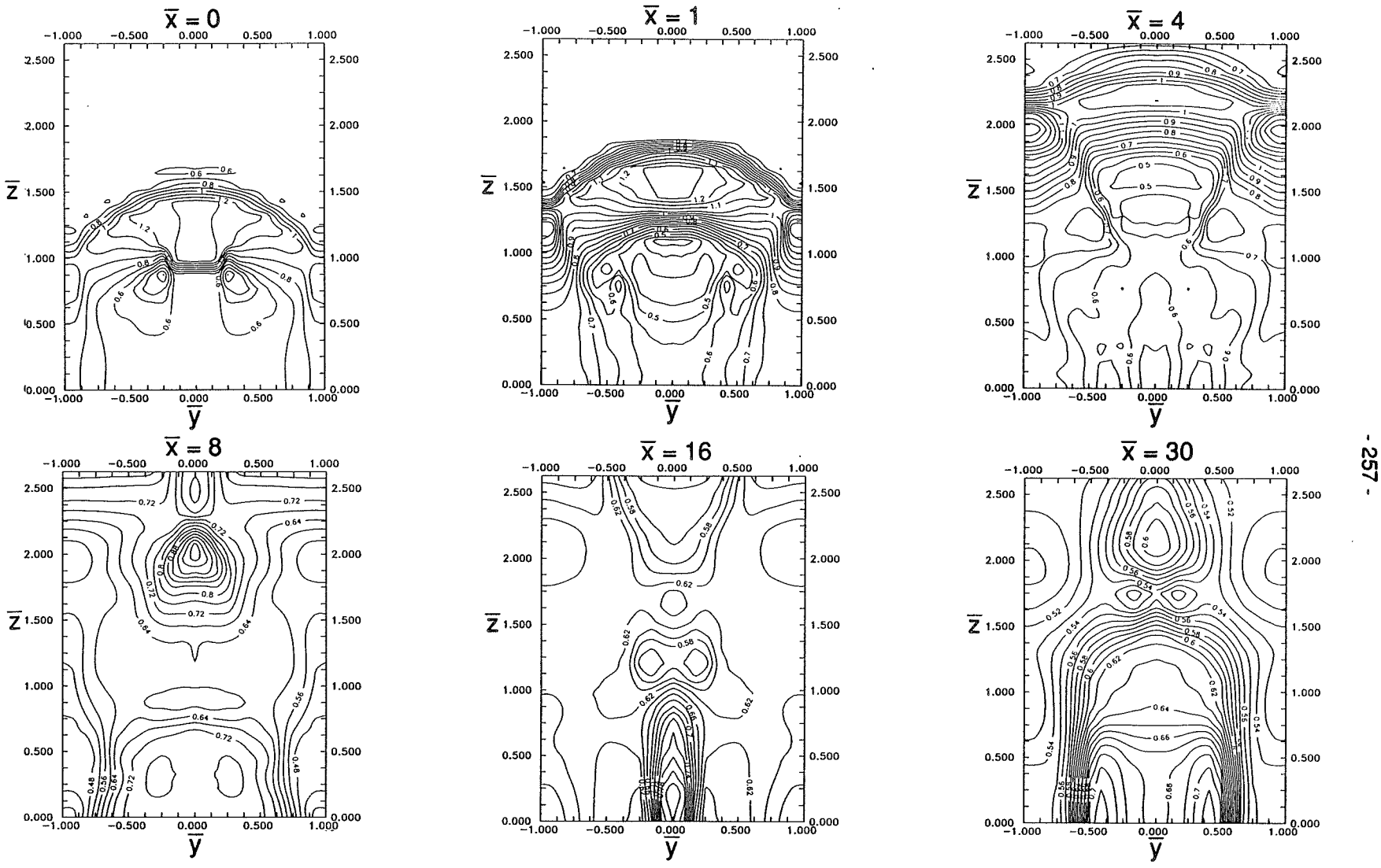

Figure 135. Static pressure (psia). Wide spacing, $\bar{\delta} = 0$ (invicid b.c.), $\bar{p} = 1.0$, $\bar{v} = 1.0$, $\alpha_c = 9.46^o$, $\alpha_e = 0^o$ (computational).

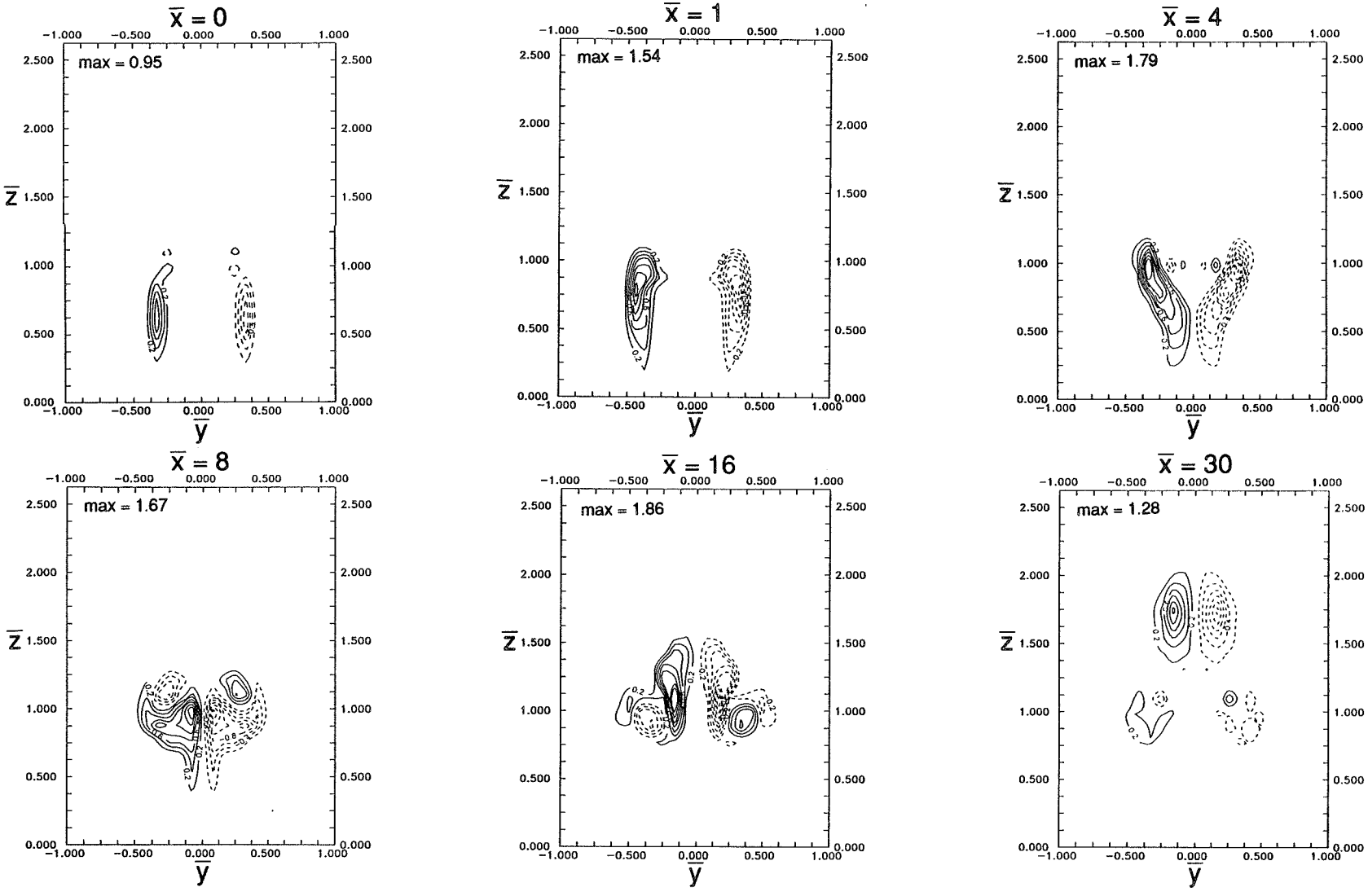

Figure 136. Vorticity, $\omega_x \left(\frac{h_i}{U_\infty} \right)$. Wide spacing, $\bar{\delta} = 0$ (invicid b.c.), $\bar{p} = 1.0$, $\bar{v} = 1.0$, $\alpha_c = 9.46^o$, $\alpha_e = 0^o$ (computational).

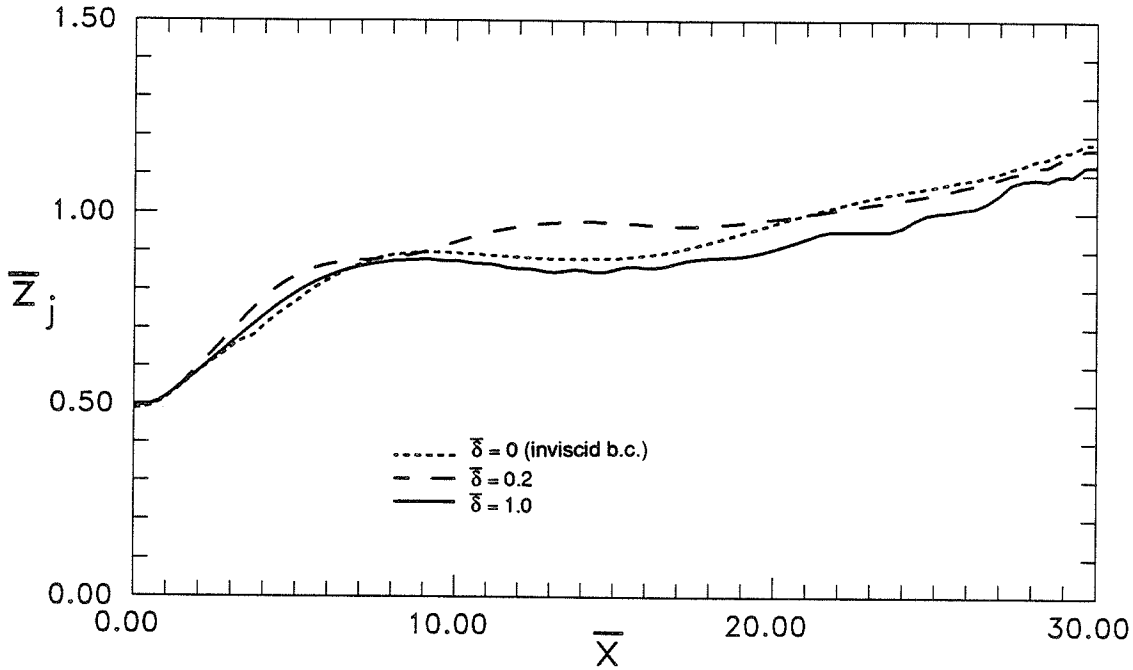

Figure 137. Effects of boundary layer thickness on jet lift-off for the no-shock model.

Wide spacing, $\overline{p}$ = 1.0, $\overline{v}$ = 1.0, $\alpha_c = 9.46^o$, $\alpha_e = 0^o$ (computational).

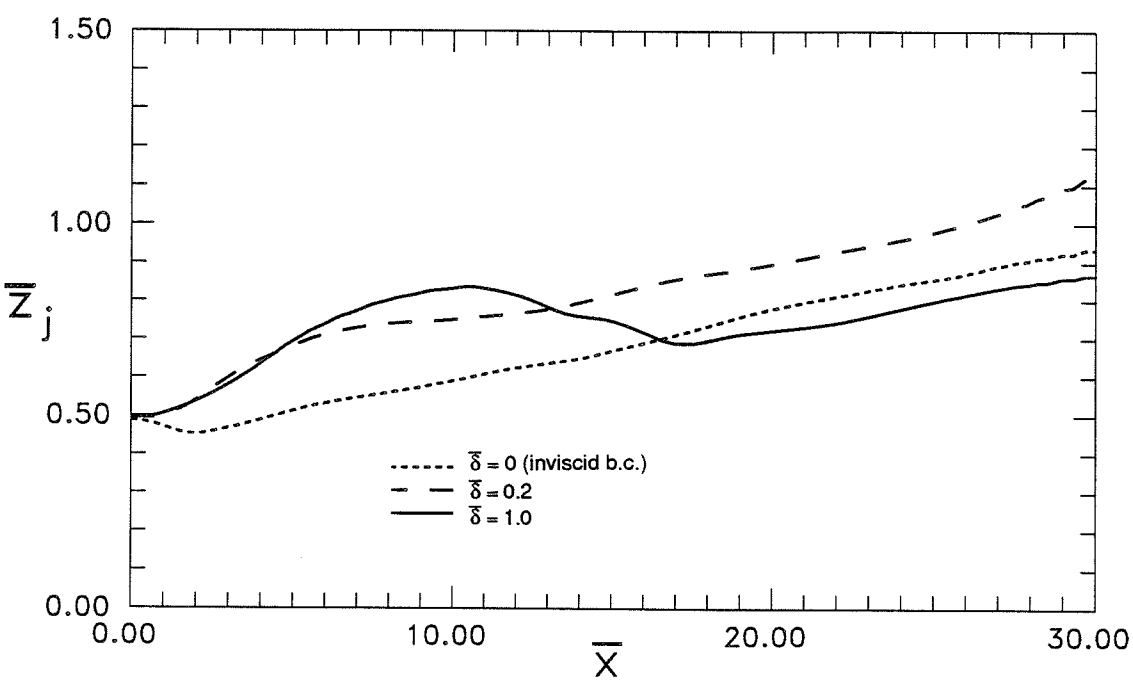

Figure 138. Effects of boundary layer thickness on jet lift-off for the all-shock model.

Wide spacing, $\overline{p}$ = 1.0, $\overline{v}$ = 1.0, $\alpha_e = 4.76^o$ (computational).

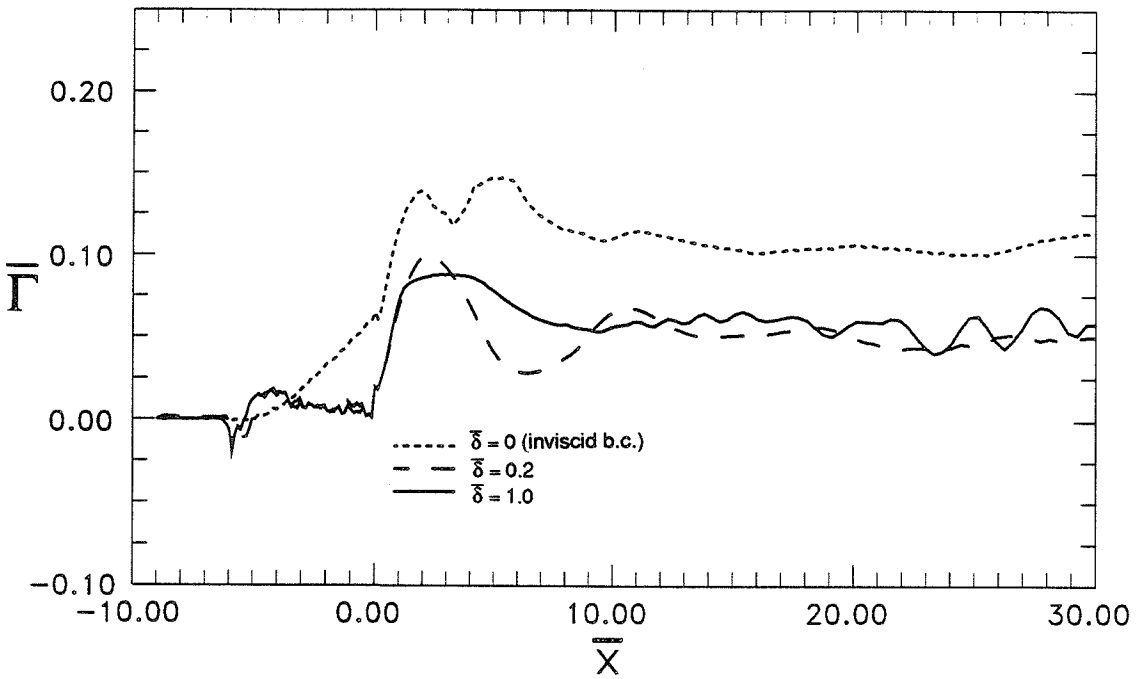

Figure 139. Effects of boundary layer thickness on circulation for the no-shock model.

Wide spacing, $\overline{p} = 1.0$, $\overline{v} = 1.0$, $\alpha_c = 9.46^o$, $\alpha_e = 0^o$ (computational).

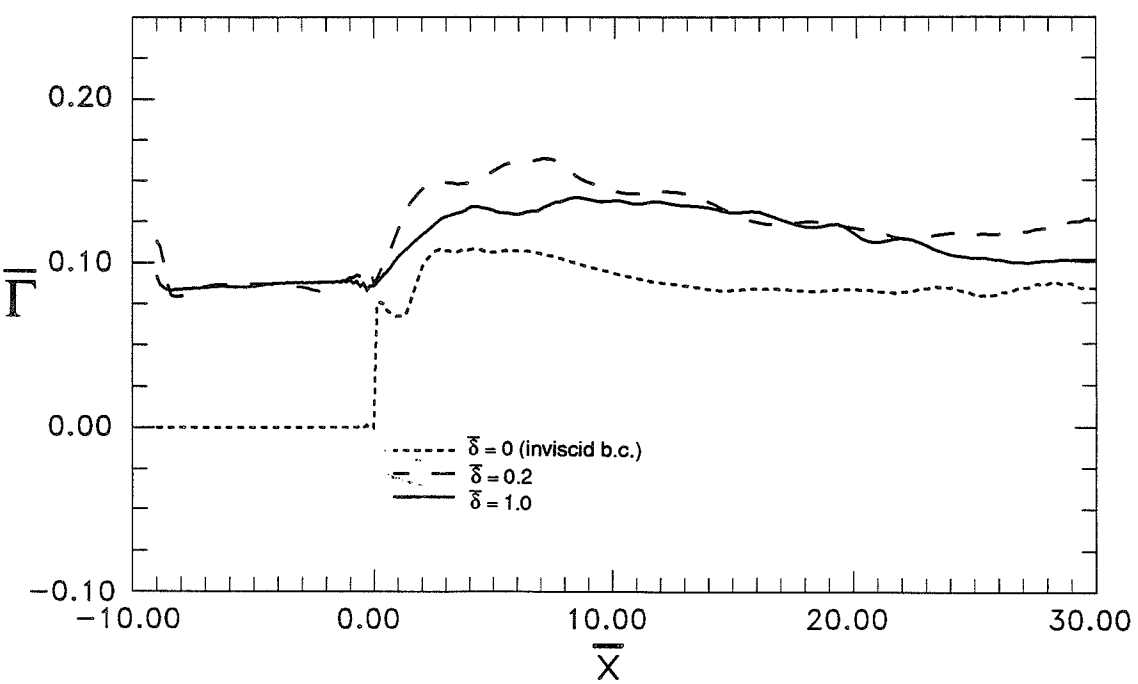

Figure 140. Effects of boundary layer thickness on circulation for the all-shock model.

Wide spacing, $\overline{p} = 1.0$, $\overline{v} = 1.0$, $\alpha_e = 4.76^o$ (computational).

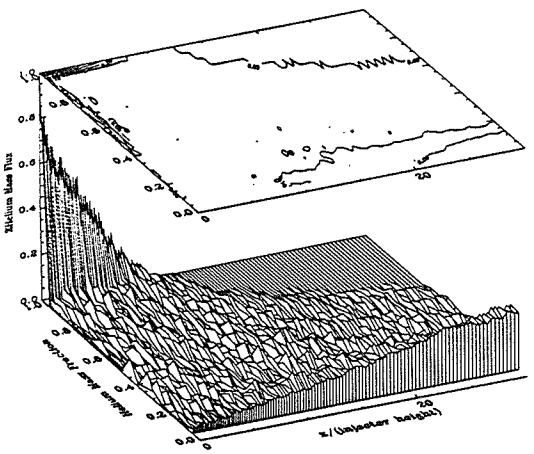

a. All-shock, $\alpha_e = 4.76^o$, $\overline{\delta} = 0$ (invicid b.c.)

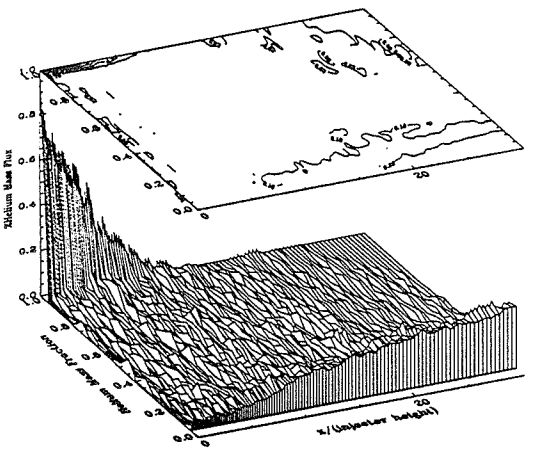

d. No-shock, $\alpha_c = 9.46^o$, $\alpha_e = 0^o$, $\overline{\delta} = 0$ (invicid b.c.)

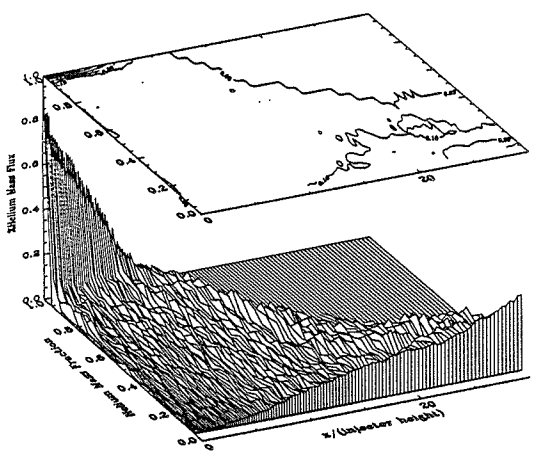

b. All-shock, $\alpha_e = 4.76^o$, $\overline{\delta} = 0.2$

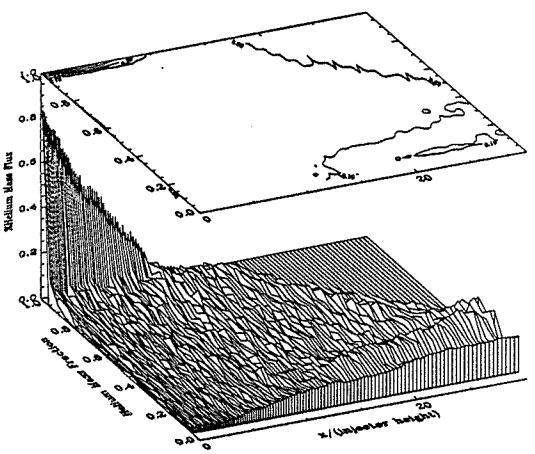

e. No-shock, $\alpha_c = 9.46^o$, $\alpha_e = 0^o$, $\overline{\delta} = 0.2$

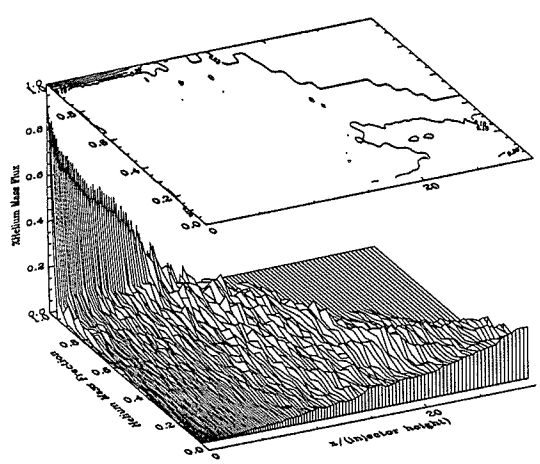

c. All-shock, $\alpha_e = 4.76^o$, $\overline{\delta} = 1.0$

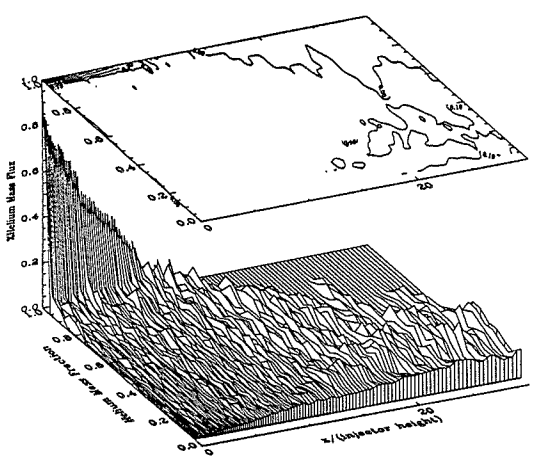

f. No-shock, $\alpha_c = 9.46^o$, $\alpha_e = 0^o$, $\overline{\delta} = 1.0$

Figure 141. Mixedness Measure for various boundary layer thicknesses for all-shock and no-shock models, $\overline{p} = 1.0$, $\overline{v} = 1.0$ (computational).

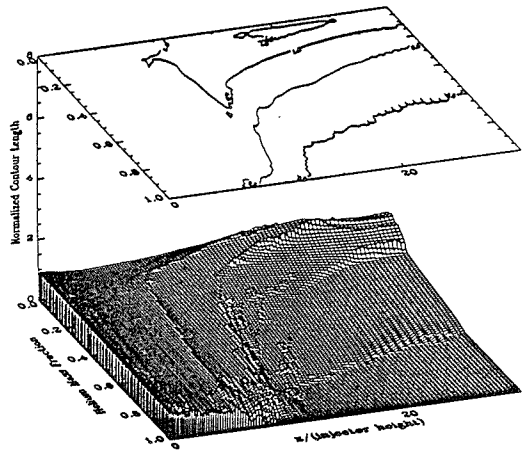

a. All-shock, $\alpha_e = 4.76^o$, $\overline{\delta} = 0$ (invicid b.c.)

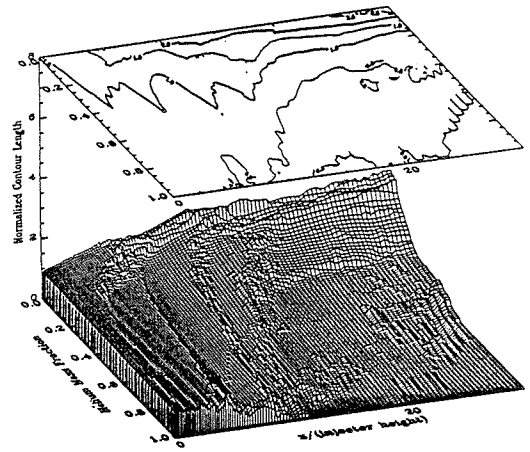

d. No-shock, $\alpha_c = 9.46^o$, $\alpha_e = 0^o$, $\overline{\delta} = 0$ (invicid b.c.)

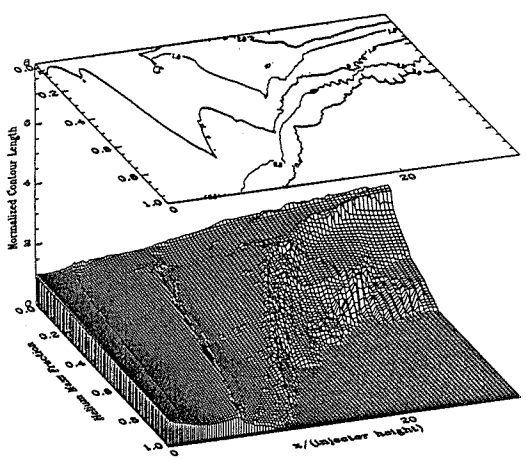

b. All-shock, $\alpha_e = 4.76^o$, $\overline{\delta} = 0.2$

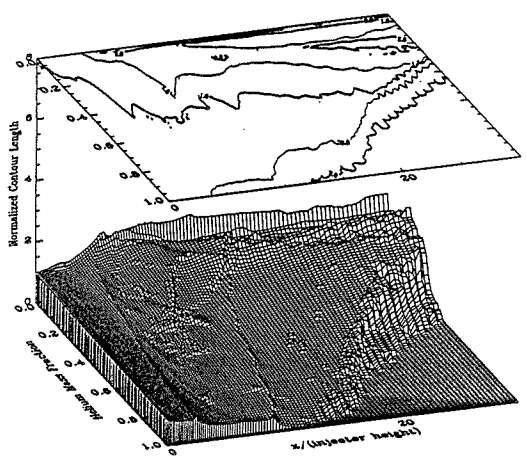

e. No-shock, $\alpha_c = 9.46^o$, $\alpha_e = 0^o$, $\overline{\delta} = 0.2$

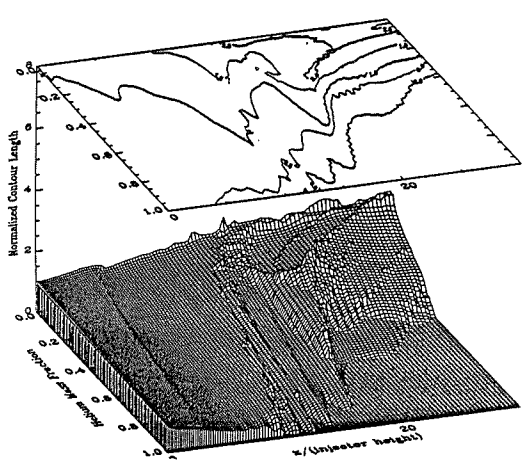

c. All-shock, $\alpha_e = 4.76^o$, $\overline{\delta} = 1.0$

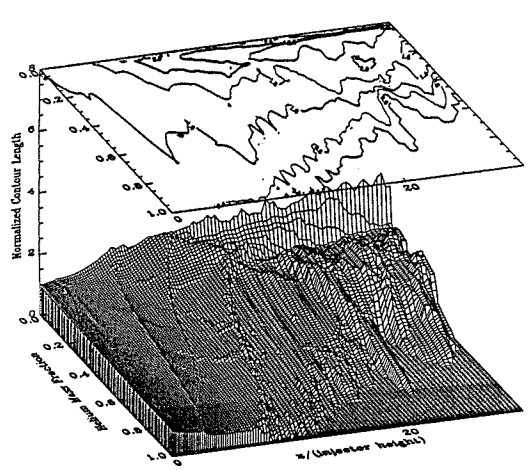

f. No-shock, $\alpha_c = 9.46^o$, $\alpha_e = 0^o$, $\overline{\delta} = 1.0$

Figure 142. Length of contours of constant mass fraction for various boundary layer thicknesses for all-shock and no-shock models, $\overline{p} = 1.0$, $\overline{v} = 1.0$ (computational).

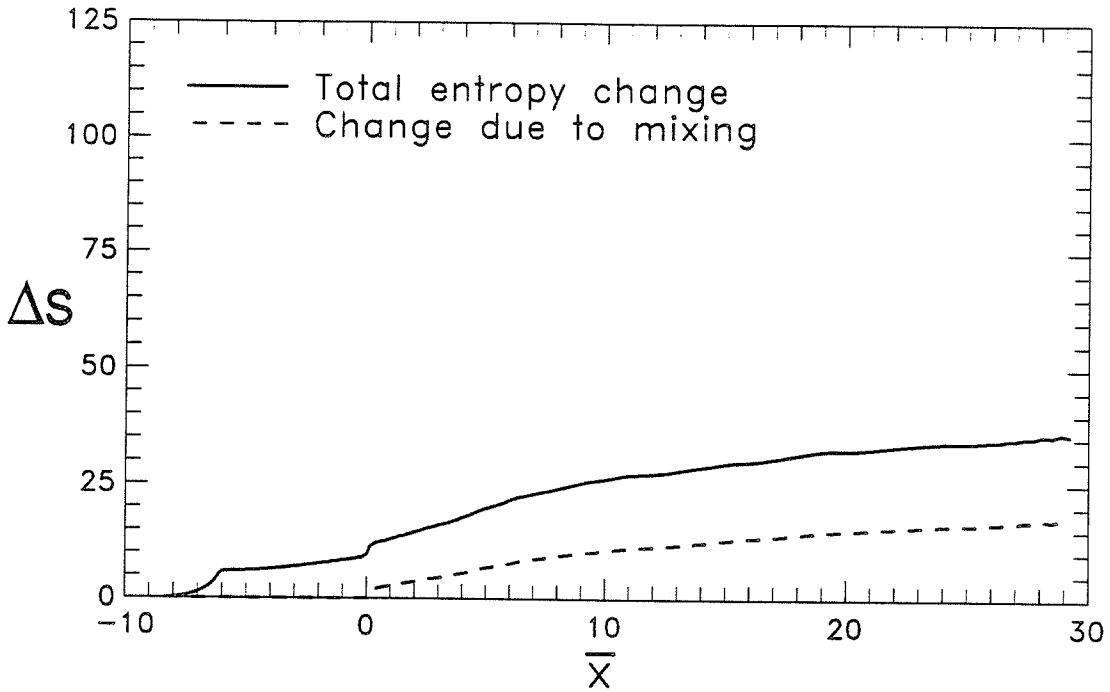

Figure 143. Entropy measure. Wide spacing, $\overline{\delta} = 0$ (inviscid b.c.), $\overline{p} = 1.0$, $\overline{v} = 1.0$, $\alpha_c = 9.46^o$, $\alpha_e = 0^o$ (computational).

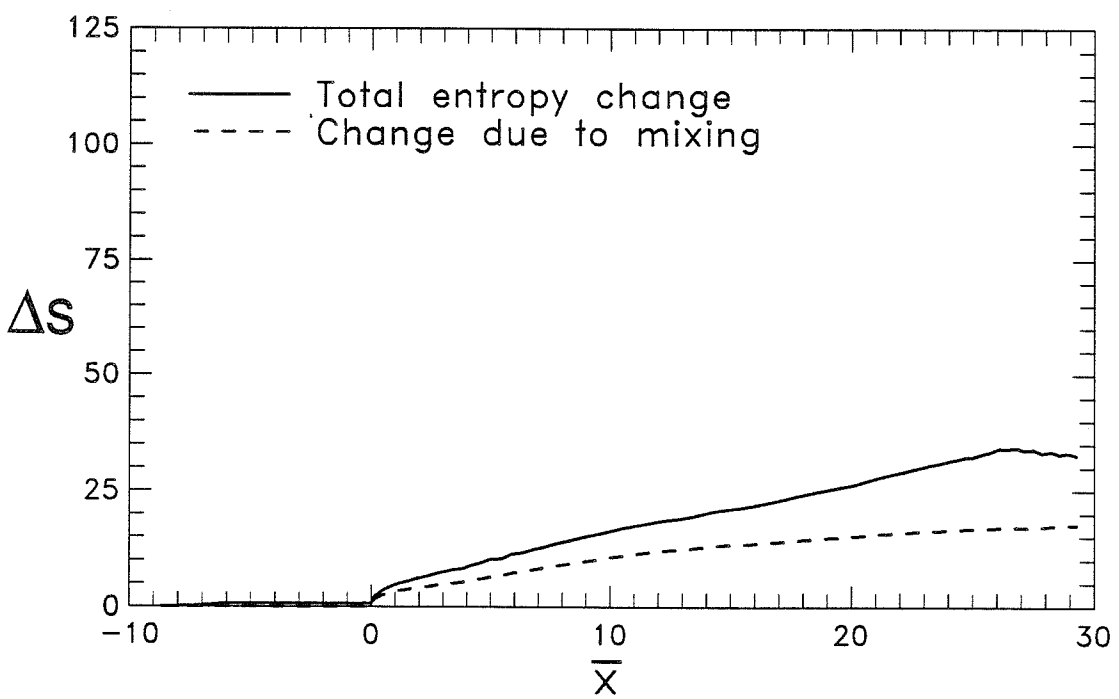

Figure 144. Entropy measure. Wide spacing, $\overline{\delta} = 0$ (inviscid b.c.), $\overline{p} = 1.0$, $\overline{v} = 1.0$, all-shock geometry, $\alpha_e = 4.76^o$ (computational).

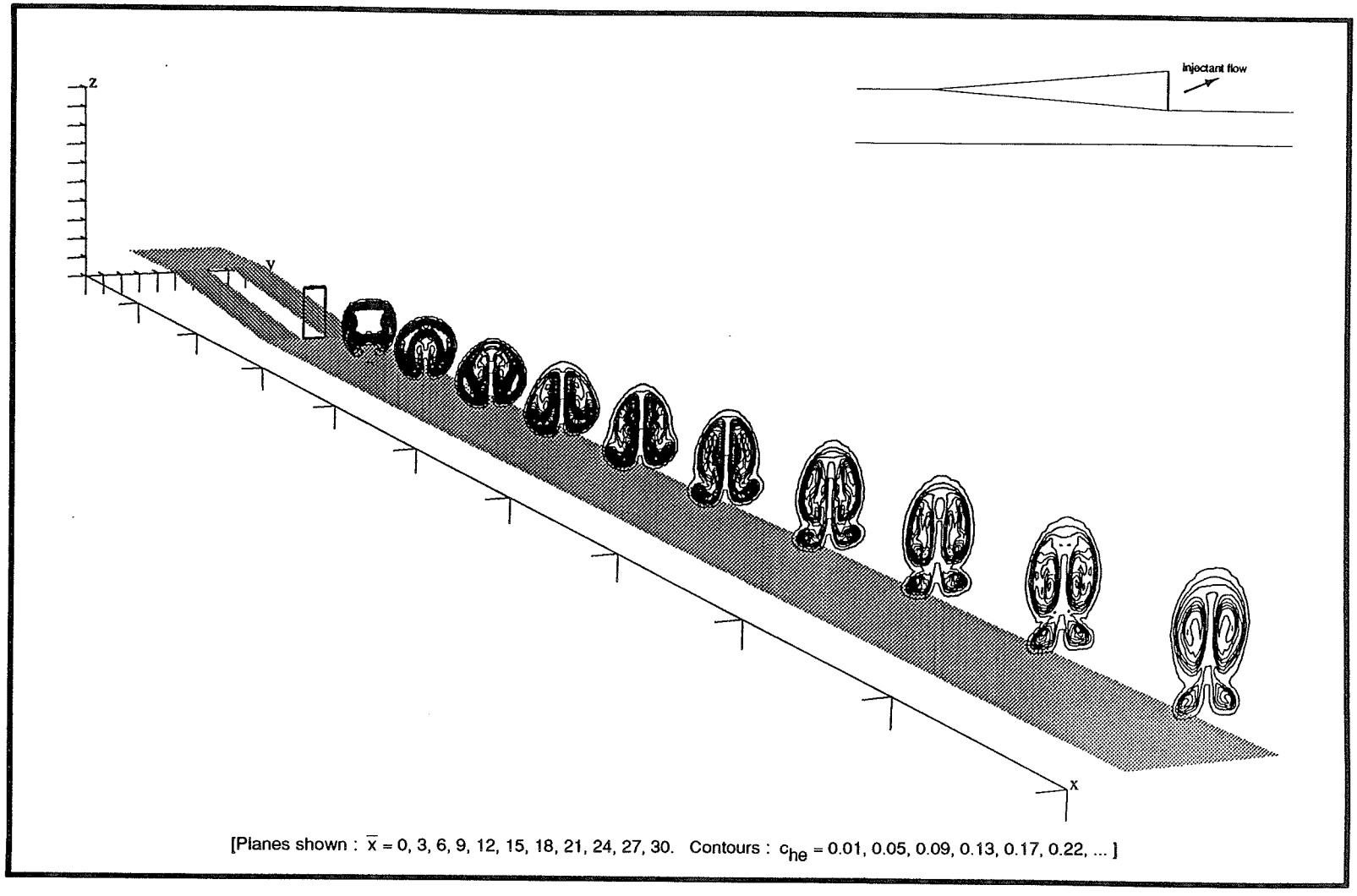

Figure 145. Contours of constant helium mass fraction.

Wide spacing, $\overline{\delta}$ = 0.20, $\overline{p}$ = 1.0, $\overline{v}$ = 1.0, $\alpha_c = \alpha_e = 4.76^o$, angled injection $\alpha_i = 7.5^o$ (computational).

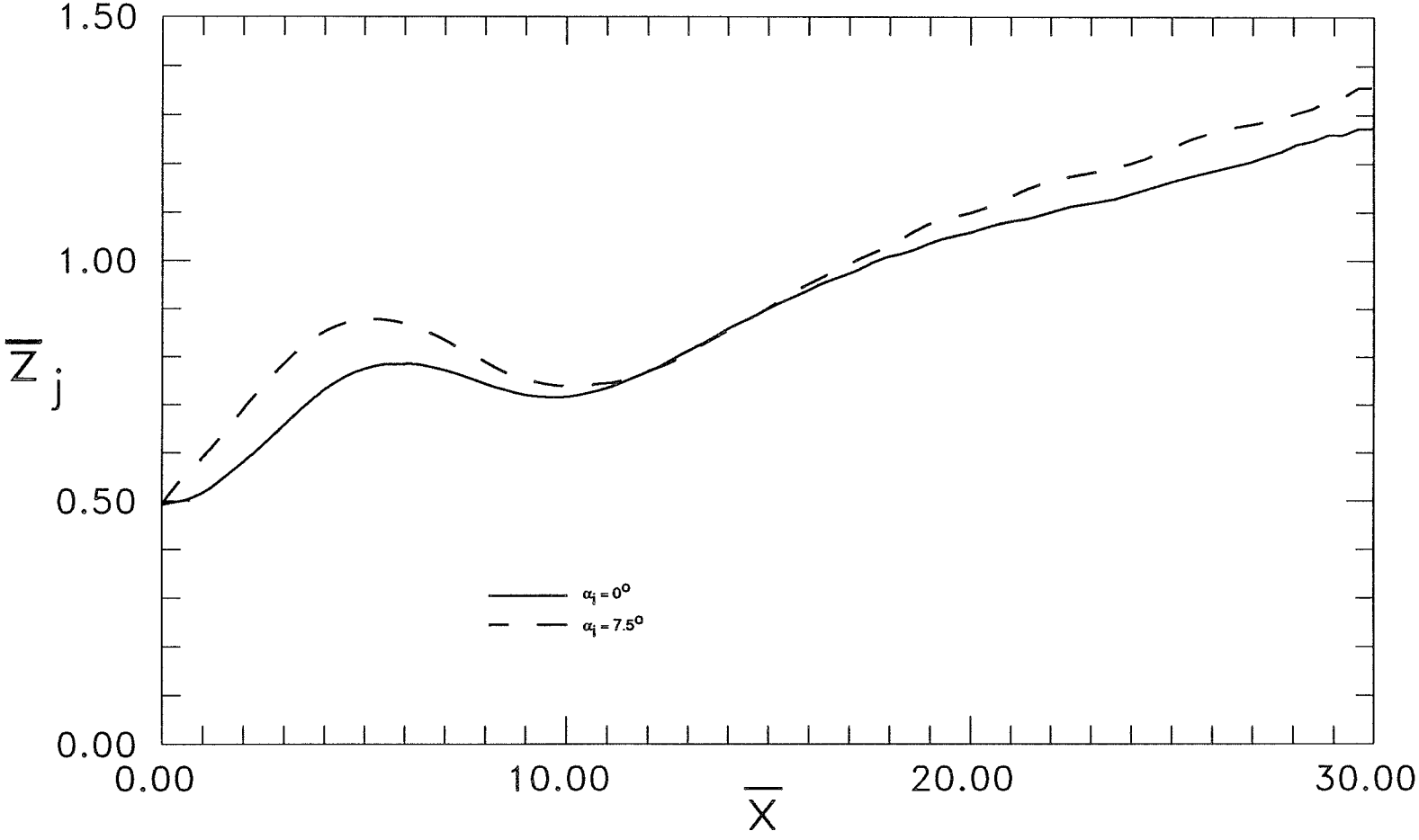

Figure 146. Effects of injectant flow angle on jet lift-off.

Wide spacing, $\overline{\delta} = 0.2$, $\overline{p} = 1.0$, $\overline{v} = 1.0$, $\alpha_c = \alpha_e = 4.76^o$ (computational).

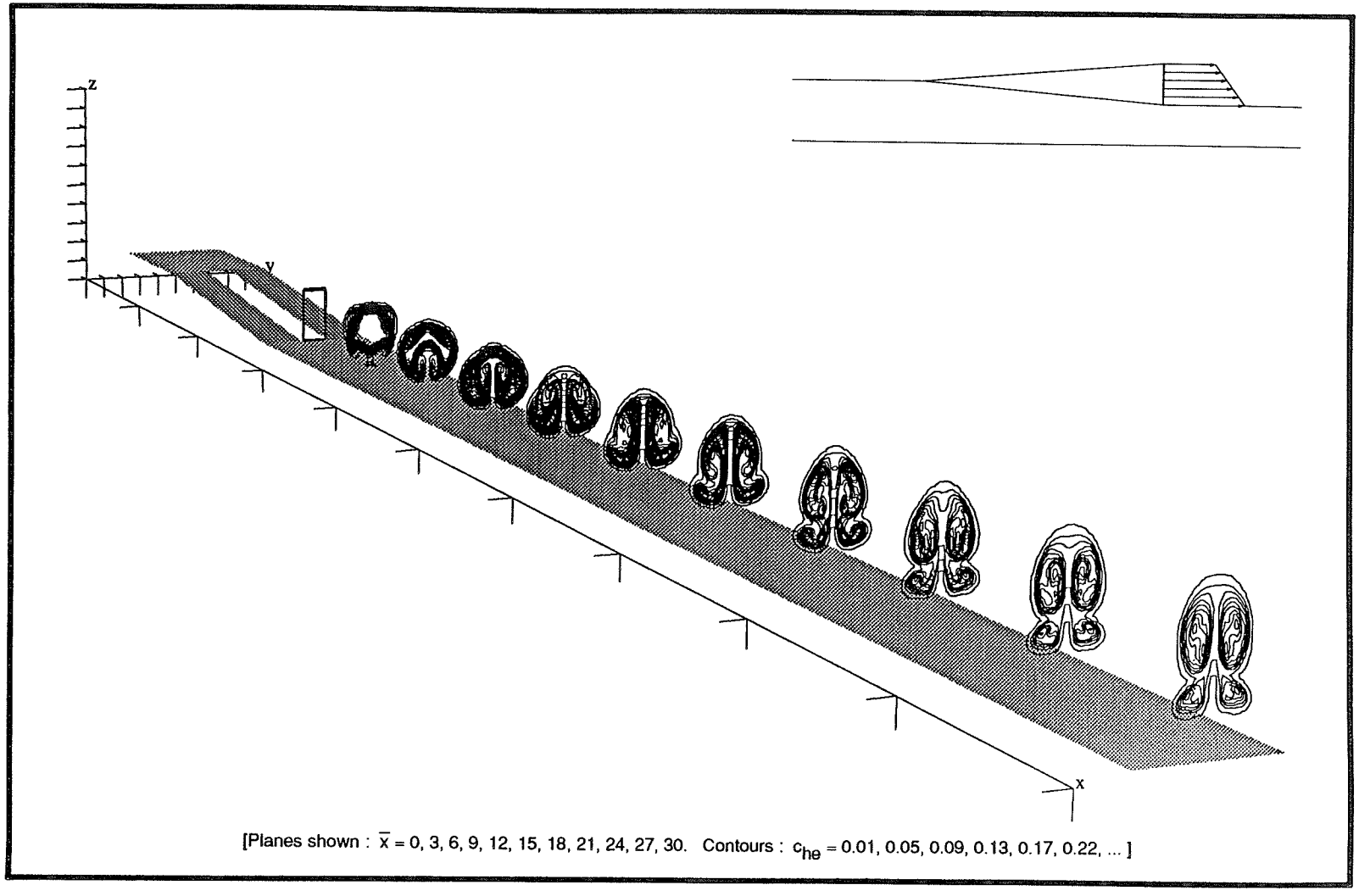

Figure 147. Contours of constant helium mass fraction.

Wide spacing, $\bar{\delta}$ = 0.20, $\bar{p}$ = 1.0, $\bar{v}$ = 1.0, $\alpha_c = \alpha_e = 4.76^o$, non-uniform injectant Mach number profile : ramped from 1.9 to 1.5

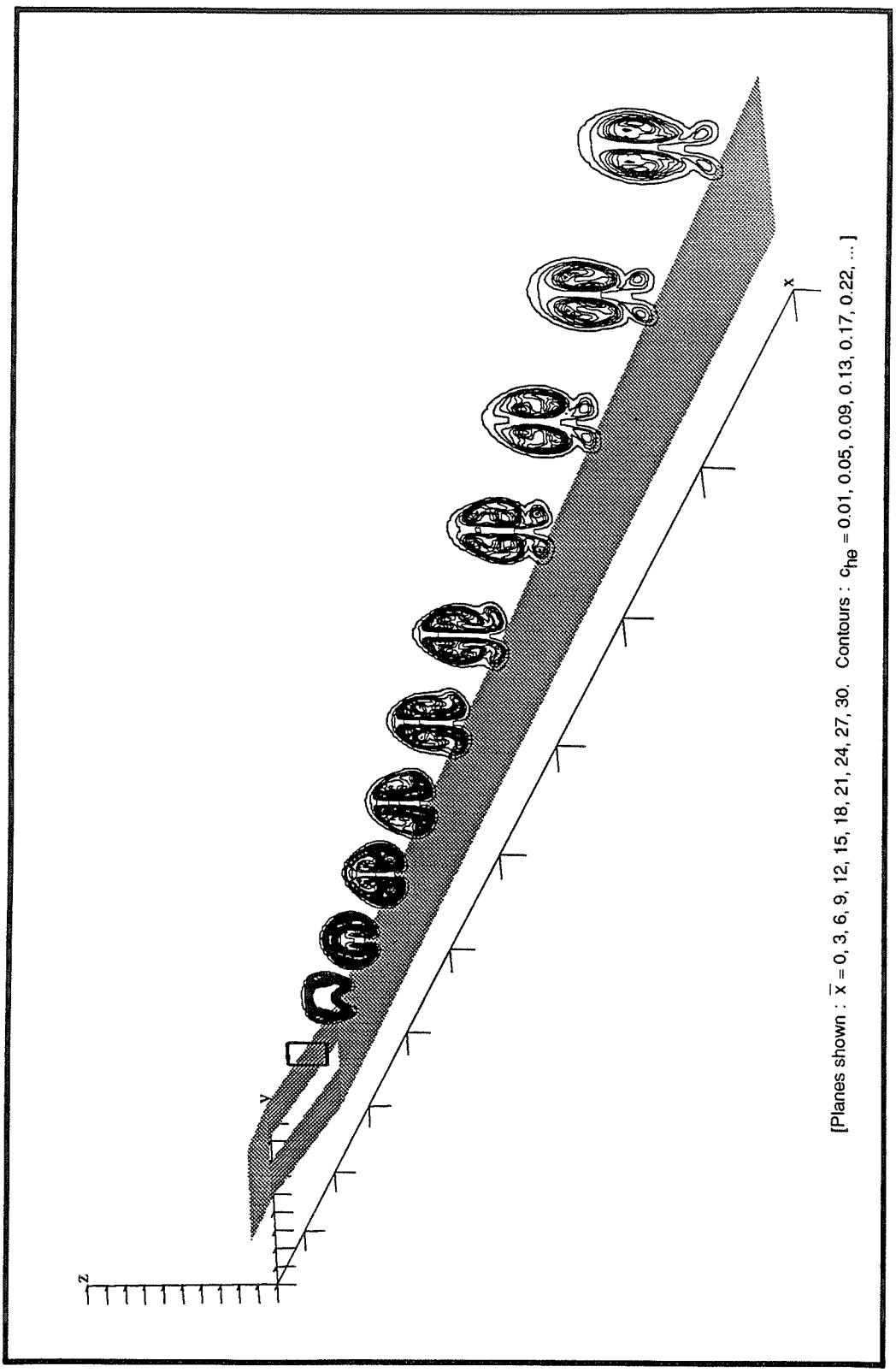

Figure 148. Contours of constant helium mass fraction.

Wide spacing, $\bar{\delta}$ = 0.20, $\bar{p}$ = 1.0, $\bar{v}$ = 1.0, $\alpha_c = \alpha_e = 4.76^o$, injection elevated above surface (computational).

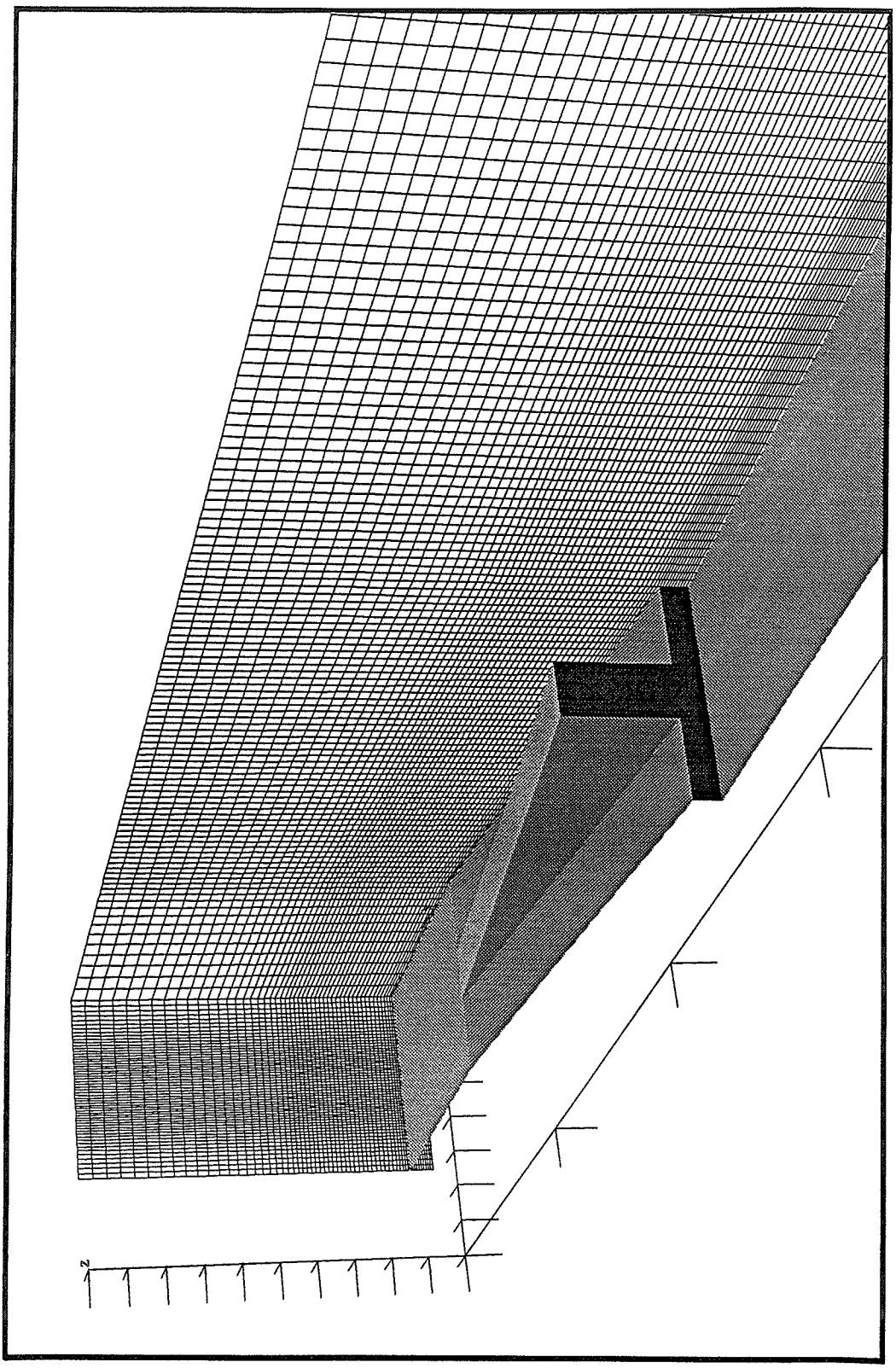

Figure 149. Addition of film-cooling to the injection scheme, $\alpha_C = \alpha_E = 4.76^0$.

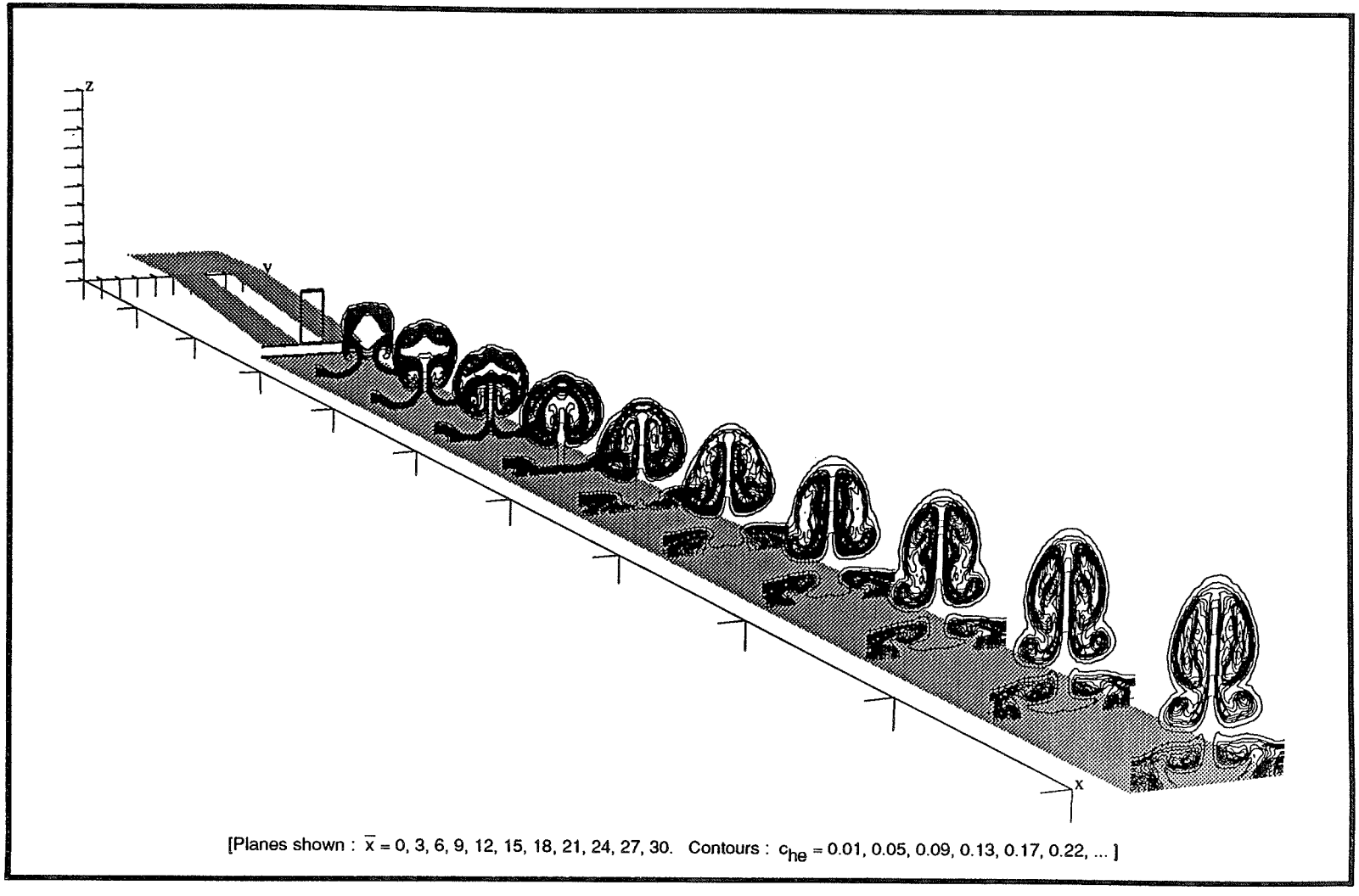

Figure 150. Contours of constant helium mass fraction.

Wide spacing, $\overline{\delta}$ = 0.20, $\overline{p}$ = 1.0, $\overline{v}$ = 1.0, $\alpha_c = \alpha_e = 4.76^o$, film-cooling model (computational).

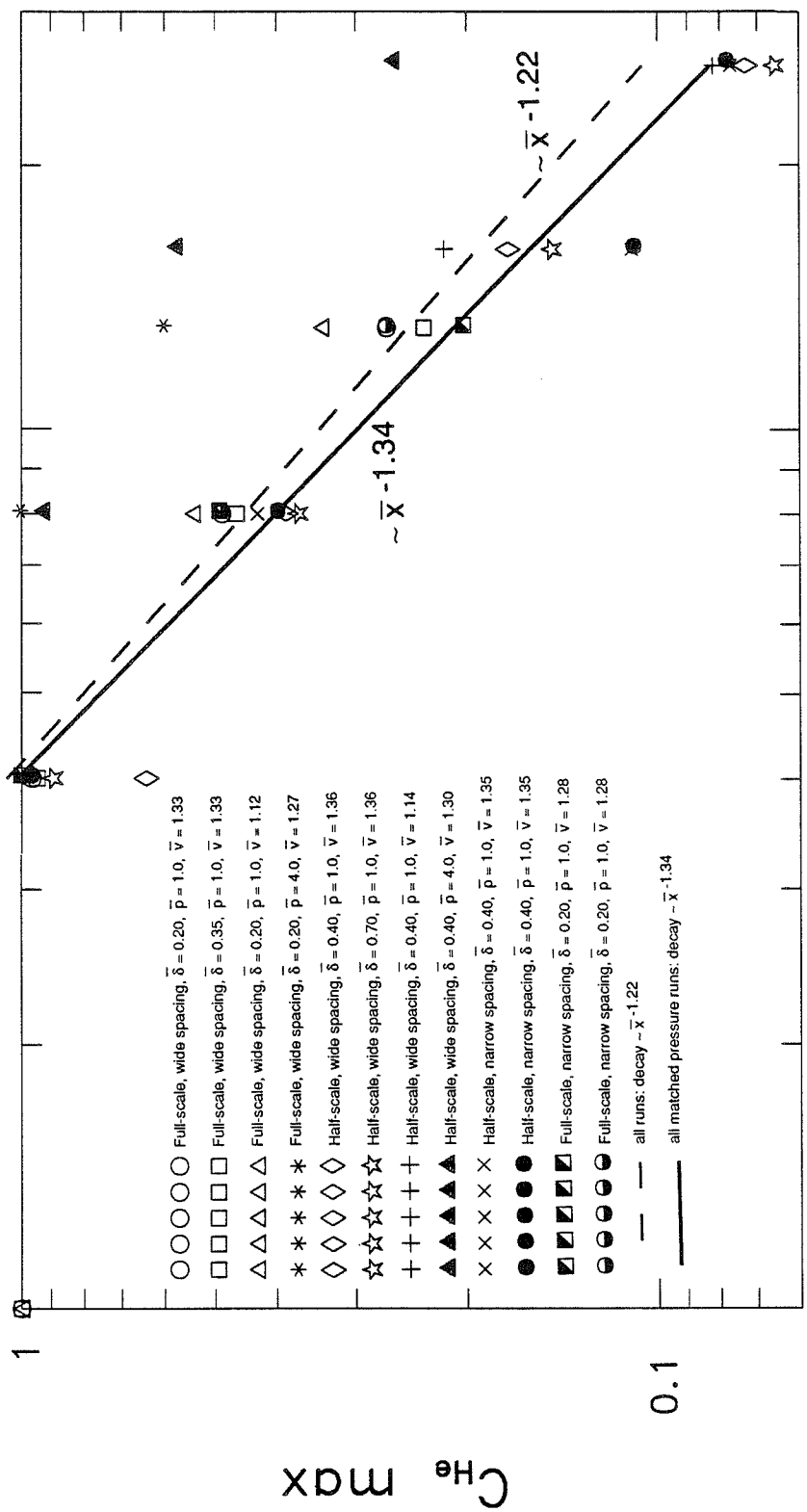

Figure 151. Decay of maximum helium concentration for experimental data.

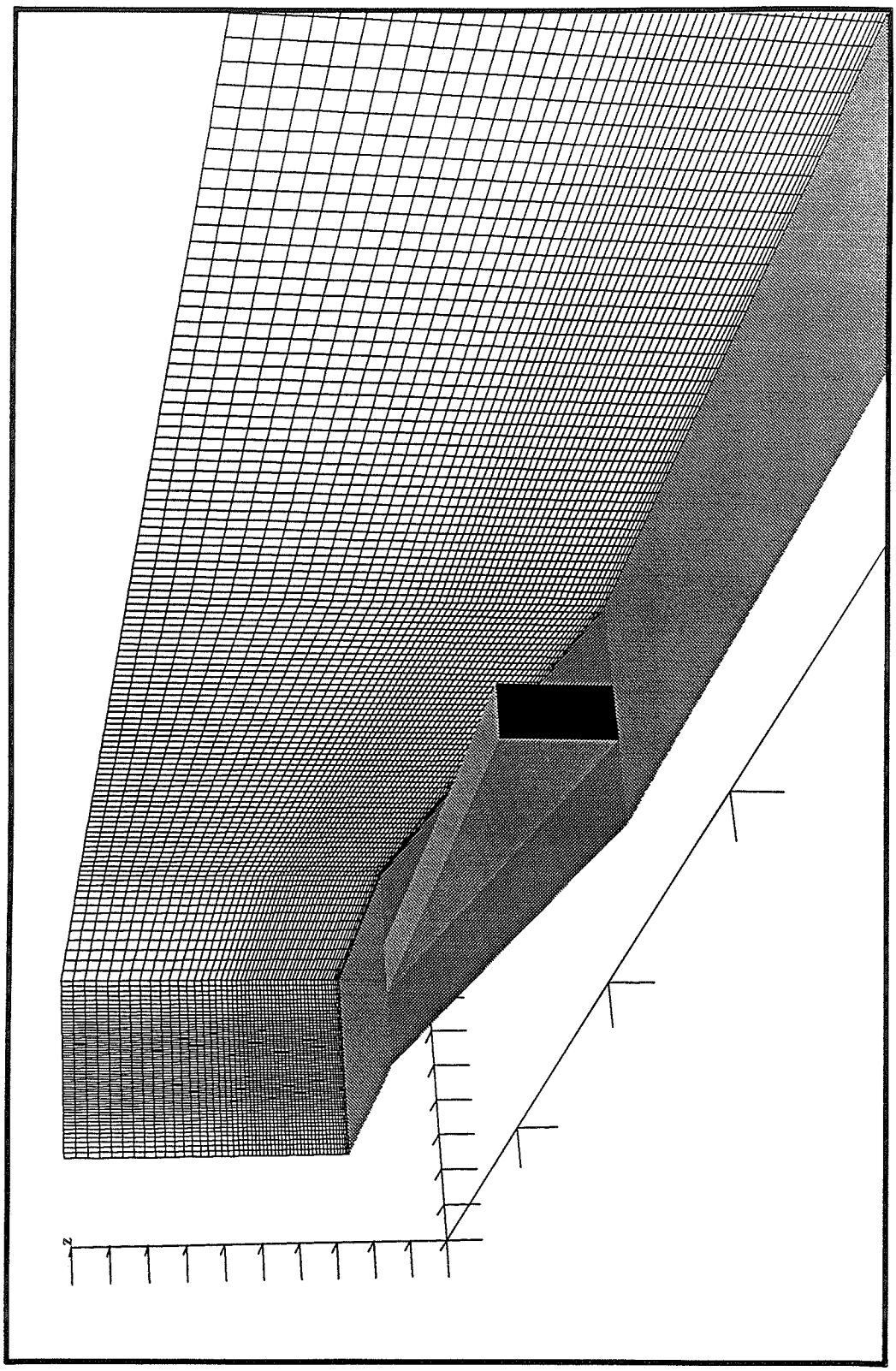

Figure 152. The all expansion geometry, $\alpha_c = 0^o$, $\alpha_e = 9.46^o$

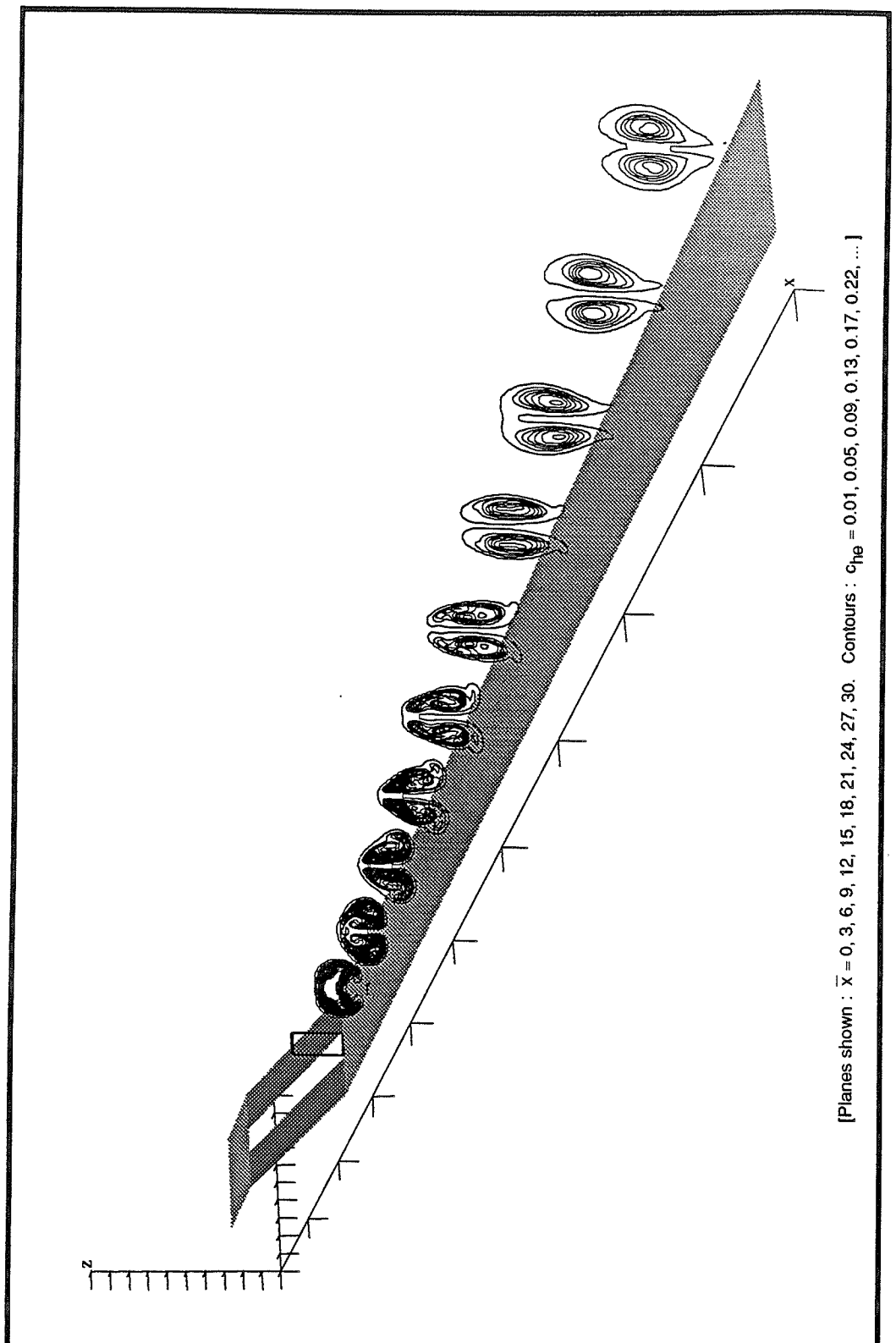

Figure 153. Contours of constant helium mass fraction.

Wide spacing, $\bar{\delta}$ = 0.20, $\bar{p}$ = 0.4, $\bar{v}$ = 1.0, $\alpha_c = 0^o$, $\alpha_e = 9.46^o$ (computational).

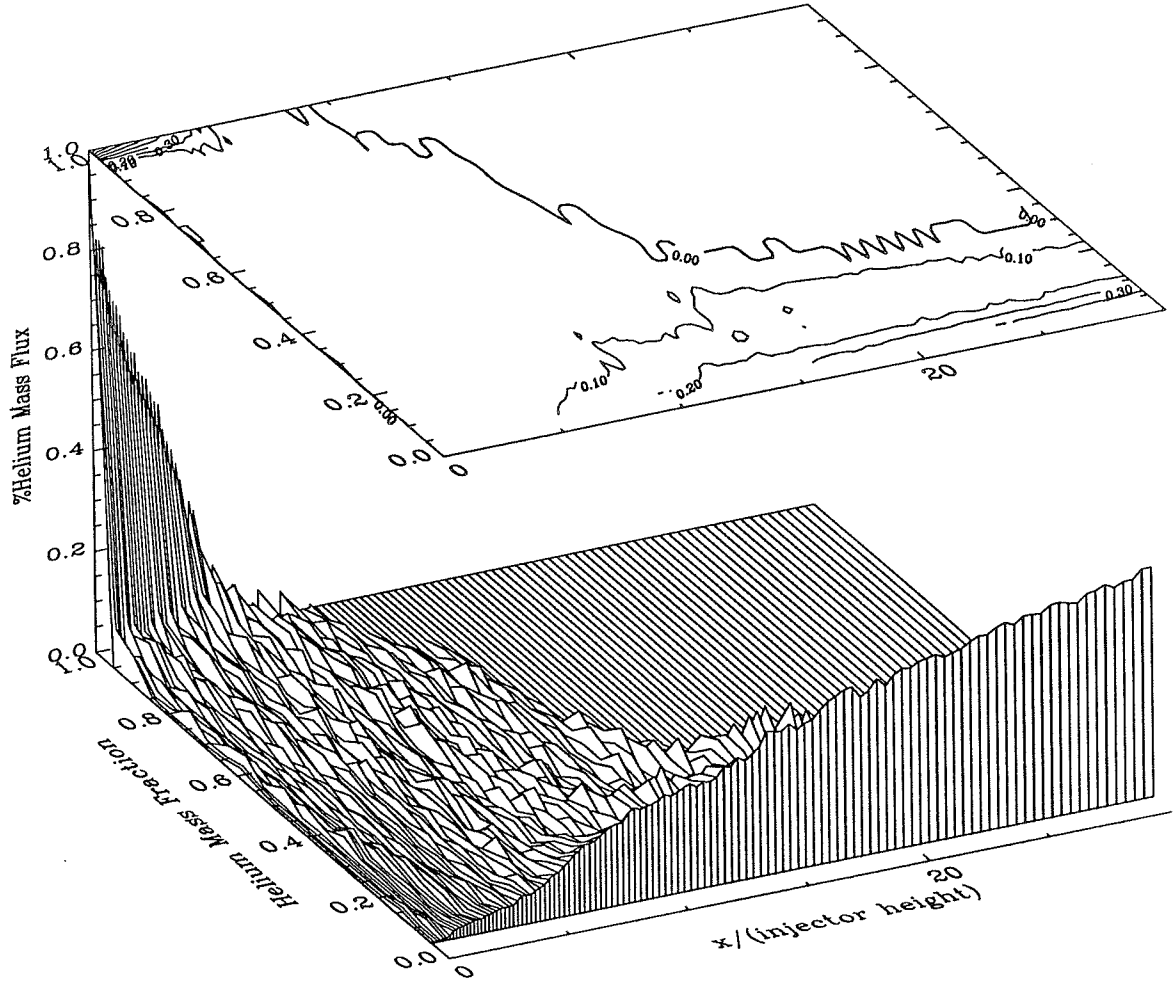

Figure 154. Mixedness Measure. Wide spacing, $\overline{\delta} = 0.20$, $\overline{p} = 0.4$, $\overline{v} = 1.0$, $\alpha_c = 0^o$, $\alpha_e = 9.46^o$ (computational).

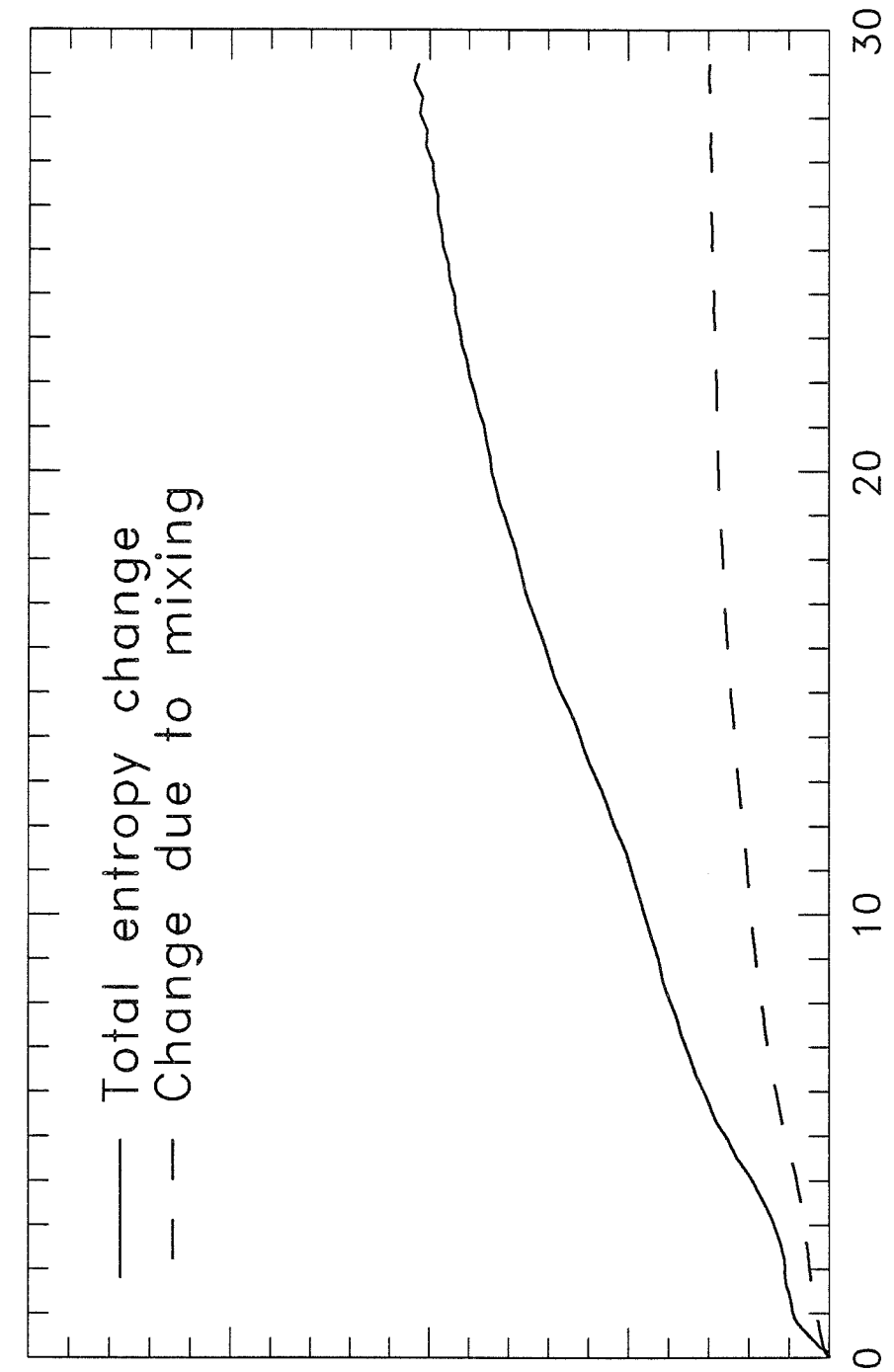

Figure 155. Entropy measure. Wide spacing $\bar{\delta} = 0.2$, $\bar{p} = 1.0$, $\bar{v} = 1.0$, $\alpha_c = 0^o$, $\alpha_e = 9.46^o$ (computational).

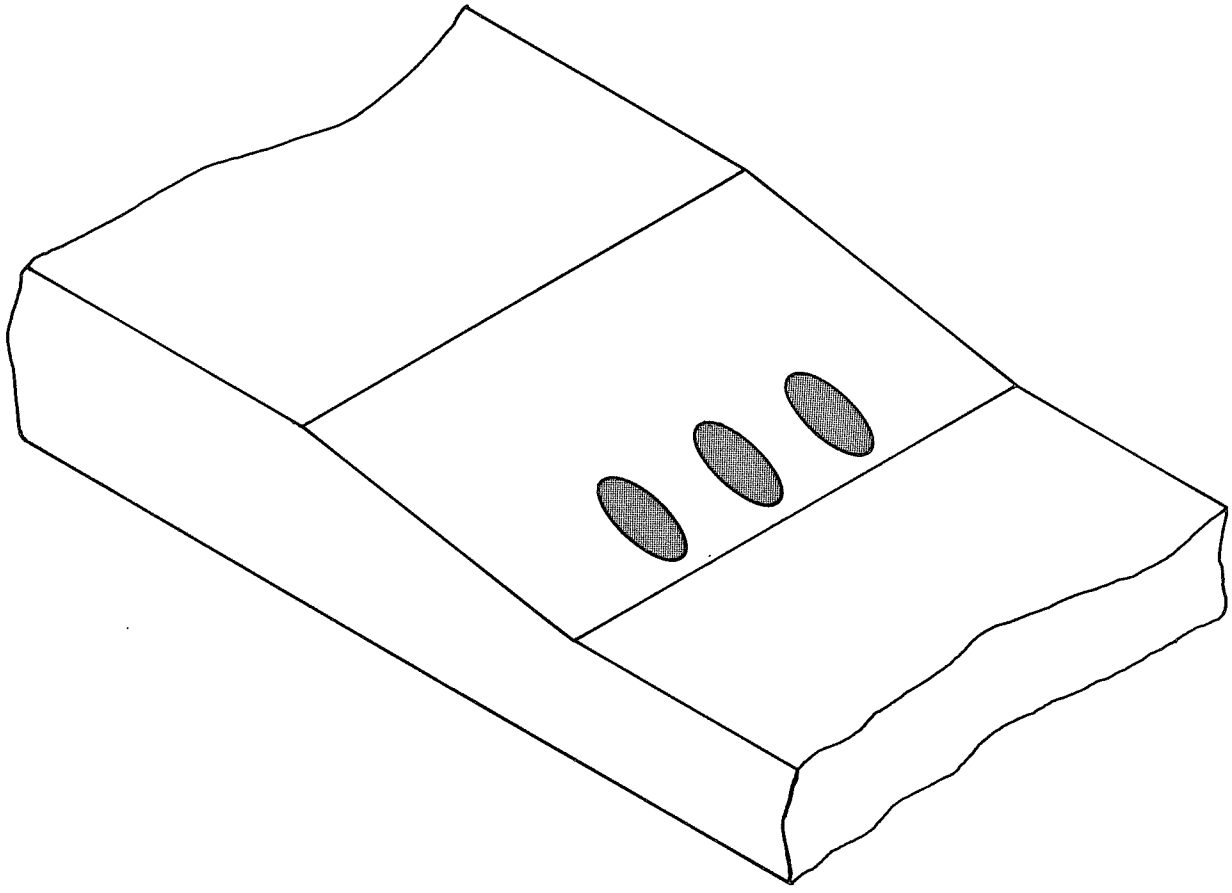

Figure 156. Combination of angled transverse injection and shock-enhancement.